(NASA-CR-155234) FAR-INFRARED PHOTOMETRY WITH AN 0.4-METER LIQUID HELIUM COOLED BALLOON-BORNE TELESCOPE Ph.D. Thesis (Cornell Univ., Ithaca, N. Y.) 282 p HC A13/MF A01 CSCL 14E G3/43

N78-11449

Unclas 52788

CORNELL UNIVERSITY

Center for Radiophysics and Space Research

ITHACA, N. Y.

CRSR 673

FAR-INFRARED PHOTOMETRY WITH AN 0.4-METER LIQUID HELIUM COOLED BALLOON-BORNE TELESCOPE

A Thesis

Michael Ray Jacobson

FAR-INFRARED PHOTOMETRY WITH AN 0.4-METER LIQUID HELIUM COOLED BALLOON-BORNE TELESCOPE

A Thesis

Presented to the Faculty of the Graduate School

of Cornell University

in Partial Fulfillment for the Degree of

Doctor of Philosophy

by

Michael Ray Jacobson

August 1977

FAR-INFRARED PHOTOMETRY WITH AN 0.4-METER LIQUID HELIUM COOLED BALLOON-BORNE TELESCOPE

Michael Ray Jacobson, Ph. D.
Cornell University, 1977

An 0.4-meter aperture, liquid helium cooled multichannel far-infrared balloon-borne telescope has been constructed to survey the galactic plane by a team from Cornell University and the University of Arizona. On its first flight in August, 1976, we achieved sky background limited performance at 100 microns with a sensitivity of 210 Jy/Hz$^{\frac{1}{2}}$. Nine new sources, above a 3-σ confidence level of 1300 Jy, were identified. Although two-thirds of the scanned area was more than 10 degrees from the galactic plane, no sources were detected in that region; all nine fell within 10 degrees and eight of those within 4 degrees of the galactic equator. Correlations with visible, compact HII regions associated with radio continuum and with sources displaying spectra steeply rising between 11 and 20 microns were noted, while stellar objects were not detected.

Along with data analysis, this thesis consists of an exhaustive description of the instrument, followed by an outline of testing and flight staging procedures. The gondola's performance and improvements since flight are discussed at the end. A short chapter on ballooning and appendices on strategies for infrared observations through or above the atmosphere and on infrared emission mechanisms are included.

BIOGRAPHICAL SKETCH

Born in [redacted] on [redacted] the author embraced amateur astronomy at the age of six. He graduated from Taylor Allderdice High School as Valedictorian in 1967 and Harvard College in 1971 with Honors in Physics. After six months at Tel Aviv University's Wise Observatory, he registered in Cornell University's Astronomy Department in January, 1972. He married [redacted], a recent Ph. D. from Cornell's Chemistry Department, in June, 1973. Consolidation of the Balloon Infrared Astronomy experiment necessitated a move to the University of Arizona's Steward Observatory in 1975, where the gondola was completed. Exactly four weeks after the flight in August, 1976, his first son, Tivon Elan, was born.

DEDICATION

To Simone, my wife and companion,

אֵשֶׁת חַיִל מִי יִמְצָא וְרָחֹק מִפְּנִינִים מִכְרָהּ.
בָּטַח בָּהּ לֵב בַּעְלָהּ וְשָׁלָל לֹא יֶחְסָר.
גְּמָלַתְהוּ טוֹב וְלֹא רָע כֹּל יְמֵי חַיֶּיהָ.
עֹז וְהָדָר לְבוּשָׁהּ וַתְּשַׂחַק לְיוֹם אַחֲרוֹן.
פִּיהָ פָּתְחָה בְחָכְמָה וְתוֹרַת חֶסֶד עַל לְשׁוֹנָהּ.

A good wife who can find?
She is worth far more than rubies.
Her husband trusts in her,
And he never lacks gain.
She brings him good and not harm,
All the days of her life. ...
Dignity and honor are her garb;
She smiles looking at the future.
She opens her mouth with wisdom,
And kindly counsel is on her tongue.

Proverbs, 31: 10-12, 16-17.

ACKNOWLEDGMENTS

Graduate study, for the fortunate student, is a microcosm of the scientific world. In my case, over the past five years, I have participated in the realization of an ambitious instrument for surveying uncharted astronomical terrain. I have worked in laboratories and libraries, machine shops and mountain tops, and air bases and balloon bases in faraway places. Since entering Cornell, I've done teaching, research, and administration. Numerous individuals have made these years profoundly educational, and, indeed, inspiring.

Martin Harwit, my advisor, by demonstrating faith in my efforts during the difficult period of Cornell/University of Arizona project consolidation, created not only an astronomer, but a friend. His solid judgment and generous nature embody the essence of humane research. Dennis Ward introduced me to the techniques of far-infrared research on the Lear Jet Observatory and later fabricated the detectors that made the balloon flight a success. Jim Houck added technical advice and personal encouragement at critical moments during the Cornell years. Gerry Stasavage's laboratory experience and skill made his advice valuable; while in Tucson, he served as liason with the Cornell infrared establishment, a thankless task I deeply thank him for performing. Perry Phillips and Ming Hing Tai, office mates and IR group members, offered help and friendship, which continue. Peter Gierasch served on my committee and rekindled a fascination with meteorology; Yervant Terzian and Ken Greisen have graciously served on my committee as well. Carl Sagan, as Field Representative, brought me to Cornell and sustained an interest in my progress. The entire astronomy faculty provided a very high level of instruction; my notes remain an authoritative source of information. I extend special thanks to the

skilled and helpful CRSR staff for their cooperation and competence in handling a somewhat unusual set of technical and administrative problems.

When I arrived in Tucson, Bill Hoffmann became a second advisor and advocate during the unexpectedly long Spring away from my wife, who had a teaching commitment at Cornell. He continues to amaze me with his energetic involvement in a number of innovative projects. A special acknowledgement of gratitude goes to Murray Campbell, a young scientist with remarkable patience, tenacity, and common sense, who set a superb example in bringing the experiment to fruition. Much of my scientific education at the University of Arizona is to Murray's credit. Paul Harvey and Jim Mueller have always shared their knowledge of things astronomical and electronic, respectively. The Steward Observatory machinists, Stan Mileski and Bob Miller, do extraordinary work, despite the exotic demands of balloon astronomers. I owe the same thanks to the Physics Department professionals: John Murphy, our welder, and Bud Smith, head of the Liquid Gas Facility. Bill Marum drafted the figures in the thesis with flair and accuracy, and Rich Schiff photographed, rephotographed, and printed the numerous plates with skill and good humor. I am grateful to the Steward Observatory staff for help on countless occasions.

In Texas, I met the members of the world's most competent, versatile, and friendly balloon facility. Through the five solid weeks of frantic flight preparation, they supported and encouraged us, and on the night of August 4-5, 1976, they made the tricky business of balloon launching, flight, and recovery look easy. Finally, I acknowledge the Research Assistantship from NASA Grant NGR-33-010-172 for the years 1974-1977.

Tucson, Arizona

July, 1977

TABLE OF CONTENTS

LIST OF FIGURES

LIST OF TABLES

PREFACE ON UNITS AND TERMINOLOGY

A few words on format and units will be helpful to the reader. Because this thesis is partially devoted to the technical aspects of balloon astronomy and of our instrument, some cross-referencing is made. Cross-references follow the outline format of the Table of Contents, where the Roman numerals are Chapters, the upper case letters are Parts, and the lower case letters are Sections. For example, the Cornell University photoconductors are discussed in III. G. 2. References are made by author and year of publication; they refer to a single bibliography at the end of the thesis. Depending on context, the author is either included with the year of publication in parentheses or precedes the parentheses. For example, I may write either " ... the HII regions observed by Hoffmann, et al (1971b) ... " or " ... HII regions were observed (Hoffmann, et al, 1971b) ... ". Figures, Tables, and Equations are numbered sequentially within each Chapter.

Spelling and usage follow Webster's New Collegiate Dictionary, Merriam-Webster, 1976.

The metric system is used, except in descriptions of most telescope components, which were designed in the English system. "Mil", "in", "ft", "oz", and "lb" denote one-thousandth of an inch, inch, foot, ounce, and pound, respectively. Infrared astronomers used the micron, abbreviated "μ", as the basic wavelength unit, and cm^{-1} as the basic frequency unit. For radio astronomy observations, millimeters and centimeters are employed.

Frequency units are standard — "Hz, kHz, MHz, and GHz" for "1, 10^3, 10^6, and 10^9 cycles per second. Time and right ascension units are "s", "m", "h", "dy", and "yr" where abbreviated.

Coordinates are numerous. First of all, "°", " ' ", and " " " refer to arc degree, arc minute, and arc second. Feet and inches are spelled out! Square degrees are called "deg^2"; steradians are "sr". Telescope and gondola coordinates are defined in Figure III-2. Celestial coordinates are reduced to Epoch 1950.0. Elevation and azimuth are abbreviated "el" and "az". Strictly, the telescope's azimuth coordinate is cross-elevation, but we did not distinguish the two in analyzing the first flight. Galactic coordinates are in the IAU system (l^{II} and b^{II}) and are denoted as "l" and "b" for longitude and latitude.

Apparent magnitudes are abbreviated by "m", with an appropriate upper case subscript for the spectral band. Fluxes are usually reduced to Janskys, or "Jy", which are equivalent to 10^{-26} W/m^2-Hz.

Temperatures are given in degrees Kelvin, " ^{o}K ", or degrees Centigrade, " ^{o}C ". Effective, brightness, and color temperatures are "T_e, T_b, and T_c" respectively.

Frequently used abbreviations include:

"CABBAGE" — Cornell-Arizona Balloon-Borne Astronomy Group Experiment,

"IR" — infrared; "near-IR" covers 1 to 40 microns, and "far-IR" covers 40-1000 microns,

"pc" — parsec, or 3×10^{18} cm,

"PC" — photoconductor, and "BOL" — bolometer,

"Ge:Ga" — the former elemental symbol is the host crystal and the latter is the dopant,

"LN_2" — liquid nitrogen, and "LHe" — liquid helium,

"NSBF" — National Scientific Balloon Facility, which is operated by "NCAR", the National Center for Atmospheric Research.

CHAPTER I

Introduction

A. The Far-Infrared Frontier: The Need for a Survey

Only ten years ago, Hoffmann, et al (1967) carried out the first sky surveys at far-infrared wavelengths with a one-inch balloon-borne telescope. Astronomy's relatively recent development between 40 and 1000 microns is due to the atmosphere's extreme opacity — Farmer and Key (1965) observed no solar emission from a 5200 meter peak in Bolivia between 40 and 300 microns. The rotational spectrum of water vapor (Figure I-1) is the primary absorber; telescopes aboard aircraft, balloons, and rockets overcome this limitation when lifted above the tropopause, beneath which most of the water vapor is concentrated. Balloons remain the best vehicles for surveys, since they float for hours at altitudes with nearly complete transmission and low emissivity in the far-IR (Figure II-1). Lower-flying aircraft must contend with higher backgrounds, while rockets must deal with very short observation periods.

Hoffmann's efforts bore fruit with the discovery of an intense 100 micron source at the galactic center in 1968 (Hoffmann and Frederick, 1969). He then replaced Gondola A, the one-inch, with Gondola B, a twelve-inch telescope, and made the major contribution to our knowledge of the galactic plane at 100 microns (Hoffmann, et al, 1971b). The sixteen-inch telescope we designed and constructed at Cornell University and the University of Arizona represents Gondola C, the next step toward greater sensitivity and more complete sky surveys in the far-IR. Figures I-2 and I-3 and Appendix A trace other landmarks in the development of infrared astronomy.

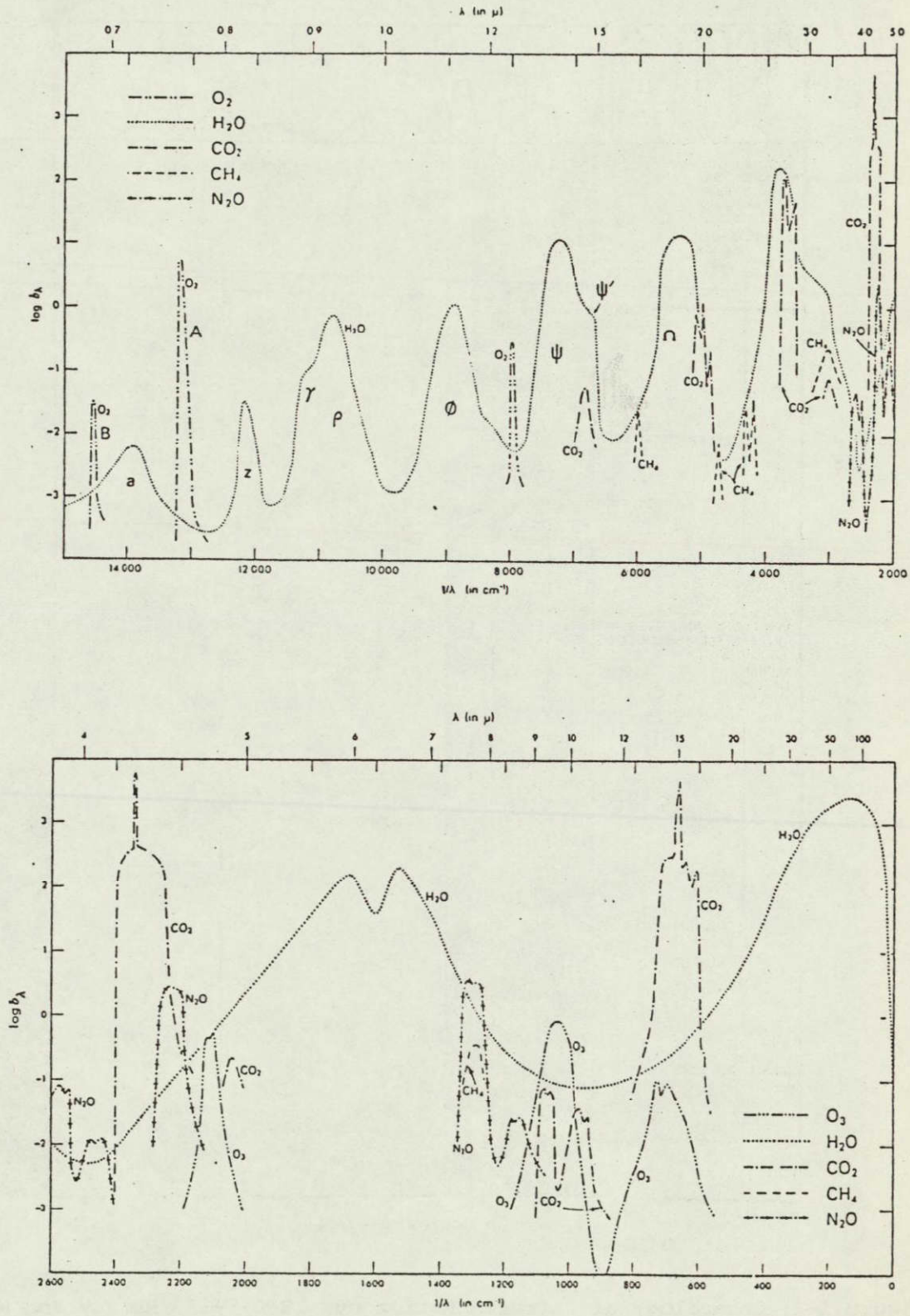

FIGURE I-1: Atmospheric absorption in terms of b_λ, the reciprocal of the thickness (in atm-cm units) that would give 50% absorption or transmission. From Allen, (1973).

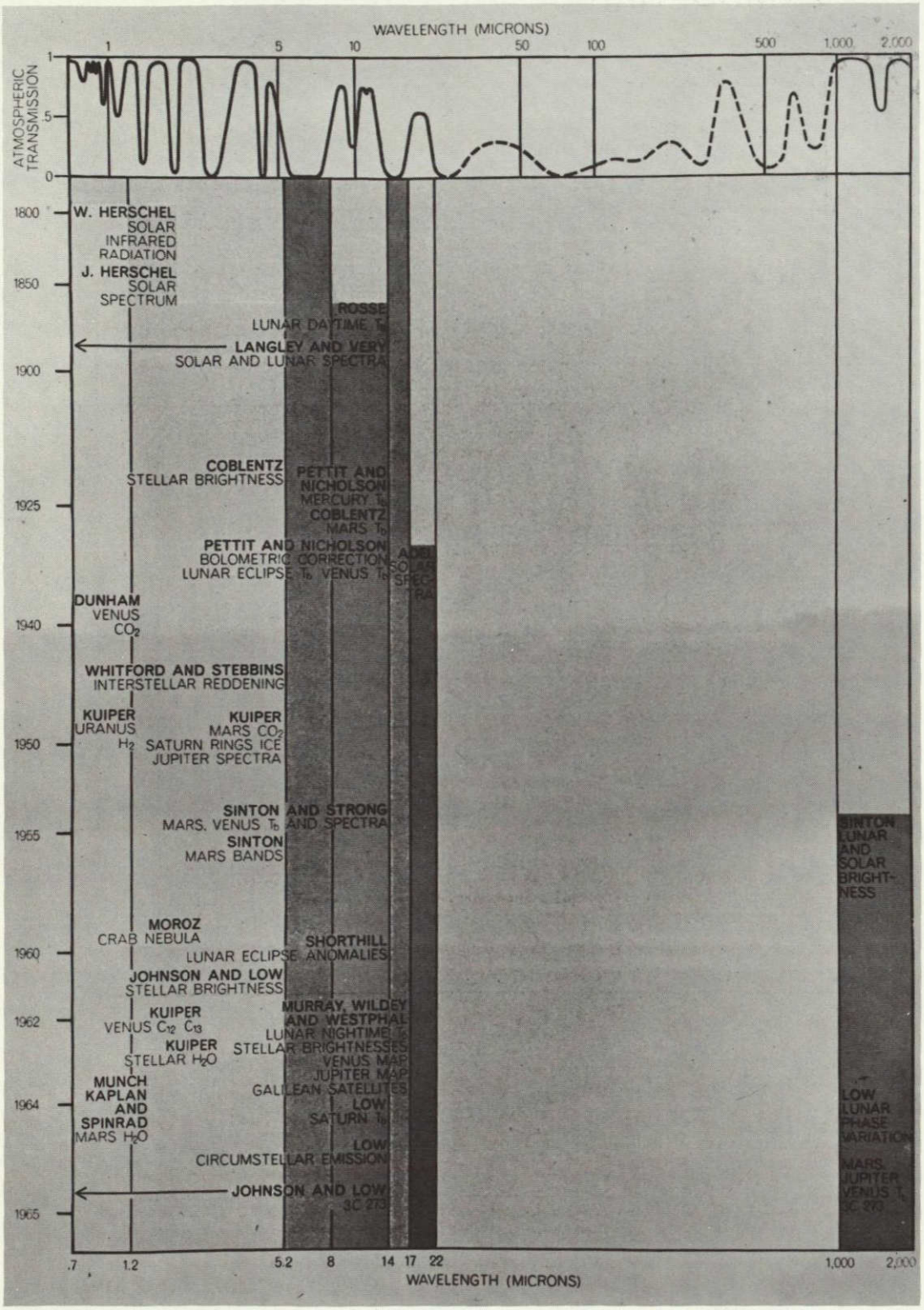

Figure I-2: Chronology of Infrared Astronomy, 1800-1965 (Murray and Westphal, 1965). The transmission curve at the top is qualitative, showing conditions near 10,000 feet in the near-IR and 30,000 feet in the far-IR.

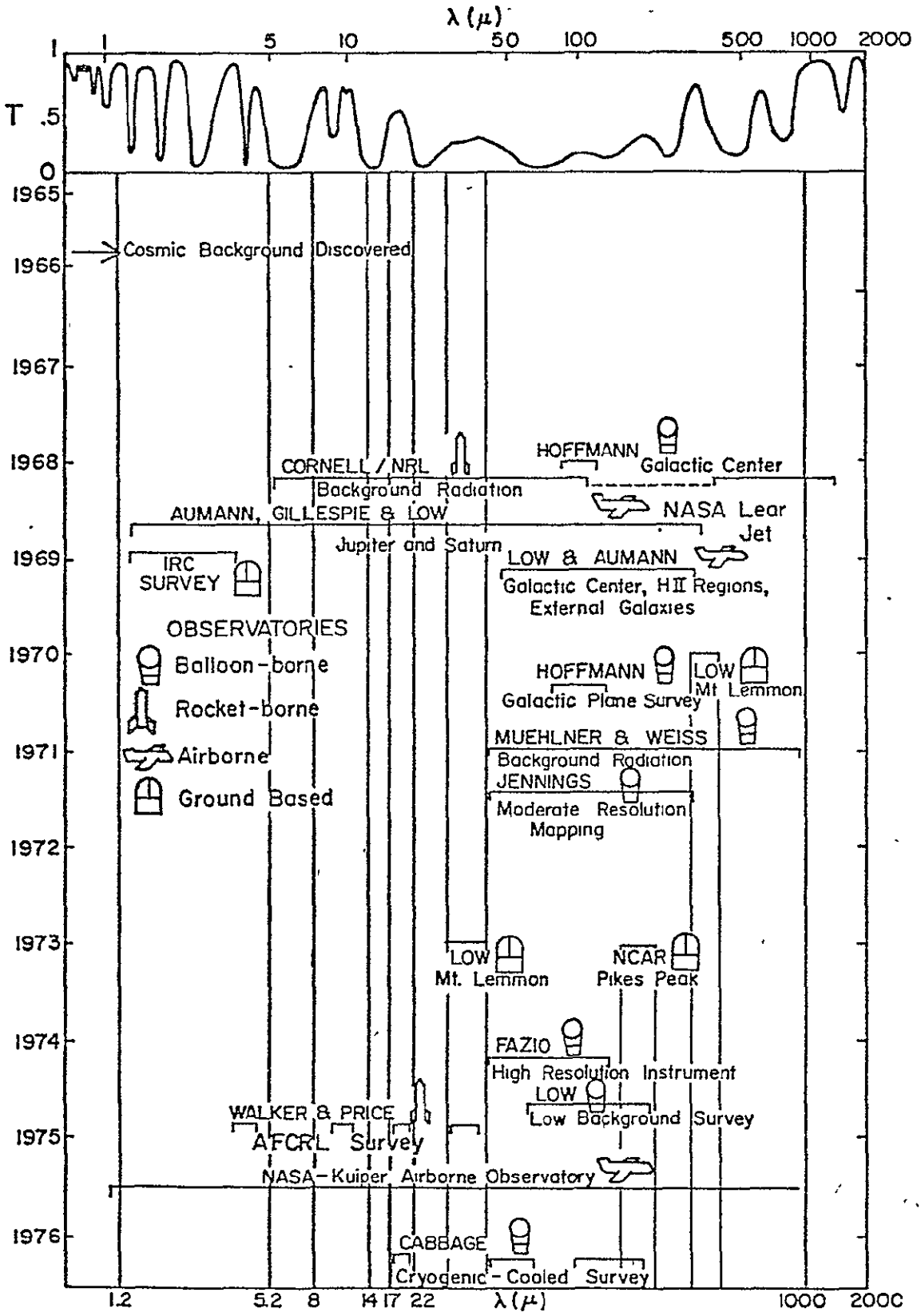

Figure I-3: Chronology of Infrared Astronomy, 1965-1976. References are found in Appendix A. The transmission curve and format follow Figure I-2.

At present, no systematic surveys of the sky exist between the Air Force Geophysics Laboratory's rocket survey (Walker and Price, 1976) at 4, 11, 20, and 27 microns and radio continuum surveys near 21 cm. Even the galactic plane is not well mapped shortwards of 6 cm (Altenhoff, et al, 1970; Goss and Shaver, 1970). Because of the different emission processes that dominate in the wide gap between the surveys, interpolation helps little in identifying dominant far-IR sources. Evidence accumulated thus far indicates that stellar photospheres and circumstellar envelopes are too hot to be prominent at 100 microns, and free-free continuum radiation, emitted by hot, ionized gas in HII regions, is similarly feeble in the far-IR. (See Figure I-4 and Appendix B.) Lower temperature phenomena engender the strongest sources in this spectral region. A survey is needed to classify such objects, including new types of sources, to permit statistical analysis, and to flag interesting examples for detailed study.

Chapter I proceeds with brief introductory material on far-IR objects, their impact on astronomical questions, and other balloon-borne surveys. A more comprehensive review on the emergence of IR astronomy comprises Appendix A. Chapter II relates general infrared techniques and the more specialized concerns of balloon astronomers, while Chapter III exhaustively covers the instrument, including the heretofore undocumented electronics, pointing, and suspension systems of Gondola B, which were only slightly modified for use in Gondola C. Chapter IV describes the ground support equipment, testing procedures, and flight staging. The results of Flight C-1 are contained in Chapter V, and Chapter VI notes technical improvements planned or made since the flight and observational goals for future flights.

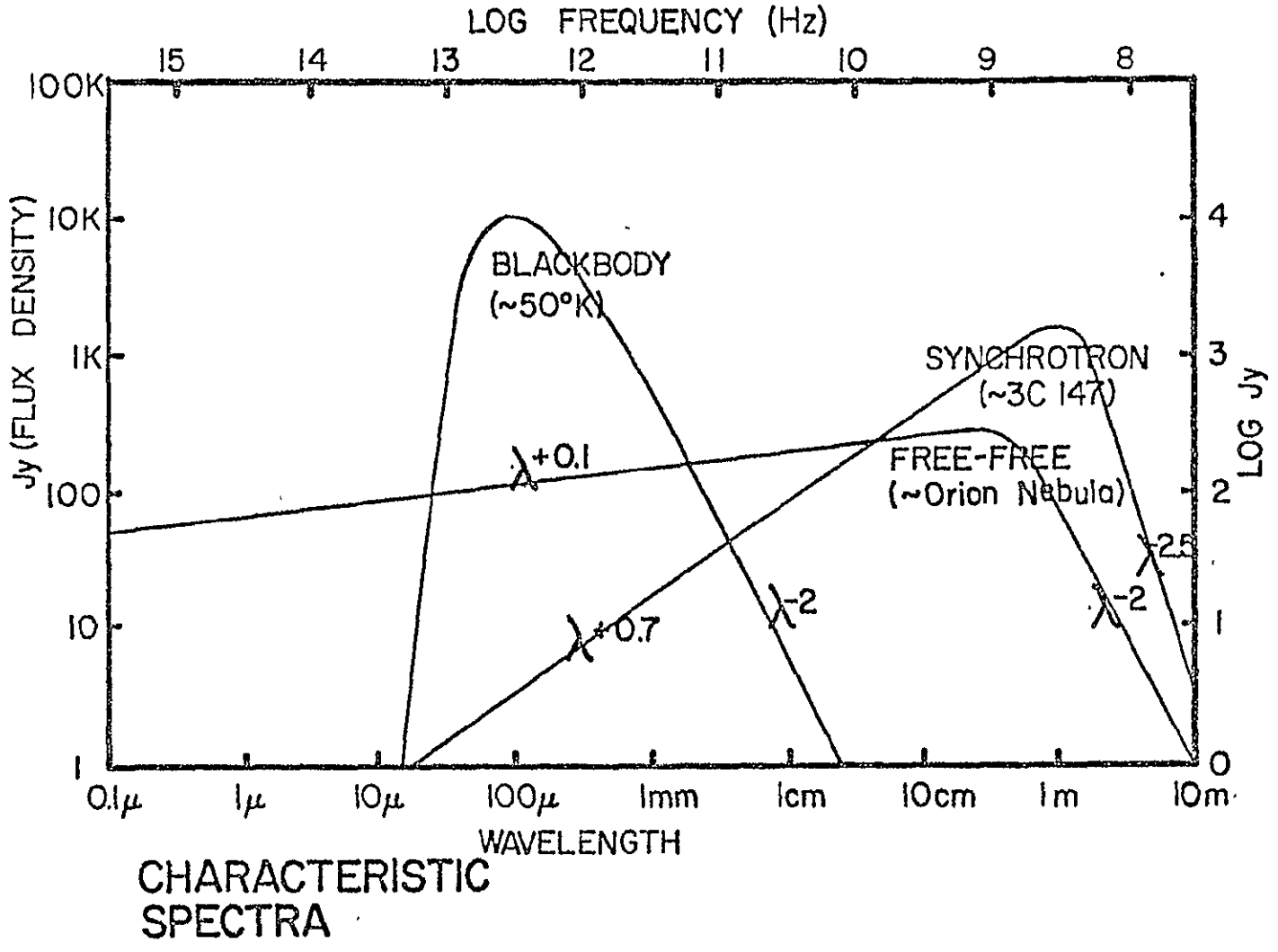

Figure I-4: Characteristic spectra for three emission processes in the far-infrared. See Appendix B for references.

B. Far-Infrared Sources

At present, five broad categories of objects with peak emission in the far-infrared[1] have been distinguished: HII regions, molecular clouds, diffuse galactic plane emission, the center of the Galaxy, and other galactic nuclei. For all but some external galaxies, dust reradiation of absorbed stellar photons is the probable emission process. Roughly two-thirds of the objects tabulated by Hoffmann,et al (1971b) are identified with HII regions, with flux densities ranging from the survey limit of 10^4 Jy to 6.4×10^5 Jy for Sgr B2, the most luminous known HII region at 100 microns. In these objects, dust captures both Lyα photons scattered within the region and Lyman continuum photons directly from the hot stars and emits thermally in the infrared at a temperature that depends on its emissivity. This has been demonstrated by the rough correlation of radio continuum and far-IR fluxes, related to gas and dust components, respectively, for several HII regions (Harper and Low, 1971; Furniss, et al, 1974). As additional surveys have extended sensitivities to 10^3 Jy, HII regions continue to comprise at least half of the new sources. This indicates that dusty HII regions are common, and that the very luminous stars responsible for the ionization of the gas heat large volumes of dust as well, giving HII regions their far-IR prominence.

Most of the remaining objects are associated with dark, dusty clouds, which are often rich in molecules detectable by radio-wavelength spectroscopy. Dickman (1977) distinguishes between molecular

[1]Nearby solar system objects are prominent in the infrared; the outer planets emit strongly in the far-IR and are useful for calibration and beam profile determination.

clouds, which are large, rather dense, and very massive (often embracing several thousand solar masses), and dark clouds, which are smaller, less dense, and less massive. The former are usually associated with HII regions and are bright far-IR objects. Such molecular clouds do not always exhibit radio continuum, indicating that cooler, non-ionizing stars or proto-stars lie within, heating the dust. The brightest at 100 μ is the Kleinmann-Low Nebula in the Orion Nebula complex with a flux density of 10^5 Jy (Low, 1977b). Dust temperatures are typically cooler in molecular clouds than in HII regions. A 350 micron study by Righini (1975) illustrates a strong spatial correlation between cooler dust and molecular emission.

Diffuse emission along the galactic plane between 40 and 200 microns has been detected by a number of observers (Ricker, et al, 1973; Pipher, 1973; Rouan, et al, 1977; Serra, et al, 1977; Low, et al, 1977a). A narrow band of emission underlies individual sources and widens from less than a degree to at least four degrees at the galactic nucleus. Apparently, a dusty disk heated by numerous, cooler stars in addition to more isolated, hot stars is responsible.

The galactic center produces the greatest apparent brightness at 100 μ —1.5×10^6 Jy (Hoffmann, et al, 1971a) — of any source outside of the solar system and represents a rich array of IR phenomena. Gatley, et al (1977) have presented a model, based on detailed maps, explaining the far-IR flux that requires only thermal emission from dust heated by the dense, late-type star concentration seen at 2.2 μ and the hot stars which ionize HII regions in the same volume. Only three external galaxies have been seen at 100 μ as of mid-1976: M82, NGC 253, and NGC 1068. About 200 have been observed in the near-IR, and most fluxes can

be attributed to dust-mediated stellar emission. The brightest IR emitting galaxies may require dust reradiation of non-thermal radiation (Rowan-Robinson, 1977).

Other classes of far-IR objects are likely to be discovered as sensitivity increases and sky coverage becomes more complete. Low (1977b) speculates that very cold clouds of dust, heated only by diffuse starlight and peaked at 300 μ, are probable, and that dust-laden galaxies, detectable only in the far-IR, are possible. Somewhat better resolution may isolate smaller dark clouds and dark globules — very dense, cold, and compact dust clouds — which may be sites, along with molecular clouds, of star formation (Bok, 1977; Dickman, 1977).

C. Impact on Basic Astronomical Questions

Far-IR surveys, by tying together optical, near-IR, and radio observations of known sources and revealing otherwise unobservable sources, promise to clarify several basic problems, including the loci and rate of star formation in the Galaxy, the nature of the interstellar medium, the overall structure of the Galaxy, and the activity in some classes of external galaxies.

Recently, phenomena related to star formation have been discerned through detailed studies of a few complexes of molecular clouds, HII regions, and young stars. For example, the Orion Nebula and W3 complexes have been probed in papers by Werner, et al (1976) and Mezger (1976). Typically, large, dense molecular clouds contain smaller, hotter knots made up of proto-stars or young stars with attendant HII regions. Radio continuum surveys, by detecting the free-free emission from ionized regions, identify hot stars in spite of heavy obscuration by dust, while

IR maps point out areas of reradiation by dust and indicate the presence of both early- and later-type stars. A far-IR survey, in tandem with radio maps, will assemble a larger sample and permit us to judge whether luminous, nearby complexes like the Orion Nebula are typical and to estimate the level of star formation activity over much of the Galaxy. Other questions concern the scale on which molecular clouds collapse and the types of stars presently being formed. In what proportions do large clouds collapse as a whole, breeding populous star clusters, or contract piecemeal, engendering smaller groups or individuals? What is the distribution, among young stars, of mass and luminosity? Can the additional information from multi-band photometry improve our ability to identify regions of star formation through spatial and spectral relationships? A complete survey will contribute to large scale statistical analysis and will flag interesting complexes for higher resolution mapping on smaller scales.

The interstellar medium can be probed by a variety of direct and indirect means; one of the most direct is thermal emission by dust. Its color temperature, intensity, and relationship with sources of heating and with emission from the more abundant interstellar gas all carry important information. A survey may show how uniformly dust is distributed on various scales and how well visual obscuration correlates with IR observations. The effects of young, main-sequence, and evolved stars on the interstellar medium are also of interest.

Recent research on the morphology of the Galaxy, as evidenced by neutral atomic hydrogen in opposition to ionized hydrogen, molecular hydrogen, carbon monoxide, and other tracers, has been reviewed by Burton (1976). The distribution of dust, as a function of galactic

longitude and latitude, will add important data in tying down the Galaxy's basic structure and how it compares to external galaxies. Moreover, cataloging the contents of the Galaxy — masses of obscured stars and cold dust, and the infrared luminosities of the dust, and by inference, hidden stars — will allow refinement of galactic models. Lastly, the preceding questions must be applied with special vigor to the galactic nucleus, where a rich variety of phenomena, apparently distinct from the rest of the Galaxy, must be explained. Likewise, the diffuse galactic emission, which broadens abruptly as the nucleus is approached, must be probed as well.

An unbiased survey at high galactic latitudes will be necessary to determine whether far-infrared emission is typical of external galaxies. The three galaxies that have been seen, as of mid-1976, at 100 μ, were suspected of IR activity on other grounds. The steeply rising spectra toward the far-IR of certain external galaxies and quasi-stellar objects is another cogent reason for a far-IR survey, since reliable statistics on such phenomena may help solve problems of cosmological relevance.

To summarize, the impact of a multi-channel, large beam survey in the far-IR should be greatest in areas concerning source properties on a large scale, such as total extent and luminosity, source statistics, and spatial relationships with optical and radio data. The untangling of smaller structure, such as the problem of whether the dust in evenly mixed with or depleted in compact HII regions[2], must rely on lower throughput mapping instruments. Similarly, the small angular extent and rela-

[2]For a preliminary verdict on this question, obtained with the help of a balloon-borne mapping instrument, see Rodriguez and Chaisson, (1977). For nine galactic HII regions, they limit the radius of dust depletion to 25% of the Strömgren radius.

tively high temperatures of IR stars and circumstellar shells make these objects inconspicuous to large throughput, far-IR survey telescopes (Hoffmann, et al, 1971b).

D. Balloon-borne Surveys

To survey effectively, the gondola must be stable and fully steerable, the beam rather large (∿10-45 arcminutes half-power beamwidth) — in order to sense extended sources and to cover the sky in a reasonable amount of time, the background from telescope and sky low, and the positions reliably computable. Many experiments have been built along these lines and dedicated to survey work, while several others with somewhat higher resolution, for mapping, and lower resolution, for diffuse emission, have performed survey work as a secondary objective. Table I-1 lists these projects. The columns contain parent institutions, primary investigators, gondola edition if more than one, aperture, beamwidth, sensitivity, detectors (PC=photoconductor and BOL=bolometer), bandpasses, flights to date, a reference, and comments. Information unavailable to me is simply left out; I apologize here to any group inadvertently omitted.

Of the dedicated survey instruments, Washington University's predated Hoffmann's. Scanning in full azimuthal circles, it covered about 7% of the sky and detected four sources in 1970. Their second gondola, flown in 1973, scanned similarly and revealed twelve more sources. Neither set was correlated to the galactic plane, and none have been confirmed, but succeeding surveys have stayed near the plane. An approach involving an uncooled Herschellian telescope with very low emissivity was pioneered by the MIT/University of Arizona group. Gold-plated sur-

TABLE I-1· BALLOON-BORNE SURVEY INSTRUMENTS

INSTITUTIONS	INVESTIGATORS	EDITION	APERTURE cm	BEAMWIDTH '	SENSITIVITY 10^4 Jy	DETECTORS	BANDPASSES μ	FLTS	REFERENCES	COMMENTS
Goddard Institute	Hoffmann	A	2.5	138		BOL	300-360 80-120	3*	(Hoffmann and Frederick, 1969)	Galactic center observation
Goddard Institute	Hoffmann	B	30	12	1	BOL	80-120	9*	(Hoffmann, et al, 1971b)	Galactic plane survey
Univ. of Arizona/Cornell	Hoffmann/ Harwit	C	40	12	0.14	PC PC PC BOL	75-130 45-70 18-24 75-120	1	(Campbell, et al, 1977; Jacobson, this thesis, 1977)	Cryogenically cooled telescope
Washington U.	Friedlander	A	20	34	1	BOL	45-250	1*	(Friedlander and Joseph, 1970)	High galactic latitude sources
Washington U.	Friedlander	B	40	40	55	BOL	50-500	2*	(Friedlander, et al, 1974)	
MIT/ Univ. of Arizona	Ricker/Low		20	45		BOL	50-350	1*	(Ricker, et al, 1973)	Galactic plane survey
Univ. of Arizona	Low		20	15	0.1	BOL	60-300 150-300	13	(Low, et al, 1977a)	Galactic plane survey
Univ. of Groningen	Olthof	A	20	30	2	BOL(2)	71-95 115-196†	12*	(Olthof, 1974)	HII region study
Univ. of Groningen	von Duinen	B	60				Four bands	1	(Hoffmann, 1977)	Higher resolution
University College, London	Jennings	A	40	7.5	3	BOL	40-350	16*	(Furniss, et al, 1975)	HII region study and survey
University College, London	Jennings	B	60					1	(Furniss, et al, 1976)	Higher resolution and spectrometry
Max Planck-Heidelberg	Lemke		20			BOL	50-250	1	(Lemke and Haussecker, 1976)	Chopping primary
Meudon Obs.-Paris	Serra			42		BOL	75-95 115-196	1	(Serra, et al, 1977)	Diffuse emission study

*Project completed. †Also 30-38, 84-130, and 111-154μ.

faces and a minimum of structure were employed. Their instrument flew in 1973 and surveyed the plane between $l = 348^{\circ}$ and the galactic center. The University of Arizona group continued the project through 1976 and covered the plane from $l = 348^{\circ}$ to 32.5°; more flights are planned. A team from the University of Groningen first launched in 1969; a number of successful flights in 1971 and 1973 revealed about 20 HII regions in the region $350^{\circ} < l < 35^{\circ}$. Finally, Hoffmann's Gondola B covered the plane in the intervals $260^{\circ} < l < 310^{\circ}$ and $35^{\circ} < l < 88^{\circ}$.

Telescopes not completely dedicated to surveys include an instrument from University College, London which observed known sources and surveyed for new objects at moderate resolution. Between 1971 and 1974, about 50 HII regions were investigated; nearly all were within a few degrees of the plane and many were in a surveyed interval between $l = 327^{\circ}$ and 353°. The new University of Groningen gondola is also meant for moderate resolution, multi-band photometry, while the next University College, London, telescope is designed for spectrometry as well. Two groups with lower resolution are from the Meudon Observatory in Paris and the Max Planck Institute in Heidelberg. The former covered the plane in 1976 between $l = 38^{\circ}$ and 55° and observed diffuse emission underlying brighter sources. A liquid helium cooled rocket experiment dedicated to measuring the far-infrared cosmic background radiation also contributed by observing three HII regions; on two of these Cornell University flights, two regions near the galactic center and one near $l = 160^{\circ}$ were detected (Soifer, et al, 1972). A number of groups are building survey instruments; the most ambitious being from the University of California at Berkeley, involving a 1-meter, low emissivity telescope with seven channels between 10 and 1000 microns for a full sky survey.

Therefore, we find that far-IR surveyors have covered most of the galactic plane to a flux level of roughly 10^4 Jy between $l = 260^\circ$ and $l = 90^\circ$ and within about 3 degrees of the galactic equator. This amounts to about 1000 square degrees or 2.5% of the celestial sphere. On the order of 250 square degrees have been examined at higher galactic latitudes. Thus, nearly half of the galactic plane and nearly all of the rest of the sky await investigation.

Such an investigation is the goal of Gondola C, or CABBAGE, the Cornell-Arizona Balloon-Borne Astronomy Group Experiment. Our 16 inch telescope projects a $12'$ beam on the sky; with corrections for the undersized secondary, a high throughput of 7.9×10^{-3} cm^2-sr results. Not one but four IR detectors reside on the focal plane; on Flight C-1, this capability was deployed on bands centered at 20, 50, and 100 microns for the photoconductors and at 100 microns for the bolometer. A sky coverage rate of 75 square degrees/hour is required for overlapping, well-calibrated scans. For the $\sim$ 3600 square degrees in the zone $b < |5^\circ|$, 48 hours of observing are needed; with six good hours of data per flight, eight flights would be needed. Of course, two or three of these would have to take place in the Southern Hemisphere. With overlapping scans, source positions should be determined to $3'$ of arc. A survey limit of between 500 and 1000 Jy is expected, depending on scanning mode, balloon altitude, and effective system efficiency for the flight. Such a program would complete the survey of the galactic plane and should catalog several thousand sources, provide color temperature information, map the extended diffuse emission from the galactic plane, and overlap with near-IR and radio observations.

Coverage of the entire celestial sphere to the same standards would

require an order of magnitude more effort (Hoffmann and Aannestad, 1974). Long duration balloon flights would be needed. The role of short duration flights would be two-fold: the observation of suspected extended IR objects and the surveying of randomly selected areas for far-IR emission.

The first flight of Gondola C in August, 1976 proved the technique by discovering nine new sources of far-IR emission at relatively low flux densities. With certain improvements made in the subsequent year, the experiment promises to meet the goal of efficient, productive reconnaissance in the far-infrared.

CHAPTER II

Balloon Infrared Astronomy

A. Basic Infrared Techniques

A number of fundamental considerations and techniques are involved in broad-band IR photometry, quite apart from ballooning. This part deals cursorily with these topics and is meant to be helpful to the reader of this thesis uninitiated in infrared astronomy. An excellent, concise review on IR photometry has been written by Low and Rieke (1974).

1. Chopping

Chopping is the comparison of a signal input containing a potential source with a reference input (or, in terms of the orthodox scientific method, with a control) at frequencies between a few and a few thousand hertz. In radiometers the signal is compared to a blackbody of known, controlled temperature, providing an absolute calibration. Most IR photometers used in astronomy are calibrated in two stages; the input beam is wobbled one to ten times its own width to an adjacent patch of sky for a relative measurement, which is ultimately compared to the signal found by similarly chopping a known source. Since weak IR signals, which are on the order of 10^{-13} to 10^{-14} W, must compete with backgrounds of about 10^{-7} W in an uncooled instrument and 5×10^{-9} W, at 100 μ, in our cooled telescope, chopping is essential; it cancels the sky background to expose IR signals. The chopping frequency should exceed the frequencies of changes in the sky background and of drift in the detector response. Also, AC amplifiers are generally more stable than DC-coupled devices; the more

faithfully amplified signal can be rectified with the aid of the reference frequency provided by the chopper. Background cancellation is typically near 10^5 for a chopping system.

How does one chop? Any part of the optical train is a candidate. The size and mass of the primary mirror discourages modulation, but at least one group (Lemke and Haussecker, 1976) does so with a 20 cm mirror. Wobbling the smaller secondary is the most widely used approach. Solenoids pull and/or push alternate sides of the mirror, which is mounted on a flexible hinge or spring. The third general method employs a rotating sector wheel with polished surfaces near the focal plane; a stationary mirror behind the wheel and the wheel itself are alternately seen by the detector. A somewhat better technique, which avoids temperature differences between mirrors and edge effects, exploits a vibrating mirror at 45° to the optical axis near the focal plane. Attesting to the present stature of IR astronomy is the provision for wobbling secondaries in most new observatory telescopes.

Nodding is a refinement of chopping, aimed at cancelling any assymmetry, or offset, between signal and reference beams, in which the beams switch roles. The resulting differences are subtracted, doubling the signal and nulling the offset. Offset can be caused by a gradient in the sky background or unequal emission from opposite sides of the telescope structure. Typical nods are made every 20-30 seconds.

Chopping is an inherently differential technique. Therefore, sources with small flux gradients, such as extended, rather uniform objects, are difficult to detect when chopped. On the other hand, modest sources with sharp gradients, like compact HII regions with dust at different temperatures within and without, are conspicuous. Also, chopping leads to con-

fusion when discrete sources are densely distributed, with separations on the order of a beamwidth or chopper throw. Both of these subtle selection effects must be kept in mind when assessing surveys performed with the chopping technique.

2. Cryogenics and Background Reduction

To reduce the background over the bulk of the detector's solid angle not exposed to the sky, its mounting cavity must be drastically cooled, by either LN_2 for very near-IR work or by LHe for the far-IR. Cooling the telescope as well, an innovation of some cosmic background radiation experiments and of the instrument described in this thesis, cuts the background further. (See Muehlner and Weiss, 1973 and III. E., respectively.) To hold LN_2 or LHe, a dewar is employed. Made of two nested vessels with an intervening vacuum space, the dewar isolates cryogen in the inner vessel from the outside world. A neck of small cross-section and thermal conductivity holds the vessels together, while the vacuum space is often filled with or bounded by reflective material to impede radiative transfer. Generally, the detectors and associated optics are bolted to the inner vessel's underside in the vacuum space; variations occur in large dewars which enclose the entire instrument.

Besides cooling, telescope background can be diminished through careful structural design. In optical instruments, large secondaries and spiders, for example, do no more than obscure incoming light; in IR telescopes, they are actually incandescent. Minimizing these structures, tight baffling to exclude all but the sky from the field of view, and blackening the interior to absorb stray light are some strategies. Low and Rieke (1974) go into telescope design in some detail.

3. Detectors

Generally speaking, the IR spectal region lies between two detection technologies. Optical photons are energetic enough to induce chemical or photoelectric effects on a detector, such as a photographic plate or photoelectric photometer. Radio photons have low enough frequencies for detection by conventional superheterodyne techniques. Broad-band IR photometry relies on incoherent detectors of two types: thermal detectors, which heat up measurably as photons are absorbed by their nearly black surfaces, and quantum detectors, which contain holes and electrons that IR photons excite into conduction bands (photoconductive detectors) or have p-n junctions that separate holes and electrons generated by IR photons (photovoltaic detectors). Thermal detectors have rather uniform spectral response and $\sim$ millisecond time constants; quantum detectors have threshold energies and more rapid response times. Both require cryogenic cooling for far-IR observations. More on detectors can be found in Appendix A and in III. G. 2., 3., and 4. Reviews on bolometers and photoconductors have been written by Low (1963) and Putley (1964), respectively.

4. Field Optics, Field Stops, Filters, and Windows

Field optics image the entire telescope exit pupil on the detector, removing fine spatial information in favor of a stronger signal. In addition, problems arising from variations over the face of the detector are avoided. Lenses, off-axis mirrors, and waveguides or light pipes are used, depending on the wavelength. Losses, whether due to absorption or diffraction, can be turned to advantage for filtering.

Field stops are employed to limit the field of view. Multiple

field stops are often mounted on a wheel for easy interchange. They enable the observer to determine, in the absence of direct imaging, the concentration in angle of an IR source.

Filters are used to define the detector's bandpass. Several types are effective in the IR; many commercial enterprises produce filters to detailed specifications. Properties that filter include selective absorption and reflection, refraction, scattering, interference, and diffraction. The work of Armstrong and Low (1973) on diamond powder deposition for high frequency blocking filters, of Wijnbergen (1972) on restrahlen reflection filters, and of Ulrich (1967) on metal mesh interference filters have been particularly useful for far-Ir applications. Most far-IR photometry has been in rather broad bands, with $1 < \lambda/\Delta\lambda < 3$. Narrow-band photometry and spectrometry with grating spectrometers and Fourier interferometers has begun in the past three years.

Windows are necessary for all but rocket-borne platforms to keep the atmosphere out of the cryogenic area, lest it condense on the optics. Here, durability is a requirement beyond acceptable transmission properties. Normally, windows are mounted to a flange on the outer wall of a small dewar; in large dewar systems, the window must be positioned in front of the optical train in the incoming beam.

5. Preamplification

In cryogenic systems, the bulk of the electronics is usually some distance from the detector. To preserve an intelligible signal, a preamplifier is placed as close to the detector as possible; the detector's load resistor and often, an impedance transforming FET, are placed in the dewar with the detector. Gains on the order of one thousand are typical.

The preamp output is sent to another amplifier for phase-sensitive detection based on the chopper's reference signal.

B. Ballooning

Because balloon techniques are likely to be less familiar to the majority of modern astronomers than those of optical, radio, or even space astronomy, the remainder of this chapter surveys scientific ballooning and presents some of the considerations that constrain the design of a balloon-borne experiment. I proceed here with the basic modes of balloon flight feasible today and the advances that made them possible. In Part C, the environmental problems that confront the stratospheric platforms are discussed; the operational constraints involved in zero-pressure ballooning follow in Part D.

Around 240 B. C. E., Archimedes correctly conceived the principle of buoyancy in water; in 1250, Bacon hypothetically extended the notion to flotation in air, pending discovery of a lighter-than-air fluid. de Lana, c. 1670, suggested a vacuum balloon; Cavendish, in 1766, discovered hydrogen. Real, vigorous progress, however, appeared in France, beginning in 1782, when the Montgolfier brothers used hot air to launch small paper balloons. By 1785, in France, England, and the American colonies, ballooning engaged leading scientists who developed the hydrogen balloon (with many basic features still in use today), crossed the English Channel and climbed to 2.7 km, initiated atmospheric observations, and determined that gas expands when heated. Over the ensuing century the hydrogen balloon continued to set distance and altitude records, and even emerged on the battlefield. However, the seeds of modern ballooning were sown in the decades straddling 1900: Hermite and Besancon, in 1892, in-

vented instruments for unmanned flight, Ramsay, in 1895, and Cady and McFarland, in 1903, discovered helium in the earth's atmosphere and in natural gas, respectively, and Assmann, in 1901, devised rubber sounding balloons, commencing the quest for better fabrics.

Today, advances in solid state electronics and polymer chemistry pace progress in ballooning by increasing performance while reducing weight. Compact instrumentation facilitates the taking and handling of data and uses less power in the process, thereby reducing the number of bulky batteries. Better balloon fabrics are more resistant to cold and stress and are lighter, which is vital, since the weight of the fabric itself eventually limits balloon performance. In fact, such developments have led to small super-pressure balloons, which are distinguished from standard zero-pressure balloons by containing the small positive pressures caused by diurnal heating. In the zero-pressure case, the spilling of helium through the appendix, the tube at the balloon's bottom, relieves excess pressure. Super-pressure balloons, by retaining the original charge of float gas, permit long-duration flights, on the order of months. However, the majority of scientific packages are carried aloft by single or tandem zero-pressure balloons; for many experiments flight duration is limited in any case by other factors, such as telemetry range and cryogenics. More on ballooning can be found in the Scientific Ballooning Handbook edited by Morris (1975).

To conclude, two types of balloons, zero- and super-pressure, are used for basic research from the stratosphere. Two other categories are worth mentioning for completeness: the disposable super-pressure type, represented by the weather balloon which never stabilizes in altitude, but maintains a growing differential pressure as it rises, until it bursts,

and the hot-air types, used mostly for sport. Research naturally divides into two basic areas, atmospheric and astronomical. Of flights from the National Scientific Balloon Facility in Palestine, Texas, the latter has predominated of late, as cosmic particles, gamma, X-, ultraviolet, and infrared radiation have been observed from platforms borne by zero-pressure balloons.

C. The Stratospheric Environment

In the stratosphere, the strange layer that separates the familiar trophosphere from the alien environment beyond, sail scientific balloons. The survey of this unique environment strongly motivated ballooning in the first place and does so today; ozone destruction and global-circulation research, to mention just two "active" areas, rely heavily on balloon-borne platforms. Stratospheric conditions determine many aspects of any experiment carried out aloft. The effects of low pressure and density, frigid temperatures, float winds, and residual atmospheric emission are discussed below.

The low pressure in the statosphere largely determines the cryogenic and convective characteristics of our experiment. Above 67,000 feet, or 3.83 cm of Hg, liquid helium is in Phase II; at 100,000 feet, LHe attains a temperature of 1.7 ^{o}K. Such cold, which degrades photoconductor performance slightly, improves bolometer operation. Moreover, the extremely high thermal conductivity of LHe in Phase II prevents turbulent boiling, a source of microphonic noise, so the availability of a large-volume "environmental pump" — the stratosphere — is quite fortunate. Thirdly, the low ambient density at float altitudes greatly diminishes the efficiency of convective heat transport, which represents

a cryogenic problem at sea level densities (see IV. B.).

Actually, stratospheric temperatures rise with altitude, due mainly to the direct absorption of solar energy by ozone.[1] This "temperature inversion produces the strong, stable stratification that gave the layer its name. At the nominal altitude of 30 km, however, the air is still cold enough — 220 ^{o}K — to warrant special precautions for electronic and electromechanical devices. Fortunately, the waste heat from the power module in our main electronics box keeps the other modules warm; otherwise, components meeting military specifications or special heating arrangements would be needed. Our two preamplifier units, necessarily located outside the electronics box, are insulated and heated to keep certain components in range. To prevent freezing, bearings and DC motor planetary gear trains are thoroughly cleaned and either run dry or lubricated with instrument oil (MIL-L-6085A). All adhesives and tapes used in the experiment have been tested in liquid nitrogen to ensure their adhesion in stratospheric conditions; the choice of Teflon- over PVC-coated wire was made on the basis of flexibility at low temperatures.

Float winds refer to the mean stratospheric flows at the balloon's float altitude. Unlike the cloudy, turbulent trophosphere or the auroral ionosphere, the stratosphere rarely displays visible phenomena. Thus, the winds and jets that concern the balloonist were not known until this century; even today, the number of stations obtaining high altitude wind information is small.[2] Fortunately, the stratospheric wind field is rather

---

[1] The inversion was first measured independently by Assmann and de Bort in 1901, but had been inferred earlier from meteor trail heights and audibility of explosions at great distances. Both phenomena stem from the positive temperature gradient.

[2] Routine sounding rockets fly only from Wallops Island, Va., Cape Kennedy, Fla., Ft. Churchill, Canada, and White Sands, N. M. Special stratospheric radiosondes (weather balloons) can be flown from the NSBF, if required.

smooth, since global variations of surface and terrain have much less influence than in the troposphere. Forecasters at the NSBF, using current observations and known tendencies, can give the experimenter float trajectories more reliably than surface prognoses. Stratospheric circulation is highly seasonal: strong westerly winds (normally 25 m/s, but occasionally as high as 50 m/s, at 30 km) prevail in the winter; persistent easterly winds (20 m/s at 30 km) dominate in the summer.[3] In May and October come the "turn-around times", the best periods for long duration flights, as the unsteady, light winds may not push the balloon out of telemetry range. A fascinating variation on the above pattern is the "sudden warming", a winter polar effect that can suddenly reverse the vigorous winter westerlies in January, February, and March.

Float winds, of course, completely control the flight path. Since overflights of Mexico are generally forbidden, and recovery of a package in rough terrain is difficult and over water in nearly impossible, the projected wind field may severly restrict favorable launch periods from the Texas facility. Moreover, the telemetry range nominally extends only 350 miles. A scientist requiring long flights must either wait for ideal float winds or use "down-range" telemetry or both. If wind vectors deviate from predictions, a flight may be terminated early. A result of the "free-floating" nature of balloon astronomy is the need for adaptibility in flight planning and control.

Finally, aspects of the stratosphere relevant to infrared astronomy are the residual atmospheric absorption and emission. The work of Traub and Stier (1976) gives emissivities, fluxes, and transmission coefficients for four altitudes: 4.2, 14, 28, and 41 km. Figure II-1 shows the relative

[3] 1 meter/second, or m/s, equals 2.24 miles/hour.

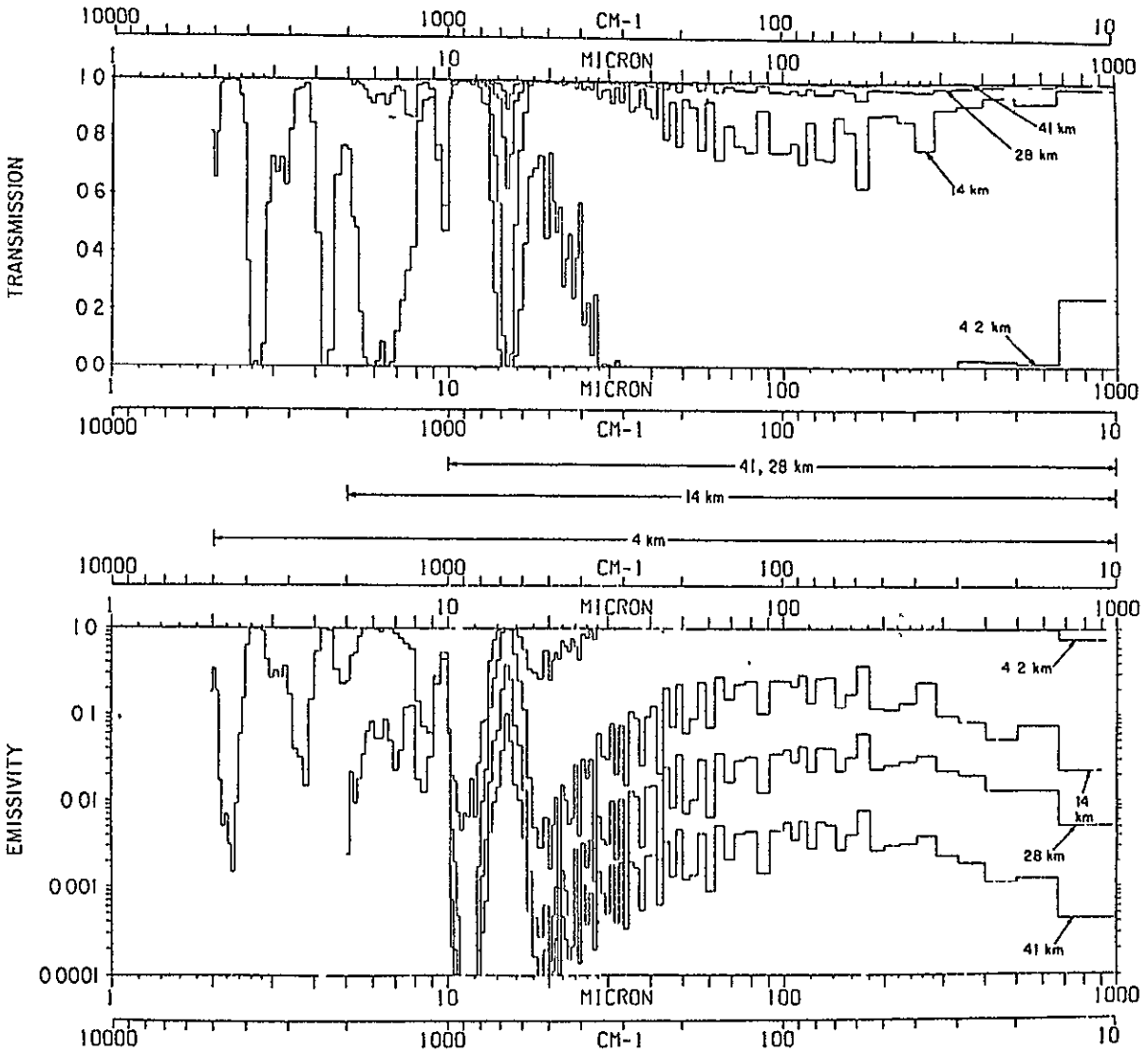

Figure II-1: Atmospheric Transmission and Emissivity at Four Altitudes. From Traub and Stier, (1976).

values of transmission and emissivity at the four altitudes, and demonstrates the advantages of balloon-borne (28 and 41 km) over ground-based (4.2 km) and airborne (14 km) platforms. Ultimately, the background flux at a given float level limits the system's sensitivity by loading the detectors and overwhelming faint or diffuse sources. The following table, based on Traub and Stier (1976) but adjusted to an altitude of 30 km and an elevation angle of 50°, gives the mean emissivities, fluxes, and flux densities in our four channels with our throughput.

TABLE II-1: SKY BACKGROUND

Ch. No.	Half-Power Points	Mean Emissivity	Total Flux $W\ cm^{-2} sr^{-1}$	Total Flux Density Jy
1	75-130μ	1.7×10^{-2}	1.1×10^{-6}	5.6×10^{6}
2	45-70μ	1.0×10^{-2}	2.6×10^{-6}	9.4×10^{6}
3	18.4-24μ	3.0×10^{-4}	2.8×10^{-7}	6.3×10^{5}
4	75-120μ	1.7×10^{-2}	1.0×10^{-6}	5.7×10^{6}

The benefit to be gained from floating at 41 km — a five-fold reduction in sky background — is outweighed, in our case, by the need for much larger balloons and the increase in wind speed, which would shorten the length of the flight. The flux densities tabulated above illustrate that chopping is required to achieve a survey limit of around 10^{3} Jy, a reasonable survey goal. Summing up, our float level represents a compromise between reducing sky background and cooling below the λ-point, or phase transition, of LHe, and the expense and limitations of very high altitude flights.

D. Operational Constraints

Designing a gondola for zero-pressure ballooning and planning a flight involve several considerations not discussed in the preceding part. These include weight limitations, launch and recovery weather, pointing and tracking techniques, and mechanical shock on launch and impact. Savings in weight increase float altitudes for a given balloon or decrease balloon and parachute size. Smaller balloons are easier to launch and are more reliable. In addition, lighter packages improve the safety margins of universal joints, bearings, motors, and other devices in the gondola's suspension and pointing systems. Finally, the rigors of recovery are eased, since more crash protection per momentum can be arranged. For these reasons, the gondola designer should employ strong, light materials whenever possible.

Wind is the main weather concern during balloon launch, assuming fog or precipitation are not present. When inflation of the balloon begins, a strong gust for even a few seconds can move the small bubble across the ground, exposing the film to damage. However, steady winds of up to 5 m/s are not dangerous. Once the balloon is sufficiently inflated to lift itself up, this problem passes. In standard upwind dynamic launches, the balloon is restrained and paid out by a large spool on a special vehicle; to initiate the launch, the spool swings open and releases the bubble, which floats over the package, held by the launch vehicle. Release of the package is a tricky procedure. In a proper launch, the launch vehicle maneuvers until it moves in the same direction but more slowly than the wind-driven balloon, so that the gondola is lifted up and away without violent shock or swinging. Anticipation of the right moment drops the package on the launch pad; undue delay exhausts the

available launch pad area. This crucial, irreversible act demands the greatest judgment and skill of the launch crew chief. Other weather conditions that can postpone launch are cloudiness above 50% at any level, conditions that impede visual tracking, and poor visibility at the recovery site or enroute, since an aircraft is normally dispatched to relay telemetry commands and otherwise manage the impact sequence. As balloons get larger, many of these constraints, especially the highest acceptable wind velocity, become more stringent. Additional limitations arise from the need to avoid aircraft; the FAA prohibits launches or recoveries that might interfere with airport operations.

At float, problems of stabilization and tracking must be overcome. Most important is altitude control, achieved largely by the release of ballast. A balloon deviates from its assigned altitude because float gas changes its temperature and/or escapes. Cooling or escape permits descent, while heating of the float gas by radiation absorbed by and transferred from the balloon film causes ascent. Venting of gas and release of ballast prevent upward and downward excursions, respectively. In overnight flights, only ballast release is necessary to maintain a constant altitude. Another effect that concerns the experimenter is balloon rotation (up to 6°/minute occurs half of the time) about its axis of symmetry. Turbulence or second order effects of small vertical oscillations cause the rotation, requiring swivels in the suspension to reduce the coupling with the gondola. Finally, the gondola itself pendulates in response to wind shear, turbulence, or wind acceleration; many gondolas actively point at different celestial positions, introducing transient motions.

To stabilize, many different pointing systems have been developed; most use gravity and the earth's magnetic field for vertical and azimuthal orientation. More precise pointing is possible with offset guiding. Slewing in azimuth is accomplished by spinning an inertia wheel; conservation of angular momentum forces the rest of the gondola to rotate in the opposite sense. In some systems, gyro stabilization permits finer pointing.

The gondola is tracked simultaneously by several means to insure against its loss and consequent hazard to aviation. During clear, daylight ascents, visual tracking with a theodolite is possible. Radar, at the NSBF, is also used; a radar target is provided on the flight train. A radiosonde device accompanies the balloon and transmits at 1680 MHz; this radio "beacon" is followed by an antenna at the NSBF. The resulting azimuth and elevation of the balloon, combined with the pressure altitude telemetered from the gondola, provide good positions out to 250 km. A tracking aircraft, if used, can be positioned under the balloon by eye or by tuning its direction finding gear to the carrier frequency of the telemetry, after which the pilot uses his own avionics. Finally, the Omega system, developed by the Navy, uses eight low-frequency transmitters, at least three of which are detectable anywhere on earth. Phase comparisons of any three stations determine location; these computations are carried out at the ground station. With corrections for ionospheric variations, an accuracy of two to four kilometers is typical. Accurate tracking provides balloon astronomers with reliable terrestrial coordinates which are needed to calculate correct celestial positions; it also enables the flight controllers at the balloon facility to update the trajectory and to terminate

the flight in a safe, reasonable manner.

The final major consideration is shock. While most launches are gentle, most landings are not. Experimenters commonly build a flat bed under their packages, to which large cardboard slabs are attached. In an ideal vertical impact, these slabs crush, absorbing energy and reducing forces. However, if the system is swinging at the moment of impact, or if the parachute becomes an inflated sail, the package can flip over and roll, exposing it to lateral forces that are more difficult to soften. Stranger circumstances occur (see V. A.). Whatever happens, the recovery crew brings the payload back to the balloon facility, where it is often repaired if necessary, retested, and reflown.

Most American and many foreign experiments are staged at and launched from the National Scientific Balloon Facility in Palestine, Texas, between Dallas and Houston (see Figure V-1). When the central location of Texas militates against long-duration, overland flights due to strong winds, the NSBF crew can launch from bases in Arizona or the Southeast. Many foreign countries, including Canada, France, Italy, Argentina, India, and Australia, operate scientific balloon facilities as well. Despite the advent of space vehicles, balloon-borne experiments still offer astronomers a quick, cost-effective means of obtaining observations.

CHAPTER III

Instrumentation

A. Introduction

Today, the typical astronomer acquires his or her data by utilizing existing observatories, which currently cover a great deal of the electromagnetic spectrum from ground, airborne, and orbiting platforms. In some cases, one can concentrate entirely on the astrophysics, leaving the responsibility for and detailed understanding of the data-taking system to a highly specialized group of scientists at the operating institution. Many other workers rely on a system's infrastructure but add novel instruments for gathering and analyzing the data, such as spectrometers and photometers in optical and IR work and amplifier/filter arrangements in radio research. In our case, we had to build an entire unmanned observatory, with structural, pointing, optical, cryogenic, detection, power, and communication systems. Therefore, Chapter III, the description of the experiment, is by far the longest in this thesis. As the only detailed documentation on the gondola in the literature, it is meant to explain what the instrument does, how it works, and why it was designed that way.

The aim of the CABBAGE (Cornell-Arizona Balloon-Borne Astronomy Group Experiment) is to survey the sky at several far-infrared wavelengths to a level set by the sky background rather than the telescope. To perform this experiment, six interrelated systems — two support and four telescopic — are required:

1) To provide communications, power, and control for the rest of the gondola, an electronics system is required. A veteran of Gondola B (Hoffmann, et al, 1971b), this system is outlined in Part B.

2) To stabilize and direct the telescope and to suspend the gondola from the parachute and balloon above, a pointing and suspension system is needed. Basically unchanged from Gondola B as well, this system is explained in Part C.

3) To carry the telescope and mate with the rest of the gondola, a structural system is required. Provisions for mounting subsystems and for protecting the entire gondola on impact are included. This area is covered in Part D.

4) To achieve low background from the telescope, a cryogenic system is employed. This is discussed in Part E.

5) To gather infrared radiation, while excluding unwanted off-axis radiation, is the task of the optical system. The chopper, calibrator, and visible star telescope are subsystems and are included in Part F.

6) To detect, transmit, and preamplify, a sensitive infrared detection system is demanded. This area is reviewed in Part G.

This chapter reflects the gondola as of Flight C-1 in August, 1976; as I write, we render the description partially obsolete through improvements suggested by that flight. The first three Figures were drawn or photographed in mid-1976 and are frequently cited in this thesis. Figure III-1 provides a cutaway view of the telescope alone as it would operate at float, with the lid open, the thin membrane exposed, and helium gas flowing through the telescope. Figure III-2 contains a photograph of the gondola during staging at the NSBF. The sketch on the right

corresponds to the photograph and defines both the telescope and gondola axes, which differ since the telescope moves with respect to the rest of the gondola about the elevation axis. Figure III-3 was taken a few minutes before the launch of Flight C-1 and affords an excellent overview of the package. The small table in the lower right conveniently list dimensions and weights.

A few general statements are in order before proceeding. In the early planning stages of Gondolas B and C, a decision was made to build most of the systems in-house, for simplicity, flexibility, and considerable savings in cost. However, the gondola is heavier and larger than state of the art technology could manage. For example, much of the electronics is "off-the-shelf" and most of the structure is made of aluminum angles and channels, bolted together. Even so, the scientific payload weighs about three-quarters of a ton, a load that can be lifted to a 30 km float level by a balloon of modest size. Secondly, because our pointing system uses magnetometers for orientation, magnetic materials must be avoided whenever possible. Fasteners are made of stainless steel unless otherwise indicated; aluminum is the primary structural material. Lastly, the detection system has six channels in all: four IR channels and two optical channels. All four IR detectors are located at the focal plane of the main telescope; their characteristics are summarized in Figure III-4 and Table VI-1. One optical detector sits at the focus of the visible star telescope, shown in Figures III-1 and III-2. The second resides at the center of the main telescope's focal plane, among the IR detectors, and is referred to as the "focal plane monitor".

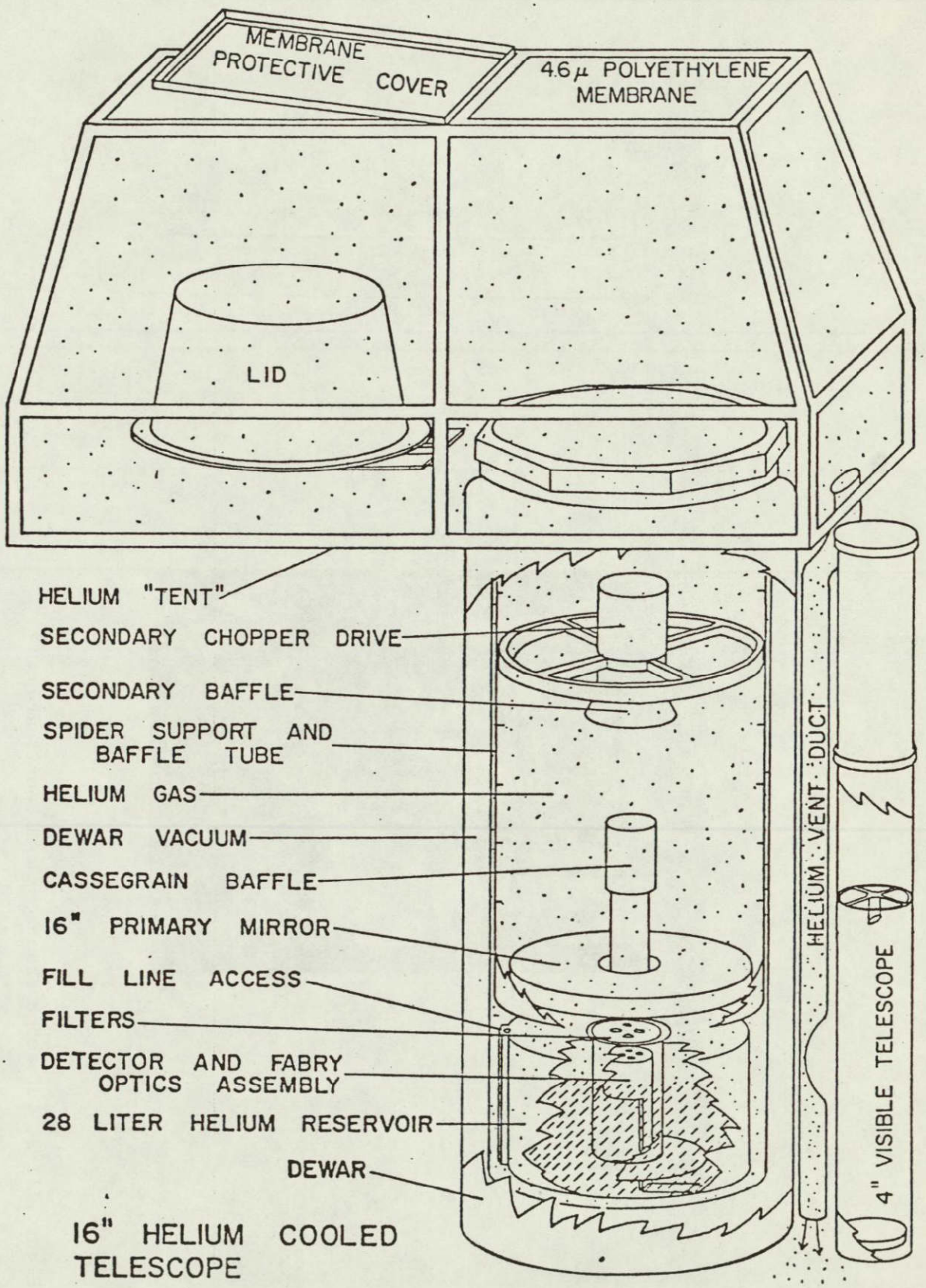

Figure III-1: 16-Inch Helium Cooled Telescope Cutaway Drawing

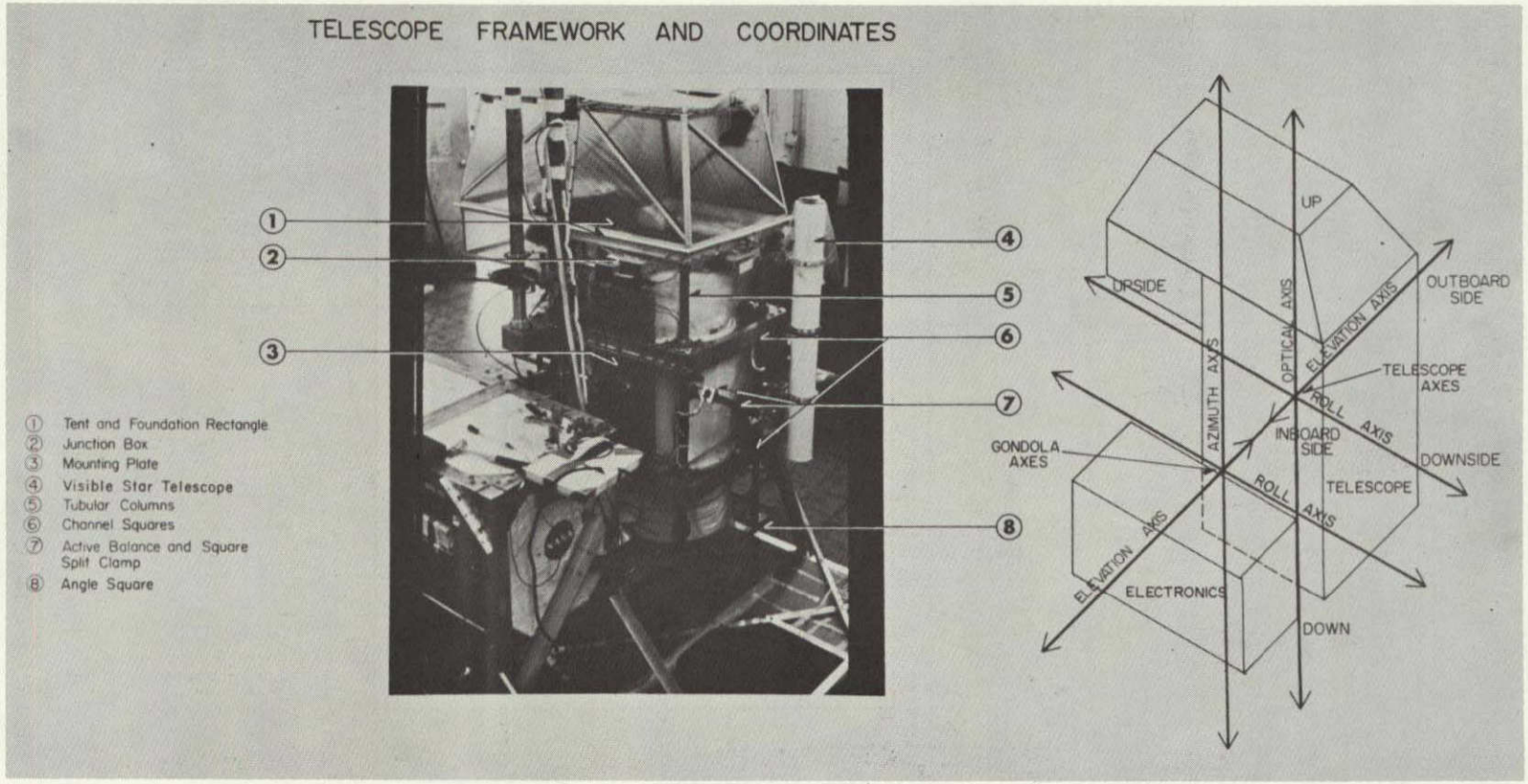

Figure III-2: Telescope Framework and Coordinates.

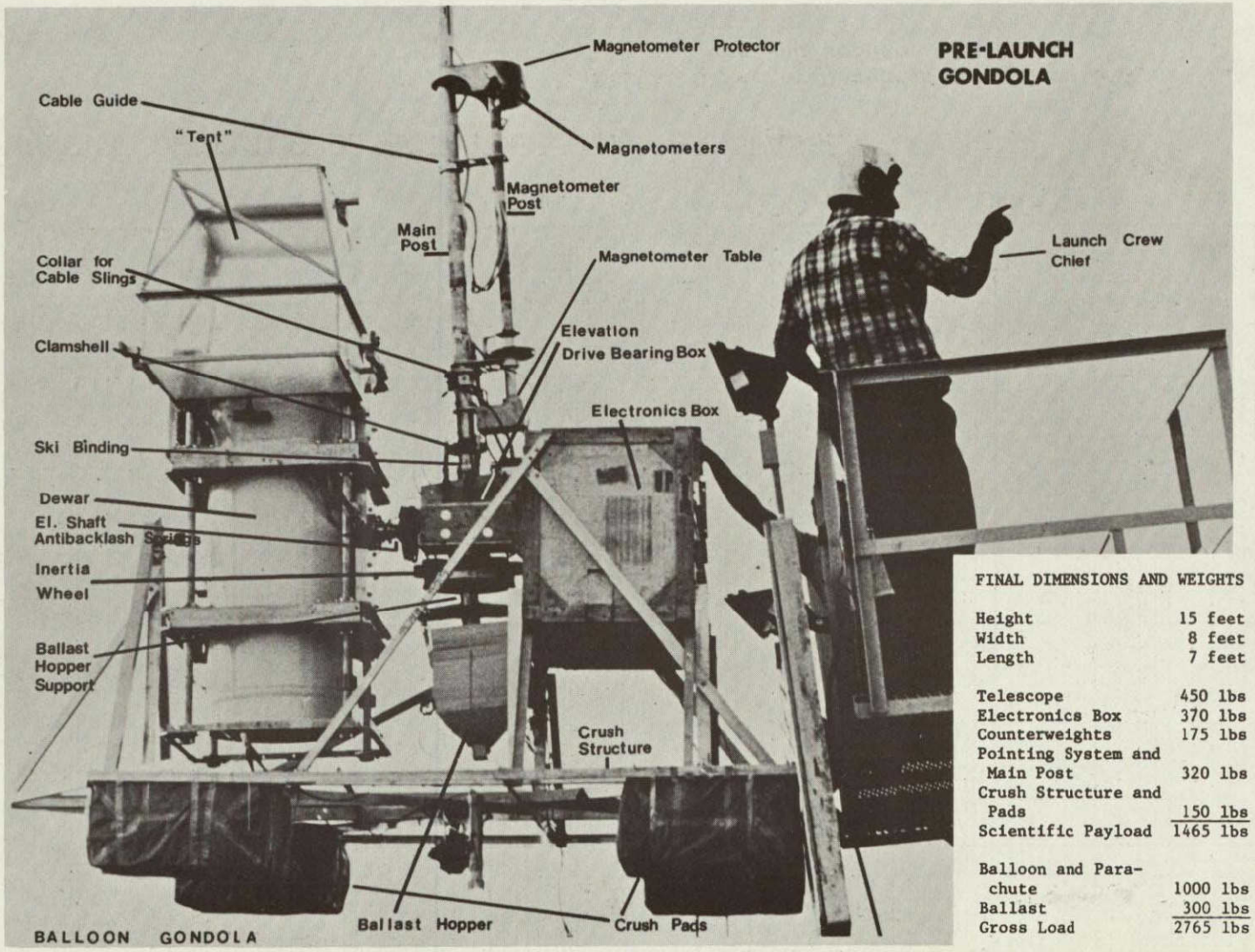

FINAL DIMENSIONS AND WEIGHTS

Height	15 feet
Width	8 feet
Length	7 feet
Telescope	450 lbs
Electronics Box	370 lbs
Counterweights	175 lbs
Pointing System and Main Post	320 lbs
Crush Structure and Pads	150 lbs
Scientific Payload	1465 lbs
Balloon and Parachute	1000 lbs
Ballast	300 lbs
Gross Load	2765 lbs

Figure III-3: Prelaunch Gondola; Final Dimensions and Weights.

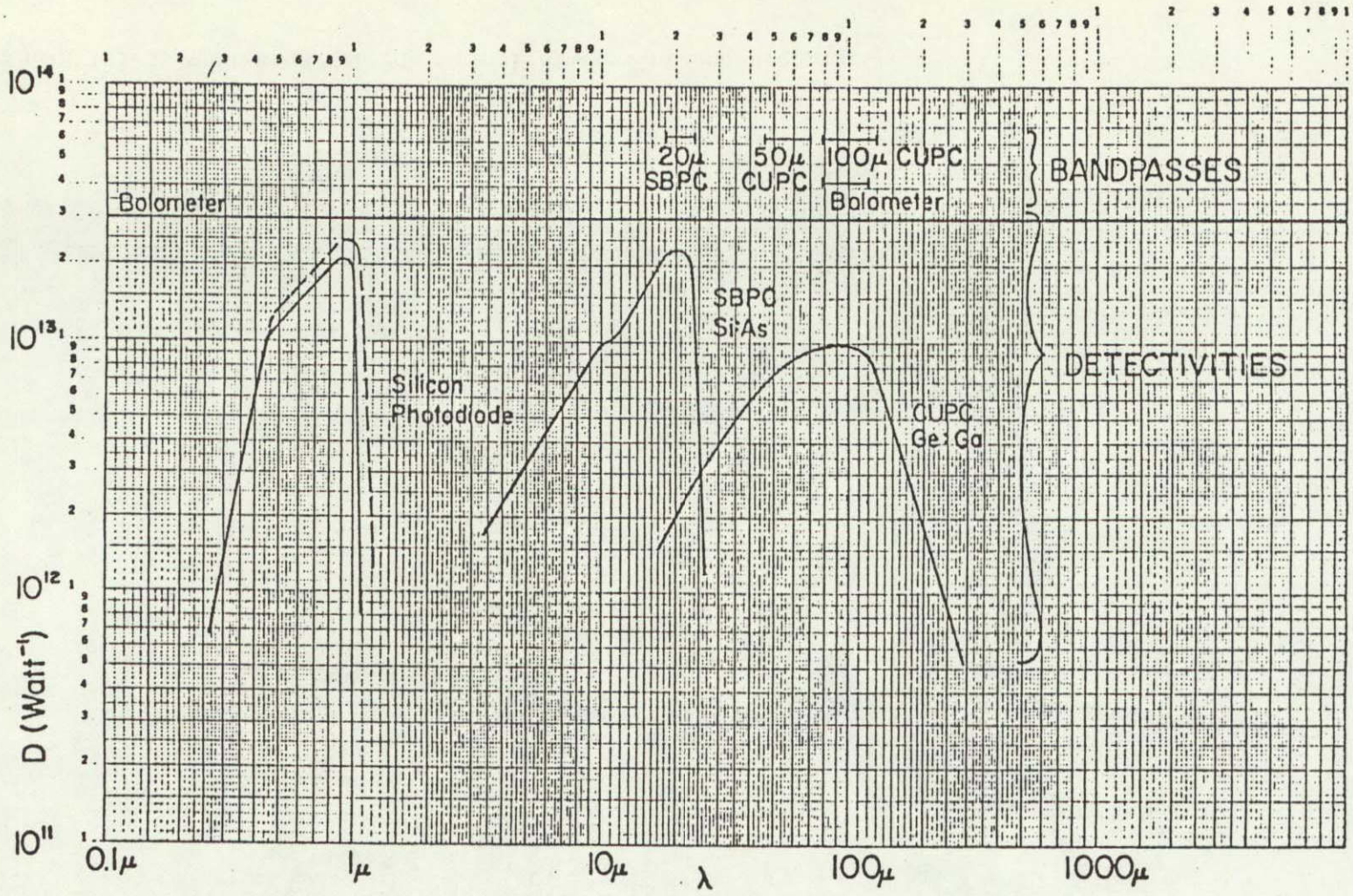

FLIGHT DETECTOR DETECTIVITIES AND BANDPASSES

Figure III-4: Flight Detector Detectivities and Bandpasses. Ge:Ga curve from Jeffers and Johnson (1968).

B. Electronics Systems

1. Electronics Box

Power, control, and communication systems are concentrated and carried in the electronics box (see Figures III-3 and III-5). A much-flown veteran of Gondola B, the box consists of a framework of 2-1/2 inch by 1/8 inch aluminum angle, joined at the corners by eight welded corner brackets with captive nuts. Polyurethane foam panels two inches thick comprise the sides, which are pressed into the outer framework by an inner structure made of four horizontal and six vertical jacks. The horizontal jacks are 3/4 inch rods with an internal thread on a bolt at one end; the ends bear on aluminum angles that force the foam into place. The vertical jacks, two at each end of the electronics box and two in the middle, press the top and bottom panels against the outer framework through baseplates that run from front to back. Split clamps join the horizontal jacks to the pair of vertical jacks in the middle. The back foam panel is located by the ends of the internal angles; the front access panel mounts before flight by external corner brackets and lateral braces that squeeze the foam against the inner structure. Two 3 inch channels, fastened vertically to the outer framework, mate with bracket flanges from the elevation system's bearing box, so that the electronics and pointing/suspension systems are rigidly connected and do not share the telescope's motion in elevation. Coarse balance of the electronics box is attained by bolting lead weights to the top of the outer framework. The overall dimensions of the box are 48 by 24 by 28 inches; allowing for the foam thickness, the interior provides about 12 cubic feet of useful volume. This approach of outer and inner frame structures separated by rigid foam insulation isolates the electronics thermally, me-

ELECTRONICS BOX

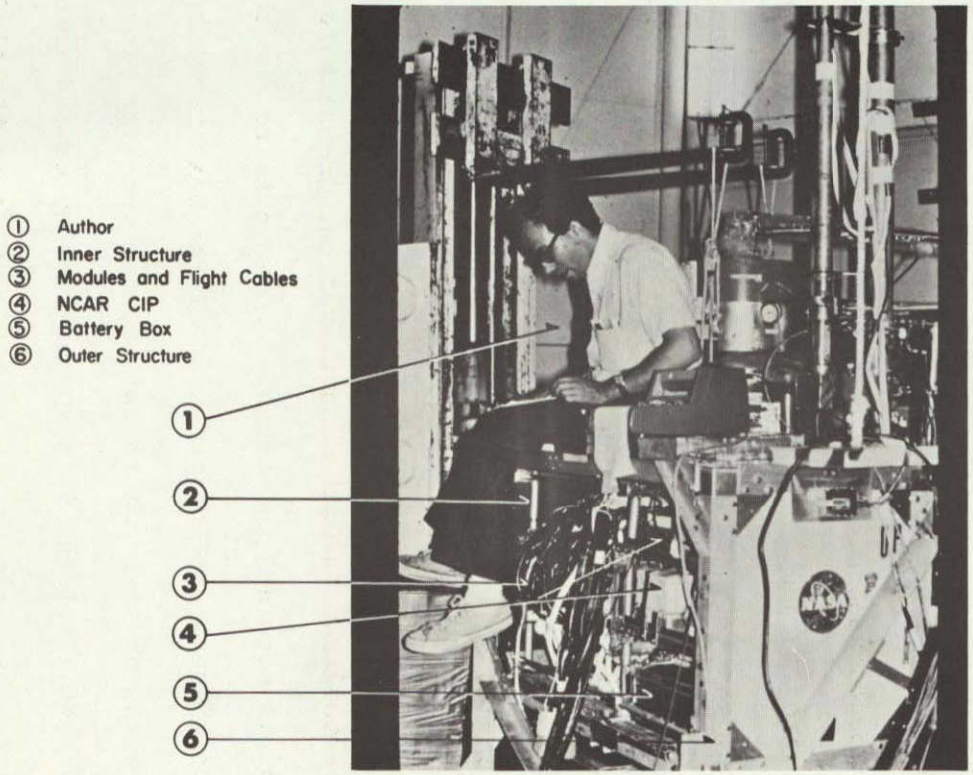

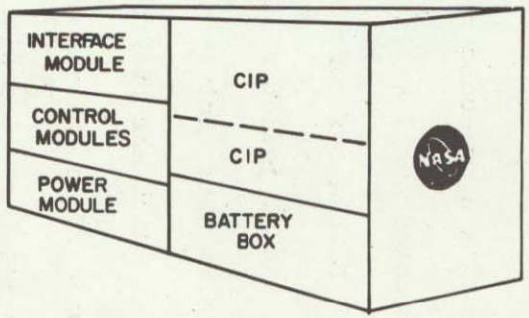

Figure III-5: Electronics Box: In the right-hand key diagram, CIP stands for "Consolidated Instrument Package", which represents the telemetry, telecommand, and navigation electronics supplied by NCAR.

chanically, and electronically from the outside environment.

Inside the box, the inner structure's middle jacks divide the volume in half (see Figure III-5). The left bay contains the interface, control, and power modules, from top to bottom. The control modules are housed in enclosures from Vector; several printed circuit boards fit into each 10 inch deep, 5½ inch tall, and 3 to 11 inch wide module. Within each module, the boards slip into grooves in bottom and top plates, with the card terminals facing toward the front plate's connectors and controls. A rack about 20 inches wide carries two tiers of these boxes; side rails slip between split clamps on the inner structure for insertion and a front flange bolts to another set of clamps to lock the rack in place. Above the rack, the interface module is anchored by additional clamps and braces to the inner structure. Below the rack, the power module is tied to the baseplates of the left and middle pairs of vertical jacks.

The right bay shelters the "NCAR electronics" — the package of electronics provided by the National Center for Atmospheric Research, the government institution that operates the NSBF — and the battery pack. The former, a variety of telemetry and housekeeping components, are bound together and to a pair of aluminum shelves by thin aluminum straps (see Table III-4 for a complete list). The heavy battery pack fits snugly into a teflon-lined aluminum box which is fastened to the baseplates of the middle and right pairs of vertical jacks at the box's bottom. A few other details are worth mentioning: the magnetometers' electronics units are attached to the side of the control module rack, cables enter and leave the box via holes sawed through the foam panels — including the telescope cables which run through the hollow center of the elevation shaft, and the power module, which gets rather warm, is cooled with copper

radiation fins and a hole in the bottom foam panel.

An explanation of the MS series multipin military connectors used throughout the gondola is appropriate. These plugs and sockets use crimp pins which are pressed into and out of the connector inserts with special tools; the result is convenience and versatility combined with reliability. A convention, involving six connector configurations, has been followed with few exceptions. Large currents, such as those from the main battery, are carried by heavy pins in eight-pin connectors. Power cables transmitting smaller currents to individual modules feature ten-pin connectors. Signal cables to and from the modules end with 19-, 26-, or rotated insert 10-pin connectors, depending on the required number of channels. All but the 19-pin connectors use female pins in the bulkheads. A sixth configuration with five heavy pins terminates a cable running directly from the digital to the signal module. Exceptions concern the connectors in the telescope collar: four unrotated 10-pin hermetic bulkheads from Deutsch communicate with the dewar interior. Lastly, the same conventions are followed, whenever possible, on ground support equipment, such as the circuit board testers.

Nine modules participate in telescope control; they are listed in Table III-1, along with their functions and where to look for a description. Four modules involving several systems are covered in the following part.

2. Interface, Signal, Digital, and Power Modules

The most diverse of the nine modules is the interface box, which concentrates the complexity of connecting the eight other modules with power, telemetry, and each other. The box's top panel swings open for

TABLE III-1: GONDOLA C-1 ELECTRONICS MODULES

MODULE	FUNCTION	SECTION, PAGE
Interface	Links NCAR telemetry to other modules; Mediates delivery of power to modules; Holds circuitry inappropriate elsewhere.	III. B. 2., 43
Signal	Processes signals from preamp.	III. B. 2., 48
Chopper	Energizes and controls secondary chopper.	III. F. 2., 124
Balance	Operates moving weight on telescope.	III. C. 3., 86
Engineering	Prepares thermometric outputs.	III. E. 3., 103
Digital	Contains reference oscillator, time mark generator, bleep generator, and ramp calibrator.	III. B. 2., 51
Azimuth	Points telescope in azimuth; Oscillates active bearing.	III. C. 1., 70
Elevation	Controls telescope in elevation; Stows telescope.	III. C. 2., 82
Power	Receives battery power via interface and delivers regulated voltages via interface to modules.	III. B. 2., 54

access and bears the outputs to the NCAR equipment: 13 FM channels on BNC coaxial connectors and four 56-pin Elco connectors for everything else. Completely covered with our standard MS bulkhead connectors, the front panel links the other modules and the main batteries. For all but the signal and power modules, one power and and one signal cable are provided. The signal module requires two input/output signal leads, while the power module needs three connectors: one receives battery power, another sends it to the power module, and a third returns regulated power to the interface. A "test plug" connector can substitute for the telemetry cables in laboratory tests. Direct connections to the telescope occur in two instances: the signal bulkhead for the eighth module mates with a cable for miscellaneous telescope functions (lid mechanism, thermometers, heaters, and the like), and one of three other available bulkheads services the visible star telescope. Figure III-6 displays these interconnections.

Inside the box, power distribution is handled by a set of buss lines that run lengthwise along the bottom of the box near the front panel's power connectors. The different supplies are discussed in the power module subsection below. The central volume of the box is occupied by a "rats' nest" of multicolored wire. In the back, two narrow boards extend the length of the box, one above the other, and perform a variety of functions.

Beginning at one end of the lower board (PC Board 10.1), we find an array of level shifter/attenuators for eight of the thirteen FM channels; five of these inputs run through two pole relays that can inject a calibration ramp from the digital module. To the right, seven of eight interface opamps condition signals from the telemetry. Two of these have unity gain and carry the ramp/calibrate and IR channel #4/focal plane monitor

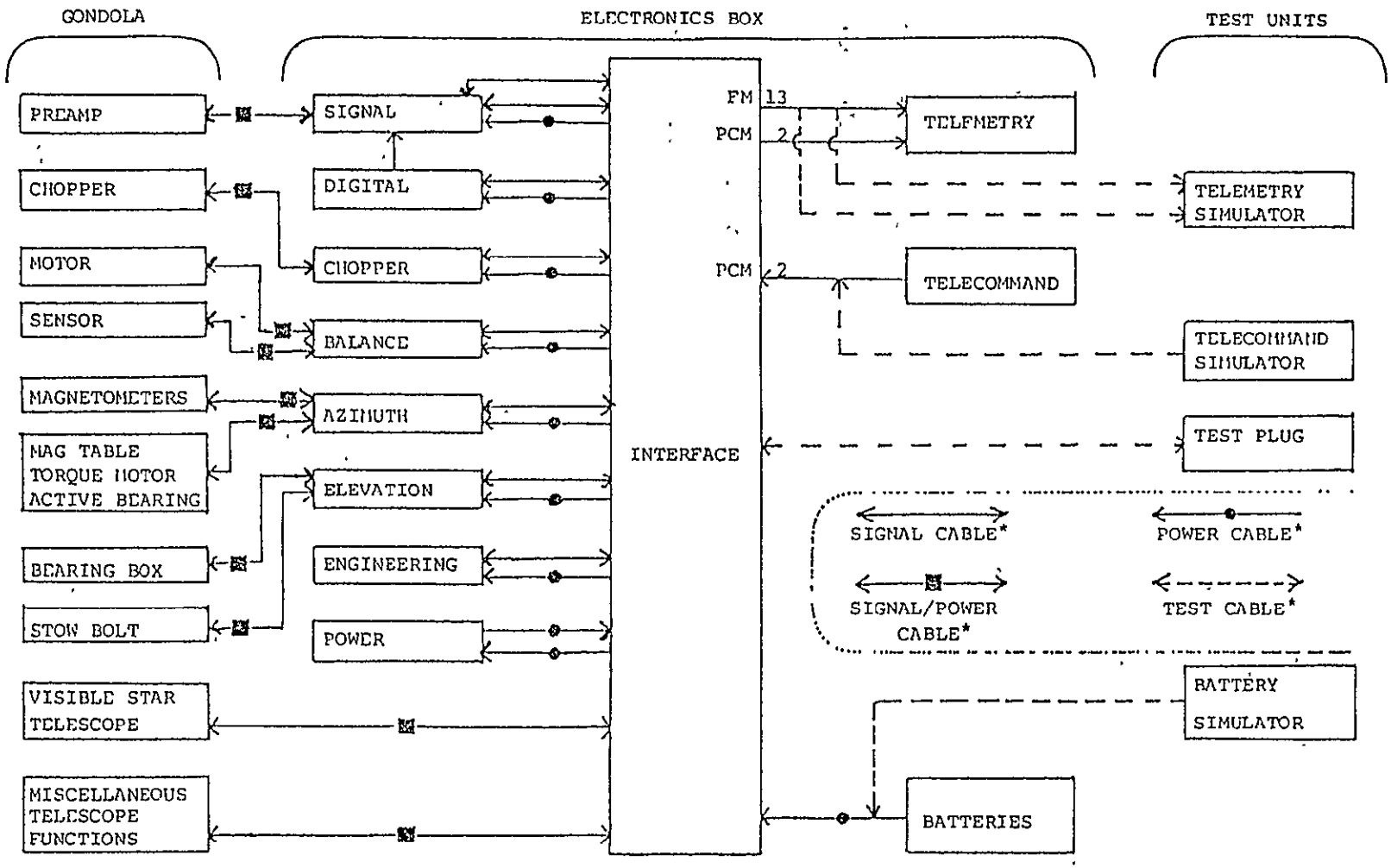

Figure III-6: Interface Module Block Diagram and Cable Connections. * Unless otherwise indicated, there is one cable per arrow.

latch sense to the FM inputs. The other opamps produce various DC gains for the elevation true and scan pots, the magnetometer coarse and vernier pots, the visible star telescope signal, and the battery current monitor. Moving on, voltage dividers for the 26 PCM (pulse code modulation) channels generally change ±10 volt outputs to a 0-5 volt span. Another 14 dividers attenuate various power supply voltages on the gondola to NCAR's 0-5 volt range as well, so that they can be monitored at the ground station. Next, 11 diodes isolate the test plug from internal logic circuitry. A pressure switch set for 16,000 feet appears a bit further to the right; the switch automatically initiates the stow sequence for the telescope during descent, should telemetry commands fail. The remainder of the board contains a portion of the lid circuitry (the lid motor relay and status indicators), the interface reference voltage supply (3.33 volts) for shifting the PCM levels, and the preamp and cryogenic heater status monitors.

The upper deck of circuit boards complements the functions of the lower. Starting on the left (PC 10.2 and 10.3) we discover the remaining FM level shifter/attenuators, the eighth interface opamp, and the lid's open/close command circuitry. On the next board (PC 10.4) are found the cryogenic and preamp heater command latches and relays, plus the lid motor current limiter and timer, set at 125 seconds. The same board carries the command and timer for the calibrator's solenoid and a timer for the LED on the calibrator arm; an output for biasing the bleep in the digital module is included to invalidate data taken while the arm is extended. Also, the up/down command, which modifies other commands, making them "double-throw", drives a status circuit, and another latching command selects whether IR channel #4 or the focal plane monitor will be

amplified at the signal module. The succeeding board (PC 10.5) is dedicated to the calibrator's solenoid drive, which must start the action with a 30 volt, 0.2 second pulse and drop to a 15 volt level when holding the arm out. Finally (PC 10.6), an array of 28 command buffers, which adapt out TTL logic to that of the NCAR electronics, relays a command only when the command pulse itself grounds the desired channel and a 24 volt switch is momentarily closed. The latter occurs whenever any command is received and provides a means of confirming the process at the ground station.

The outputs to the telemetry embrace 9 of 13 available FM channels and numerous PCM outputs. Included in the former are the four IR channels, the visible star telescope, the elevation and azimuth scan outputs, the time signal (bleep), and the chopper sensor. Four of these are also carried on PCM channels. The four Elco connectors transmit PCM information. One 56-pin cable handles analog and one moves digital data; inputs from the telecommand section are carried on the other two 56-pin cables. More on the telemetry and telecommand subsystem is found in III. B. 3.

The detection and preamplification of IR and visible radiation by the gondola's two telescopes is discussed in III. G. Further amplification of the visible star telescope's signal is handled in the interface module; phase-sensitive amplification of the main telescope's channels is the topic of this subsection. A block diagram of the signal module appears as Figure III-7. Note that four virtually identical channels are available; the addition of the focal plane monitor led to the latter's sharing of IR channel #4. Essentially, we have a variable gain amplifier (VGA), a lock-in amplifier, and a two-pole active filter in series,

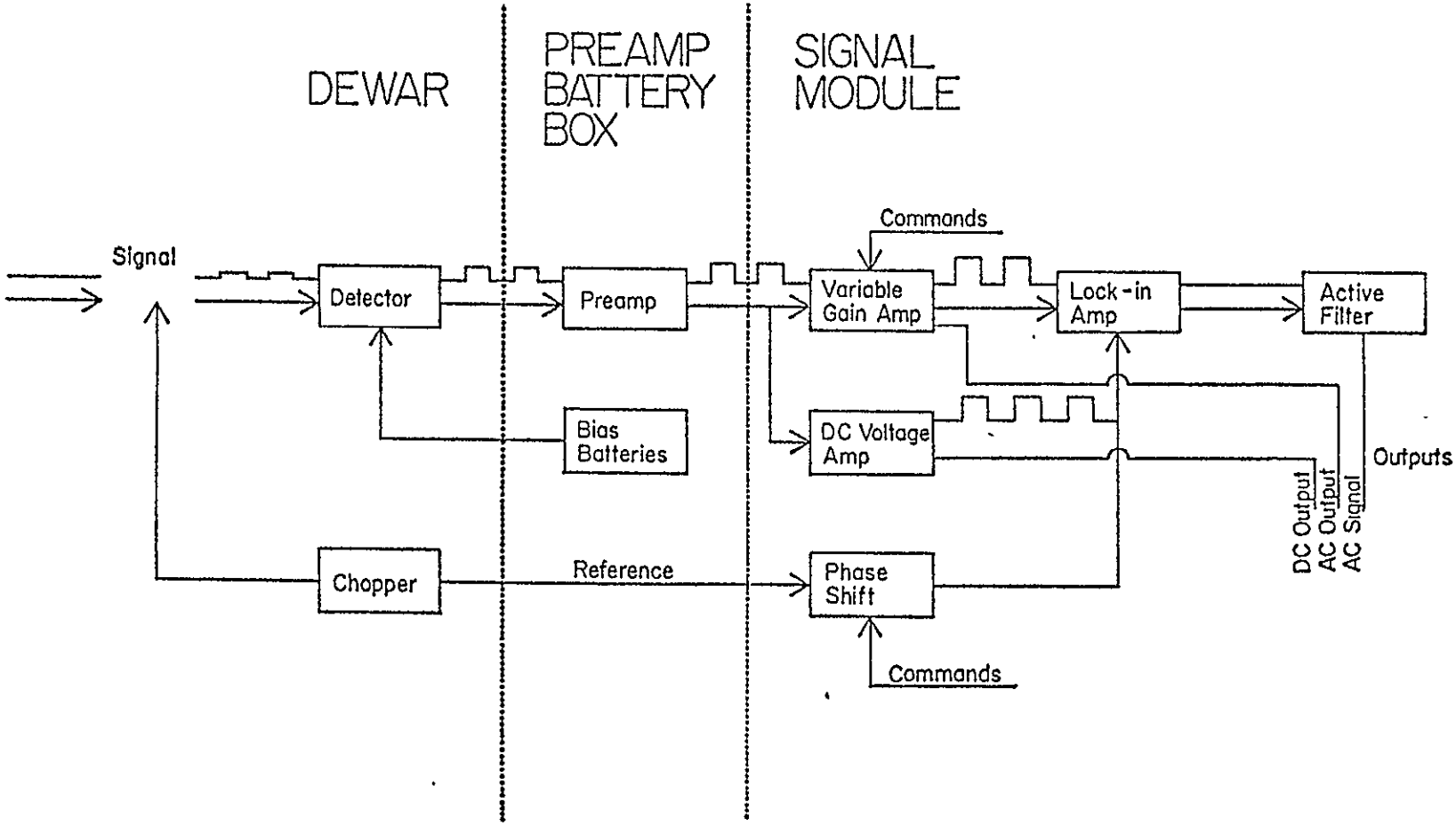

Figure III-7: Signal Module Block Diagram. The square wave is shown for graphical purposes; the chopper in our instrument is a resonant, sine-wave device.

with auxiliary units for gain and phase shift control, plus a direct voltage amplifier. More detail follows.

The VGA uses a noninverting opamp with a feedback network controlled by commands to an Analog Devices multiplexer. Eight gains are provided: 1, 4, 16, 64, 128, 256, 512, and 1024. The feedback network is referenced to the common input ground through another opamp which presents a low impedance to the circuit. For one channel on Flight C-1, the AC output at this stage was telemetered for diagnostic purposes. Finally, transient suppression pulses, generated by the module's control card, ground the output momentarily during gain and phase shift changes.

Next, the signals encounter the lock-in amplifier, where a double throw IC switch, timed by the phase-shifted chopper reference, alternately relays the noninverted positive and inverted negative parts of the AC signal to the active filter. Unity gain opamps send the signal and its inversion to the switch; the result is an essentially recitified output. The subsequent active filter has two stages: a high-pass filter with a gain of 3.15 followed by a bandpass filter with a gain of 5. The combined response is level between 0.008 and 4 Hz, a property of Butterworth type active filters; above this band, a steep 80 db/decade attenuation appears, while below, a more gentle 20 db/decade rolloff occurs. Again, transient suppression pulses keep the output clear. The signals then emerge and head for the telemetry, via the interface.

Controlling the variable gain and lock-in amps is the job of the control board (not pictured in Figure III-7), which accepts gain commands, phase shift commands, and digital module timing pulses. Produced here are the bits that operate the multiplexer in the VGA, the sequence that turns on the transient suppression FET's in the VGA and active filter, and the

pulses that are counted in the phase shifter. The chopper reference also enters the board, where it is inverted; both are sent on to the phase shifter, along with a "toggle pulse" at double the reference frequency, which is done by detecting both state changes during one cycle. Finally, one section of the control board receives the DC and AC signals before and after the VGA and feeds them into a voltage limiter based on pairs of zener diodes, which activates the overload diagnostic when levels above ±10 volts appear. Incidentally, unlike the phase shifter, all four channels share the same gain.

The phase shifter uses the up/down and phase shift commands in a counter that emits bits for a multiplexer. The latter determines what resistance appears in an RC circuit, in order to define a time delay. At the heart of the shifter is a flip-flop, whose state is set by the normal and inverted reference outputs from the control board. Armed by the toggle pulse, the flip-flop reverses after the appropriate time delay, resulting in a phase-shifted reference for the lock-in. Shifts of 1, 56, 74, 93, 112, 130, 148, and 166 degrees are provided; they are needed to compensate for delays elsewhere in the system.

The last board contains DC voltage amplifiers that use the inputs from the preamp. These voltage outputs are actually diagnostic, as they imply detector resistances which indicate background levels. It differs from the other boards, in that it has a fifth channel available.

The module with the most interplay with the others, except for the interface, is the digital module, which is home for the reference oscillator and the derived timing pulses. Four boards are involved here: the reference oscillator, the time mark and bleep generators, and the ramp

calibrator. Outputs from the module not only clock the IR observations, but they pace the step commands to the azimuth, elevation, and signal modules, and indicate through logic culminating here whether data is valid. A block diagram (Figure III-8) sketches the flow through the module.

The first board has three circuits: the 6 MHz oscillator with a divider sequence that emits 20 kHz, the logic start command that resets the network, and the ramp calibrate command. An array of dividers comprises the second board, with outputs ranging from 10, 5, and 4 kHz, 800, 80, 16, and 1 Hz, 2 and 6 seconds, and 1, 5, 15, 30, and 60 minutes. Next, the third board generates the "bleep". Named for the bleep-like sound heard when modulated for the lab loudspeaker, the unmodulated bleep appears on the strip chart records of IR and visible star telescope data as a series of 1 Hz pulses. Every minute, the pulse in doubled in height, every fifteen minutes, tripled, and every hour, quadrupled. When the scan sense, a status indicator derived from elevation and azimuth module logic when steps or scan turnarounds are in progress, is low, or when the solenoid or ramp calibrate commands are being executed, the bleep is strongly biased in a negative sense. This level shift clearly marks any invalid data. One other subtlety of the board is the direct supply of 1 Hz pulses to the signal module; similar pulses to the azimuth, elevation, and solenoid circuitry go through the interface. Lastly, the ramp calibrator uses the two second pulse from the time mark generator to drive a pulse counter and digital switch which injects a sequence of eight voltages into the azimuth and elevation scan and three signal FM outputs at the interface. Used periodically during flights, this procedure checks the total system performance.

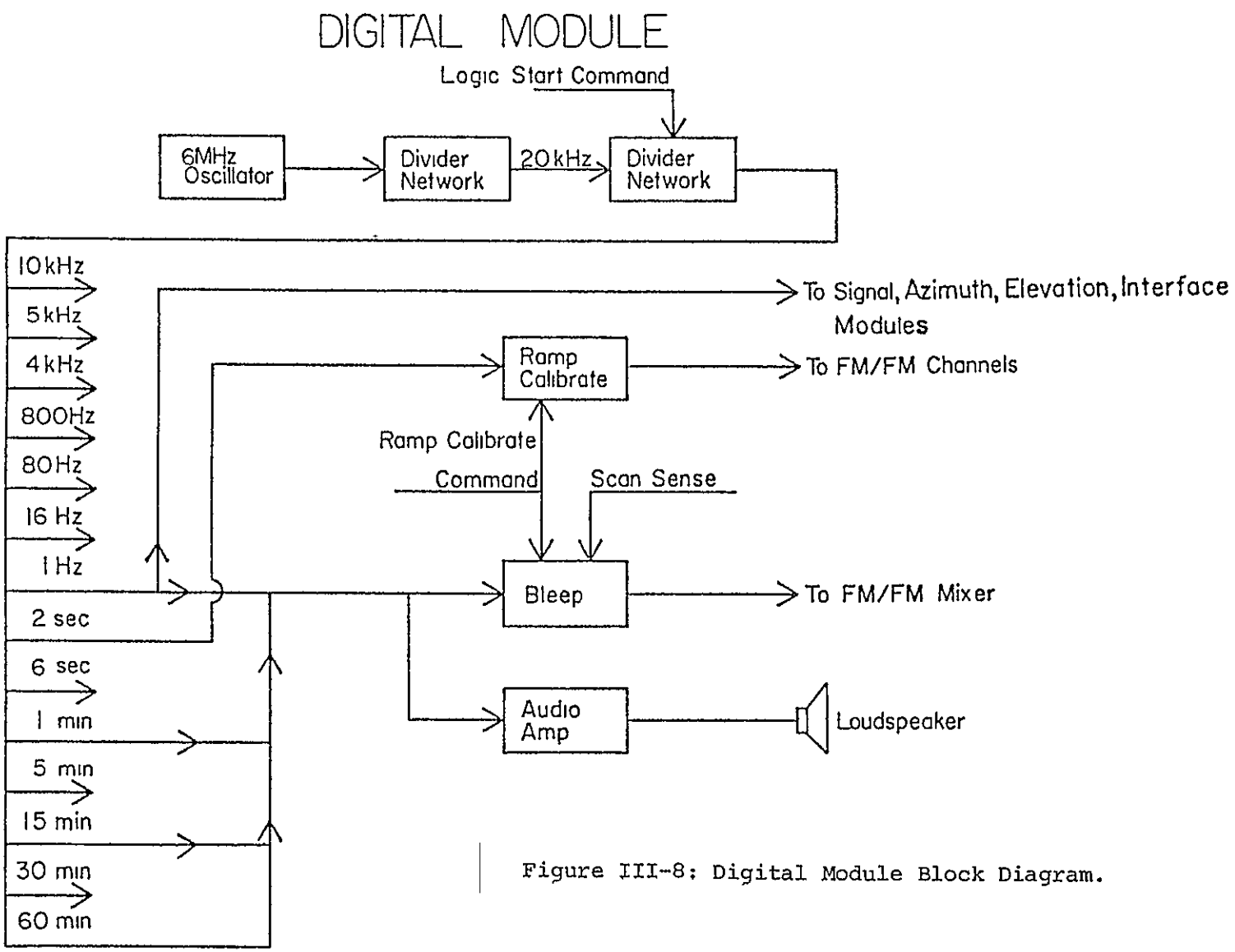

Figure III-8: Digital Module Block Diagram.

The power module contains one board and switches several Technipower DC/DC converters. Incoming battery power flows through a Magnecraft latching relay to the Technipower units, arrayed in parallel. One produces +5 volts for logic (V_{CC}), a pair generates a clean ±15 volts for circuitry (V_B), and a similar pair creates ±15 volts for motors (V_C), which engender noise and transients throughout the supply. A sixth supply emits +28 volts (E+) for the magnetometers. The relay latches up by telecommand or by the opening of a pressure switch at 16,000 feet. In each case, a charged capacitor drives a transistor switch which allows current to flow through a relay coil. A similar process shuts the power off on descent below 14,000 feet.

Our balloon-borne observatory's powerhouse consists of 22 Yardney silver cadmium "Silcad" cells connected in series. Each battery averages 1.08 volts under load, so the pack voltage is around 24 volts. Moreover, they are rated at 100 ampere-hours capacity, so 2.4 kilowatt-hours can be stored for flight. The cells are extremely rugged, which is fortunate, since the electrolyte and cadmium electrodes are quite toxic and balloon landings are rather rough. Each cell weighs about 3.3 pounds; the batteries plus housing add up to about 90 pounds. The batteries will operate as low as -65° F, but they are conveniently heated by the adjacent and somewhat inefficient DC/DC converters in the power module. Easily charged, the cells last up to three years on the shelf and can withstand at least 200 cycles of 95% discharge. The battery case contains a "warm" thermistor to monitor temperatures (see III. E. 3.). Figure III-9 shows the battery box.

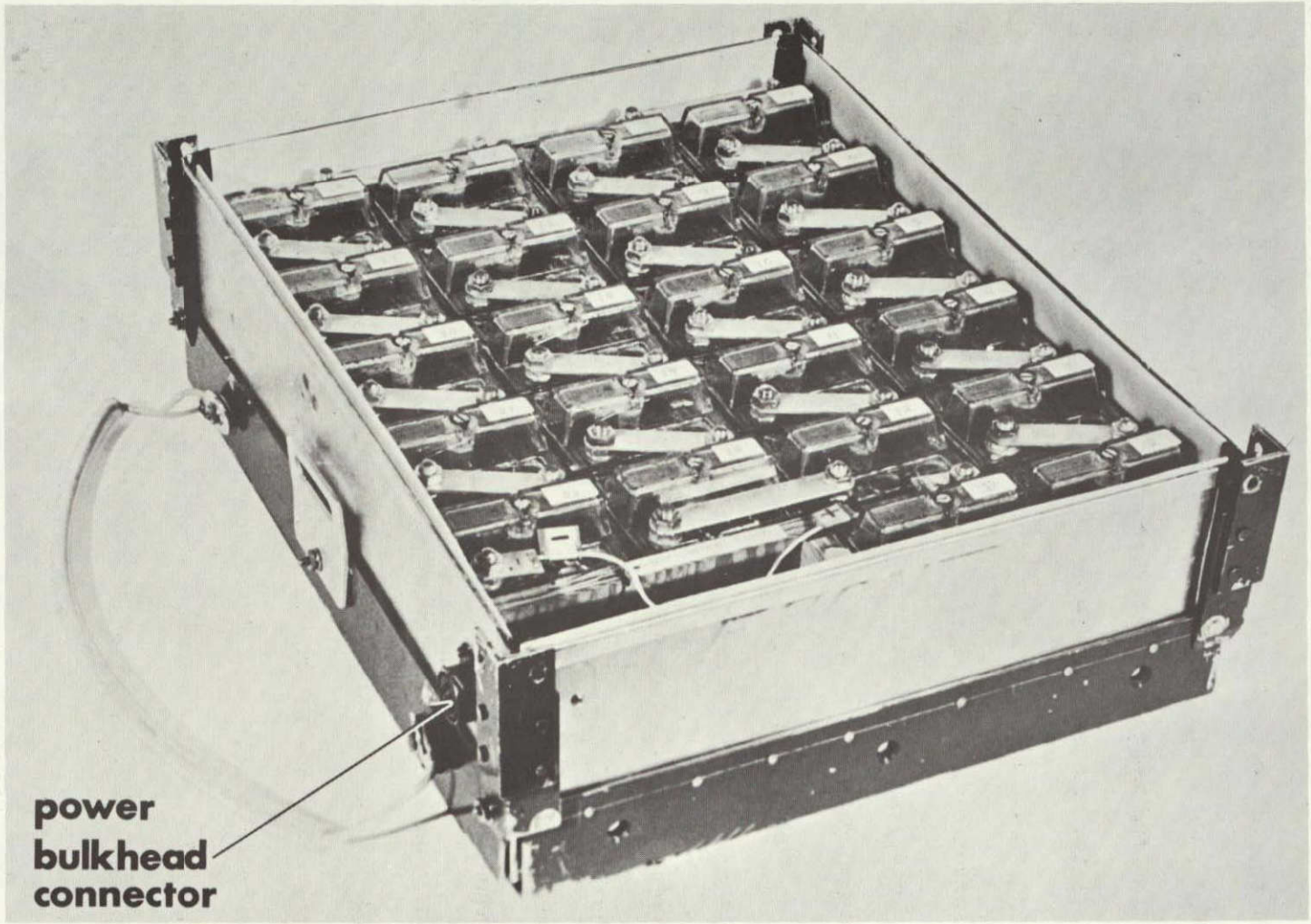

Figure III-9: Main Battery Box.

3. Telemetry and Telecommand Systems

Fortunately for balloon experimenters, NCAR has developed a Consolidated Instrument Package (CIP) which combines both control and scientific functions into a relatively compact set of components. Moreover, the CIP easily merges with both gondola electronics and the ground station system. The NCAR equipment divides conveniently into three parts: the telemetry, for transmission of data from the gondola, the telecommands, for reception of commands from the ground, and the navigation instruments, including pressure-altitude and location devices. A block diagram, Figure III-10, shows the telemetry system and the ground station configurations we employed during Flight C-1.

The two basic types of multiplexing systems are frequency division and time division. The former carries data on several channels simultaneously, allowing each to modulate one of several assigned frequencies which modulate, in turn, the FM carrier; the latter samples channels in a predetermined sequence and transforms the result into a bit stream that modulates the FM carrier. Frequency division suppresses thermal noise, microphonics, and crosstalk considerably, while time division handles both analog and digital signals and samples different channels with greater flexibility. The complexity and expense of time division demands many channels for justification, however. Our telemetry exploits both systems: frequency division handles a total of twelve gondola outputs (FM/FM), while time division translates the balance of 104 scientific and control channels (PCM/FM).

In FM/FM, the analog outputs, conditioned to range between 0 and 5 volts, drive voltage controlled oscillators (VCO's) whose outputs are mixed, amplified, and mixed again with the FM carrier. The oscillators

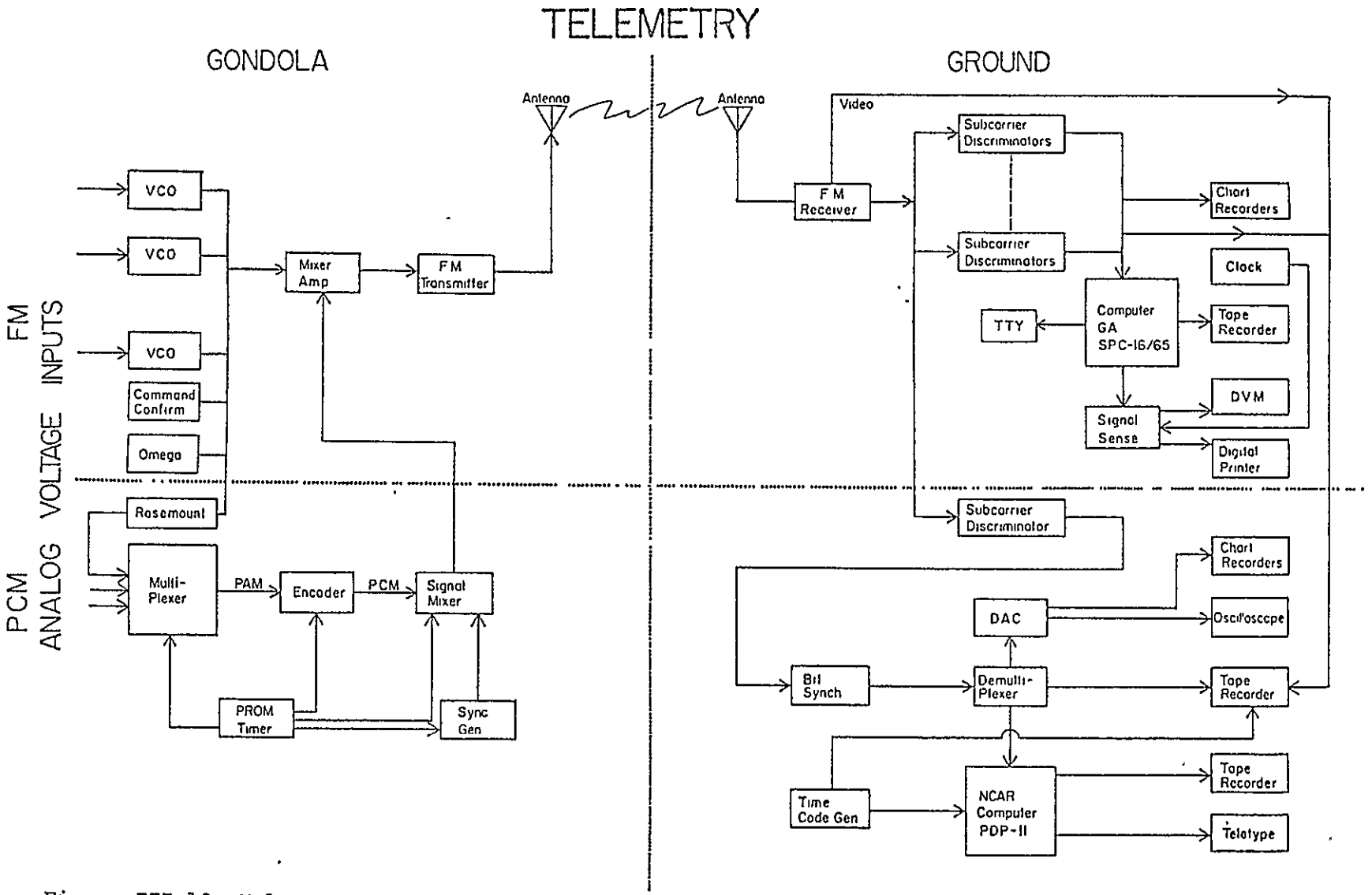

Figure III-10: Telemetry Block Diagram.

conform to IRIG[1] subcarrier frequencies, with widths of 6, 11, 20, 35, 45, 59, 81, 110, 160, 220, 900, and 2100 Hz, while the standard carrier is in the L band, between 1435 and 1535 MHz. To remind the astronomers reading this, the carrier band lies between the 21 cm line of hydrogen and the quartet of hydroxyl lines! Since we require a 10 Hz bandwidth for most of our FM signals and 100 Hz for the chopper sensor and bleep, the first NCAR channel was assigned to the command confirm, an NCAR function; bleep and sensor were deployed at the broadest subcarriers. After broadcast and reception by the ground station, the signal is demodulated from the carrier and imposed on a bank of discriminators, or bandpasss input plus low-pass output filters. These recover the original analog outputs for recording on tape, chart recorders, or display on meters and oscilloscopes.

PCM is a bit more involved. Signals from the interface enter a multiplexer, or commutator, that runs through a sequence stored in a programmable read only memory (PROM). The versatility inherent in such a controllable system enables one to supercommutate, or sample the same signal more than once per cycle, and subcommutate, or inspect a signal less than once per cycle. Even sub-subcommutators can be arranged. Our PROM featured a loop of 32 steps divided into four similar frames. Figure III-11 contains a graphic representation. The first six steps of each frame were identical and were thereby supercommutated (128/sec). The seventh step in the first two frames held a 32 step subcommutator with identical 16 step subframes (4/sec), and the seventh step in the

[1] IRIG, the Inter-Range Instrumentation Group, represents the Range Commanders Council at the White Sands Missile Range. They publish standards for telemetry, such as frequencies, time codes, and pulse configurations.

Figure III-11: PROM for Flight C-1

FRAME

1	^{1}A1	^{2}A2	^{3}A3	^{4}A4	^{5}A5	^{6}A6	^{7}S3	^{8}A54
2	^{9}A1	^{10}A2	^{11}A3	^{12}A4	^{13}A5	^{14}A6	^{15}S3	^{16}A55
3	^{17}A1	^{18}A2	^{19}A3	^{20}A4	^{21}A5	^{22}A6	^{23}S4	^{24}A56
4	^{25}A1	^{26}A2	^{27}A3	^{28}A4	^{29}A5	^{30}A6	^{31}SY	^{32}

A stands for analog input
D stands for digital word input
AD stands for differential input
SY stands for synchronization subframe

SUBFRAMES

	S3	S4
1	A7	A17
2	A8	A18
3	A9	A19
4	A10	A20
5	A11	A21
6	A12	A22
7	A13	A23
8	A14	A24
9	A15	A25
10	A16	A26
11	AD26	A27
12	A53	A28
13	D1	A29
14	D2	A30
15	D3	A31
16	D4	A32
17		A33
18		A34
19		A35
20		A36
21		A37
22		A38
23		A39
24		A40
25		A41
26		A42
27		AD22
28		A45
29		A46
30		AD24
31		A49
32		A50

third frame contained another 32 step subcommutator (1/sec). The fourth frame's seventh step held a synchronization subframe, and the eighth step of all four frames were singly commutated pulses (32/sec), which we didn't use. The 128/sec rate was reserved for the azimuth magnetometer and vernier pot, the bleep, chopper sensor, and IR channel #1 outputs, both AC and lock-in. The middle rate (4/sec) took in elevation and other azimuth information, plus cryo heater and chopper circuit data. Output concerning phases, detector voltages, temperatures, power supplies, chopper amplitude, and preamp heater were checked at the 1/sec rate. The digital words, which relate current command conditions of the azimuth and elevation scan widths, signal gains and phase shifts, chopper modes, and others also commutated at the slowest pace.

At this point, we have a pulse amplitude modulated (PAM) signal, the height corresponding to the analog signal strength. The encoder is

next, consisting of an amplifier, a sample-and-hold circuit, and an analog-to-digital converter, which emits PCM data. A signal mixer injects digital words from other sources, such as the synch generator. The bit stream from the mixer modulates a 4950 Hz bandwidth FM channel; from here, the FM/FM section's transmitter and antenna take over. The bit rate for Flight C-1 was 10.24 kilobits/sec.

On the ground, the reverse procedure takes place. A receiver feeds a tape recorder and a bank of discriminators, described above, one of which extracts the PCM channel and subjects it to a demultiplexer, programmed to recognize the format we use. Some signals are converted back to analog, while the rest flow into a PDP-11 computer, which controls, which controls the PCM recovery system, along with an IRIG B time code generator. The outputs are both taped and typed for real-time monitoring.

Commands are made with a PCM system, except for four NCAR tone commands, used for balloon control and termination. All command systems must be extremely reliable, so that transients or noise are not recognized as signals and vice versa. The ground system starts with a command encoder. Thumbwheel switches are set at the proper octal address by the operator, after which the control and timing unit converts the settings into 16 bits, which are coded and frequency-shift-keyed to modulate a VHF transmitter. Each command is sent twice for redundancy. On board the gondola, a command decoder does a bit-by-bit comparison before sending the 6-bit address on for decoding. If valid, the rest of the bits are released and a strobe pulse emerges to drive the proper command relay. The telecommand system is shown in Figure III-12. We used 28 of 50 available PCM commands for the scientific gondola functions. A few more PCM channels, along with

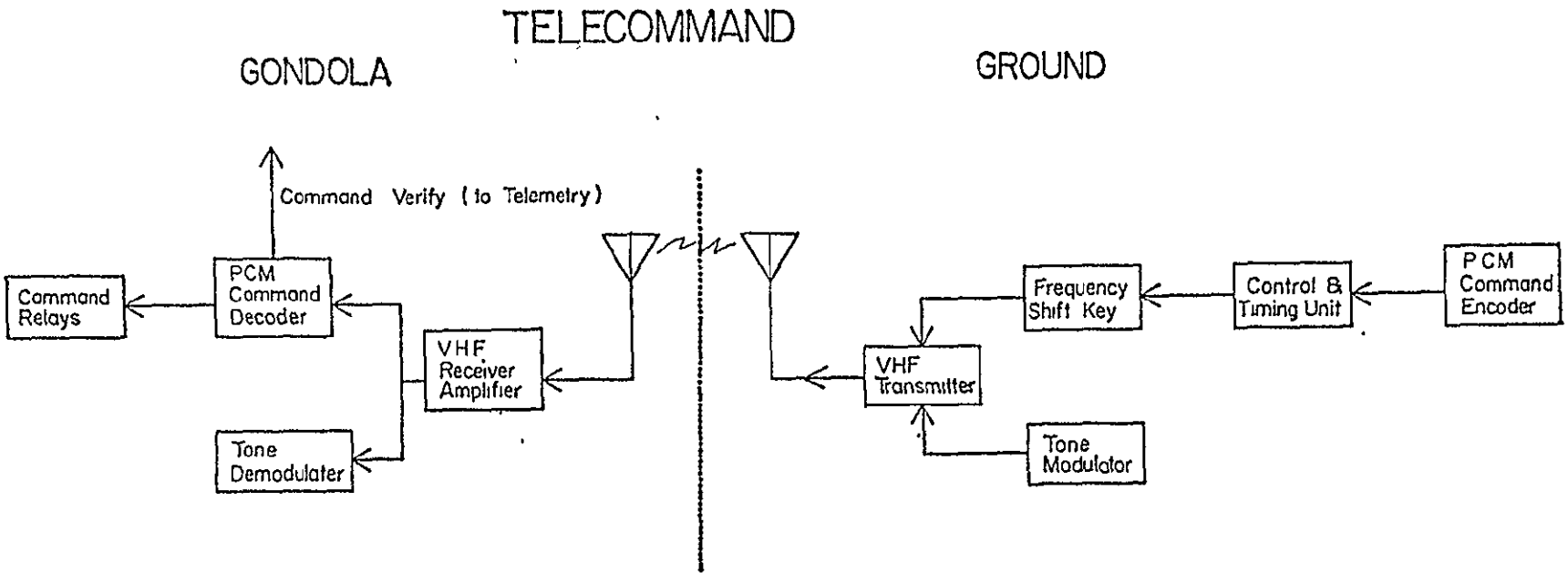

Figure III-12: Telecommand Block Diagram.

the tone commands, were used by NCAR for dropping the beacon antenna and turning it on and off, transmitter control, ballasting, switching the Rosemounts, release of the telescope at float, separation of the parachute from the balloon and destruction of the latter at termination, and gondola separation and clamshell opening before impact. The tone command system is straightforward, in that audio oscillators simply modulate the RF carrier, and resonant reeds or active filters separate the tones in the balloon-borne receiver. Table III-2 lists the commands.

The Rosemount 830A altitude sensor is best described by direct quotation from Smith (1974),

"To cover the entire pressure range, three pressure sensors are used, covering ranges from the surface to 70 mb, from 70 to 7 mb, and from 7 to 0 mb. An automatic switching circuit was developed so that data from the three sensors need to occupy only one data channel. Pressure measurements are made with a variable capacitance in an oscillator circuit. One plate of the capacitor is held at a vacuum reference while the other is varied with pressure. The oscillator frequency varies around 200 kHz, which is converted to an output ot 0-5 volts. The oscillator will respond to a pressure variation in 1 msec and can easily measure a pressure change that would be equal to an altitude of less than 30 meters."

Our system used the low and medium altitude Rosemounts which fed both an FM/FM and a PCM/FM channel. A radar reflector below the parachute enables tracking from the base, and the beacon, 1.679 MHz transmitter, provides the tracking aircraft with a reference. Finally, the balloon-borne Omega system, based on phase comparisons among any three of eight world-wide transmitters, consists of an amplifier and an antenna. The 13.6 kHz Omega carrier, 200 Hz wide, is mixed into another FM/FM band for ground analysis. Completing the NCAR package are batteries and the light beacon, a rather large, pulsed flashlight, plus flight timers, which terminate float at some predetermined maximum period. A list of all NCAR equipment appears in Table III-3.

TABLE III-2: FLIGHT C-1 COMMANDS

SCIENTIFIC		NCAR	
Momentary	Latching	Momentary	Latching
Elevation Step	Up/Down	Parachute Release	Transmitter
Elevation Scan	Cryogenic Heater	Telescope Release	Ballast
Ramp Calibrate	IR Channel #4/ Focal Plane Monitor	Rosemount Low	Beacon
Logic Start		Rosemount Medium	
Signal Gain	Preamp Heaters	Gondola Squib (Clamshell)	
Chopper Mode	Lid Open/Close		
Manual Balance	Power		
Auto Balance			
Azimuth Step			
Azimuth Scan			
Stow Bolt			
Phase #1			
Phase #2			
Phase #3			
Phase #4			
Solenoid			

TABLE III-3: NCAR FLIGHT ITEMS

1. Transmitter
2. Omega
3. Beacon
4. FM/FM
5. Command Receiver
6. Command Decoder
7. PCM Encoder
8. Low and Medium Rosemounts
9. Rosemount Switch
10. Relay Command and Junction Box
11. GMD Radiosonde
12. Command Batteries
13. Telemetry Batteries
14. GMD Batteries
15. Receiver Antenna
16. Transmitter Antenna
17. Omega Antenna
18. GMD Antenna
19. Beacon Antenna
20. Light Beacon
21. Telemetry Battery Extension
22. Clamshell Squib Assembly
23. Telescope Squib Assembly

Also managed by NCAR are the provision and installation of squibs, powder-actuated cable cutters that execute various mechanical functions. Fired by telecommand from the base or tracking aircraft, the squibs can cut the cable tying the clamshell (see III. C. 4.) together, for example. Usually, two squibs slice each fastener, in case one should fail. This in one of many tasks we gladly leave in the competent and steady hands of the NSBF personnel.

C. Gondola Pointing and Suspension Systems

1. Azimuth System

Azimuth, an Arabic word (as-sumūt, the way) from the era of navigation by astrolabe, refers to directions in the plane perpendicular to the gravitational vertical, defined for our purposes by the main post suspended from the balloon. To point and stabilize our telescope in this plane, we use a magnetometer to identify the nulls in the earth's magnetic field and a servomechanism to slew, scan, and stabilize the gondola. Several components, shown in a block diagram, Figure III-13, and in a pair of photographs, Figures III-14 and III-15, are involved.

A magnetometer table incrementally rotates the magnetometer post relative to the gondola by ground command, thereby generating an error signal used by the servomechanism electronics in the azimuth module. The electronics can also generate artificial error signals to induce a set scan pattern in azimuth. To slew the gondola, the electronics drive an inertia wheel by means of a torque motor; the gondola reacts to conserve angular momentum by rotating in the opposite direction. A tachometer reports on the inertia wheel's angular velocity to ground and to the active bearing, which can minimize coupling with or slowly transfer excess angu-

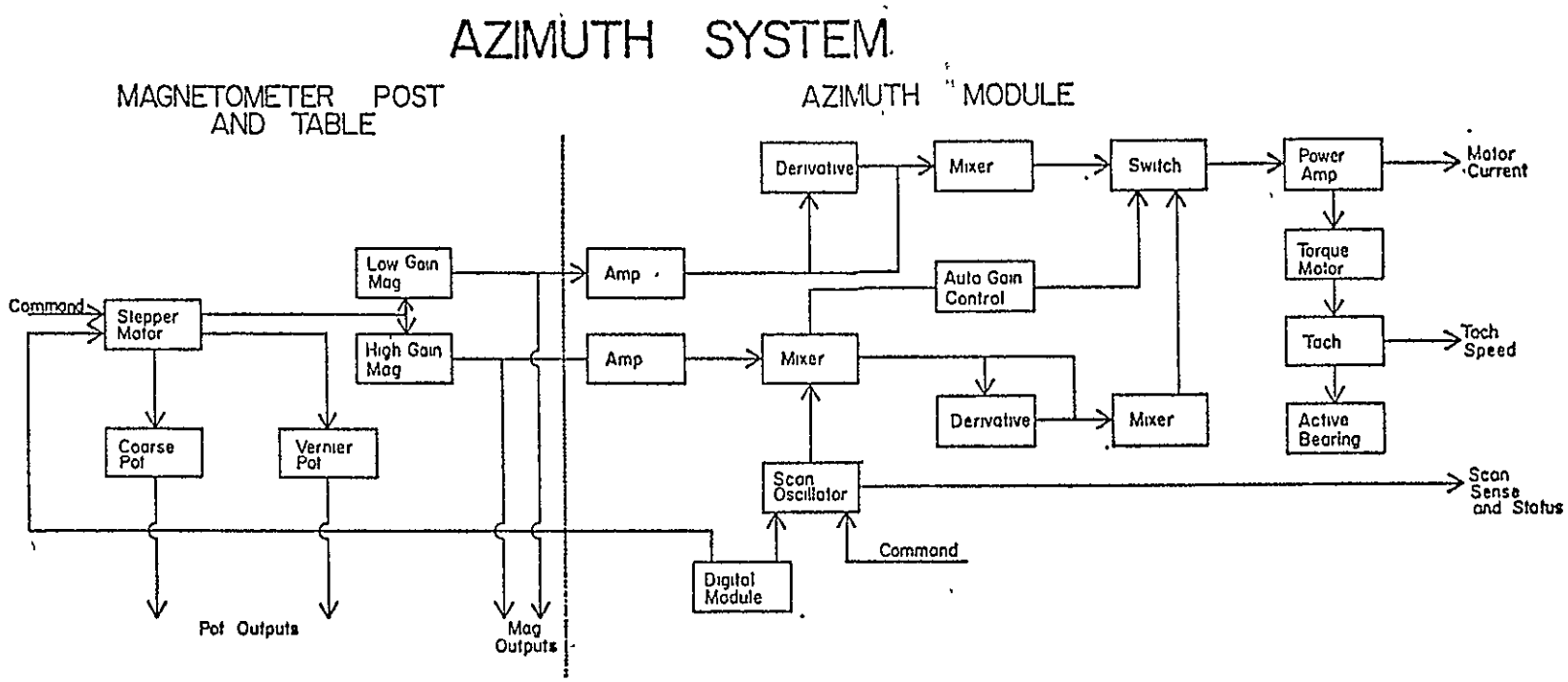

Figure III-13: Azimuth System Block Diagram.

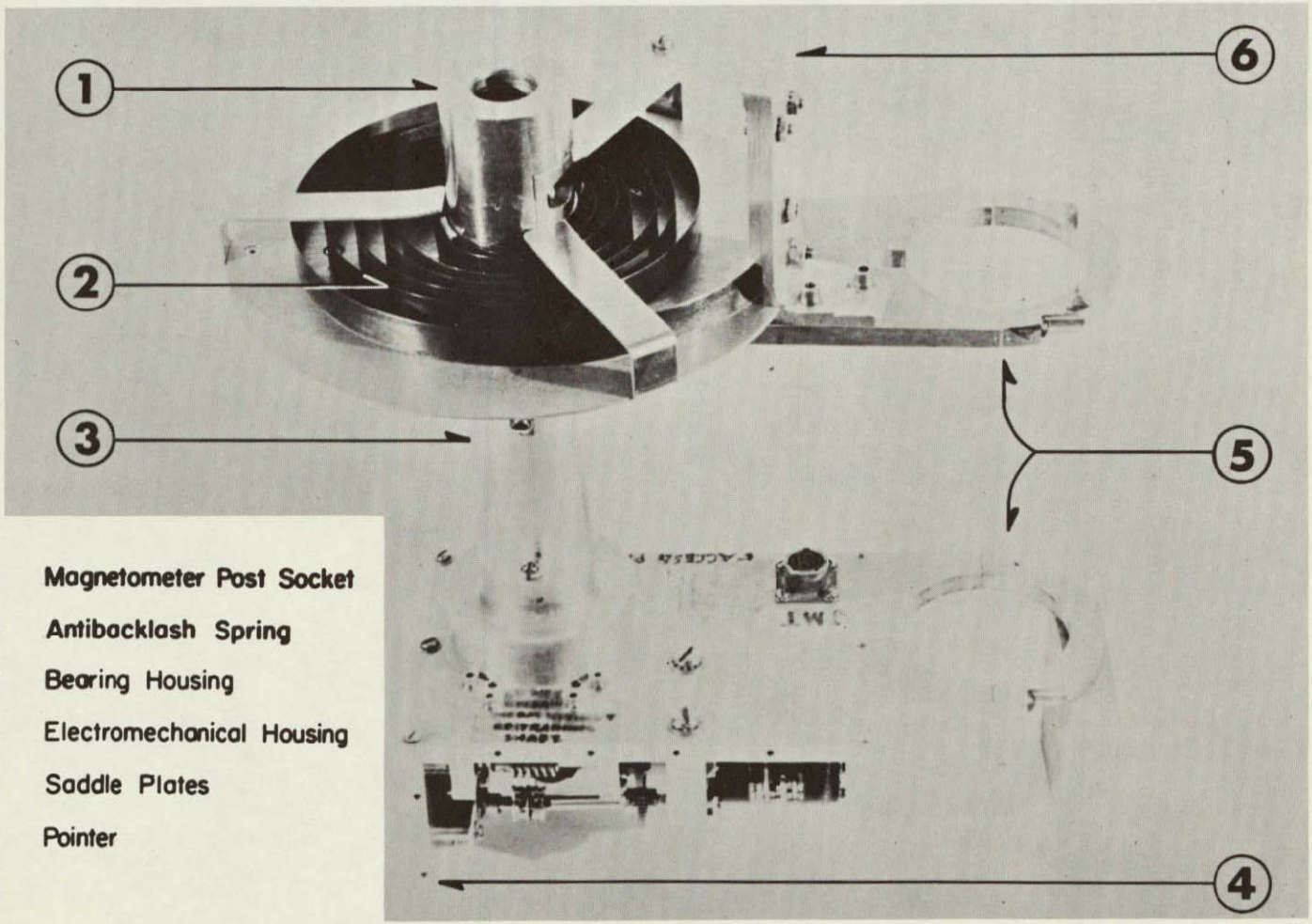

Figure III-14: Magnetometer Table A. Overall View.

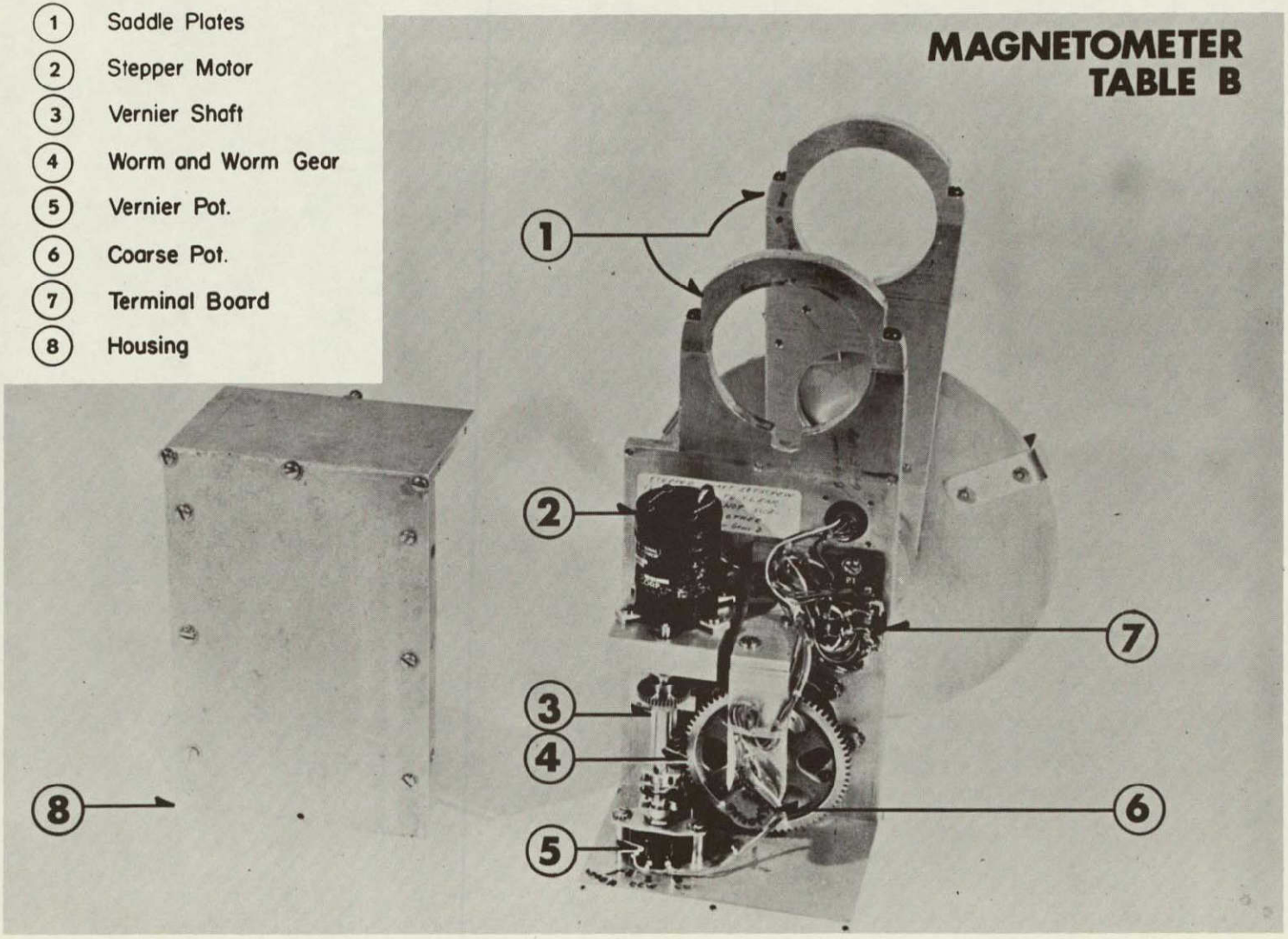

Figure III-15: Magnetometer Table B. Bottom View.

lar momentum to the balloon. I will describe each of these parts in more detail below.

The magnetometers themselves come from the Schonstedt Instrument Company and operate on the saturable-core or flux-gate principle. Basically, the device has a permeable core with two two-part windings, one of which, the excitation coil, is wound as shown to the left, so that the net flux through the core is zero. The excitation current is such that the permalloy core is quickly saturated; its frequency is about 10 kHz. In the other, sensor coil, a voltage is induced at twice the excitation frequency, as the core goes in and out of saturation twice in each cycle. If a steady, constant component, such as the earth's magnetic field, is superposed, it survives the subtraction in the halves of the sensing coil and emerges as a sinusoidal signal at the excitation frequency's second harmonic. Then, amplification and phase-sensitive rectification are executed in the separate electronics unit. A more complete description is available in Lion (1959).

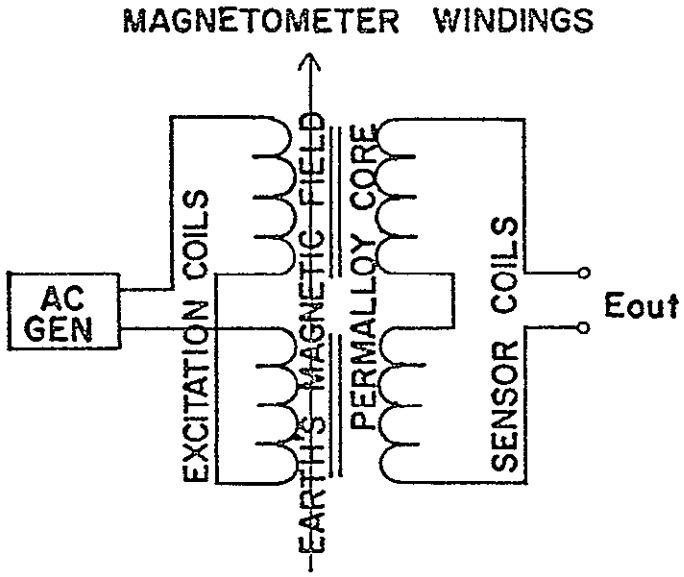

Two Schonstedt magnetometers are employed: one with low gain — 4 mV/millioersted and a ±600 millioersted range (#RAM-5B-NB), and one with high gain — 100 mV/millioersted and a ±25 millioersted range (#MND-5C-25NB). Each magnetometer has two parts, the sensing element, 3 inches

long and 5/8 inches in diameter, containing the coils described above, and an electronics unit, embracing the regulated oscillator, signal oscillator, and phase-sensitive recitifier. A cable with four leads for each magnetometer (two for each winding) is taped to the main post and runs from the sensing elements, mounted in a solid lucite cylinder atop the magnetometer post, to the electonics units, housed in the electronics box (see Figure III-3). Their output, in turn, is cabled to the azimuth module. Fortunately, the magnetometers are small, light-weight, and rugged; they are specifically designed to survive the shock, acceleration, and vibration encountered in rocket flights.

The lucite cylinder rests on a four-foot tall, two-inch aluminum tube well above the elevation system's bearing box for isolation from magnetic disturbances originating in DC motors and other devices. Additional mechanical protection is afforded by a large, inverted magnesium-aluminum roasting pan, suitably sculpted and clamped to the main post so that it shelters the magnetometers. Moving down the magnetometer post, we encounter a guide ring (see Figure III-3) for support should the post sustain a strong lateral force, and an adjustable setting circle. Below this, the post ends with a one-inch tip that is retained by a split clamp socket at the top of the magnetometer table mainshaft.

An overall photograph of the table appears as Figure III-14. Still moving from top to bottom, the upper saddle plate, clamped to the main post, carries a bracket for the setting circle's lucite pointer and a stainless steel anti-backlash coil spring, with appropriate restraints. The spring torques the mainshaft toward decreasing azimuth. Between the upper and lower saddle plates, the mainshaft runs six inches between two Conrad bearings within a bone-shaped bearing block and is retained in

thrust by two truarc spring washers and loaded by a wave washer below the lower bearing. Felt seals keep the bearing block's interior clear of debris. Under the lower saddle plate, also the top of and mounting surface for the magnetometer table, the mainshaft terminates with a worm gear, and further down, a potentiometer. The Boston worm gear mates with a worm on a shaft driven by a Curtiss-Wright 28 volt bidirectional stepper motor. Initiated by ground command, each step is 36°. An Oldham delrin coupling links the motor to the worm, which drives the 72 tooth worm gear. Since each step in one tenth of a motor revolution, and each tooth of the gear is 5°, each step rotates the mainshaft $\frac{1}{2}^{\circ}$! Two pots participate: a 10K, 3-turn Bourns "coarse" pot runs directly off the mainshaft via another Oldham delrin coupling, and a 10K, continuous "vernier" pot is activated by a shaft parallel and linked to the worm shaft by identical spur gears (see Figure III-15). A Rembrandt wafer spring coupling absorbs misalignment on the vernier shaft. A spring on the worm shaft loads it to minimize backlash. The pot elements' ends are connected to a resistor/diode network on a small circuit board which also serves as a terminal strip for the bulkhead connector; both board and connector mount to the table's upper plate.

Attention now shifts to the azimuth module. There, a circuit board drives the stepper motor using the ground station's up/down and step commands and the digital module's one Hz pulses to produce stepper pulses and corresponding signals for telemetry back down, plus a reset pulse for the azimuth scan oscillator. Returning to the magnetometer signals, which we followed up to the azimuth module, we find both entering the preamplifier circuit card. They are first respectively amplified by 5.7 and 4.6 for low and high gain, producing sensitivities of 0.1 and

2 V/degree. Beyond these points, whose voltages are telemetered, the two preamps differ in one respect. The high gain preamp receives an artificial error signal from the azimuth scan oscillator, a ramp generator that induces azimuthal scans of several widths — 1.5, 2.5, 3.75, 5, 7.5, and 10 degrees — that can be requested from the ground. A mixer superposes the high gain magnetometer and scan oscillator outputs and sends the result to the automatic gain switch, which it controls, as well as to the remaining stages of the preamp, which is similar to the low gain unit. Both signals are differentiated and compared to the undifferentiated signals in the succeeding opamps. The results go to the gain switch, which chooses between magnetometers on the basis of the high gain magnetometer's second stage output. Dial pots on a panel adjacent to the azimuth module adjust the differentiator and comparator gains for both preamps. In this way, we can adjust the damping of the gondola oscillations through the derivative gain and the overall response via the comparator gain. The purpose of the two gain azimuth servo is to provide a low gain, high range linear loop for initial acquisition when the servo is first turned on. Thereafter, it operates in high gain mode.

The gain switch employs a two-pole Teledyne relay that normally keeps the high gain magnetometer connected to the power amplifier. However, if the second stage output from the high gain magnetometer — henceforth, the control voltage — exceeds ±10 volts, equivalent to $\pm 5^{\circ}$ from null, one of the two parallel opamps is turned on and saturated by positive feedback, thereby acting as a bipolar switch. This delivers a positive voltage to a transistor base at their mutual output, which turns it on and switches the relay, allowing it to carry the low gain magnetometer signal. The inverting opamp, when switched, feeds its output to the non-

inverting opamp, preventing both opamps from switching. Should the control voltage drop below ±5 V or ±2.5°, the switched opamp turns off, returning the relay to the high gain magnetometer side. The hysteresis is accomplished by biasing both positive opamp inputs with feedback from a pair of resistors at both outputs leading to a common dial pot, whose setting determines the magnetometer crossover points. Thereby, jitter at a single critical voltage is avoided. A few other biasing arrangements enable the opamps to run symmetrically about the magnetometer null. The other relay pole tells the ground station the switch's status. Finally, the selected signal enters the power amplifier, where twin opamps, inverting and non-inverting, feed the magnetometer signal to dual banks of power transistors and provide a high impedance current source. A gain of 0.6 A/V sends up to ±3.75 A at up to ±25 V to the torque motor.

Produced by Inland Motors (#T-5134C), the DC device delivers torque in response to current with high linearity. The entire assembly is 6-1/8 inches in diameter and 1-5/16 inches thick; it can produce 2.7 ft-lb of torque and rotate as much as 22 rad/sec. Built without a frame, the motor has three parts: a brush ring, which carries four brushes, a permanent magnet assembly, to which the former is mounted, and a rotor assembly consisting of a commutator and armature and surrounded by the brush ring and field magnet assembly. A similarly constructed tachometer generator is located about 2-1/2 inches above the torque motor. Both permanent magnets and brush rings slip into and fasten to the upper housing section, a 6-1/2 inch outer diameter aluminum cylinder which bolts to the bearing box's bottom plate and contains internal steps for a bearing and the motor parts. A hollow upper spindle fits through the 2-3/8 inch torque motor inner diameter and mates with a hollow lower spindle, clamping

the rotor in between. The upper and lower spindles are borne by 4-3/8 and 6-1/4 inch O. D. radial bearings in the upper and lower housings, respectively. The lower spindle carries the inertia wheel's 14 inch diameter, ¼ inch thick stainless bottom plate, whose outer rim bears a 1-1/2 inch thick, 2-1/2 inch wide aluminum annulus, which supports, in turn, eight 7-pound brass weights. Altogether, the inertia wheel weighs about 140 lbs, equivalent to 1.6 ft-lb-sec^2 of rotational inertia. At the maximum velocity of 22 rad/sec, 33 ft-lb-sec of angular momentum is available; since the gondola represents about 80 ft-lb-sec^2 of inertia, the wheel, at maximum output, can rotate the gondola at the adequate rate of .42 radians, or 23^o per second. Bolted to the bearing box above and protruding through the centers of the spindles, a 1-13/16 stainless rod supports the telemetry and ballast hanger on a universal joint (see Figure III-3).

Should the inertia wheel reach its maximum spin rate and need to dump angular momentum, the active bearing can transfer the excess to the balloon. This unit, mounted atop the main post, consists of three concentric parts, rather than two parts as in normal bearings. The outer housing holds two large bearings to align the middle part and carries a Globe DC motor in a side enclosure, which is geared to the middle part as well. The middle part, in turn, embraces two more bearings that retain the inner part, a stainless rod that emerges from the top of the assembly and mates with a swivel. The purpose of this arrangement is to avoid sticking friction in the balloon coupling by keeping the middle part, the race of the inner part, constantly in motion. By changing the duty cycle of the DC motor, a net angular momentum goes into the balloon, via sliding friction.

To control the process, a tachometer (Inland TG-2801D), bolted to the torque motor's hub, is employed. Its output emerges from the brush ring and

is telemetered and sent to the active bearing drive, where it shifts the DC level of the triangular wave produced by an oscillator run at a frequency, nominally 0.6 Hz, controlled by a dial pot at the azimuth module. Then a comparator produces a square wave with the proper duty cycle. A power amplification stage supplies 500 mA of current at ±10 V at maximum to the active bearing motor; a trim pot eliminates motor hysteresis and capacitors round the corners of the square wave so the motor reverses gently. The power amplifier uses EMF feedback to develop a stable, controlled motor speed for a given input voltage.

The last unit in the electronics is the scan sense circuitry, which tells us when the scan data are valid. The conditions that inhibit this sense circuit are turnarounds in the azimuth scan, scanning in azimuth and elevation concurrently, and stepping in azimuth.

Overall, the azimuth system is controlled by just three commands: the stepper, scan, and up/down switches. Up/down sets the sense of the azimuth steps and selects the direction in which the sequence of scan commands, including servo and off, are cycled. For instance, if we are on the 1.5^{o} scan width (command one of eight) and wish to widen to a 5^{o} scan width (command four of eight), we would set up/down to up and activate the scan command three times. Diagnostic readouts are numerous: magnetometer readings, gain switch status, azimuth coarse and vernier pots, azimuth scan command in use, and tachometer voltage. The ground computer calculates an accurate azimuth by extracting an integral degree value from the difference between coarse and vernier pots by rounding off and then adding in the vernier pot result. In Flight C-1, this variety of telemetered data saved the flight when the torque motor failed. The low gain magnetometer provided the fundamental azimuth information, with the

computed azimuth readout calibrating the system and the sense of the azimuth steps reported before data-taking giving the sense of rotation.

2. Elevation System

Since the gondola, hanging well below the balloon, represents a reasonably good plumb bob, the elevation system relies on the main post for definition of the vertical. The entire system, excepting the active balance weight on the telescope framework, resides at the bottom of the main post in the bearing box (see Figure III-3). One wall of the box, referred to below as the "elevation baseplate", carries both drive and sense gear trains, while the end of the bearing box far from the telescope, henceforth the "electronics end", supports the stow bolt system. The elevation shaft, running through the bearing box, meshes with the gear trains through two hubless gears. Another module in the electronics box handles the command and servo circuitry. A block diagram and photographs of the heart of the system appear in Figures III-16, III-17, and III-18; the following description moves from structural to electromechanical to electronic considerations.

The elevation shaft, a 2-3/8 inch O. D., ¼ inch wall stainless tube, runs for two feet from the telescope mounting plate through the bearing box. On the telescope end, a 3/4 inch thick, 5-5/8 inch diameter stainless flange backed with a thinner, 1-1/4 inch long step is both shrink fitted and welded to the shaft. Next, an elevation setting circle, retained by a set screw and indexed by a pointer arching over the coil springs, permits manual slewing. Further down, a 3-1/4 inch wide split clamp holds three stainless anti-backlash coil springs and intermediate separator sheets; their free ends are bent over and torque against a

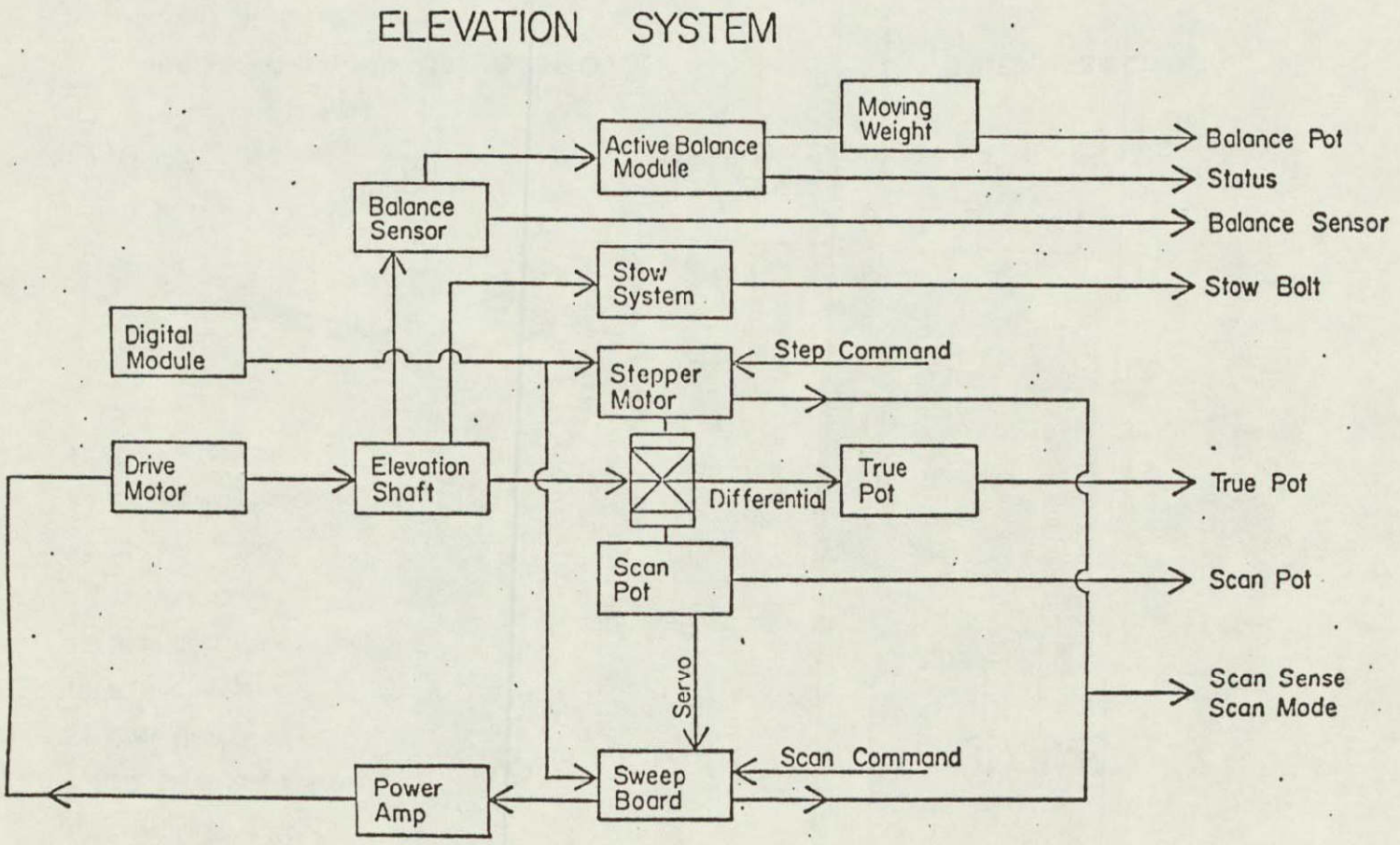

Figure III-16: Elevation System Block Diagram.

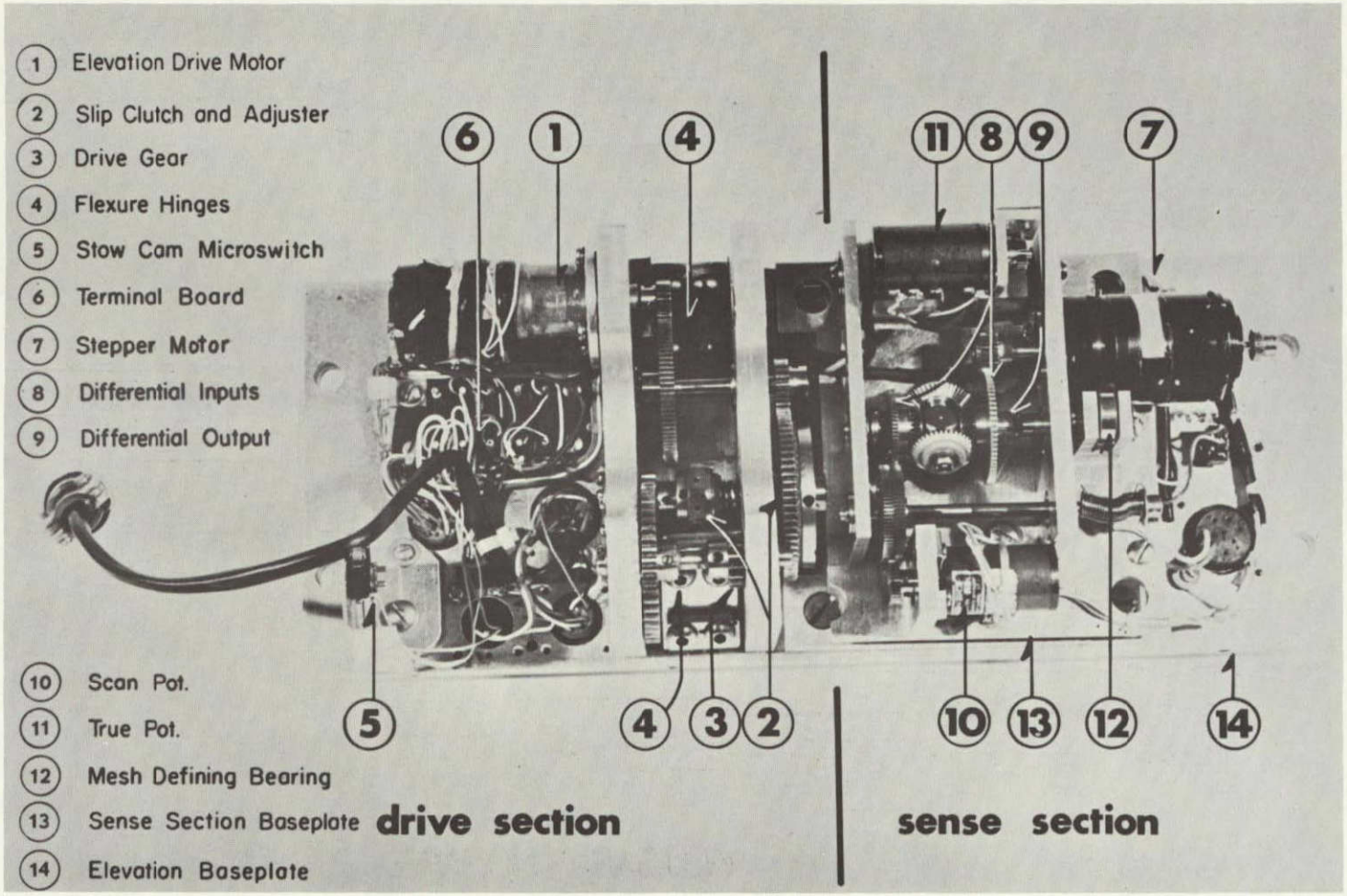

Figure III-17: Elevation Drive A. Inside View of Elevation Baseplate.

ELEVATION DRIVE B

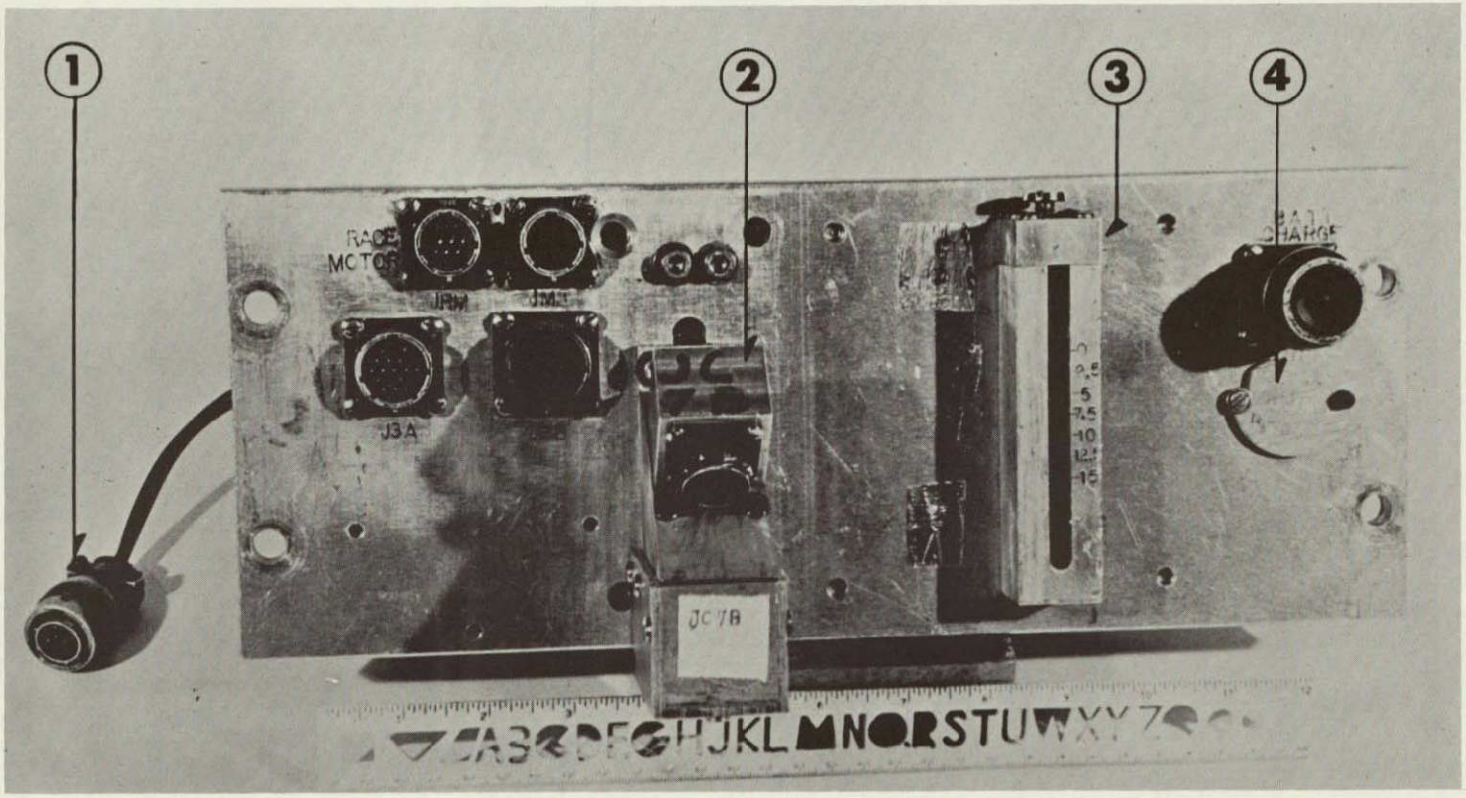

1. Torque Motor Cable
2. Active Balance Sensor
3. Maximum Value Accelerometer
4. Auto Stow Switch

Figure III-18: Elevation Drive B. Outside View of Elevation Baseplate.

stainless rod extending from the bearing box end plate. At this point, the shaft enters the box through a 4-1/4 inch radial bearing held by a step in the end plate and a square retainer bolted to the end plate's outer surface. Inside, a 4.000 inch pitch diameter, 1/8 inch thick, 80 pitch spur gear backed by a set screw mounted ring provides angular information on shaft position; an adjacent brass ring impinges on an elevation baseplate bearing to define the spring loading of the gear. Further down, a 4.000 inch pitch diameter, 3/8 inch thick, 24 pitch spur gear, also backed by a mounting ring, transfers drive torque to the elevation shaft. At the far, electronics end plate, a cam on the shaft trips a microswitch on the elevation baseplate to indicate the telescope's approach to a vertical attitude for stowing. The bearing arrangement in the electronics end plate is identical to that on the other side. Outside the bearing box again, an anodized split clamp on the shaft contains a socket which receives the stow pin.

The rest of the bearing box is just that. The end plates bear the shaft, the bottom plate supports the torque motor and ballast hanger, the respective side plates carry the gear assemblies and provide access to the shaft's other side through adjacent rectangular windows, and the top plate hangs from the main post. Twin, ½ inch thick bracket plates, continuations of the side plates outside the box, extend and fasten to the inner flanges of two vertical channels on the inboard side of the electronics box. These brackets also position the stow bolt motor mount, guide, and microswitch plate; one bracket includes a shelf for placing a mechanic's level during balancing.

Considering the gear assembly in more detail, we divide it into two mechanically independent sections, linked only by their mutual meshing

with the two gears on the elevation shaft (see Figure III-17). The section on the left is the drive section; that on the right is the sense section. Starting on the left, a B-3A-671 Globe DC motor, bolted to the left shaft support — the elevation drive motor — activates a series of Pic spur gears on three shafts, which reduce the motor speed by a factor of about 300 in four stages. On the middle shaft to the right of the right shaft support, a 2 inch slip clutch, lined with 1/16 inch cork gasket material, permits the assembly to slip when the torque on the telescope exceed roughly 10 ft-lbs. Otherwise, breakage of gear teeth would be possible. On the same shaft, a brass adjustment assembly permits the spring to load the clutch properly. The output spur gear or drive gear mates with the large gear on the elevation shaft. Suitable bearings, treated for low temperature operation, retaining rings, and spacers are provided. The shaft supports are bolted together at the bottom and ride on the clamped upper edges of 1 inch wide, .032 inch thick stainless steel flexure hinges; the lower edges are clamped to the elevation baseplate. Used with a linear variable differential transformer (LVDT) outside the baseplate (see III. C. 3.), the hinges allow us to sense telescope imbalance due to vaporizing liquid helium.

The sense section on the right is a bit more complicated. A Northrop bidirectional stepper motor starts the action by driving one end of a precision differential; the other end rotates a Spectrol 10-turn, 10K "scan" pot on the opposite side of an idler anti-backlash gear. The differential output[2] emerges from a bearing in the gear that meshes with the stepper motor; it rides the sensing gear on the elevation shaft.

[2] In this description and in Figure III-17, the differential inputs and output are named by the convention that the bevel gears meshing with the spider are the inputs; the shaft attached to the spider is the output. Functionally, the nulling device, the Spectrol pot, is the output.

A coil spring on the anti-backlash shaft loads the scan pot toward the middle of its range, while the entire sensing section rests on a hinged baseplate, which three coil springs press onto the elevation shaft. A bearing adjacent to the stepper motor defines the resulting mesh. The additional, "true" pot, identical to the scan pot, provides an independent readout of the elevation shaft's position.

Let us follow a step command through the system. A 30° step from the motor drives its end of the differential with the output locked by the mesh with the elevation shaft. Therefore, the pot end of the differential is driven about 18° in the same direction, an overall reduction of about 1.7. This offset enters the electronics as an error signal for a servomechanism and exits as a voltage to the drive motor. The latter can reduce the error signal from the scan pot by turning the shaft in the opposite sense, which drives the differential output, magnified ten times by the gear ratio. With the stepper motor end of the differential locked, the output motion propagates directly to the scan pot, magnified by a factor of about 1.8. Qualitatively, the stepper motor induces an error signal in the pot, which the servo constantly tries to keep centered. As in azimuth, the electronics produce error signals as well when scanning is commanded; more on that below.

Other features of the assembly include a small circuit board that regroups cables from the bulkhead connectors and a microswitch that senses the elevation stow cam. A connector for charging the batteries with the electronics box sealed and a maximum value accelerometer for measuring landing shock are provided on the baseplate's outer face (Figure III-18).

The stow system consists of a Globe DC motor, a spring loaded bolt, and a socket on the elevation shaft. The bolt is hardened and is attached

to a wrist pin that slides on an arm offset from the motor shaft. When we wish to unstow the telescope, a command energizes the DC motor, which lifts the bolt out of its socket and continues until a pair of microswitches is encountered by a disk around the bolt; one opens the stow bolt motor circuit while the other closes an indicator loop. Dropping the pin can be initiated by either commanding the lid to close or by a Precision Sensors pressure switch that closes when the gondola descends below 12,000 feet. In either case, the logic circuitry slews the telescope into the vertical stow position and reverses the stow motor. The former stops when a cam on the elevation shaft trips a third microswitch; the latter halts when a cam on the stow motor shaft touches a fourth one. If the latter occurs first, the stow bolt rides the socket clamp until the telescope is vertical, when the compressed spring forces the bolt home; otherwise, the telescope is already in position when the stow motor stops and the bolt falls in place immediately. As the bolt drops, a fifth microswitch stops the elevation drive motor if not previously turned off by the third switch, while a sixth one closes an indicator circuit. Lastly, a manual toggle switch behind the motor allows us to unstow directly, bypassing the electronics. Another toggle switch on the elevation baseplate sets up the automatic stow sequence, triggered by the pressure switch.

Because the elevation drive and sensing systems are linked indirectly by gear trains, rather than tightly as in the azimuth system, the electronics are not designed as a strict servo system. Qualitatively, dead reckoning is used. When the scan pot is offset by a step or simulated by a scan command, the elevation module powers the drive motor at a constant

speed in order to rezero the scan pot. The drive motor slows down at a predetermined point near the null such that the telescope winds up by stopping at zero. The motors constant slew rate is set at ½ degree per second, which matches the digitally controlled pace of one half-degree step pre second. When the system finds the null, the drive motor is turned off to prevent a creeping, stalling motion.

In more detail, we turn our attention to the elevation sweep board. Figure III-19 shows the situation schematically. The scan pot's input enters the inverting input of an opamp, whose output is wired to the inverting input of a second opamp. Between the two, a digital switch controls the first opamp's feedback. In the servo mode, the switch feeds the second opamp's feedback to the noninverting input of the first, producing a linear amplifier with a gain of about six. The second stage features its own capacitative feedback, which integrates and smoothes the output, preventing mechanical transients. The combination contains a clipping circuit so that they saturate easily at a level that defines the maximum motor speed and telescope slew rate. Therefore, unless near a null, the output is constant. In the scan mode, the elevation scan pot and input opamp, acting as a comparator, behave as a set of reversing limit switches which produce a triangular scan motion. The digital switch acts as an incremental pot; it controls the limit voltage and feeds the first opamp's output back to the noninverting input, thus isolating the second stage and saturating the first with positive feedback. The digital switch is set by the elevation scan commands, which include widths of 1.5, 2.5, 3.75, 5, 7.5, and 10 degrees. Higher voltages are picked off the resistor chain for greater widths. In this configuration, the second stage eases the scan turnarounds, while the first stage becomes a comparator which flips at

C-2

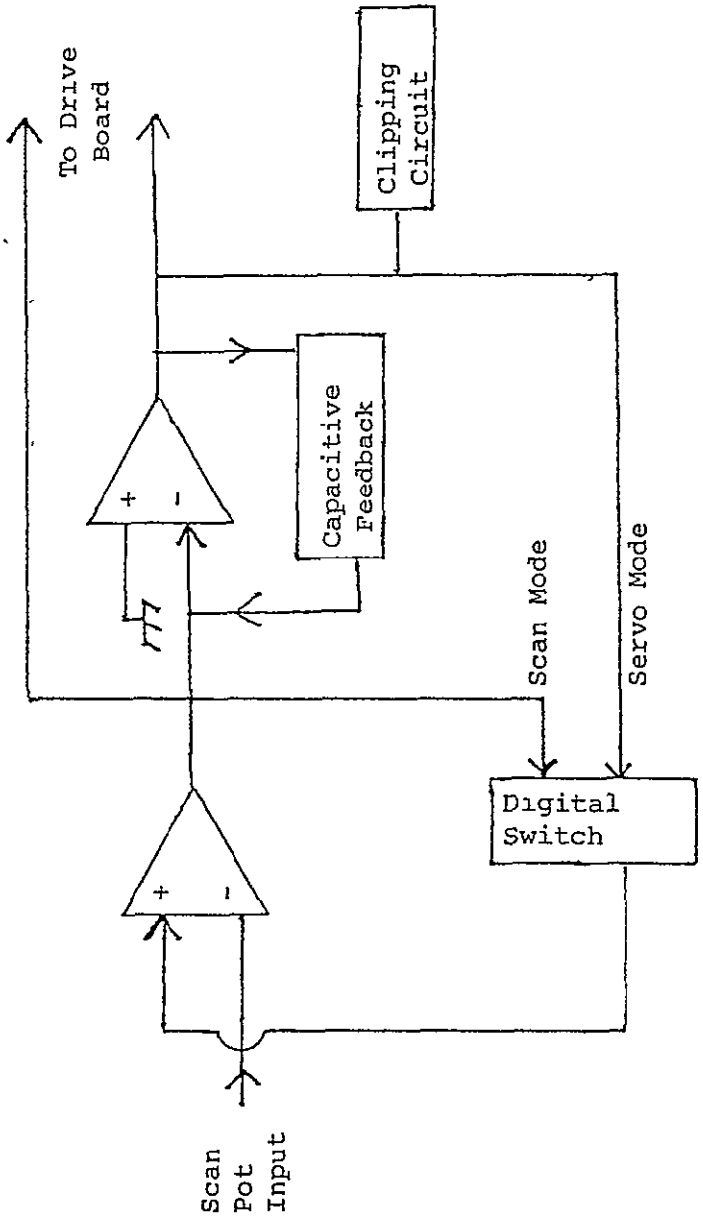

Figure III-19: Elevation Sweep Block Diagram.

the scan extremes. Finally, the first stage output runs to a bipolar voltage sensing circuit on the drive board that turns the motor off when close to a null.

The output of the sweep board flows into the elevation drive board, essentially a current-limited, push-pull amplifier with EMF feedback for stabilizing DC motor speed. It is capable of 20 V at 0.55 A and nominally 11.7 V at 0.2 A. Another eight position digital switch is used as a three position switch to control the gain of an opamp right before the power transistors. The device can either turn off the motor when the system is nulled, run it at low gain for the 1.5^{o} scan, or drive it normally. A trim pot ensures scan symmetry. Lastly, a double throw relay in front of the motor can be switched directly to the main battery to drive the telescope to vertical when the stow procedure is activated.

The stepper motor board takes timing pulses and elevation step plus up/down commands to generate stepper motor pulses. The same board contains the logic circuitry that takes scan mode and scan extreme (turnaround) information to produce the "scan sense" indicator, which advises the digital module and ground station when data is acceptable. In addition, a reset pulse for the scan mode's digital switch and the stow circuitry emerges from the stepper board. The fourth circuit board embraces the scan extreme sensor, a means of lengthening the scan sense pulse, and the stow bolt system, which is a complicated array of switches, transistors, and relays whose effect is described above.

Operation of the elevation system from the ground station corresponds closely to the azimuth system. A sequence of eight scan states, selected by up/down and elevation scan pulses, includes off, servo, and six scan widths. Slewing is accomplished by elevation step commands. Diagnostics

are numerous: scan and true pot voltages, elevation scan sense, scan mode, and stow bolt position. The ground station computer also calculates a "computed elevation" by subtracting scan pot from true pot readings, already converted to degrees. This gives the servo or scan center position. In practice, elevation angles are limited to a range between 50 and 70 degrees, due to cryogenic inefficiency for low elevations and the presence of the balloon at high elevations. The latter is an absolute limit, while the former can be pushed as low at 20 degrees at a price of higher LHe boiloff caused by a change in the telescope's temperature profile. In Flight C-1, the elevation system performed without major problems.

3. Active Balance System

To maintain balance as liquid helium boils and leaves the telescope, replacement of the lost moment, fully 7 lbs at 18 inches, or 10.5 ft-lbs, becomes vital. We accomplish this with a moving weight that is mounted so that one motion — outboard and toward the helium vessel — adequately compensates. Figure III-2 shows how two square split clamps with brackets on the frame's downside locate the ends of an anodized 1-1/4 inch square aluminum tube with 1/8 inch walls. This 30 inch long bar carries an 18 inch Pic rack, along which a C5A-1106 Globe DC motor drives a pinion. The motor, in turn, bolts to a bifurcated aluminum block, whose inner faces hold bearings that roll along the anodized tube; four long bolts loaded with stiff springs hold the halves together. A block of lead is fastened to the upper aluminum block to furnish the required total weight of 20 pounds. In addition, a 10-turn pot fitted with a small gear to the motor's pinion senses the weight position; microswitches at either end of the carrier bar limit weight travel to 15-1/2 inches.

As explained in the previous section, a pair of flexure hinges connect the elevation gear assembly's drive section to the baseplate. A linear variable differential transformer (LVDT) from Schaevitz (050-HR) senses displacements between the core and the coil, mounted to the baseplate and LVDT housing, respectively. See Figure III-20. Normally, the anti-backlash springs are set at 4 ft-lbs to increase elevation. The flexure hinges are set a 1 ft-lb in the opposite sense so that a net torque of 3 ft-lbs holds an adjustable stop, part of the gear assembly, against the housing and tends to raise the telescope. Eventually, enough helium boils away to make the telescope top-heavy; when the resultant torque exceed 3 ft-lbs, the flexure hinges lift the stop from the housing and the telescope begins to drop in elevation. The balance electronics react to the derivative of the LVDT output, which changes abruptly when movement begins.

When 4 ft-lbs of torque are applied to decrease elevation, the baseplate itself is stopped by the housing. The range of the LVDT output swings from +2 volts at the adjustable stop to -8 volts at the fixed stop in a distance of .016 inch, providing a sensitivity of 600 V/inch. The automatic balance cycle intentionally unbalances the telescope by driving the weight upwards. When the LVDT senses motion, its steep negative ramp output reverses the weight for a set time (12.5 seconds on Flight C-1) which restores balance and loading on the adjustable stop. Also, a manual command moves the weight either up or down for a fixed time (also 12.5 seconds on C-1). With the weight in motion, the electronics ignore all additional balance commands. Both LVDT and balance pot can be monitored on the ground. Since the clutch is set a 10 ft-lbs, the automatic balance system, operating properly, prevents unwanted slip-

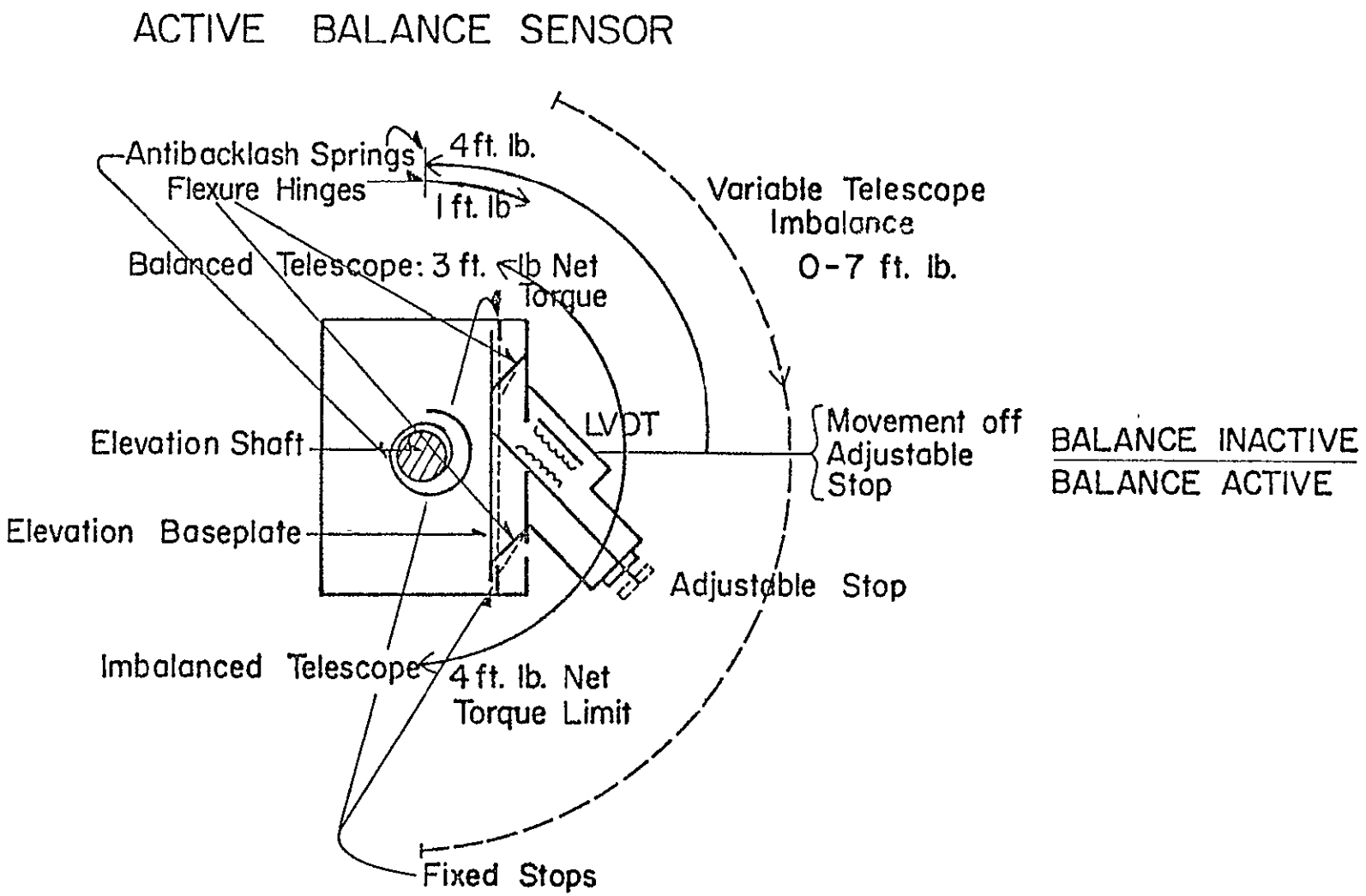

Figure III-20: Active Balance Sensor. The circularly curved arrows represent torques. Only when the variable telescope imbalance exceeds 3 ft-lbs does the balance become active.

page in the gear assembly during flight.

4. Suspension System

The main post, connecting the bearing box to the balloon rigging, has several functions in flight and at landing. I will discuss these features in linear rather than topical order, beginning from the bottom (see Figure III-3). Starting at the bearing box, we find a damper for wobbling in the plane of the elevation shaft and the main post, about the roll axis (see Figure III-2), constructed something like a ski binding. This wobble is equivalent to a double pendulum, where the whole gondola and the flight train is the primary pendulum, swinging about a point in the balloon. We prevent this by providing a lossy coupling between the mass of the gondola and the main post at the wobble frequency (1-2 Hz) and a rigid coupling at zero frequency. A 3-3/4 inch aluminum cylinder, bolted to the bearing box, contains an internal well of 1-7/8 inch square cross-section to accommodate a 5-1/2 inch long, 1-1/2 inch square aluminum peg with its own 3-3/4 inch flange. With its flange up, the peg pivots in the well on an 11/16 inch shaft centered 1-1/2 inches from the flange and borne by bearings in the surrounding cylinder. At the bottom of the peg, a hole at right angles to the wobble plane holds another pin that runs outside the cylinder through oversize holes, where the ends of the pin are clamped between the halves of a spring-loaded split ring. Between the clamping points, the split ring carries an adjustable spring and an adjustable stop that butt against opposite sides of the cylinder in the wobble plane. Motion in one direction is damped when the pin in the internal peg separates the split ring, compressing the load springs, while motion in the other

direction is damped by the adjustable spring. Two other adjustable stops limit the displacement on each side.

Further up, the aluminum peg mates with the lower clam flange. The "clamshell" assembly is meant to mechanically separate the main post from the bearing box before landing, so that torque from the parachute, if filled by wind after impact, cannot roll the package. The "clams" are matching conical flanges, whose bases meet and are held together by the "clamshell", three sectors of an annular clamp made of heat-treated, strain-relieved stainless. A steel cable wound around the clamshell edge can be cut by squibs fired by telemetry command; the clams then separate, dropping the package onto four steel cable slings shackled from the top of the bearing box to a collar mounted on the main post above the upper clam. This connects the post to the gondola in a flexible manner. For location during assembly, the lower clam has an extension that runs into the hollow center of the upper clam, which is retained in the main post proper by three radial bolts. Above and below the steel cable collar, the magnetometer table saddle plate clamps are attached.

The main post itself is a 2-3/8 inch diameter, 3/16 inch wall aluminum tube, rising 88 inches from the upper clam to the active bearing. The only other features in this interval are the two ring clamps for the inverted pan and post guide that protect the magnetometer assembly. Above the active bearing, which is described in III. C. 2., a universal mates with a simple swivel and fitting for the launch vehicle, both supplied by the NSBF. For lab assembly, a rope can be threaded through the main post and clamshell to the wobble damper peg. For lab operation, a "balloon simulator", capable of slow rotation, replaces the swivel and presents the gondola with a situation requiring azimuth stabilization.

C. Telescope Structural System

1. Frame and Passive Balance

The IR telescope, contained in the large Cryogenic Associates dewar, depends on an external frame for support and protection. For ground-based telescopes, such a framework evenly conveys the weight of the optical components to the mounting; a balloon-borne telescope requires shielding against the shocks of launch and landing as well. These two considerations guided the design of the mounting plate, frame, dewar brackets and balance mechanisms. Figure III-2 shows the components described below.

The mounting plate accepts the flange on the elevation shaft from the gondola; eight 5/16 inch bolts hold them together. To achieve strength and stiffness, the 5/16 inch thick plate is composed of 7075-T6 aluminum — a high strength "aircraft" alloy — and is gusseted by 3 by 1-1/2 inch aluminum channel welded to one side. The mounting plate, in turn, mates with the load-bearing channel squares in the framework. An array of holes in the mounting plate permits the telescope to be coarsely balanced along the optical and roll axes.

Shifting our attention to the frame itself, we can identify four components: the channel squares, the angle square and tent foundation rectangle, the tubular columns, and the dewar brackets. Four lengths of 3 by 1-3/8 inch 6061-T6 aluminum channel are joined by 3/16 inch thick 7079-T6 corner plates to form 30-3/4 inch squares. The angle square below is made of 1-1/4 inch angle; the rectangle above is made of both angle and channel. High strength corner plates are employed here, too. Aluminum split clamps are attached to each corner plate to accommodate the columns — 1-1/2 inch outer diameter stainless steel tubes 58 inches long — which connect the upper rectangle and the lower squares together. The resulting

rigid framework supports eight pairs of brackets, at each corner of the channel squares. Four of these pairs extend above and below each of the two mounting rings welded to the dewar; a long 5/16 inch bolt clamps each assembly together. The brackets are made in two parts with slots, rather than holes, provided for the bolts. Should excessive force be encountered on landing, the bracket pieces can slip, sparing the dewar. Finally, the fasteners going through the channel flanges, which have the tapered "American Standard" cross-section, are leveled with bevel washers, cut from an extra section of channel.

A receptacle for a 1 inch tube, serving as a boom for a trim weight, is provided on the side of the mounting plate; this enables us to balance the instrument along the telescope's roll axis. Along the optical axis, balance is achieved by heavy brass split clamps on two of the tubular columns. To balance along the gondola's elevation axis, we deploy small weights on the crush structure. Accessories, such as the active balance weight and visible star telescope, are mounted on plates attached to additional split clamps on the columns. Casters slip into the bottoms of the columns for laboratory handling. After one flight, the frame suffered some bending below the lower channel square, but the dewar was unharmed and the columns were easily straightened.

2. Tent and Mechanism

Condensation of air on cryogenic baffle and optical surfaces represents a crucial difficulty in low background, far-infrared astronomy. Our hopes that boiled off helium leaving the system coupled with the inherent thermal stability of the general gas flow would be adequate proved naive during testing in our lab and at Hughes (see IV. B.): tilting the tele-

scope induced violent convection and entrainment of air into the dewar. Therefore, we introduced a 4.6 micron polyethylene membrane into the system atop a "tent" structure. This space frame of 3/4 by 3/4 by 1/16 inch aluminum architectural angle mounts on a rectangle of similar angle and 2 by 1 by 1/8 inch channel that is part of the telescope framework — the tent foundation rectangle (see Figures III-1, III-2, and III-3). Big enough to accommodate the lid as it swings open, the tent and the space between the foundation rectangle and the upper part of the dewar is enclosed by a layer of .005 inch Stratofilm polyethylene, except for a duct that runs down the downside of the dewar to a simple valve made of a length of spring-loaded cord girdling the dewar.

A plastic container of dessicant is clamped to one side of the tent and is open to the region between the thin membrane and the membrane cover to prevent icing of the membrane during ascent. This membrane cover protects the thin membrane during assembly, cooldown, and ascent. Two Globe DC motors are used to drive and clamp the square membrane cover frame in concert with the flight lid. The motors are operated from a small junction box, which also contains a pair of switches for manually bypassing the gondola electronics. Lastly, holes for hoses that hook up to the flight lid's plumbing are located in the foundation rectangle.

3. Lid and Mechanism

The Cryogenic Associates dewar, unlike most dewars, is cylindrical, with a cross-section at the neck no smaller than anywhere else. To insulate the dewar interior during fill, testing, and ascent, a lid is required; to open and reclose the lid at float, a reliable mechanism is needed. Lid weight must be minimized since any increment must be counter-

balanced; moreover, a tight seal must be realized. We discovered during preparations for Flight C-1 that a lid capable of sustaining an internal vacuum would have been desirable, so the system described below is being upgraded to bear atmospheric pressure. A photograph of the closed lid appears as Figure III-21.

The lid itself consists of .030 inch stainless steel; a 1 inch long cylinder with triangular tabs bent inward from its upper edge is spot welded to a 19 inch disk. A rigid polyurethane foam plug 9 inches thick, constructed of nine layers of 1 inch foam, interleaved sheets of aluminum foil as radiation shields, and copious amounts of Elmer's Glue, fits into the short stainless cylinder at the top. A sheet of .030 inch aluminum, painted with Nextel — a "black" paint — and carrying LED's for alignment and monitoring ice buildup plus diode thermometers, is attached to the plug's bottom. The sandwich of stainless lid top, foam plug, and aluminum bottom is held together by three lengths of nylon threaded rod. Radial tunnels through the foam channel cold helium gas rising along the circumference of the dewar toward the center, where a vertical passage vents the gas to a system of valves and diffusers soldered to the stainless lid top. A slot on one side of the plug permits the calibrator arm to extend into the beam. Finally, a hole through the lid provides access to the dewar interior for cryogen transfer lines. Overall, the lid weighs only twelve pounds.

Twin, parallel lengths of 2 by 2 by 1/8 inch aluminum angle run across the lid top to a pair of partially split clamps on the lid shaft. Another pair of split clamps on the ends of the lid shaft — a 36 inch piece of 1 inch O. D. by 1/8 inch wall stainless — hold the sections of thinwall aluminum tubing that carry the lead and aluminum counterweights.

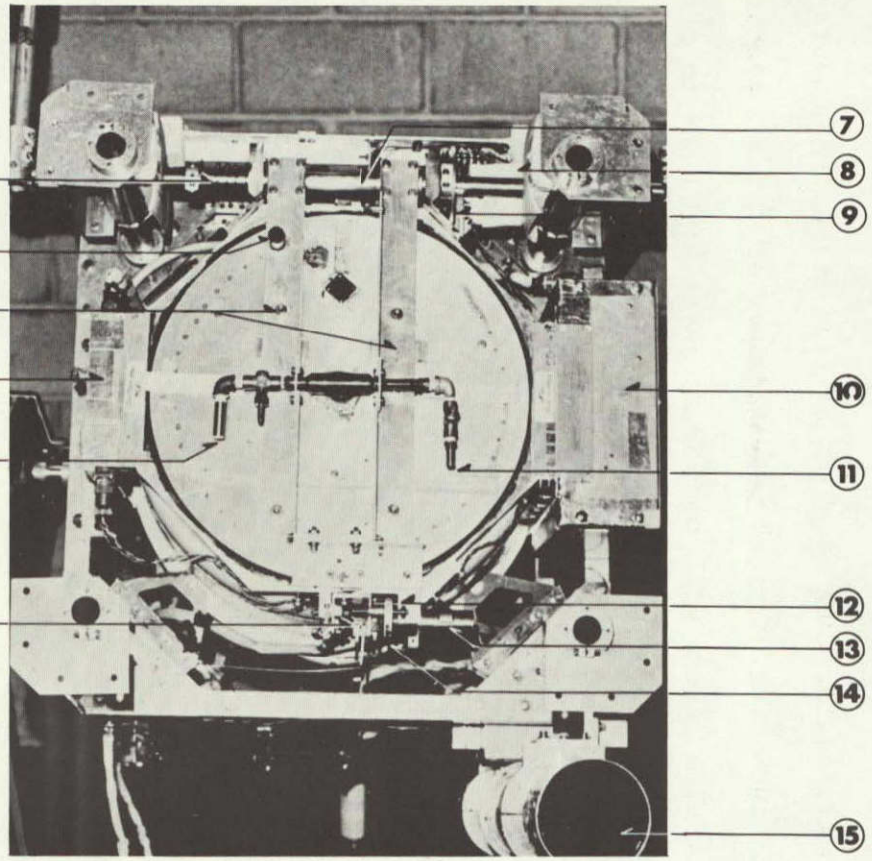

① Antibacklash Spring
② Fill Port
③ Lid Mounting Angles
④ Junction Box Top
⑤ Diffuser Port
⑥ Microswitch Array
⑦ Lid Shaft
⑧ Insulated DC Drive Motor
⑨ Drive Spur Gear
⑩ Preamp / Battery Box Top
⑪ Flush Port
⑫ Pry and Snib Ramp
⑬ DC Cam Motor
⑭ Cam Supporting Pry and Snib Shafts
⑮ Visible Star Telescope

FLIGHT LID

Figure III-21: Flight Lid.

The shaft is borne by radial bearings that are pressed into stainless pillow blocks that are, in turn, bolted to the dewar collar.

The lid mechanism is comprised of six microswitches and two Globe DC motors. When shut, the lid is snibbed by the force of a shaft-mounted bearing on a ramp which is firmly bolted to the twin mounting angles that cross the lid. Opening proceeds as follows. A pair of leads from the junction box provides full battery voltage to the DC cam motor, which drives the offset snibbing bearing off the ramp. The same rotation brings another offset shaft-mounted bearing against the flat bottom of the ramp, prying the lid off the flexible polyurethane gasket and breaking any ice or frost adhesion if necessary. Moments later, the other end of the snibbing shaft touches a microswitch, which transfers power to the DC drive motor on the other side of the dewar. This motor's ½ inch pinion engages a 4 inch gear on the lid shaft, which swings the lid open until a double-pole microswitch is encountered; one pole shuts off the drive motor and the other informs the ground station that the lid is open. To prevent backlash, a spring is wound about the shaft from a pillow block to a split clamp on the shaft.

Closing the lid occurs in a similar manner. Full battery voltage of the opposite polarity reverses the drive motor until a small cam actuates a microswitch in the pry-snib mechanism. Immediately, the cam motor moves the prying bearing out of the way; when the snibbing shaft clears yet another microswitch, the drive motor stops. In the remaining seconds, the snibbing bearing climbs the ramp, the prying bearing's shaft touches a fifth microswitch that turns off the cam motor, and a sixth microswitch reports that the lid is closed.

To ensure low temperature operation, all bearings are run dry so that

the grease will not freeze. DC motor gear heads throughout the gondola undergo ultrasonic cleaning and lubrication with instrument oil; small foam blocks insulate them and their mounts are thermally isolated from the cold collar by either stainless or Teflon. The gasket, a strip of flexible polyethylene foam painted with RTV, remains tough, if not so flexible, at low temperatures. Happily, the lid minimized boiloff, and the mechanism, tested in the Hughes chamber (see IV. B.), proved itself dependable in the flight.

4. Octagonal Collar and Junction Box

Bolted to the top of the dewar is a 1-7/16 inch thick aluminum collar with an octagonal perimeter — 20 inches between opposite edges — and an inner diameter equal to that of the dewar — 18 inches. An O-ring between the dewar and the collar, compressed by eight flat-head bolts, produces a tight seal. Another O-ring groove on the top of the collar is available for lab testing with a vacuum lid; for Flight C-1, a polyethylene foam gasket, coated and glued to the same surface with RTV, provided the seal. Four 1-1/8 inch holes, on both inboard and outboard sides of the dewar, hold hermetic connectors for the signal, bias, chopper, and thermometer cables, as well as feedthroughs for the fiberoptics and calibrator; two plugged holes serve as spares. Lastly, the collar furnishes tapped mounting holes for the lid shaft's pillow blocks, the lid mechanism's DC motors and microswitches, the preamplifier box, and the junction box. The junction box gathers leads from the thermometer cable, the lid and tent mechanisms, the ambient thermistor, and the calibrator into one 26-pin gondola cable. It also carries a test connector for preflight checkout and joins the chopper's hermetic collar connector to a 10-pin gondola cable.

5. Crush Structure

The most traumatic moments of the experiment — and the experimenter — occur at launch and landing. Once in a great while, the two moments are only seconds apart! However, extremely rough treatment upon "pulling the pin" at launch is unusual. The same cannot be said about landing. If scientist wish to reuse their instrument, they must expend substantial effort on cushioning terminal velocities of about 6 m/sec and preventing swinging and rolling of the package upon impact. These are the challenges a protective crush structure must face:

1) Shock must be absorbed in the structure.

2) Tipping over should be made less likely.

3) Extremeties must be protected.

4) Potentially large bending moments should be identified and paralleled in the structure.

5) Access to the instument should remain clear, while interference with moving components must be avoided.

6) Materials should be light and neither overly flimsy nor too strong.

7) Overall weight, balance, and moment of inertia must be considered.

We evolved a crush structure, shown best in Figure III-3, which adequately meets the above requirements. The framework consists largely of aluminum angle (6063-T52) held together by at least two bolts at each intersection. Welding was avoided to permit quick replacement of damaged members. The four, main girders parallel the edges of the electronics box, to which they are attached by four pillars. Four more members surround the main girders, defining an eight by nine foot rectangle which extends at least one foot beyond the payload in all directions. Another X-shaped pattern, oriented at 45^{o}, strengthens the structure against horizontal

shearing forces. Vertical forces impinging on the framework are guided to the electronics box by the pillars mentioned above and by sloping members from the perimeter, except on the telescope side, where they extend as far as telescope motion permits. For the elevation shaft and telescope, embodying a large, cantilevered load, support on landing is provided by a pyramidal framework, attached to the structure by a sturdy T-beam and two thinner girders. This pyramid supports a plate at its apex; an oversize hole in the plate accommodates a thick aluminum pin, firmly attached to the main telescope frame by a ¼ inch thick aluminum channel.

Cardboard blocks, made of hexagonal cells arrayed vertically, are the standard means of absorbing kinetic energy and limiting accelerations on impact. For our requirements, less than 15 g's, four blocks, each about two feet square and a foot thick, are taped to the corners of the structure where a few pieces of aluminum Dexion angle are added to retain their upper edges. Each block, however, is not solid cardboard, as 16 ft^2 would be far too strong to crush easily.[3] Rather, they are built with some empty volume in the middle, so that each presents about 1 ft^2 to the structure.

Overall, the structure provides a low center of gravity without overly exposing the instrument to impact damage from below. This goal is abetted by bolting nearly all of the extra lead for counterbalancing the telescope to the sturdiest main member, a box beam under the electronics box. The added rotational inertia remains within the limits of the stabilization system. The framework helps us to balance and handle the entire package and weighs only 150 pounds. Its successful performance in an unusual landing involving a tree encourages us to rebuild it without major changes.

[3] NSBF cardboard yields at about 11,000 lb/ft^2; 16 ft^2 require 176,000 lbs. The 1500 pound load would require about 120 g's to begin crushing the blocks.

E. Cryogenic System

1. Cryogenic Associates Dewar

The large dewar in which our telescope resides, to permit cryogenic cooling for background reduction, makes our experiment quite sensitive and unique among far-infrared survey instruments. Commonly, detectors, filters, and apertures are mounted in a small dewar at the focal plane; such a dewar, typified by the ubiquitous "Low" dewar, from Infrared Laboratories, is about 12 inches tall and 7 inches in diameter. Hoffmann's 12-inch telescope (Hoffmann, et al, 1971b), our predecessor, used just that approach. In contrast, our dewar has an outer diameter of 22 inches, stands 52 inches from base to neck flange, and weighs around 100 pounds. Manufactured by Cryogenic Associates of Indianapolis, Indiana, the dewar has proven rugged and reliable since its purchase in 1973.

A few details of technique and construction are of interest. In essence, the dewar is a vacuum cavity between nested, beaker-shaped vessels; no liquid nitrogen jacket is involved. The bottom is dished to support loading from atmospheric pressure. A cylindrical skirt attached to the outside at the base enables us to stand the dewar upright. The entire outer wall and the lower section of the inner wall consist of 1/16 inch thick 6061 alloy aluminum; the various sections are assembled with heli-arc welds. The upper section of the inner wall, subject to most of the temperature gradient, is comprised of alternating fiberglass cylinders and thicker aluminum hoops; tongue-in-groove fabrication, with the fiberglass epoxied into channels in the aluminum, seals the joints tightly. The inner and outer walls are epoxied and welded, respectively, to the neck flange, a 3/4 inch thick and 1/2 inch wide aluminum annulus with tapped holes and an O-ring groove for mounting and sealing the octagonal

collar or vacuum lid (see IV. A.)

Along the outer wall, a 1/2 inch Veeco bellows-sealed valve permits evacuation, and a burst disk enables explosive pressures to escape non-destructively, should liquid gases accumulate in the vacuum casing. Within the vacuum casing, sheets of superinsulation — aluminized Mylar — and a charcoal getter to trap air molecules minimize heat transfer into the dewar. Greater detail on the internal arrangement is a proprietary secret. Finally, the mirror mounting plate, which carries the entire telescope, fastens to the dewar by eight ring segments with tapped, helicoiled, ¼-20 holes which are welded to the inner wall, 36-1/2 inches from the top, while the dewar bolts to the outer framework via two 3/4 inch thick, 1 inch wide aluminum rings welded to the outer wall.

All Cryogenic Associates dewars are built to withstand 5 g's. By placing bumpers in the vacuum space which bear the internal load when the inner wall deflects an amount safely within its elastic limit, that constraint can be eased. Our dewar is engineered to take 11 g's in a vertical attitude; it apparently survived its first, rather rough, landing.

2. Helium Vessel

As the ultimate heat sink for the entire optical system as well as the detector block, the liquid helium vessel plays a crucial role in the experiment. The present vessel represents the third attempt at optimizing helium confinement and heat transfer. The first can, made of copper, failed due to inadequate solder and epoxy seals. Although the second can, of welded stainless, held helium well, it shared the doughnut design of its predecessor, where the detector block resided in the central hole and dispersed heat through overly long copper fingers which bolted to the

doughnut-shaped can in the following way: copper plugs with studs were soldered into the vessel bottom at four points and the copper fingers were drawn onto the plugs by nuts with large washers. Indium coils between the surfaces improved thermal contact. Unfortunately, fairly rapid changes in heat load on the block overwhelmed the conductive capacity of the fingers and plugs, causing unacceptable temperature changes. The third can, a simple vessel which immerses the block in cryogen, solves the problem.

The entire vessel is made of .030 inch stainless steel and is welded together. A cylindrical wall, 8.60 inches high and 16.875 inches in diameter, holds a flat bottom, with a turned-down edge to avoid a butt joint, and a stainless mounting ring of ¼ inch square stock at the top. On the outside wall, a channel is welded vertically to receive the transfer line; the channel encloses a ¼ inch hole in the wall that allows the cryogen to enter the can. A semicircular top panel is welded into a groove in the mounting ring on the downside and contains captive Rivnuts for attaching the overlapping, removable top panel on the upside. Twelve 6-32 flat-head bolts run through the mirror mounting plate and fiberglass standoffs to tapped holes in the mounting ring on a 16.438 inch bolt circle to mount the vessel.

The vessel's bulk capacity for LHe is about 29 liters, and when the volume of detector block, filter block, and other internal components is subtracted, this falls to 28 liters. Stainless steel wool, which inhibits sloshing and displaces another liter of cryogen, without being susceptible to corrosion, is packed into the can before final assembly. Of course, the capacity of the can drops as the dewar is tilted, since liquid can pour over the permanent upside panel. The available volume declines from about 22½ liters at 70° to 10½ liters at 20° elevation. Since about 8 liters are

lost during the time interval before launch and the further cooldown during ascent, the reduction in capacity when the telescope is tilted is important mainly in lab testing. We slow convection between the top of the vessel and the mirror mounting plate with absorbent cotton, packed right before integrating the components (see Figure III-22). A fiberglass cylinder attached to the filter block flange keeps the cotton from covering the detectors. Three cables and the fiberoptics bundle emerge from the helium can via slots, protected with grommets, at the edge of the removable top panel; all are heat sunk to the filter block cooling fin. The helium boiloff escapes mainly from the gap between the filter block cylinder and the detector block and from the space between the can's top panels and the filter block flange. In both cases, most of the gas moves upwards through the Cassegrain baffle. More on the cryogenic performance follows in III. E. 4.

3. Temperature Sensors, Cryogenic Heater, and Level Sensor

Monitoring and controlling the cryogenic performance of the dewar during cooldown, testing, and flight requires remote sensing, since the telescope, once cooled in the closed dewar, is beyond direct observation. Three different thermometers, sensitive at different temperature ranges, are deployed in the telescope. A ceramic heater resistor for increasing the boiloff rate if extra purge gas is needed, along with a deceptively simple cryogenic level sensor, sit in the helium vessel. I will discuss these devices in that order.

For high temperatures, between -70 ^{o}C and +100 ^{o}C, we use two types of Yellow Springs Instruments Precision Thermistors: a "warm" version (-26 to +100 ^{o}C, 10K at 25 ^{o}C, YSI #44006) which monitors the power mod-

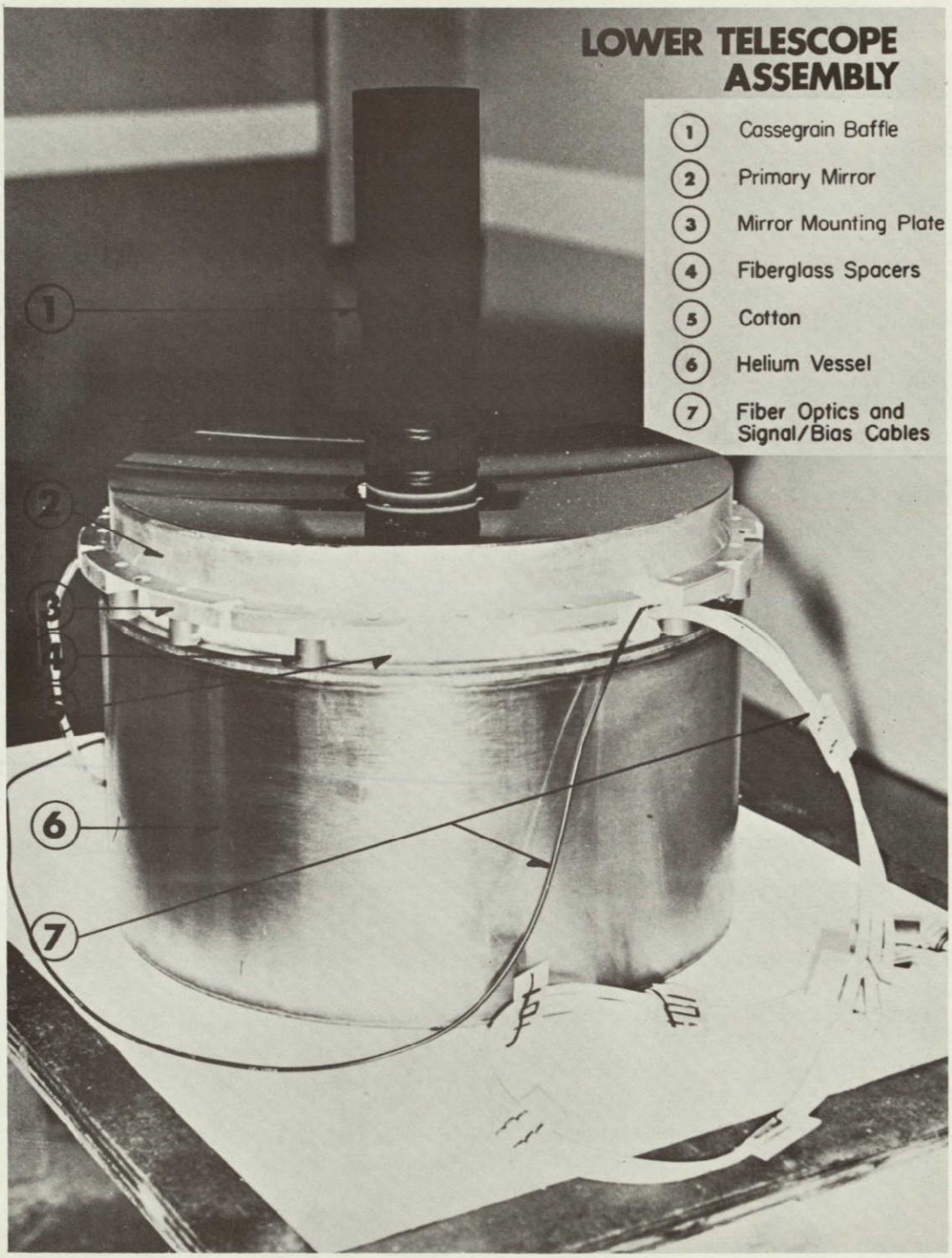

Figure III-22: Lower Telescope Assembly.

ule, batteries, and telemetry, and a "cool" version (-70 to 50 ^{o}C, 1K at 25 ^{o}C, YSI #44003) which checks on the ambient temperature and the preamplifier. The latter also serves in the thermostatic heater circuit for the pream and bias battery unit. They possess a steep negative temperature coefficient of resistance, running at around the inverse tenth power of temperature and permitting them to resolve fractions of a ^{o}C, easily meeting our requirements.

Forward biased diodes are excellent thermometers for the range from LN_2's boiling point to ambient. We station IN4002 silicon diodes, in series with 1.5M resistors and biased with 15 V, on the octagonal collar and at two adjacent locations on the calibrator arm, where the gradient is extremely high. The lid bottom also has a diode, but the reading is not telemetered. As temperatures fall, the voltage drop rises linearly from .35 V at 300 ^{o}K to .98 V at 77 ^{o}K, about 2.75 mV/^{o}K. At around 30 ^{o}K, a knee in the curve occurs; below this point, a larger slope, about 50 mv/^{o}K, characterizes the diodes.

At extremely low temperatures, from 2 to 77 ^{o}K, Allen-Bradley 1K (at 25 ^{o}C) carbon resistors take over. Resistance climbs exponentially as temperatures fall: at 77 ^{o}K, they average 1.4K, at 4.2 ^{o}K — 34K, at 2.2 ^{o}K — 340K, and when pumped to 1.8 ^{o}K — 1M. Actually, carbon resistors can be exploited as bolometers (Kimmitt, 1970, p. 71). In our system, these resistors are found in the secondary yoke and baffle, the Cassegrain baffle. and the detector block.

All of the telemetered temperature measurements are routed to the engineering module, where different circuitry for each type of thermometer, involving a voltage regulator, biasing network, and Zeltex opamp, produces a voltage swinging between 0 and 5 volts. These voltages are

pulse-code-modulated and telemetered to the ground, where a computer looks up or computes the corresponding temperature to be printed on command.

The cryogenic heater is quite simple: a 250 ohm, 10 W Workman Electronic Products ceramic resistor, driven by the main battery supply of 25V. Capable of delivering roughly 3 W directly to the cryogen, the heater can vaporize an extra 4 liters of LHe per hour. A Teledyne relay switches the heater on ground command; the heater current can be monitored as well.

Lastly, the level sensor deserves a short description in this section, even though it is strictly ground support equipment. A photograph of the device appears in Figure III-33. The unit hangs from the removable top panel in the upside of the helium can and is meaningful only when the telescope is vertical. Eight 1K Allen-Bradley carbon resistors, the components we use as cryogenic thermometers, are wired in series, spaced along the helium can's vertical axis, and oriented parallel to the can's horizontal plane. These elements suddenly gain resistance when covered by cryogen; the effect is easily measured for LN_2 and is dramatic for LHe. The resistors are spaced 0.9 inches, or 2.9 liters, apart, except in the middle, where I left a gap of 1.8 inches, double the normal spacing, to provide a marker should we lose count of resistors immersed in cryogen. Glued to each carbon resistor is a 619 ohm, 1/8 W Dale metal film resistor, whose purpose is heating the carbon resistor enough to prevent its chilling by cold gas to liquid cryogen temperatures. In other words, the resistor pair senses the difference in cooling power between liquid and gaseous cryogen. The heater resistors are connected in parallel to a voltage supply. Each resistor pair must not be heat sunk to the ladder's supporting structure, lest the entire chain cool to the liquid's temperature. A network of fine, Teflon-coated Constantan wire, of low thermal conducti-

vity, supports the chain and anchors to the superstructure, a channel made of flat pieces of fiberglass circuit board and assembled with Armstrong A-12 epoxy. Nylon lacing cord winds around the channel to protect its open side; the entire piece is tied to a .030 inch thick stainless steel inverted "L", whose base bolts to the removable top panel.

We operate the sensor with a circuit card mounted in a patch panel designed for testing circuit boards (see IV. A.). For LN_2 monitoring, 15 volts is supplied to the heater, whose parallel elements present about 78 ohms. A 100K resistor is put in series with the 8K sensor chain and 5 V bias the circuit (see Figure III-23). The voltage drop across the whole chain runs from .418 V on the verge of covering the first resistor to .522 volts when all eight are covered and the can is full, corresponding to a resistance climb from 8.62K to 11.09K, or a 3% effect per resistor. To work for LHe, 8 V power the heater circuit, and a 5M resistor in series with the sensor chain produces a 1 μA current from the same 5 V supply. The resulting voltage drop has the same numerical value in mV as the total resistance in Kohm; the chain begins at 42K and grows to 95K when totally immersed. The ∿8K jump in resistance per element has a 20% effect on the total chain resistance for the first resistor which declines to a 9% effect for the eighth, making the steps extremely clear-cut. Since the system returns faithfully to the same value moments after the heater circuit, which dissipates about ½ W, is turned on, LHe can be conserved by running the system intermittently. A separate circuit board carrying a five minute timer with an 11% duty cycle can be interposed in the heater circuit at the patch panel. A Varian strip chart recorder, run from the patch panel as well, writes a permanent cryogenic record. The chain can be checked during fill operations by simply tilting the entire

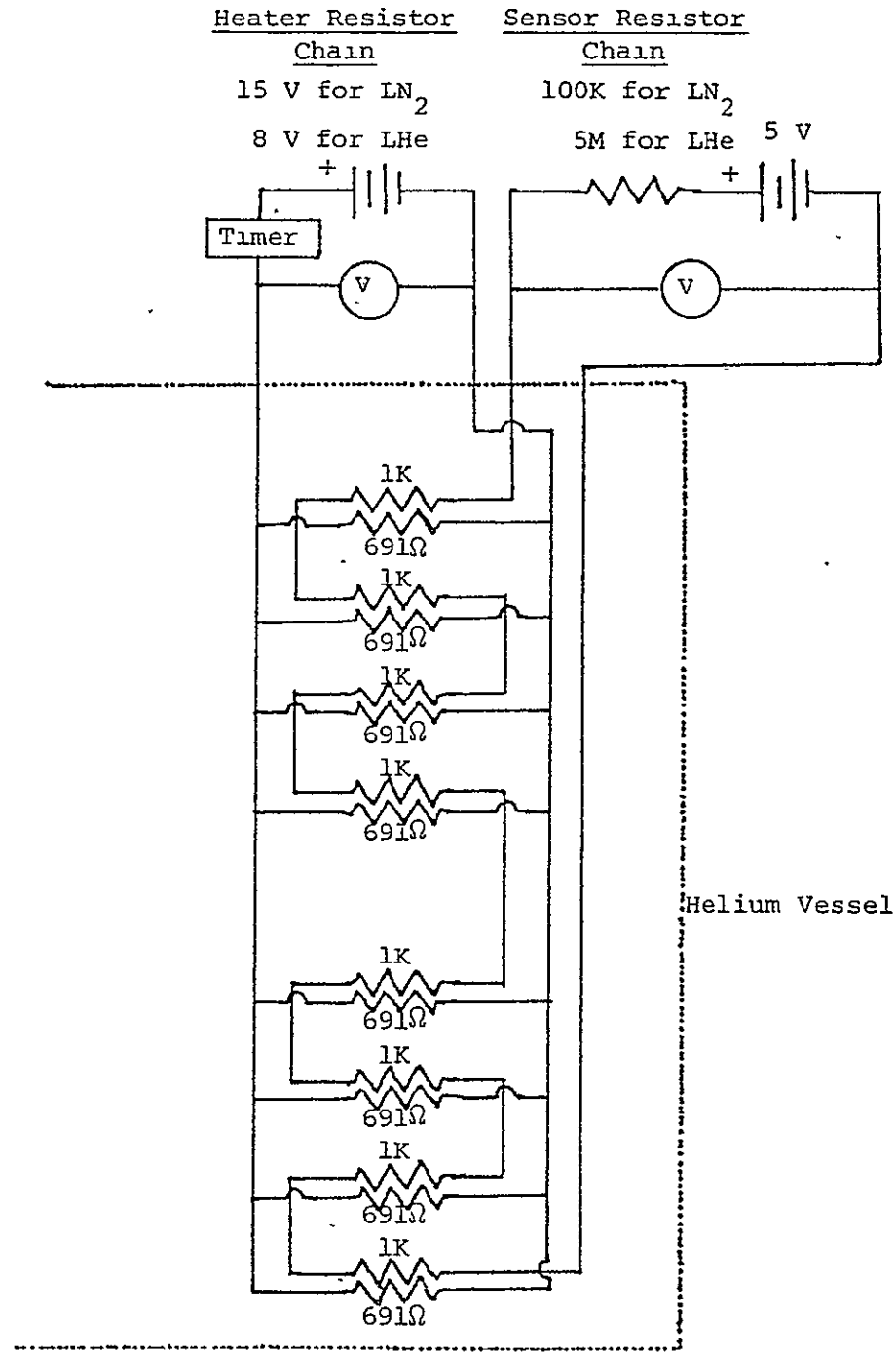

Figure III-23: Cryogenic Level Sensor.

dewar; as resistors are immersed and emersed, steps can be observed.

Summarizing, after a great deal of experimentation, we have evolved a straightforward, reliable level sensor, without which our cooldown, requiring rather large amounts of time and cryogen, would be difficult and wasteful.

4. Cryogenic Performance

Having described the dewar, helium can, and monitoring devices in the last three sections, a look at the cryogenic performance is in order. Of course, one must ask the fundamental question: what temperatures did the structure assume at float? Other considerations include temperature variations and air condensation. The short discussion here focuses on the situation in the dewar during flight; the lengthy procedure of cooldown and flight preparation is covered in Chapter IV.

The detector block, immersed in environmentally pumped helium[4] — the ambient pressure was 11.6 mb or 8.7 mm of Hg — stayed at 1.62 ^{o}K throughout the critical half hour of data taking (see V. A. and B.) when we maintained constant elevation; until tilt tests began 2½ hours later, the block temperature stayed between 1.59 and 1.65 ^{o}K. During those tilt tests, which went down to 25^{o} elevation, the block again equilibrated around 1.62 ^{o}K less than a minute after slewing. Thus, the recorded data strongly confirm that the detector cooling met expectations right up to the end of the flight, with a partial charge of cryogen. The lack of large variations is vital due to detector sensitivity to temperature changes.

[4]The atmospheric pressure given indicates an LHe temperature of 1.7 ^{o}K. A systematic error of about 0.1 ^{o}K may be present, either in the thermometer or barometer calibration. Clearly, the thermal consistency is more relevant.

Nearby, the Cassegrain baffle stayed around 5.8 ^{o}K during data taking; less tightly coupled to the helium bath, it rose to 6.1 ^{o}K at the end of the flight during tilt testing. Above this, at the secondary, wider excursions took place. The yoke and baffle began the half hour of observations at 22 ^{o}K and ended at 27 ^{o}K. Till the end of the flight, they remained between 20 and 30 ^{o}K; they then warmed up to about 40 ^{o}K when the dewar was tilted to low elevations. The lower and upper diodes on the calibrator arm reported 116 and 136 ^{o}K, respectively, during data taking; tilting caused each to heat about 10 ^{o}K for slewing to 25^{o} elevation and proportionately less for intermediate elevations. The dewar collar remained at about -80 ^{o}C, or 30 ^{o}C colder than ambient, throughout the flight.

These numbers show that the cryogenic system behaves as desired. At or below the secondary, the gradient is small, and with the cold source below, stable (see Figure III-24). In the 20 inches between the Cassegrain baffle and the secondary resistors, a 20 ^{o}K rise takes place, about one degree per inch. On the other hand, along the calibrator arm, the temperature jumps 19 ^{o}K in 7/8 inch, or about 22 ^{o}K/inch. This high gradient holds from the diodes to the collar. The gradient drops rapidly as the secondary is approached. Therefore, the goal of keeping the Cassegrain and secondary baffles, and the primary and secondary optics, cold — below 30 ^{o}K — is achieved.

Gas flow with the lid open at float is directed from the Cassegrain baffle. As long as the boiloff remains gentle, we expect the emerging, frigid gas to settle out around the baffle and push the surrounding, lighter and warmer helium upward. At low temperatures, such density variations from even tiny temperature differences are significant, as

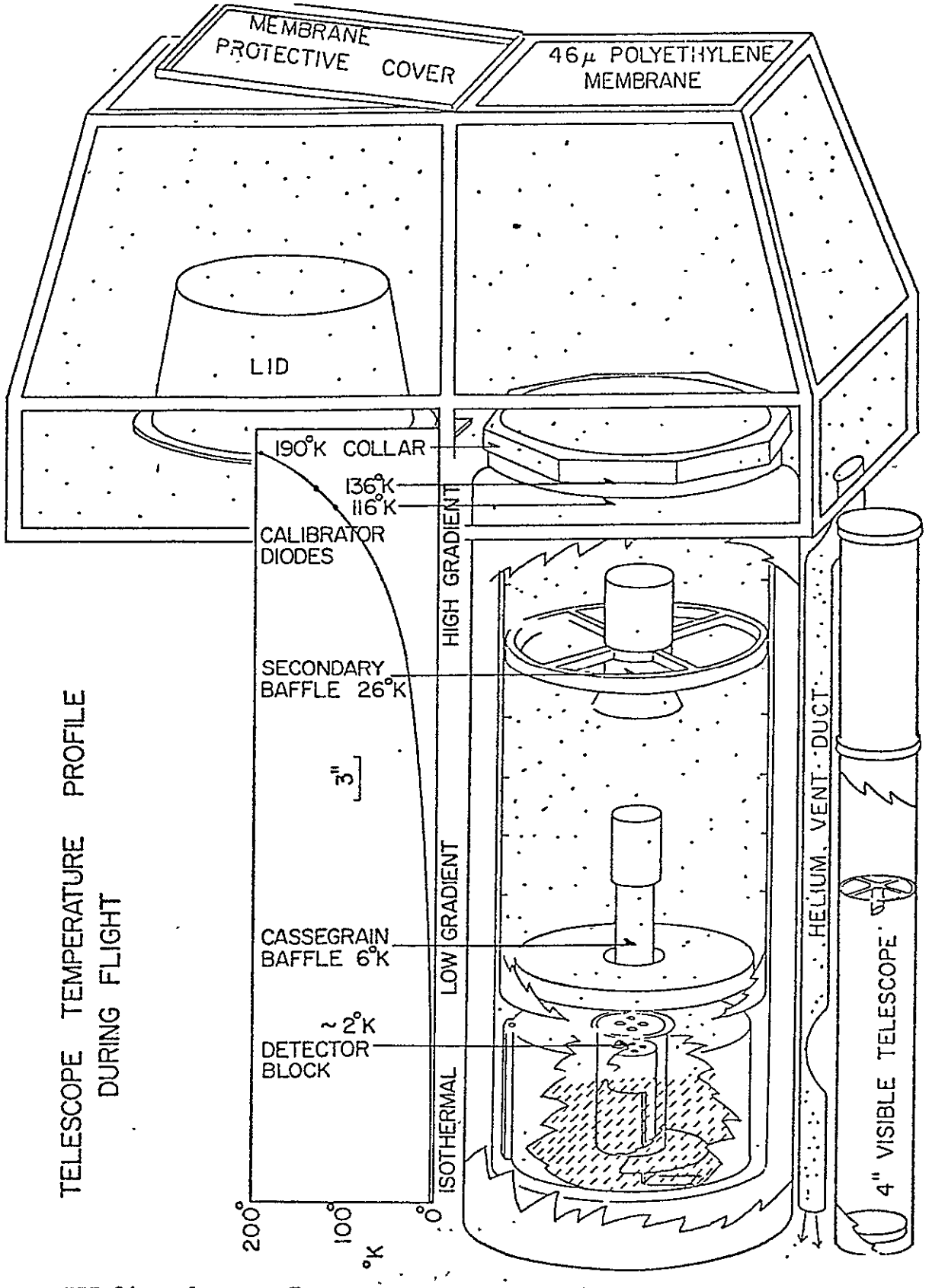

Figure III-24: Telescope Temperature Profile During Flight.

we discovered during chamber testing (see IV. B.).[5] Presumably, helium smoothly departs from the dewar at roughly constant temperatures along a given horizontal dewar plane, fills the tent, and escapes through the downside duct. With the lid closed, gas forced to the dewar circumference by the lid's plug is gathered by radial tunnels in the foam and streams out of a central tube, making the overall flow similar.

Apparently, condensation, a disappointing phenomenon on the ground, did not occur at float; in fact the calibrator's extended/retracted ice ratio (see III. F. 4.) improved marginally during the flight, indicating slight sublimation. The frost deposition on the ground will be dealt with by installing a vacuum lid, enabling us actively to pump out residual nitrogen gas from LN_2 precooling and to seal the dewar more effectively. Otherwise, the cryogenic arrangement solved the intertwined problems of detector cooling and background reduction.

F. Optical System

1. Primary and Secondary, Beam Profiles, and Membrane

To cool not only a detector block, but an entire telescope, with LHe, the entire assembly must fit into a dewar of modest size, with the detectors at the coldest point. Thus minimum physical length with reasonable magnification and axial symmetry are desirable. On the other hand, we can tolerate limited aberration as the survey employs photometry with non-imaging Fabry optics. Therefore, a compact Cassegrain system, with spherical optics, was selected. We obtained the primary and secondary mirrors

[5] Since $P \propto \rho T$, for small pressure gradients ($\Delta P \sim 0$), we can set $\Delta T/T = -\Delta\rho/\rho$. For helium boiling off, this quantity can be on the order of 1/10, driving convection at higher efficiencies that our 300 $^{\circ}K$ experience indicates. If densities are high, the process leads to overwhelming heat transfer due to high velocity convective flow, as we discovered during an early test at Hughes Aircraft in Tucson (see IV. B.)

from the Muffoletto Optical Company of Baltimore, Maryland. Both mirrors are made of 6061 aluminum coated with electroless nickel, over which a layer of silicon monoxide is deposited; they are spherical to within two waves at 5461 Angstroms, or about 1 micron.

The optical configuration appears in Figure III-25. The primary is mounted on a .438 inch thick aluminum plate by eight flat-head, ¼-20 bolts; the plate, in turn, is bolted to eight tapped ring segments which are welded to the lower inner wall of the dewar. Mounting of the secondary is discussed in the following section. Sixteen inches in diameter, the primary's specified radius of curvature — 55.12 inches — implies a focal length for center, paraxial rays of 27.56 inches and a focal ratio of 1.72. The spherical secondary, placed between the primary and its focus, increases the focal length and the magnification by retarding the convergence of the rays. Because we adjust the focus and collimation of the telescope by moving the secondary, it is instructive to compute S, the vertex-to-vertex distance between the mirrors, given the focal plane position and the mirror radii. Then, illumination of the oscillating secondary by the primary can be checked and useful quantities, such as effective focal length (E. F. L.), focal plane scale, and field of view can be calculated.

The distance T in Figure III-25 equals both the secondary's object (A) plus image (B) distances and the primary's vertex to focal plane (D) plus vertex to image (F_p) distances. Since D is specified — 2.68 inches, and F_p can be found for a given distance from the mirror vertex (spherical aberration is important!), T provides one constraint on A and B. The other is furnished by the classical thin lens formula for mirrors:

OPTICS

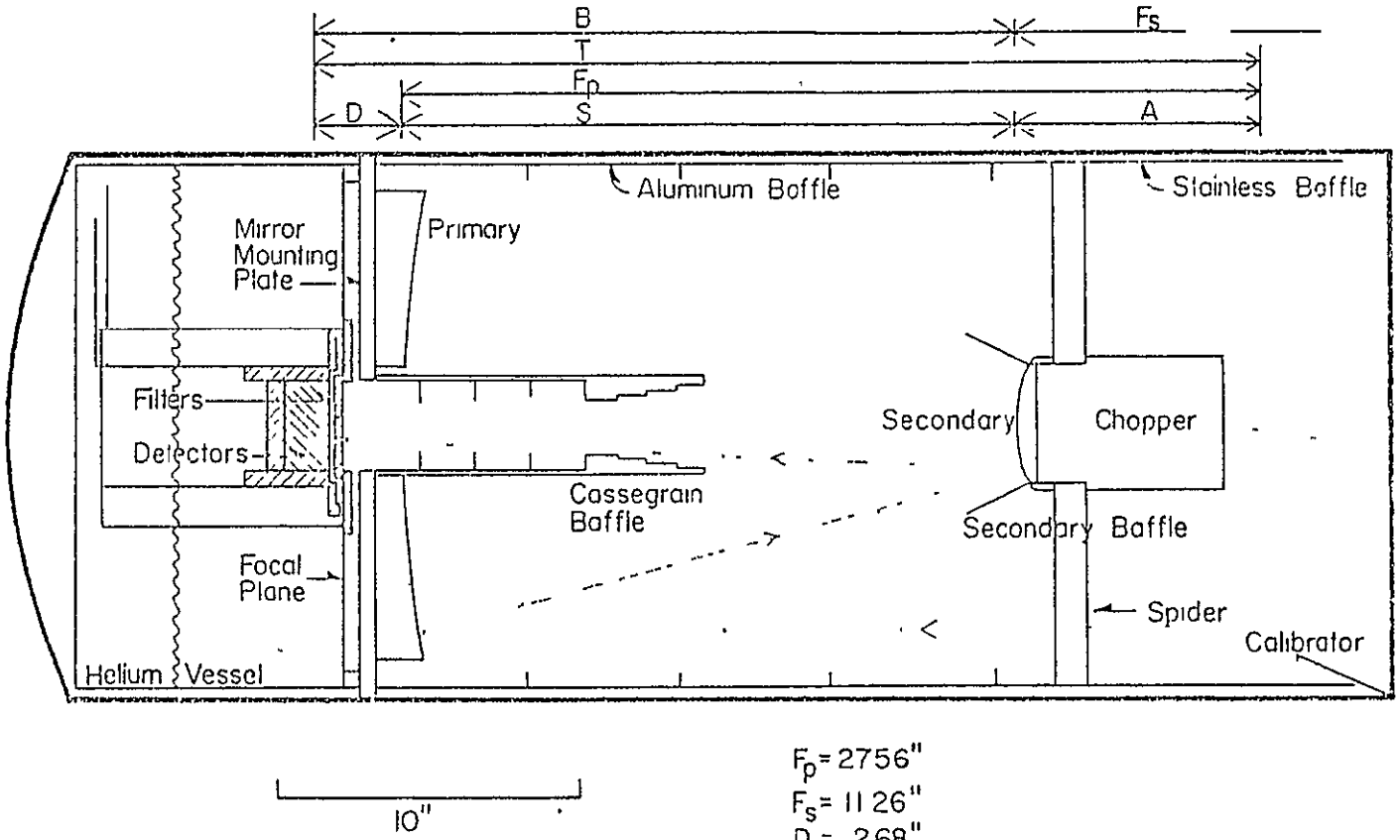

$F_p = 2756"$
$F_s = 1126"$
$D = 268"$
$T = 3024"$
$A = 753"$
$B = 2271"$
$S = 2003"$

Figure III-25: Optics. Dimensions are in inches.

$$1/A - 1/B = 1/F_S. \qquad \text{(III.1)}$$

Again, F_S depends on the radial distance from the secondary's vertex. When we solve the equations for a center ray, we find that A = 7.53 inches, B = 22.71 inches, and S = B - D = 20.03 inches. However, in a Cassegrain system, no center ray exists; as we move radially outward, the aberrations of the primary tend to shorten B, while those of the secondary have the opposite effect. The former effect dominates; to keep D constant, then, we must diminish S slightly. To divide the primary mirror into annuli of roughly equal areas, we move six inches from the vertex and compute F_p. Where that ray meets the secondary, F_S is figured. Again, we exploit the above equations, correcting for mirror curvature, and find that A = 7.45 inches, B = 22.61 inches, and S = 19.95 inches. In practice, the optimum focus for Polaris, the only convenient star for alt-azimuth mounts, lies at 20.00 ± 0.05 inches, adequate agreement for a non-imaging system.

Were chopping, diffraction, total field, and background not involved in our system, the secondary mirror could intercept edge rays from the primary with a diameter of 4.4 inches at S = 19.95 inches. Conversely, our 4 inch secondary uses only 14.71 inches of the 16 inch primary. However, chopping swings the beam about the optical axis; for an 0.3° throw on the sky, the beam must move 0.43 inch at the focal plane and 0.39 inch on the primary. Diffraction from both edges of the secondary, the defining stop of the system, at 100 microns amounts to 8.3 arcminutes, or .05 inches when projected on the primary. Moreover, the total field, represented by a 1.08 inch circle circumscribing the four detectors on the plane, is equivalent to an 0.95 inch circle on the primary. Together, 16.09 inches is needed in cross-elevation, the chopping direction, and 15.71 inches in

elevation. This is an excellent match to the 16 inch primary mirror. A very slight spillover for the 20 micron photoconductor and bolometer, aligned in cross-elevation, is suggested. In general, the undersized secondary used here efficiently reduces background and offsets from the perimeter of the field of view by just covering the primary in cross-elevation at the extremes of the chopper throw.

The ratio B/A represents the magnification factor of the secondary, which multiplies the primary's focal length to provide the effective focal length. Using our canonical figures at a radius of 6 inches on the primary, we find that $F_p \cdot (B/A)$ = 27.40 inches $\cdot$ 3.03 = 83.16 inches. Thus, the system has an effective focal ratio of 5.65 (we use 14.71 inches of the primary), while the scale at the focal plane is .689°/inch or 1.63'/mm. Our detectors' Fabry optics, with clear apertures of about 7 mm, intercept 11.4' beams. Since each detector is offset from the optical axis by about 10.2 mm on the focal plane, an offset of about 16.5' relative to the focal plane monitor in the center of the plane must be included in the data reduction; moreover, the sign of the offset is negative, as the Cassegrain optics invert the image. The total field of view, embracing all four detectors, amounts to about 45'.

Image quality matters less in a non-imaging telescope than in a true Cassegrain with a concave paraboloid primary and a convex hyperboloid secondary, where the constraint of matching the two mirrors' foci to remove aberrations determines the focal plane position. In a spherical system, a "circle of least confusion" (c. l. c.) describes the smallest circle perpendicular to the optical axis that contains the converging rays. Muffoletto specified a c. l. c. of 2.4'; our observations of Polaris essentially confirm that value with a somewhat asymmetrical 3' image. I should

note, for comparison, that the Airy disk diameter for a 16 inch mirror at 100 microns is 2.06'. Since all of these numbers are a quarter of the beam size or less, the optical performance is more than adequate. Finally, the throughput, also known as etendu, of the system is equal to the exploited area of the primary times the beam solid angle; using a 14.71 inch diameter for the primary and an 11.4' beam, the throughput becomes 7.9×10^{-3} cm^2-sr.

Beam profiles for the four detectors' Fabry optics (see Figure III-26) indicate the following full widths at half-power:

IR Channel #1 — 100μ photoconductor, 12.9°,

IR Channel #2 — 50μ photoconductor, 11.9°,

IR Channel #3 — 20μ photoconductor, 10.3°, and

IR Channel #4 — 100μ bolometer, 12.4°.

Since the secondary subtends 10.13° at the focal plane, the filter disk apertures are designed to limit the Fabry optics' fields of view to a beam slightly larger than the secondary mirror, thereby providing good throughput while minimizing the background. Aside from beam widths, the beam centers of the optics, in an ideal situation, would all point at the center of the secondary to maximize signal power on the detectors. To achieve this for the 20 micron photoconductor and bolometer, the former lens is intentionally tilted toward the optical axis twice the necessary amount, and the entire block is tilted in the opposite sense to aim both lenses properly. The efficiency of the Cornell photoconductors might be improved somewhat by a similar procedure.

Finally, the overall efficiency of the system deserves mentioning. The .00018 inch, or 4.6 micron, membrane, mounted above the telescope, transmits virtually 100% of the incident infrared radiation; the small

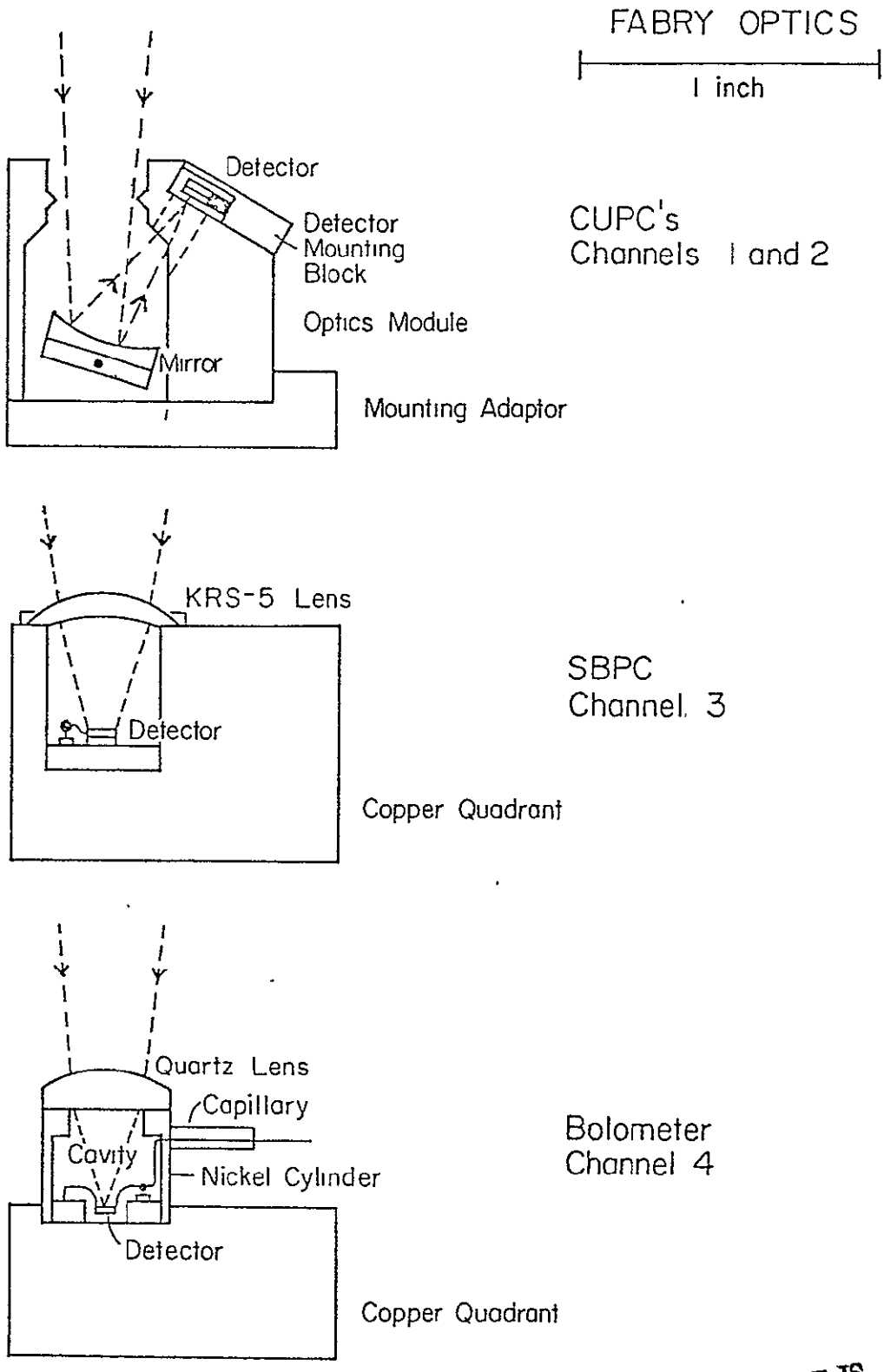

Figure III-26: Fabry Optics.

amount that is absorbed and reradiated will be dealt with in Chapter VI when detector performance is summarized. Aluminum mirrors, coated with silicon monoxide, characteristically reflect about 98% at far-infrared wavelengths. For two mirrors, a telescope efficiency of 96% results, ignoring the losses due to filters and Fabry optics. These are discussed for each detector in the description of the detection system.

2. Chopper

As mentioned in Chapter One, chopping is a fundamental technique of infrared astronomy. Wobbling the secondary modulates all channels in the most straightforward way consistent with our cryogenic, low background instrument; these requirements induced the evolution of a resonant, rather than a hard stop or linear servo chopper. The former generates sinusoidal motion about a spring's equilibrium point; the latter involves square-wave motion due to stops at extremes of the throw. Hard stop choppers are driven by solenoids, alternately energized; our resonant chopper, unique in infrared astronomy, is similarly driven. Our desire for low power dissipation, to avoid dumping excessive heat above the secondary, and minimum vibration, to limit microphonics, led to the resonant design. For a scanning system the resonant chopper is about 95% as efficient as a square-wave or hard stop chopper. Figure III-27 is a block diagram of the chopper system, Figure III-28 is a photograph of the chopper without its housing from the side, mounted on the spider's inner ring in the aluminum baffle, and Figure III-29 is a photograph of the chopper from the top. The following discussion takes up the basic mechanism, its adjustment, and the relevant electronics.

The four inch aluminum secondary mirror is ½ inch thick; ¼ inch of

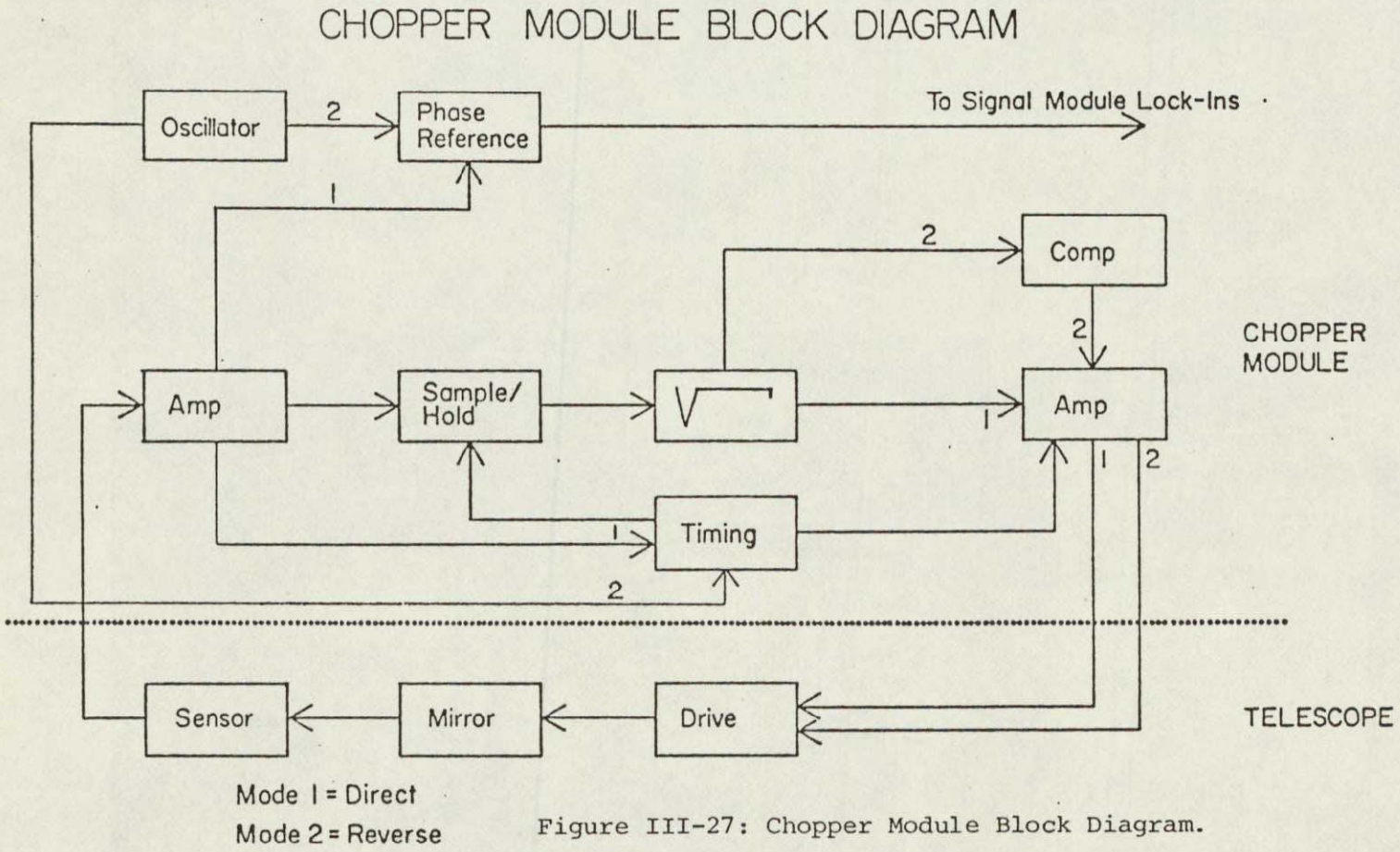

Figure III-27: Chopper Module Block Diagram.

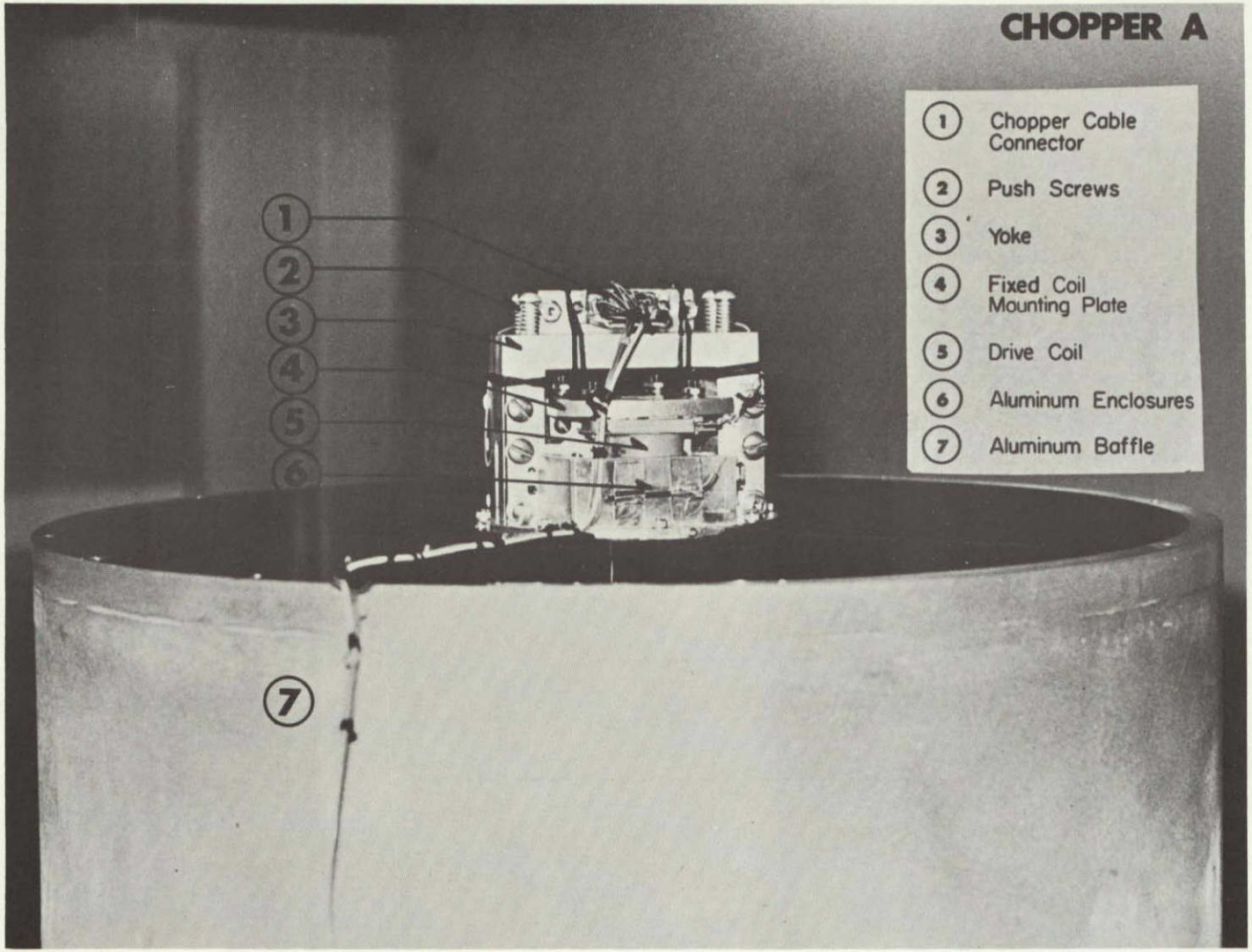

Figure III-28: Chopper A. Side View.

Figure III-29: Chopper B. Top View.

that is turned down to a 3-5/8 inch diameter, into which four radial #8 holes are evenly spaced. The mirror slips into a recess in the secondary's mounting plate and is located and retained by four 8-32 nylon screws running through the tapped recess wall. To hide the mounting plate from the detectors, its outer diameter is 3-15/16 inch. On one side of a diameter, on the back of the plate, a 3/8 by 3/8 by 2-3/8 inch bar, with three tapped 8-32 holes, machined from the same piece, protrudes; a similar bar with clear holes clamps the bottom edge of the spring between them. Pins were added to guarantee parallel mounting, as even small misalignments smear out the resonance. The top of spring is sandwiched between the mounting bracket and the upright of a T-shaped piece by six bolts and pins, while the top of the "T" clamps to a bar on another, ¼ inch plate that carries the three solenoid coils. Made of fully hardened, .014 inch, 301 stainless steel, the spring, when clamped so that the unrestrained length is .200 inch, has a frequency of 13.6 Hz; for an 18' throw, the mirror rotates 0.5^{o}.

The mounting bracket attaches to the yoke with three spring loaded bolts on either side. A pair of push screws, which butt onto a small piece of stainless shim stock to prevent their gouging the aluminum bracket, flanks a central pull screw. To focus the telescope, the pull screws are adjusted; to collimate, both pull and push screws are adjusted. Focusing is checked with an Erfle eyepiece mounted in the focal plane with the telescope in a gantry. Collimation is achieved with the telescope assembled and operated with the main telescope's focal plane monitor detecting an LED moved into the chopped beam from different positions along the octagonal collar.

The drive coils came from relays (Guardian Electronics, Series 200)

and reside on opposite sides of the upper plate 1-1/4 inch from the spring. The smaller sensing coil originated in a three-element RF choke (Miller #6306) and hangs close to the center of the upper plate. Magnetic shielding material, in a split ring, surrounds the drive coils to reduce radiation onto the sensing coil. The drive coil cores, high permeability iron rods, screw into the mirror mounting plate below, as does the sensing coil core, a permanent magnet, which induces a velocity dependent signal in the sensor. A cable carrying drive coil power, sensor signals, and temperature information runs from the chopper above one arm of the spider to the junction box.

On either side of the yoke, three-sided aluminum enclosures are fastened; these provide a means of mounting a 4.58 inch outer diameter plate that bolts to the spider's inner ring. A 3-1/2 inch tall stainless can (not pictured in Figures III-28 and III-29), which also attaches to the spider, surrounds and shields the entire chopper.

In resonant systems of reasonably high Q, frequency stability is not a serious problem. Amplitude stability, on the other hand, causes difficulties, since there are no defined stops, and variations in throw bring different parts of the mirrors and structures into the beam, causing a spurious signal, or offset. Another problem occurs when we wish to scan without chopping: the chopper responds to noise at the resonant frequency anyway. For these reasons, circuitry in the chopper module samples the mirror velocity and regulates the drive coil current. Three modes can be selected from the ground station. In Mode 1, the drive coils are active and stabilization acts to maintain a steady amplitude, in Mode 2, the drive coils are inactive unless the chopper resonates spontaneously, when they act to hold the amplitude near zero, and in Mode 0, the whole system

is simply off.

In Mode 1, the electronics sample and hold the peak of the sensor output, corresponding to maximum mirror velocity or central mirror position. This approach was taken in place of rectification and RC filtering in order to provide a quick response to changes in the chopper's amplitude. The resulting amplitude stabilization time constant is only $\sim$ 2 full chopper cycles. The sample begins a set time after zero-crossing by the sensor. A set time later, when the mirror position peaks, a correction is applied to the drive current. Since the force on the drive coil is proportional to the square of the current, we use a square-root circuit after the sample and hold to make the feedback linear. If the sampled velocity is too great, the drive coils shut off altogether. An oscil--lator starts the chopper when Mode 1 is requested. In Mode 2, the same oscillator furnishes the reference signal and times the reverse drive that holds unwanted chopper motion to a low level, set by a comparator. When switching into Mode 0 or 2, the reverse drive actively opposes mirror movement.

At room temperature, the coils present 25 ohms and operate on about 62 mA, dissipating about 100 mW; the Q equals roughly 200. In flight and cryogenic conditions, however, the coils drop to around 2 ohms; the 16 mA needed dump only ½ mW into the system, a very small load from both background anc cryogenic standpoints. Q improves somewhat at low temperatures.

3. Baffles

Tight baffling is essential in infrared telescopes, due to the IR background from the telescope structure, which is considerable, even when cooled. Moreover, for folded optics, like our Cassegrain, stray light

streaming past the secondary can flood the focal plane, unless precautions are taken. We employ three different baffles, shown in Figure III-25, to eliminate virtually all unwanted rays.

Our baffle, a large aluminum cylinder 17.50 inches in diameter, lines the inner dewar wall from its base, where it surrounds the primary and fastens to the primary's mounting plate, to its top, which is also the spider for the secondary mirror and chopper drive. Machined from a single 3/4 inch aluminum plate, the spider has 4 radial legs with beveled lower faces, to deflect scattered paraxial rays. The legs support, in turn, a four inch inner mounting ring for the secondary assembly. In addition, the aluminum baffle contains four rings, .468 inches wide, which block rays diffracted along the baffle's inner wall. Above the spider, a stainless baffle of the same diameter is bolted; it extends to the aluminum octagon at the dewar's top, where it is held in place by small bolts with Teflon spacers. The baffle assembly's entire inner surface is painted with Nextel 101-C10 Black Velvet Coating, a 3M paint composed of silicon dioxide and carbon black, to ensure absorption of stray light. The baffle also serves to guide the cryogenic transfer lines to the helium vessel with a series of holes in the inner ring baffles. In summary, the baffle tube provides a uniform, cold, black outer surface for the optical system, a rigid, precise mounting for the secondary, and a well-defined beam for the primary.

The secondary's conical baffle blocks stray light entering the system while accepting the desired beam as it converges toward the secondary from the primary. The outer diameter of the widest part of the cone is six inches, which also represents the true amount of primary obscuration. Machined from a single piece of aluminum, the cone is 1/16 inch thick, has

a half-angle of 15°, and is coated on both surfaces with Nextel. The cone's smaller end is tubular and mounts to the spider's inner mounting ring.

Finally, protruding from the hole in the primary, the Cassegrain baffle accepts the beam converging toward the focal plane from the secondary. This tubular baffle's base attaches to the mirror mounting plate and extends upward 11.00 inches. The lower 7.75 inches hold six ring baffles, whose inner diameters increase with height to accommodate the secondary's edge ray; a 3.24 inch extension, press fit over the lower tube, contains internal steps which continue to widen with height above the primary. Thus, the entire Cassegrain baffle matches the effective focal ratio, broadening from 1.75 inches near the base to 3.00 inches at the top. Again, the material is aluminum and the surfaces are painted with Nextel.

4. Calibrator

To provide a means of calibrating the detectors and monitoring the primary for air ice formation, we installed a retractable black body. The simple unit consists of a Ledex 28 ohm push solenoid (123422-032) and a 4-3/8 inch long stainless arm, pivoted above the solenoid's actuator. Operating as a lever, a solenoid motion of about .07 inch at a point .19 inch from the pivot produces a motion of 1.56 inch at the lower end of the arm, sufficient to swing into the modulated beam. Along the arm, two 1N4002 diodes (see III. E. 3.) sense temperatures 2-7/8 and 3-3/4 inches from the pivot, while an MV5020 LED at the end of the arm furnishes a source for verifying optical operation through the focal plane monitor. The arm is painted with Nextel Velvet Coating to approximate black body

emissivity. Teflon coated Constantan wire minimizes conduction from the octagon to the diodes; a 3/8 inch Pic bearing, run dry on a 1/8 inch shaft, allow rotation in cryogenic conditions. The solenoid shaft mount, housing, and electrical connector mount are bolted together and extend through one of the 1-1/8 inch openings in the octagonal collar.

The mean temperature of the arm observed by the detectors when extended is roughly equal to that of the lower diode. During Flight C-1, this diode reported a temperature of about 120 ^{o}K, producing a brightness in the 100 micron photoconductor's bandpass, assuming unit emissivity, of 3×10^{-5} W/cm^2-sr; when various efficiencies and beam size are considered, a flux density of 7×10^{-16} W/cm^2-μ, or 2.4×10^{4} Jy results. This produced a deflection of 1.1 V at the output or about 2.2×10^{4} Jy/V. However, uncertainties in lower arm temperature and emissivity, filter efficiencies, and beam size probably introduce errors of about 50% in the calibration.

When used as an ice monitor, we compared the focal plane monitor's response to the LED with the arm extended into the beam to the response with the arm retracted. A large ratio indicated little scattering, while a decrease in the direct beam coupled with an increase in the scattered beam produces a smaller ratio and warns that condensation of air as fog above or ice on the optics has taken place.

5. Visible Star Telescope

The simply state difficulty of "knowing what it's looking at" confronts anyone observing from a remote platform. For most astronomers, the solution lies in the field of visible stars, which provide easily detectable point sources of radiation whose positions and movements are well-known. The predecessor of our 16 inch telescope, the 12 inch telescope

we call Gondola B (Hoffmann, et al, 1971b), used a star camera boresighted to the telescope structure. Several disadvantages attended its use. First of all, the various mechanical provisions for picture taking — shutter activation, film transport, and time-marking, add to command channels and reliability worries. More important, synchronizing the exposures and the infrared scans introduces errors. Finally, photographic analysis, which includes magnitude and distortion estimates, increases the workload afterward. For the new instrument, a 4.25 inch Newtonian reflector was constructed and mounted on the telescope framework. The mirror's 21-1/2 inch focal length produces a focal ratio of 5.06 and a consequent scale at the focus of 6.30 '/mm. We utilize an EG&G PV-100A photovoltaic silicon photodiode with an active area filling a 2.54 mm diameter. Therefore, our beam size was 16 ', comparable to that of the main telescope. Although the photodiode responds between 0.35 and 1.05 microns, it peaks at 0.95 microns; thus, the instrument has also been named the "1-micron telescope". The detection system is discussed further in III. G. 5.

The visible star telescope was designed for easy assembly, adjustment, and testing in the field. The 48 inch tube incorporates the 25 inch telescope proper and a 23 inch extension to reduce stray light; the two segments bolt together at a small flange. Two split clamps embrace the tube and mate with slotted blocks that permit continuous adjustment in both elevation and cross-elevation with respect to the main telescope. An LED (Motorola MV5020) mounted on a removable cap can be installed over the objective end before flight. Pulsing the LED with a switched 6 V battery expedites flight line testing of the detector. Finally, the detection unit attaches easily through a tapered, beveled, anodized aluminum face plate that slips into a telescope-mounted receptacle. A bolt positions and

locks the assembly securely. Figures III-1, III-2, and III-21 show the visible star telescope's location.

We boresighted by clamping two Tensor lamps to an aluminum beam at a separation of 23-3/4 inches, equal to the distance between the optical axes of the two telescopes. The aluminum beam, in turn, was oriented parallel to the line joining the telescopes' axes, mounted on a tripod, and placed 500 feet from the gondola. By flashing each lamp at about 3 Hz and controlling its level with a Variac, we were able to acquire and center one lamp in the main telescope, and then to adjust the visible star telescope's attitude until the other lamp was detected. When the latter's signal peaked, its mounting bolts were tightened and the process was repeated to insure that each telescope was pointed at the proper lamp. This procedure aligns the telescopes to better than 2', even if the lamps are misplaced by up to 3-1/2 inches, which is unlikely.

The visible star telescope performed superbly during flight, identifying stars as precisely as the 16' beam permitted. Despite an unexpected blow during landing, which dented the tube extension and crushed the external preamplifier chassis box, the optics and electronics were quickly repaired. Clearly, this simple, light, versatile and rugged instrument will be invaluable on future flights.

G. Detection System

1. Detector Block and Filter Block

The detector block embodies the focus, both physically and figuratively, of the structural, cryogenic, and optical systems. To work properly, the block must be designed to exploit its highly specialized environment to the fullest. Structurally, it must furnish the detectors with a

firm, defined mounting and orientation. Cryogenically, it must convey the low temperature of the LHe both efficiently and continually. Optically, it must exclude unwanted radiation, in both frequency and solid angle. This section deals first with the structural and optical considerations and then discusses the cryogenic aspects. Individual detectors are described in the following sections.

Figures III-30 and III-31 are photographs of the detector block from the side and from the top, respectively; Figures III-32 and III-33 are the corresponding photographs of the filter block. Overall, the two units are assembled separately; then they are bolted together and positioned in the helium vessel. After cables are routed and the vessel is readied, we fasten the detector/filter block assembly to the mirror mounting plate, the fundamental reference surface for the optics and the most direct route to the mounting ring segments on the inner dewar wall (see Figure III-25).

Dealing with each unit in more detail, I shall begin with the detector block. The basic problem was the integration of four detectors, with different Fabry optics and mounting arrangements, into a symmetrical, compact configuration at the focal plane. To accomplish this, we divided a region 2-1/4 inches in diameter into quadrants, each one assigned to one of the four IR channels. The quadrants, all made of copper[6] for maximum thermal conductivity, have waffled bottoms and rest on a waffled disk, which we have called the "waffle", 2-1/4 inch in diameter by ½ inch thick. Apiezon N-Grease, a highly recommended (and rather expensive) heat sinking compound, is applied between the surfaces; clamping is achieved by

[6] We use both electrolytic tough pitch, a common industrial copper, and OFHC (oxygen-free high conductivity) copper in the block. Experiments at low temperature (Powell, et al, 1957) show that at 4°K, the former conducts about 300 W/m-°K. Two OFHC alloy samples are lower and higher, respectively, so we use the tough pitch value for thermal conductivity.

DETECTOR BLOCK A

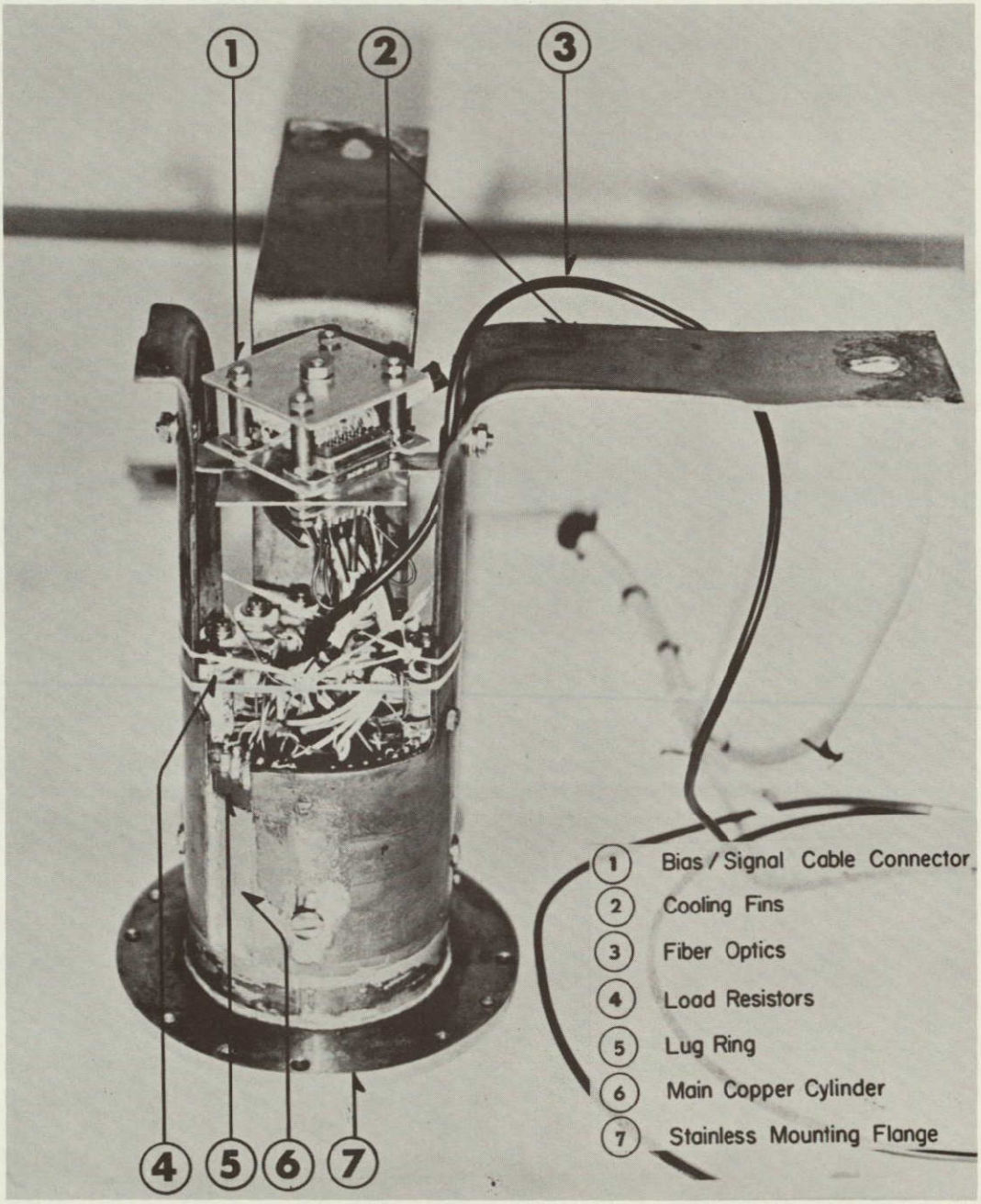

Figure III-30: Detector Block A. Side View, Inverted.

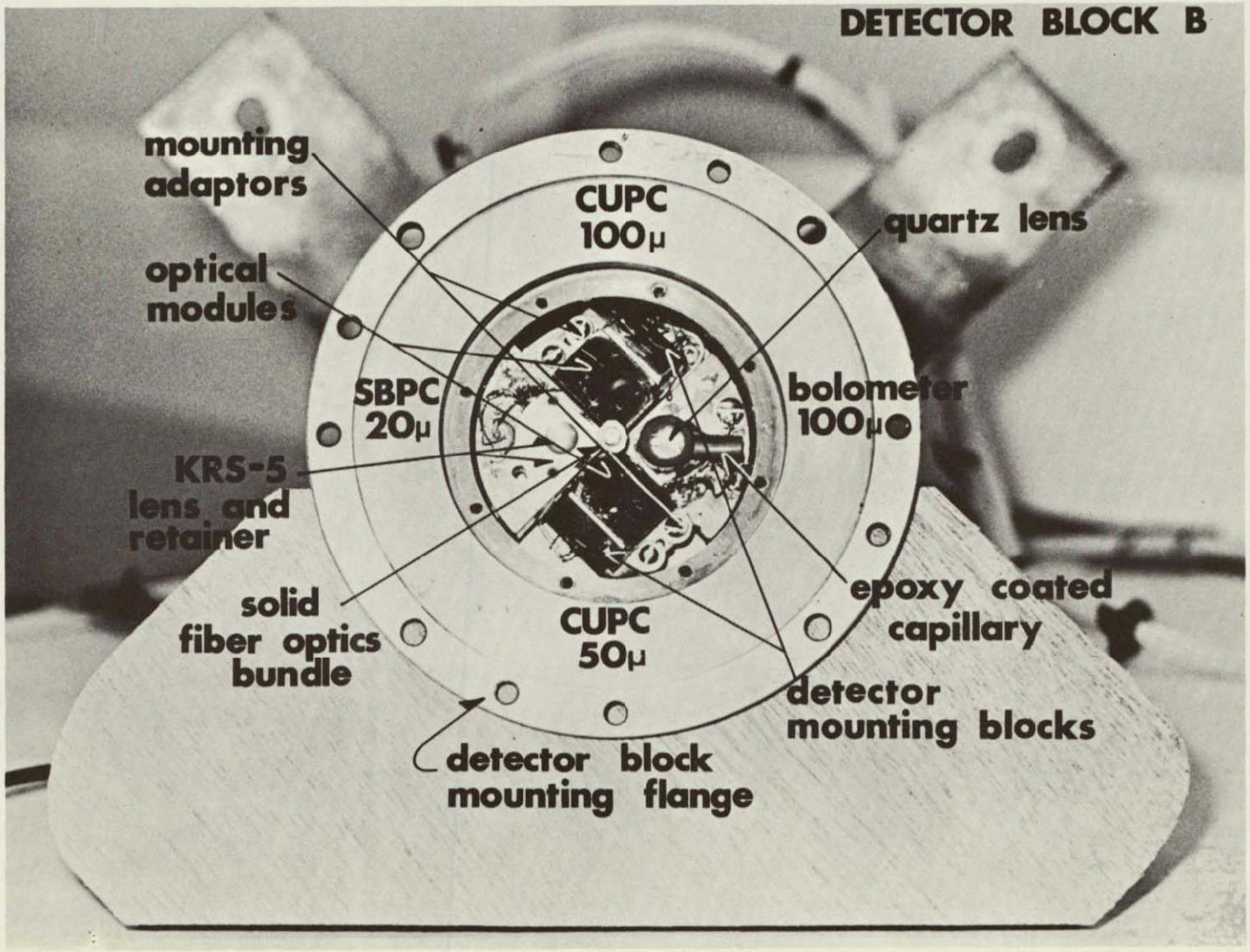

Figure III-31: Detector Block B. Top View.

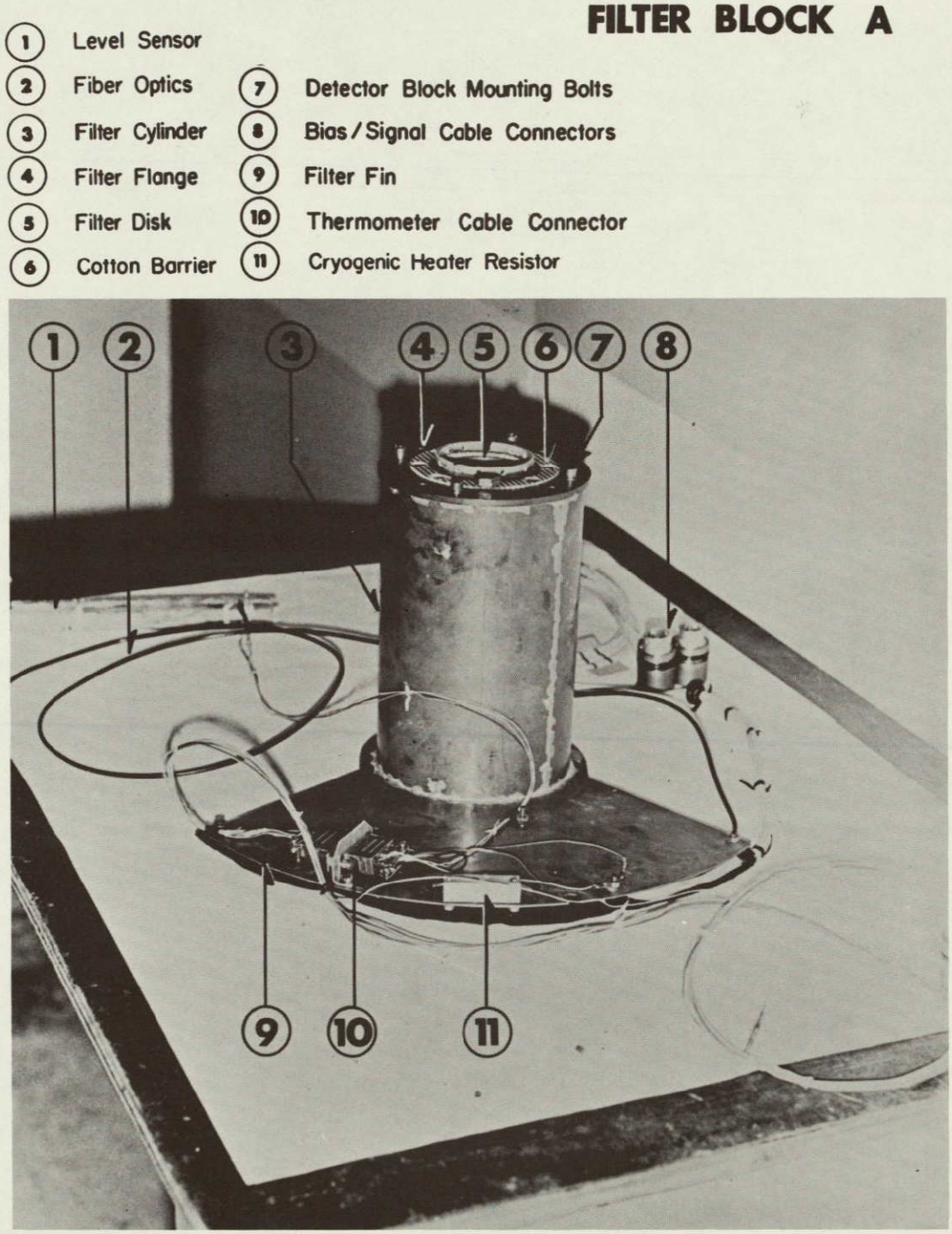

Figure III-32: Filter Block A. Downside View, Upright.

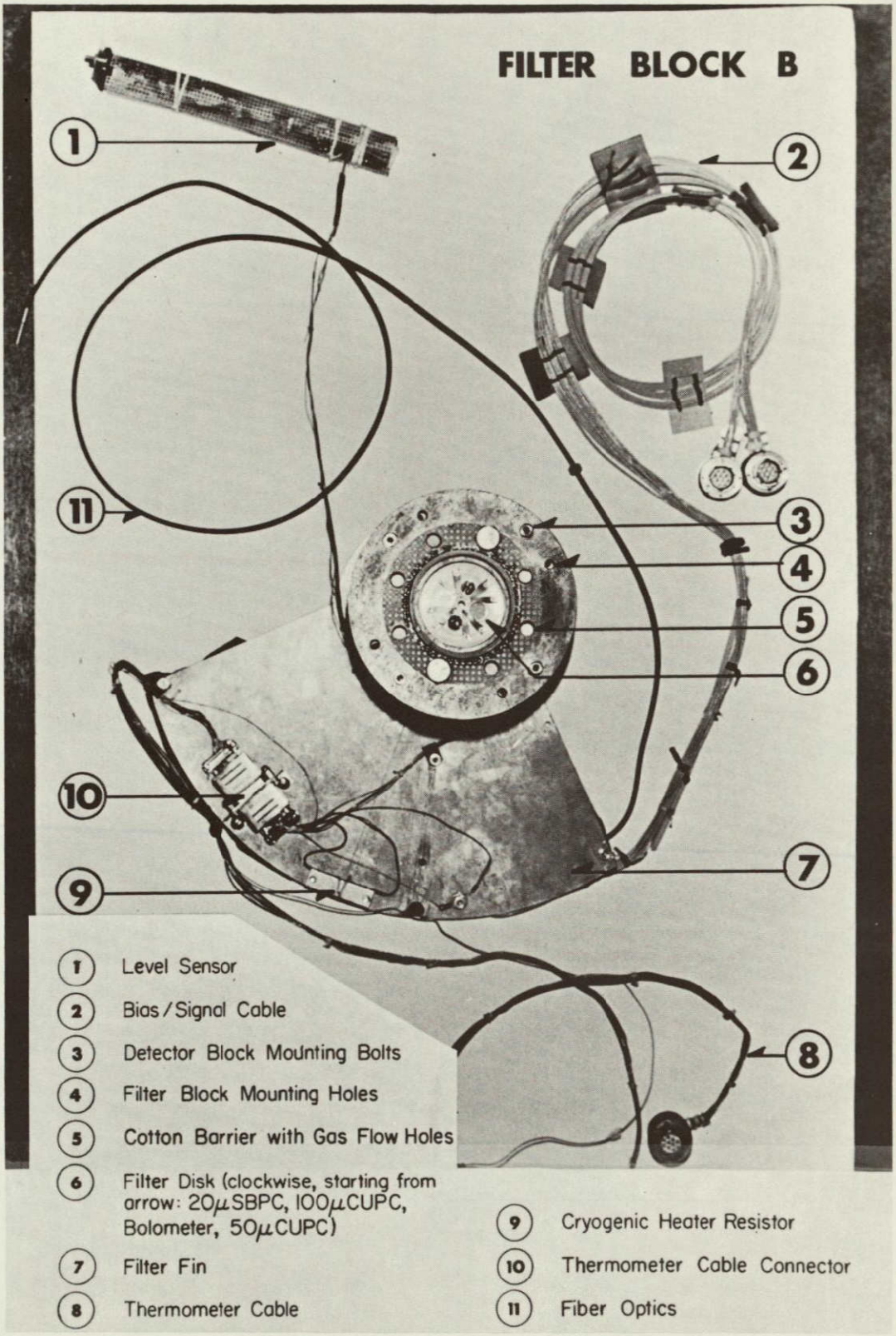

Figure III-33: Filter Block B. Top View.

pairs of bolts, extended through clear holes in the waffle into tapped holes in the quadrant bottoms. The waffle, in turn, is soldered into a copper annulus, the main copper cylinder of Figure III-30, which is 3-1/8 inches in outer diameter and 3-5/8 inches long so that the tops of the mounted quadrants are within ¼ inch of the upper end of the annulus. The same end is hard-soldered into a stainless mounting flange 4-7/8 inches in diameter which contains tapped holes on a 4-1/2 inch bolt circle for attachment to the filter block. Around the lower end of the annulus is soft-soldered a .080 inch sheet of copper, which extends downward to the bottom of the helium can; there it diverges into two copper fingers which continue across the bottom of the helium can's downside and below the filter block's cooling fin.

Wiring from the detectors begins as Teflon-coated constantan leads are threaded through small holes in the waffle and are glued with GE insulating varnish to the waffle bottom and the annulus inner wall until they reach the annulus bottom. To provide a heat sink and a junction point, a ¼ inch tall copper ring, matching the base of the annulus, is mounted here; it carries sixteen insulated standoffs and contains tapped holes to receive the 6-32 bolts that retain the load resistors. The leads from the detectors are soldered to appropriate resistor contacts or standoffs on this lug ring, enabling us to integrate the detector wiring into one compact unit. From the lug ring, low-noise Microdot coaxial cables run a few inches to a pair of Cinch (DAM-15) connectors that mate with the signal and bias cables from the preamp/bias battery box outside the dewar. The configuration leaves little room for crosstalk, prevents microphonics, and after some evolution, allows easy assembly.

The filter block consists of a filter disk, mounting flange, and a

cooling fin. A carefully machined disk, 2-5/8 inch in diameter, contains five apertures, four for the IR channels and a central hole for the focal plane monitor's solid fiber bundle. Each aperture's minimum diameter stops down incoming radiation to just include the secondary mirror's f/5.7 beam; above this stop, the apertures widen to accommodate the various filters. We have tried to standardize filter diameters to .400 inch so that different or replacement filters can be easily installed. The filters, in turn; are topped by thin aluminum retaining rings, which rise about .010 inch above the disk's top surface. There, twin phosphor bronze springs, anchored by 2-56 socket cap screws, gently clamp the retainers in place. On the other, lower disk surface are epoxied thin fiberglass baffles that extend to within ∿0.10 inch of each detector's optics, preventing radiative crosstalk. A layer of foil baffles the solid fiber bundle. Finally, the entire disk is bolted to the mounting flange by eight 4-40 bolts on a 2-3/8 inch bolt circle; Apiezon N-Grease is used to improve thermal contact.

The mounting flange, 5-3/8 inches in diameter and 3/16 inch thick, contains four bolt circles. Moving radially outward, the first is for bolts from the filter disk. The second, at 3-1/4 inches, contains four holes to allow cold helium gas to move from the concentric space between the detector and filter blocks to the central volume above the filter disk and through the Cassegrain baffle. Next, a 4-1/2 inch bolt circle contains tapped holes with stainless helicoils to receive 10-32 bolts with ∿3/8 inch fiberglass spacers from the mirror mounting plate. The spacers are machined to tilt the entire assembly 0.47° to correct the collimation of the bolometer and the SBPC Fabry optics. On the same bolt circle are clear holes for 10-32 holes to the detector block; ∿1/8 inch

spacers correct for an uneven detector block mounting flange, making the two flanges parallel. Finally, a groove 5 inches in diameter in the bottom surface positions a tube of 1/16 inch thick copper; the two parts are hard-soldered together.

The thin copper tube extends 8 inches downward where it is hard-soldered to the filter block cooling fin. Shaped to dip into the down-side of the helium can, the 1/16 inch thick fin represents the final link in the transfer of heat away from the filter disk. To the fin are attached the cryogenic heater resistor, the Cinch connector for the cryo-heater power, temperature, and level sensing cable (the "thermometer cable"), and the signal and bias cables, for heat sinking. Overall, the filter block surrounds the detector block in a cold jacket, reducing its sensitivity to radiative or advective temperature fluctuations that might cause the detectors to drift. Moreover, the uninterrupted, highly conductive paths of copper to the helium liquid, regardless of elevation angle, maintain uniform, low temperatures at both detectors and filters.

A crude but inclusive model of heat transfer among the block elements and their surroundings is shown in Figure III-34. Dominating the cooling, by design, are the copper fins, while block heating occurs mainly by advection of warmer gas. This model encouraged us to rebuild an earlier helium vessel-detector block configuration that involved longer, interrupted heat sinks to a closed, doughnut-shaped can. No major revisions seem appropriate after the system's successful performance in the laboratory and aloft.

2. Cornell University Photoconductors

At present, sensitive detection between 30 and 300 microns depends on

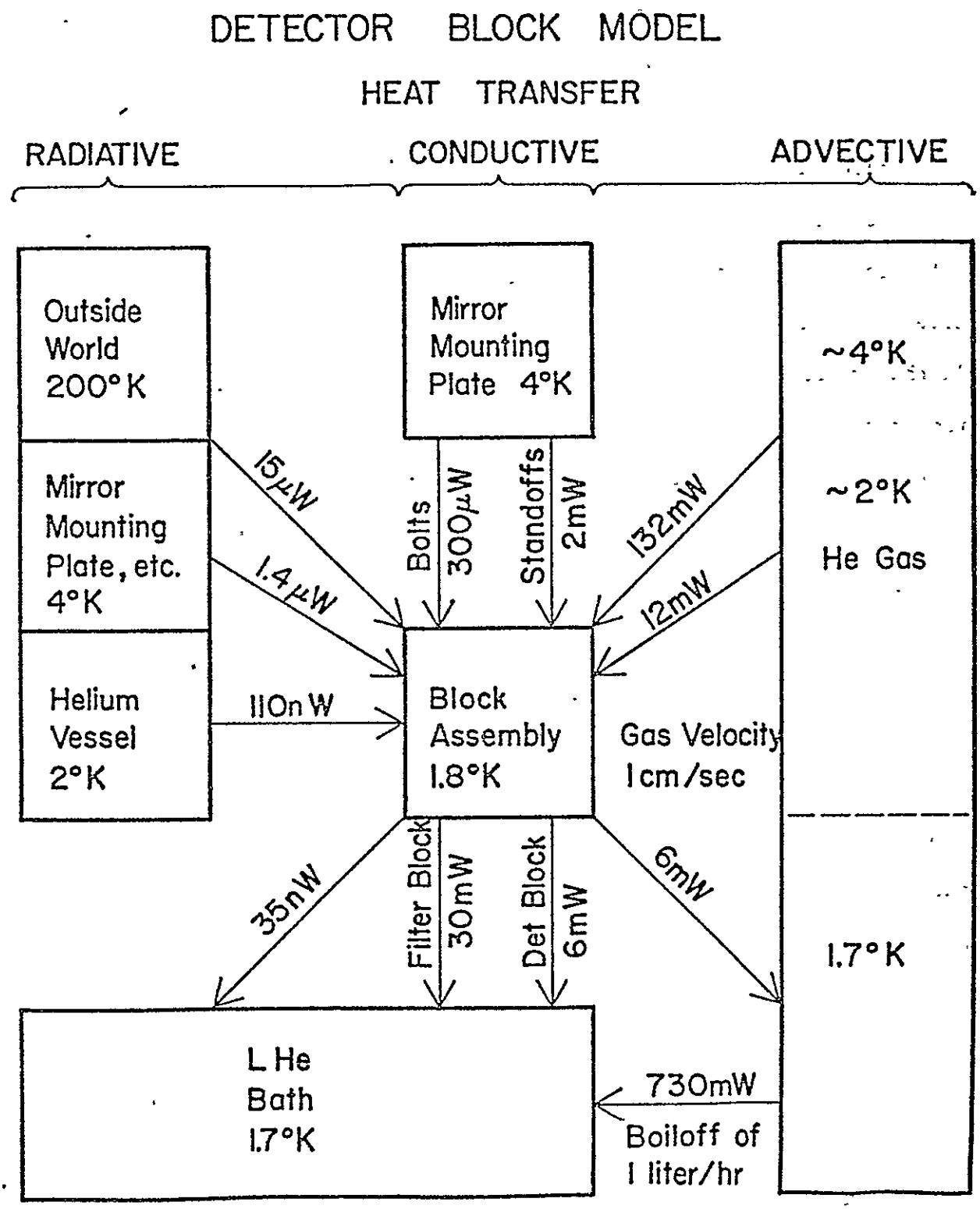

Figure III-34: Detector Block Model of Heat Transfer. Arrows show the amount and direction of heat flow between the detector/filter block assembly and its surroundings.

bolometers and extrinsic (or impurity) germanium photoconductors. The former, described in III. G. 4., are thermal detectors with a uniform spectral response; extrinsic photoconductors display explicit quantum behavior. As we see in Figure III-4, the detectivity increases gradually and decreases abruptly as wavelength increases. The slow climb demonstrates that photoconductors respond to photons, not the radiant flux, per se. Since more photons are required for the same flux as wavelength increases, the responsivity, when defined as photon events per watt, increases directly with wavelength. However, photons beyond a characteristic wavelength possess insufficient energy to vault the barrier imposed by the forbidden gap; at this point, responsivity suddenly falls. This qualitative behavior of ideal photoconductors permits us to fabricate detectors of widely varied absolute and spectral responsivities.

As outlined in a thorough review paper by Putley (1964), three types of electronic transition lead to photoconductivity. Intrinsic detectors are ideally pure semiconductors. When photons of adequate energy elevate electrons from valence to conduction bands, free electrons and holes are created, improving the conductivity. Extremely small band gaps are demanded as wavelength increases; beyond 10 microns, the best performers are extrinsic photoconductors. Such devices are doped with impurities, whose quantum structure includes levels in the forbidden gap of the host material. As the levels approach the band edges, ionization into the conduction band, producing free electrons, or from the valence band, leaving holes, requires less energy and moves the threshold to longer wavelengths. The "shallow" impurity levels of boron and gallium in germanium make these materials useful beyond 50 microns. Finally, free carrier photoconductivity relies on the poor coupling at low temperatures between elec-

trons and the semiconductor lattice. When excited by photons, the free carriers increase their mean energy above their thermal energy and usually exhibit higher conductivity. Absorption by free electrons increases as λ^2 until the light frequency equals the frequency of electron-lattice collisions; at longer wavelengths, it remains constant.[7] Thus, free electron photoconductors show a response that increases steeply and levels off as the wavelength lengthens, without a long-wavelength cutoff.

The gallium-doped germanium (Ge:Ga) detector was developed by Moore and Shenker (1965). Since gallium is a Group III impurity, its impurity level lies above and harbors electrons from the valence band, leaving holes, the mobile carrier, behind. The intervening band gap is 10.97 milli-electron volts, corresponding to a threshold wavelength of 113 microns. The spectral response curve in Figure III-4 shows that the long wavelength cutoff is less sudden than in other doped-germanium detectors, with some response out to 200 microns. This "tail" is of little direct use to IR astronomers, although it may indicate physical processes of interest to developers of very far-IR photoconductors. The curve was measured by Jeffers and Johnson (1968). Peak responsivity falls close to 100 microns, with half power points at 50 and 130 microns.

To optimize the sensitivity of a photoconductor, particular attention must be paid to the concentration of dopant and to contamination by other impurities, which may neutralize the desired carriers and reduce their lifetimes. Gallium, it turns out, is the most easily introduced dopant both in quantity and purity. The proper concentration depends on the cross-section for ionizing radiation of the impurities. As the energy gap

[7] In classical Drude theory, $\sigma = \sigma_0(1+\omega^2\tau^2)^{-1}$, where σ_0 is the conductivity at zero frequency, ω is the light frequency, and τ is the electron scattering time.

decreases, the effective radius of the impurity increases, so that the cross-section grows as the inverse square of the energy gap.[8] For Ge:Ga, we have 1.05×10^{-14} cm^2 per impurity (Moore, 1975). In principle, one might assume that increasing the impurity concentration to insure capture of all photons impinging on a detector is reasonable, but when over 10^{15} cm^{-3} dopant atoms are added, collective effects (banding) among the impurities occur. In practice, concentrations above 2×10^{14} cm^{-3} increase resistances, and consequently, noise, to a higher, less acceptable level, while the goal in detector design is reducing the fundamental statistical noise of generation and recombination of electron-hole pairs (g-r noise).[9] Thus, dopant densities of roughly 10^{14} cm^{-3} prove to be optimal.

The response of detectors, both quantum and thermal, to radiation, conforms to the general differential equation, following Putley (1964),

$$\frac{d\Delta N}{dt} = \eta \Delta J - \frac{\Delta N}{\tau}, \text{ where} \qquad \text{(III.2)}$$

ΔN is the change in either free carrier number or temperature,

ΔJ is the radiant flux increment,

η is the efficiency of the detector, in terms of change in free carrier number or temperature per unit radiant flux, and

τ is the time constant for recombination of free carrier or temperature equilibration.

For $\Delta J = \Delta J_0 =$ constant, the change approaches some limiting value ΔN_∞, as

---

[8] The Bohr atom shows this clearly: Since the Bohr radius is proportional to the principal quantum number, n, squared, and since n^2 is also the ratio of the ground state to the impurity level ionization energy, E_O/E_I, the area of the Bohr atom is proportional to $(E_O/E_I)^2$.

[9] A maximum in detector resistance as a function of impurity concentration occurs at 2×10^{15} cm^{-3} for Ge:Be. For Ge:Ga, the maximum would occur at 10^{15} cm^{-3}. See Moore, (1975).

$$\Delta N = \Delta N_{\infty}(1 - e^{-t/\tau}) \text{ , where}$$
$$\Delta N_{\infty} = \eta \Delta J_0 \tau \text{ .} \qquad \text{(III.3)}$$

Clearly, high efficiencies and long carrier lifetimes or thermal time constants produce the greatest variations. However, in IR astronomy, the background is so similar to the source in radiant flux that chopping is necessary, resulting in a varying J. If we assume a sinusoidal variation at angular frequency ω, or $\Delta J = \Delta J_0(1 + e^{i\omega t})$, the solution to (III.2) becomes

$$\Delta N = \frac{\eta \Delta J_0 \tau (1 + e^{i\omega t + \theta})}{(1 + \omega^2\tau^2)^{\frac{1}{2}}} \text{ , where}$$
$$\theta = \tan^{-1}(-\omega\tau). \qquad \text{(III.4)}$$

The factor $(1 + \omega^2\tau^2)^{-\frac{1}{2}}$ is known as the attenuation factor; for slower thermal detectors, as we shall see when we discuss bolometers, we must pay it strict attention. However, in photoconductors, τ is on the order of 10^{-7} to 10^{-8} seconds and chopping frequencies rarely exceed 10^3 Hz, so that $\omega\tau$ is much smaller than 1, and the change becomes

$$\Delta N = \eta \Delta J_0 \tau (1 + e^{i\omega t}) = \eta \tau \Delta J, \ \omega\tau << 1. \qquad \text{(III.5)}$$

Physically, the photoconductor faithfully mimics the radiation, with neither attenuation nor phase lag.

The consequent change in conductivity is

$$\Delta\sigma = \frac{e\mu\Delta N}{v} = \frac{e\mu\eta\tau\Delta J}{v} \text{ , where} \qquad \text{(III.6)}$$

v is the detector volume,

μ is the carrier mobility (velocity attained per unit electric field), and

e is the electronic charge. Then, because resistance R is inversely related to conductivity σ, we have

$$\frac{-dR}{R} = + \frac{d\sigma}{\sigma} = \frac{d\Delta J}{J} \text{ .} \qquad \text{(III.7)}$$

Substituting from (III.6), we find that

$$\frac{dR}{d\Delta J} = - \frac{R\eta\tau}{N} \approx - \frac{R}{J} . \qquad \text{(III.8)}$$

At a given bias voltage, a current will flow across the photoconductor. When the voltage-resistance behavior (generally non-ohmic, it must be tested under different background powers) is found, and when the radiant flux is determined and expressed in units of power, the responsivity can be written, following (III.8). For additional general information on photoconductors, see the review article by Putley (1964).

The Cornell photoconductors, henceforth known as CUPC's, are nominally identical Ge:Ga crystals cut from a single boole supplied by the Nucleonic Products Corporation, with a specified doping of 2×10^{14} cm^{-3}. They were fabricated, along with their optical modules and detector block mounting adaptors, by Dennis Ward in the early months of 1976. He gives the laboratory measurements listed below, when subjected to a background power of 1.1×10^{-8} W, at an effective wavelength of 85μ, in a cryostat at 4.2 ^{o}K.

Quantity	Units	Detector E	Detector F
IR Channel		100μ	50μ
NEP	W/Hz$^{\frac{1}{2}}$	8.7×10^{-14}	9.6×10^{-14}
Responsivity	mA/W	850	1070
Noise Current	A/Hz$^{\frac{1}{2}}$	7.4×10^{-14}	1.0×10^{-14}
Bias	V	0.27	0.24
Detector Resistance	Mohm	28.8	21.2

For photons at 85 microns, a background limited infrared photoconductor (BLIP) has an NEP of

$$2\sqrt{\text{Background power} \cdot \text{Energy per photon}} \qquad \text{(III.9)}$$
$$= 1.05 \times 10^{-14}\ \text{W/Hz}^{\frac{1}{2}}.$$

Consequently, the detectors are roughly nine times worse than BLIP, providing us with an idea of their quantum efficiency, η. At least part of the loss occurs through reflection and transmission effects, but the integrating cavity, a right cylindrical depression in which the photoconductor is mounted, probably improves the calculated efficiency of 0.37 considerably.[10] Moore (1975) mentions the importance of contact technology in reducing excess noise; the soldered contacts of the CUPC's are one suspected noise source.

The detectors are mounted on small copper blocks (see Figures III-26 and III-31) which attach to the optical modules, described below. One clear hole, oversized to permit adjustment, is provided for a 2-56 bolt; shim stock can be placed on the facing work surface for trimming along the optical axis. The cubic detector presents an edge to the beam to increase internal reflections and resides in a semi-cylindrical cavity, machined from the block, to further concentrate the radiation. A short copper cylinder supports the detector through an indium solder joint and is one of the two contacts. The cylinder, in turn, is isolated from the block by a layer of GE varnish and to its side is soldered a first lead. The other contact is also by indium solder joint on the opposite face, in which a thin lead is anchored. Both leads pass through small holes in the block, insulated and constrained by GE varnish; posts on the other side provide solder lugs for wiring into the detector block below.

The copper optical module (Figure III-26) uses a mirror to intercept

[10] This figure is based on the geometrical and optical properties of the detector, with multiple reflections included and an assumed cross-section per impurity atom of 10^{-14} cm^2. The detectors are 2 mm square.

the f/5.7 beam from the secondary and concentrate it on the detector, deflecting it about 34°. Made from an aluminized, plano-concave lens of 9.9 mm diameter, the mirror has a focal length of about 9.5 mm, thereby providing the detector with ∿f/1 Fabry optics. The mirror sits on an aluminum holder, attached by flexible cryogenic epoxy, which can rotate around and translate along the axis perpendicular to both incident and reflected beams for adjustment. Since mirrors are quite efficient at IR wavelengths (about 98%), losses are small; when losses due to misalignment and mismatch are included, Ward estimates $\eta = 0.80$ for the optical modules. The modules themselves are bolted and heat sunk (with Apiezon N-Grease) to mounting adaptors which mate with the waffled detector block surface. Overall, the design embodies flexibility; detector exchange involves one 2-56 bolt and two solder connections.

The filter disk, described in III. G. 1., carries the filters and baffles for the detectors. For the CUPC at 100 microns the long wavelength limit is defined by the detector itself, which loses response abruptly beyond its peak, dropping to half power at around 130 microns. The shorter wavelengths are blocked by an 0.077 inch thick BaF_2 crystal which reflects strongly between 30 and 60 microns at room temperature. When chilled to 4 °K, however, this restrahlen reflection[11] band moves to somewhat longer wavelengths and the cut-on becomes sharper. In our case, BaF_2 transmits 50% of peak transmission at 75 microns. For $\lambda < 18\mu$, a diamond scatter filter (Armstrong and Low, 1973) applied to one face of the crystal removes radiation; above it is a .004 inch black polyethylene filter for $\lambda < 3\mu$, excluding visible light. Respective transmission coefficients for BaF_2, diamond scatter, and black polyethylene, averaged over

[11] Restrahlen bands are caused by resonances between the incoming photons and a transverse lattice phonon mode.

the passband, are 0.81, 0.80, and 0.90; the combination gives a filter efficiency of 0.58. When the Fabry optics are included, this drops to 0.46.

For the 50 micron CUPC, both low and high pass filters are required, since the Ge:Ga detector remains sensitive out to about 130 microns. The low pass filter is a .080 inch thick disk of KRS-5 (42% TlBr and 58% TlI) which blocks half of its peak transmission around 70 microns. The rather high (2.3) index of refraction requires anti-reflection coating to reduce losses; our filter was optimized for 50 microns. The high pass filter is a .046 inch CaF_2 filter, whose restrahlen band ends abruptly at around 40 microns, with a half power point at 45 microns. As before, diamond scatter and polyethylene filters block wavelengths shorter than 15 microns, where the restrahlen band begins. The respective transmission coefficients for CaF_2, diamond scatter, polyethylene, and KRS-5 are 0.85, 0.90, 0.68, and 0.78, while the Fabry optics pass on 0.80. A total efficiency of 0.32 results.

The detectors are biased by 0.27 V, obtained from a 1.4 V El Eveready battery behind a voltage divider in the preamp box. Between each detector and ground is 1.9 M of load resistance (from two Daven 3.8 M ±1% wire-wound resistors in parallel), across which the modulated current generates a voltage (see Figure III-35). No cold preamplifier steps up the voltage on any of our channels; low-noise coaxial cables carry our signals directly to the externally mounted preamplifier.

3. Santa Barbara Research Center Photoconductor

Like the CUPC's, the arsenic-doped silicon (Si:As) detector purchased from the Santa Barbara Research Center operates on extrinsic photoconductivity. Silicon's band gap, however, is 1.1 eV, compared with 0.7 eV

for germanium; consequently, the impurity levels lie further from the bands. For example, the holes in Ge:As are bound by 12.7 milli-eV, in Si:As by 49 milli-eV. Si:As differs in another way from Ge:Ga in that the dopant is a Group V element and donates electrons to the valence band. The result is a detector which cuts on abruptly at 24 microns and remains useful down to around 1 micron. Specifications, provided by the manufacturer with a chopped 500 ^{o}K black body, a 295 ^{o}K background putting 4.5×10^{-9} W on the detector, and a 5 ^{o}K cryostat, follow:

Quantity	Unit	SBPC
IR Channel		20μ
NEP	$W/Hz^{\frac{1}{2}}$	4.2×10^{-14}
Responsivity	A/W	2
Noise Current	$A/Hz^{\frac{1}{2}}$	8.4×10^{-14}
Bias	V	25
Detector Resistance	Mohm	9000

An invar disk 0.375 inch in diameter and 0.126 inch thick contains a conical cavity in which the detector resides, electrically insulated by a sapphire wafer (see Figure III-26). Contacts are made to the top and bottom of the crystal; the leads are threaded through the block to stand-offs. The manufacturer furnished a 20 M resistor on the invar disk for testing purposes, but an in-line standoff enables us to use two of our Johnson noise-limited Daven wirewound resistors in series for 7.6 M of load resistance. Three E146X Eveready 8.4 V batteries in series bias the photoconductor at the recommended ∿ 24 volts. The invar disk is bolted by two 0-80 fillister head bolts to the bottom of a well in the block, one of the copper quadrants described in III. G. 1. A channel takes the leads from the well to Teflon-insulated standoffs on the outer rim of the

block. Lastly, two tapped holes on either side of the well receive 0-80 bolts that retain the Fabry lens clamp.

The Fabry optics consists of a KRS-5 concavo-convex spherical lens produced by the Unique Optical Company. With an anti-reflection coating of .004 inch polyethylene (applied by Ken Armstrong of the University of Arizona), the lens transmits 96% at 20 micron. The lens lies in the focal plane; an annular flat on the concave side affords a mounting and reference surface. With a diameter of 12.5 mm and a focal length of 11.25 mm, determined by the f/5.7 beam of the secondary and the detector area, the lens is close to f/1 and produces a blur circle of about 0.1 mm, about 5% of the detector size. With the lens clamp in place, a 7 mm clear aperture remains, somewhat reducing the lens speed.

The Si:As detector defines the long-wavelength cutoff by its own loss of responsivity. A long-wave-pass silicon multilayer interference filter. .040 inches thick, was obtained from the Optical Coatings Laboratory, to block radiation below 18.4 microns, its half power point. The pass band was specifically chosen to cover a region of low atmospheric emissivity and to avoid the CO_2 band between 13 and 18 microns. The cut-on is quite steep, rising from 10% to 90% transmission in only 0.47 micron. Filter and lens transmission factors, averaged over an 18.4 to 24 micron bandpass, are 0.46 and 0.93, respectively; consequently, T = 0.43 overall.

4. Infrared Laboratories Bolometer

A composite germanium silicon bolometer, fabricated by Infrared Laboratories, constituted our fourth infrared channel. We used it at 100 microns, in order to compare it directly with one of our Ge:Ga photo-

conductors. Unlike photoconductors, bolometers are thermal detectors; as long as wavelengths small with respect to the crystal chip are absorbed efficiently, the response is independent of wavelength. Other consequences of thermal detection include lower operating temperatures (for Low bolometers), longer time constants, and the need to consider and to optimize heat flow between the crystal and its environment. An early paper by Jones (1953) contains the general theory of bolometer performance, which was applied by Low to the germanium bolometer in his classic publication a decade later (Low, 1963). My discussion digresses with a sketch of the theory, following Jones and Low, and then returns to our particular detector's characteristics and integration into the experiment.

We must distinguish among the electrical power P, the product of voltage E and current I, that is dissipated in the detector, the steady background power Q, and the chopped signal power ΔQ. Normally, $P >> Q$ and ΔQ, so we have the following approximation:

$$G(T - T_0) = P + Q + \Delta Q \simeq P \text{ , where} \qquad \text{(III.9)}$$

G is the thermal conductance between bolometer and block, dependent on T_0 but not on T,

T is the temperature of the bolometer element, and

T_0 is the temperature of the block.

Physically, heat transport to the block balances the incident power. In order to assess the effects of a signal on the ratio of voltage change across the crystal to energy change in the crystal (in other words, the responsivity), we take the derivative of (III.9) with respect to $T - T_0 = \Delta T$. Q is constant and drops out; the change in power dissipated in the detector depends on the resistance, which depends in turn on ΔT, so, for

constant detector bias current,

$$\frac{dP}{d\Delta T} = \frac{dP}{dR} \cdot \frac{dR}{d\Delta T} = \frac{dP}{dR} R\alpha = I^2 R\alpha = \alpha P, \text{ where} \qquad \text{(III.10)}$$

$\alpha = d \log R/d\Delta T$, the temperature coefficient of resistance.

For germanium, between 1.1 and 4.2 ^{o}K, the resistance is proportional to the inverse fourth power of temperature, so $\alpha = -4/T$. In Jones's terminology, this is a negative bolometer, since $\alpha < 0$. Therefore, (III.9) becomes

$$G - \alpha P = \frac{d\Delta Q}{d\Delta T} . \qquad \text{(III.11)}$$

Physically, the difference between heat leaking from and deposited in the detector equals the signal power's change per change in temperature. The voltage behaves similarly, since

$$\frac{dE}{d\Delta T} = \frac{dE}{dR} \cdot \frac{dR}{d\Delta T} = \frac{dE}{dR} R\alpha = IR\alpha = E\alpha . \qquad \text{(III.12)}$$

The responsivity, in V/W, is the ratio

$$S = \frac{\alpha E}{G - \alpha P} . \qquad \text{(III.13)}$$

A thermal time constant, τ, can be defined as the ratio between the heat capacity, C, and the net rate of energy change, expressed by (III.11); we obtain

$$\tau = \frac{C}{G - \alpha P} . \qquad \text{(III.14)}$$

We immediately see the critical nature of G, the thermal conductivity.[12] G must be small to improve the responsivity, but large to prevent an overly sluggish time constant. The situation improves with a small C, which

[12] In a general treatment, this quantity includes radiative and convective losses, too. For Low bolometers, conduction in the leads should dominate, restricting them to a vacuum environment.

engenders a small τ without making G too large. So, bolometers are made as small as possible, but must compare in size to the beam from the Fabry optics and should be considerably bigger than the wavelength in question. A high $|\alpha|$ is also desirable, to increase responsivity. The problem becomes tractable with extremely low temperature, around 2 ^{o}K, operation. The very small heat capacity and good thermal conductivity in the crystal create a reasonable time constant. A high value of $|\alpha|$ and better control over G yield high responsivity. Finally, the moderate doping of the germanium crystal my gallium is most effective at low temperatures.

Doping is executed since pure germanium is rather transparent to far-IR photons and displays a lower $|\alpha|$. Impurities strongly couple photons to the lattice through scattering[13] and optimize the value of $|\alpha|$; as in photoconductors, gallium is introduced because it can be done with purity and precision. The boole used by Infrared Laboratories had a bulk resistivity, ρ, of 0.10 ohm-cm, which corresponds to a mobility-concentration product for the holes, $\mu_h n_h$, of 6×10^{19} (ohm-cm-coul)$^{-1}$, since

$$1/\rho = \sigma = e\mu_h n_h \ . \qquad \text{(III.15)}$$

Using 2×10^5 cm^2/V-sec for μ_h (Moore and Shenker, 1965), $n_h \simeq 3 \times 10^{14}$ cm^{-3}, as compared to 2×10^{14} cm^{-3} for the Ge:Ga photoconductor. One may ask how photoconductors and bolometers differ, ignoring the obviously dissimilar modes of operation. This is discussed in papers by Zwerdling, et al (1968 and 1972). One salient distinction is the presence of "compensating impurities", in our case, donor impurities whose electrons migrate to the acceptor, or gallium, atoms. This process is known as impurity hopping conduction, which can be triggered by IR photons. Eventually,

[13] Scattering refers to a complicated mechanism whereby energy absorbed by charge carriers is distributed rapidly among the normal modes of vibration in the crystal lattice, which itself does not absorb in the very far-IR.

such conduction creates phonons, which heat the lattice. If the donor concentration is not too high, the wave functions will not overlap much, so that thermally-activated tunneling between impurities is possible. Should the concentration exceed about 2×10^{16} cm^{-3}, however, the wave functions overlap and bands form, permitting easy conduction relatively independent of crystal temperature. Therefore, the reliance on hopping conduction to thermalize photons and the control over heat loss to exhibit temperature changes distinguish the bolometer from the photoconductor. For bolometers, higher impurity doping is permissible; the boole. used by Infrared Laboratories was only specified by a bulk resistivity, so that the actual doping, apart from the mobility-doping product, was not known.

Individual bolometers are evaluated from load curves compiled by measuring voltage changes as the bias current is varied. Two operating points on this curve are relevant: the points of optimum responsivity and of optimum signal-to-noise. The former can be found through deriving the optimum responsivity value and finding the point on the curve with that value; Low (1963) shows how this is done. The latter is located by checking signal to noise ratios at intervals along the load curve. If different from the optimum responsivity point, the actual responsivity must be derated, since a different amount of power is being dissipated in the bolometer.

As delivered, the composite[14] bolometer measures .59 by .59 by .25 mm and hangs above a copper substrate described below. When chopped at

[14] To increase absorption further, a layer of silicon, heavily doped with arsenic (10^{18} cm^{-3}) and 1.2 mm in diameter, is cemented above the crystal; hence the term "composite" bolometer. At 100 microns, more than 70% of the incident radiation is absorbed and conducted to the crystal.

20 Hz in a 1.7 ^{o}K cryostat, with a background of 10^{-8} W, it meets the following specifications at the recommended (best signal-to-noise) operating point:

Quantity	Unit	Bolometer
IR Channel		100μ Bolometer
NEP	$W/Hz^{\frac{1}{2}}$	3.2×10^{-14}
Responsivity	V/W	1.2×10^{6}
Noise Voltage	$V/Hz^{\frac{1}{2}}$	3.9×10^{-8}
Bias	μA	0.4
Detector Resistance	Mohm	1.5

Other quantities of interest are the thermal time constant, 2.5 milliseconds, which produces an attenuation factor (see Equation III.4) of 0.96 for chopping at 13 Hz, the thermal conductivity G, 0.4 $\mu W/^{o}K$, and the optimum responsivity, 2×10^{6} V/W, which indicates a derating factor of 0.64.

The bolometer is inherently fragile, both mechanically and electrically. Two gold leads suspend the bolometer above the substrate, so that a direct blow could break the prestrained wire or solder joint. Secondly, the solder joints themselves have a low melting point; they demand extreme care in soldering the ungrounded lead. Most subtly, the leads can be fused by normal bias battery voltage, so care must be taken to include sufficient load resistance, even when testing for continuity. Therefore, the bolometer sets a standard for care in handling and testing the entire instrument.

A copper substrate .276 inches in diameter and .250 inches thick carries the bolometer. The ground lead is directly soldered to the copper, while the bias lead descends through the substrate in an electrically in-

sulated standoff. Three clear holes for 0-80 bolts are provided, which mate with tapped holes in the larger copper quadrant. To control thermal conductivity, the bolometer must operate in an evacuated cavity. A simple cryopumping arrangment provides a reasonable vacuum at the bolometer's operating temperature. A nickel cylinder was hard-soldered in a .079 inch recess around the bolometer substrate to the copper quadrant, which became the cavity floor. Similarly, a copper capillary was hard-soldered through a hole in the cylinder to accommodate the bias lead which terminated in an insulated standoff near the quadrant rim. Finally, the cavity's top, a crystal quartz lens, was attached to a shoulder at the top of the cylinder with Armstrong A-12 epoxy, a rugged, cryogenic adhesive; the same epoxy sealed the bias lead in the capillary. We used nickel for the cylinder because its coefficient of thermal expansion is close to that of quartz, eliminating shear across the epoxy joint.

Electrically, the quadrant served as ground, while the bias lead's standoff was common to the load resistor and the preamp input. An Eveready E163 4.2 V battery, through two 3.8 M Daven wirewound resistors in series, was used to deliver 0.4 μA at 0.6 V to the detector (see Figure III-35). The circuit differs from the photoconductors' in that the preamp amplifies the voltage variations across the detector rather than a load resistor.

The plano-convex quartz lens, mentioned above, concentrates the beam on the bolometer 0.295 inch below its front surface. With a clear aperture of 0.280 inch, the focal ratio again is close to one; the transmission is approximately 0.66, averaged over the passband. Low temperatures change the focal length very little, since the front surface's radius of curvature and the change in the index of refraction compensate each other.

To define a passband around 100 microns for a thermal detector, both long and short wavelengths must be blocked. A BaF_2, diamond scatter, and black polyethylene combination, identical to that used by the 100 micron photoconductor, cuts on at 75 microns and averages 58% transmission. On the other side, a wire mesh interference filter built by Paul Harvey cuts on gradually between 140 and 100 microns, with a half power point at about 120 microns. The mean transmission in a 75-140 micron passpand is 0.43. Combining the lens and the filters, we obtain a transmission of 0.16.

This concludes the description of detectors in the focal plane. The photodiodes for the visible star telescope and the focal plane monitor are located in their respective preamp modules. A summary of their performance falls in VI. A., along with a helpful tabulation, Table VI-1.

5. Visible Star Telescope Detection

The detection system for the visible star telescope consists of a silicon photodiode, a preamplifier, and a container designed to minimize radio frequency interference (RFI), microphonics, and cooling by the cold stratosphere. After describing these components, I shall discuss how the output was processed.

The photodiode (EG&G PV-100A) resides in a cylindrical mount, securely locked on the focal plane, and operates photovoltaically, without bias voltage. The p-n junction develops a current proportional to incident radiation, up to saturation, from the near-UV to roughly one micron. The response curve appears in Figure III-4. The current subsequently flows into a transimpedance amplifier formed by an Analog Devices 42K opamp and a Burr-Brown 3522S opamp. The overall gain is around 400; the time constant for the amplifier is 35 milliseconds. This output signal is

telemetered to the ground and amplified by two in a signal filter that precedes the computer. A two-channel Sanborn chart recorder receives the signal, along with the bleep, forming a legible sequence of timed star sightings.

The preamp is housed in a small chassis box suspended by blocks of styrofoam in an outer chassis box. Erie RFI filters, grounded to the outer box, lie on the signal, ground, and ± 15 V leads between the preamp and the connector to the outside world. The photodiode sends its current to the preamp via a short length of Microdot low-noise coaxial cable; this precaution, when coupled with care in wiring and mounting the preamp, obviates serious microphonics. The stratospheric cold is countered by heating and insulation. Two parallel 1.8 K resistors, driven by the ± 15 volt supply, are heat sunk to the Analog Devices opamp, whose operating range stops at -25 ^{o}C. The Burr-Brown 3522S operates to -55 ^{o}C, so it requires no assistance. Then, the low thermal conductivity Dow styrofoam impedes heat flow from the preamp and a lining of aluminum tape discourages radiative losses. A compact and simple package results.

The system noise, as observed on the strip chart record, is close to .04 V peak-to-peak (p-p) or .014 V root-mean-square (rms). Saturation occurs for a 5 V signal, due to the NCAR telemetry discriminators. Assuming we can pick out a signal equal to the rms noise, our dynamic range is about 360, or 6.4 magnitudes. Where shall we deploy this range? The number of stars needed to locate our IR scans fixes the desired sensitivity. The paucity of extremely bright objects argues for letting them saturate the system. With these principles in mind, we address the question in more detail.

A digression I must make concerns the spectral response of the photo-

diode, which includes near-IR as well as visible wavelengths. This means that simply relying on visual magnitudes for deciding how much sensitivity will be needed will not work. Compounding the problem is the uncertainty in the spectral response at stratospheric temperatures. Figure III-4 shows that the long wavelength cutoff becomes sharper and moves to slightly shorter wavelengths, while the responsivity peak decreases a bit and levels off at 0.9 micron. Data blueward of 0.8 micron is simply not available from the manufacturer. However, the deviation of response with temperature is negative below 0.6 micron, implying a UV enhancement with colder conditions. The properties of silicon, increasing of and decreasing penetration by shorter wavelength photons, may be temperature dependent. I dwell on this point because B stars, whose Planck curves peak at or less than 0.27 micron, are detected by the system as if the photodiode's near-UV responsivity remains roughly as high as the visible.

For our magnitude corrections, I have assumed the detector was at ambient temperature, 221 ^{o}K, and assigned the three bands for which near-IR colors exist (Johnson, 1966) efficiency factors relative to the room temperature responsivity peak of 0.47 A/W at 0.95 micron. The V band at 0.55 micron is 55% of peak, the R band at 0.70 micron is 71% of peak, and the I band at 0.90 micron is 94% of peak. To construct a correction to the visual magnitude, m_V, I convert the colors for the appropriate spectral type and luminosity classification to intensities and use the following formula:

$$I_C = \frac{\{.55 + I_R/I_V\ (.71) + I_I/I_V\ (.94)\}\ (1-f)}{(.55)} \quad , \qquad \text{(III.16)}$$

where

I_R/I_V is the converted V - R color,

I_I/I_V is the converted V - I color, and

f is the fraction of radiation longward of 1.05 micron, as determined from the appropriate effective temperature.

I_C is then expressed in magnitudes to give m_C, a correction that can be applied to a star of known spectral type whose detection by the visible star telescope is suspected. The method, as applied to the eight brightest observed non-variable stars on Flight C-1, obtains the results in Table III-4, below:

TABLE III-4: BRIGHTEST STARS OBSERVED ON FLIGHT C-1

NAME	SPECTRAL TYPE	OBSERVED VOLTAGE V	OBSERVED MAGNITUDE m	PREDICTED MAGNITUDE m_C	m_V
α Aql	A7 IV	5.3	0.0*	-0.7	0.8
γ Aql	K3 II	2.5	0.9	1.1	3.1
β Del	F5 IV	.72	2.2	2.0	3.7
ι Her	B3 V	.56	2.4	2.4	3.8
ε Del	B6 III	.42	2.8	2.6	4.0
μ Aql	K3 III	.41	2.9	2.8	4.8
55 Cyg	B3 Ia	.24	3.4	3.5	4.9
57 Cyg	B5 V	.24	3.4	3.4	4.8

*Saturated.

As can be clearly seen, the brightest, α Aql, saturated; the other seven were used to obtain a standard deviation of 0.15 magnitudes for the procedure.

Errors in the procedure arise from many sources. First, the UV response of the detector is not well-known. Second, the beam profile of the visible star telescope has not been determined, so that stars grazing the beam may give lower signals. Third, for fainter stars, spectral information is often crude, and is usually given without luminosity classifica-

tion. Both, but especially the latter, affect the magnitude correction. Finally, estimating the signal level from the strip chart record or the digital output introduces error. Despite these problems, a few faint but extremely red variables were correctly identified, including T Aql, whose m_V runs between 10.6 and 11.0.

Returning to the original question of setting the gain, we consider the number of stars accessible to the .06 square degree beam of the telescope. In the normal operating mode, scans of several degrees are made in cross-elevation while pointing east or west, so apparent stellar motion in hour angle builds up sky coverage. If, for example, we swing through 5 degrees of arc with our roughly ¼ degree beam, we cover about one square degree. Consequently, to locate our scan, the visible star telescope should report a few stars per square degree. The average star density for $b < |10^\circ|$ has been taken as that at $b = |5^\circ|$; there are 0.6, 1.7, and 4.9 stars/square degree brighter than m_V = 7.0, 8.0, and 9.0, respectively (Allen, 1973). As explained above, the detector responds more to late- than early-type stars. By adopting the special distribution of spectral types near the galactic plane[15], I can adjust the star densities to reflect the undetected early-type stars. If we acquire, as we believe we did on Flight C-1, stars to the following depths in m_V: B0 — 7.7, A0 — 7.8, F0 — 8.0, G0 — 8.1, K0 — 8.2, K5 — 8.5, M0 — 8.7, and M5 — 9.4, we should see 3.6 stars/square degree. Away from the plane, the number is somewhat lower; for the mean density over the entire sky, 2.3 stars/square degree are within reach. At any rate, the requirement of locating at least one star per scan is met comfortably. Moreover, with

[15] See the Handbook of Military IR Technology (Wolfe, 1965) for a useful set of tables on star distribution, both spatial and spectral.

6.4 magnitudes of range, any AO star, for example, of $m_V < 1.4$ saturates the system. As stars that bright are few and easily identified, this is no problem. In short, the gain of 400 is about right for our purposes.

By checking the strip chart record, I find 18 stars in a typical scan through Cygnus during a 55 second period within 10 degrees of the plane. Since the gondola rotated at about 1° az/second, this amounted to about 55° az or 22° at 66.5° el, which meant, in turn, a coverage of about 5.5 square degrees. Thus, 3.3 stars/square degree appeared, in good agreement with the predicted number. On the flight, when the azimuth stabilization failed, the visible star telescope provided adequate star identifications in the unintended "continuous drift" mode, even when far from the galactic plane. The noise level did not exceed twice that predicted; a slow, well-behaved baseline drift did not degrade the signals. In V. B., we shall see how the data reduction was anchored by the above procedure.

6. Fiberoptics and Low-Noise Cables

Responsible for bringing the signals out of the heart of the detector block of the main telescope to the preamp are the fiberoptics and the low-noise cables, for the focal plane monitor and the IR channels, respectively. Descriptions follow, in that order.

Centered in the detector block is a 1-3/4 inch length of .135 inch diameter clad rod or rigid fiber bundle. The rod extends through a .156 inch aperture in the filter disk at one end and faces the end tip of a flexible light guide at the other, across a 1/16 inch gap. A wrapping of aluminum foil baffles the clad rod, preventing the scatter of visible light into the IR detectors below the filter disk. The flexible light

guide (American Optical LGM-2-72) itself has stainless steel end tips and is sheathed in PVC. The detector end tip resides in a stainless steel receptacle, retained by a set screw; after a six foot journey across the helium vessel, up the side of the dewar, and through a vacuum coupling in the collar, the preamp end tip nestles in another receptacle in the preamplifier, retained by a small slotted plate.

At visible wavelengths, each pair of ends accounts for a 30% loss, due to the effective packing fraction of bundles and to Fresnel reflection. The short clad rod has negligible attenuation, but the six foot flexible bundle absorbs about 40% at .55 micron. Therefore, had the bundle been perfect, 30% of the light incident at the focal plane would arrive at the preamp; actually, due to handling and cryogenic cycling, perhaps 1/3 of the fibers are broken, so the transmission is more like 20%. Despite such losses, the visible channel played a critical role as an ice detector and during the boresighting of the visible star telescope.

Bringing small signal voltages from the detector block,to the preamp frustrated numerous efforts before the proper means was found. The constraints are many:

1) Thermal conductivity must not be excessive, since the cables are a direct heat shunt.

2) The long path among different structures and along the inner dewar wall is vulnerable to microphonics which must be eliminated.

3) Coax is required since crosstalk must be avoided.

4) Reliability through handling, assembly, and cryogenic cycling is needed.

We finally settled on Microdot "Mini-Noise" coaxial cable (250-3808),

which admirably meets constraints 2, 3, and 4. The Teflon dielectric is treated to reduce, by two orders of magnitude, the noise caused by shock and vibration; Teflon is strong and behaves well at low temperatures.

After a careful treatment of the heat transfer problem, I discovered that the cable would tend to equilibrate with the dewar wall, and that at altitude, most of the conducted heat (about ½ W) would be dumped high in the dewar, where the gradient is steepest. Thus, direct losses of cryogen would be minimal. To guarantee that the cables would be cold on arrival at the block, we tied them firmly to the copper cooling fin of the filter block at the lowest part of the helium can's downside and taped them securely to the dewar wall. In comparison with previous attempts with delicate Ultraminiature Coax from Lakeshore Cryotronics, no marked difference in hold time was observed, while immunity to microphonics and reliability increased enormously.

In order to conduct vacuum tests in the dewar, the connectors in the collar, for the signal, bias, chopper, and temperature cables, had to be hermetic. Four ten-pin bulkhead feedthroughs (Deutsch DTK1H-12-10), with pins encased in glass, were soldered into brass cylinders, which slide into the holes in the collar and seal with a circumferential O-ring. At the detector block end, 15-pin connectors (Cinch DAM-15) are used. We provided adequate strain relief for all connectors, especially where unavoidable sharp bends were made. Both signal and bias cables use the Microdot coax.

7. Preamplifier and Bias Battery Unit

At the termini of the fiber optics, signa and bias cables outside of the octagonal dewar collar, a moderately sized, modified chassis box

houses the preamplifier, the battery box, and several other devices. Well insulated, the enclosure is heated to furnish an agreeable environment for batteries and components amidst the stratospheric cold. The arrangement conveniently gathers signals and housekeeping data into one 19-pin connector for a cable that runs through the elevation shaft to the signal module. I will discuss the preamp first, the battery box second, and then conclude with other details.

The general requirements for the preamp are concisely presented in Wolfe (1965),

> "The primary objective in preamplifier design is to produce an amplifier that will increase the detector signal to a level capable of being transmitted over a cable, possibly exceeding 10 feet in length, without degrading the signal-to-noise ratio available at the detector. The primary requirements of such an amplifier are low noise, high gain, low output impedance, large dynamic range, good linearity, and relative freedom from microphonics. The amplifier must be compact, since it is usually mounted near the detector, and must be carefully shielded to prevent the introduction of unwanted signals by stray fields."

To begin, the preamplifier was designed by William Hoffmann and fabricated by Jim Mueller, both of Steward Observatory. Spectrum Research of Tucson reproduced the circuit on 1/8 inch thick fiberglass circuit board, which mounts in a tightly-fitted, edge-bolted box of 1/8 inch aluminum plates, measuring only 7-1/2 by 4 by 7/8 inches. Inside, five pairs of aluminum partitions support the printed circuit board and divide it into six areas. Five of these preamplify the signal channels, four infrared and the focal plane monitor; the sixth provides a temperature compensated DC reference level for the individual preamplifiers. Thus, the rigid circuit board and snug mounting eliminate microphonics, while the internal partitions and closely fitted enclosure exclude crosstalk and interference. Moreover, its compactness allows us to shield, insulate, and mount it in the larger chassis box in an adequate, straight-

forward manner. Figure III-35 shows their relationship when assembled.

The four infrared channels (see Figure III-36) are identical except for gain and time constant. Siliconix ultra-low noise FET's (2N4867A) receive the signals and achieve an open loop voltage gain of about 22. Chosen for extremely small amounts of flicker (1/f) noise, these components contribute only 10 $nV/Hz^{\frac{1}{2}}$ at 10 Hz, well below the detector noise. The next stage provides current gain with a second Siliconix FET (2N4867, not specially selected for low noise, they have about twice as noisy as the other FET); its source output is connected to the inverting input of the Fairchild A776 opamp. Finally, the opamp's output feeds back to the source of the input FET, completing the loop.[16] R_F, a metal film resistor, builds up feedback voltage; an RC filter, $R_S C_S$, leads to detector ground for AC signals. GE tantalum capacitors and a 4.99 K resistor are involved; they define the AC gain and the low frequency 3 db point. For DC operation, the capacitors are open to the path to ground, the V_B = -8.4 V supply, includes a 499 K resistor. For Flight C-1, the preamp assumed the following configuration:

IR CHANNEL #	R_F Mohm	C_S μF	AC GAIN	DC GAIN	3 db POINT Hz
1	2.49	10	500	6	3.2
2	2.49	2000	500	6	0.016
3	.500	10	100	2	3.2
4	2.49	10	500	6	3.2

Attenuation at the chopping frequency of 13 Hz amounts to only 3%, with a phase shift of 14^{o} for all but channel #2, where these quantities are essentially zero, due to the long time constant. The entire amplifier,

[16] Essentially, we have a follower circuit, where the gain is proportional to $(1 + R_F/R_S)$, where F and S refer to feedback and source resistors, respectively. The output is not inverted, since the first and third stages do invert.

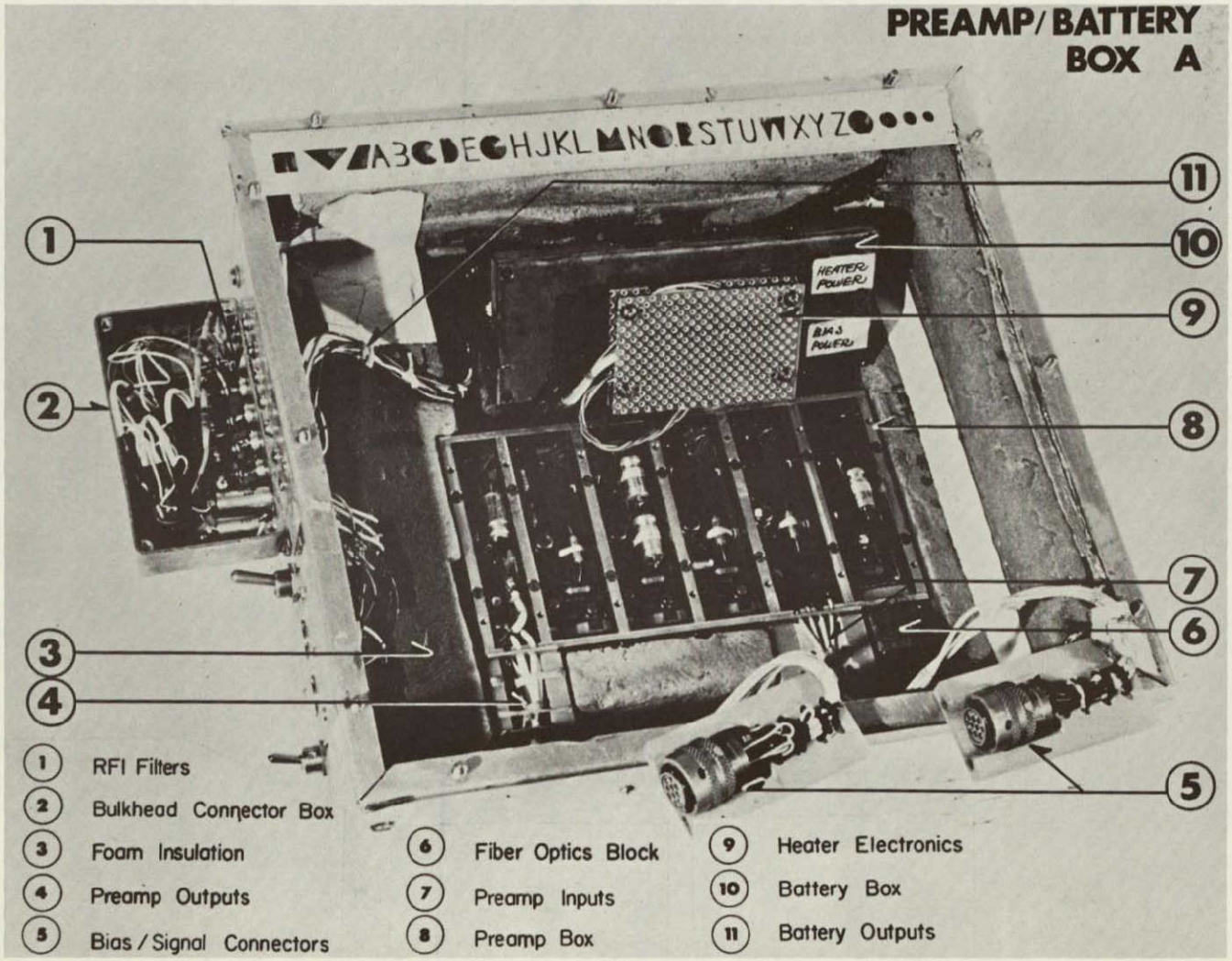

Figure III-35: Preamp/Battery Box A.

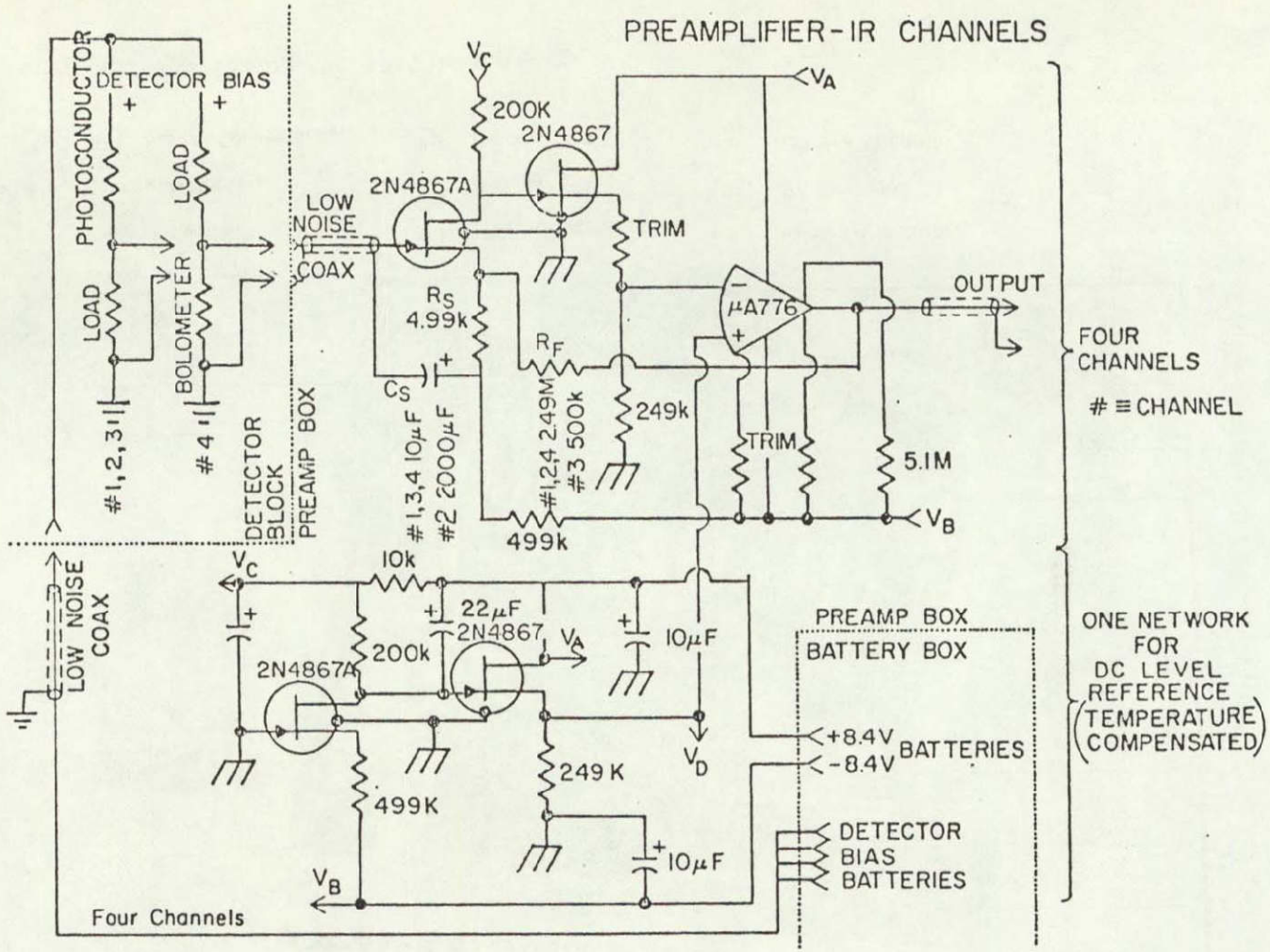

Figure III-36: Preamplifier — IR Channels. The battery box and detector are included schematically.

measured with shorted inputs, produces about 14 $nV/Hz^{\frac{1}{2}}$ rms of noise.

The high frequency 3 db point for the circuit lies around 7 kHz and is due to the opamp. This corresponds to a bandwidth of 11 kHz. Dynamic range can estimated by comparing the maximum swing of the output voltage, 14 V, to the amplified, p-p noise, which is about 21 μV; this gives a range of 6×10^5. However, since we are detector noise limited, at an amplified, p-p level of about 60 μV, the effective dynamic range becomes 2×10^5. Our eight gain levels span a range of 1024, permitting us to take advantage of the dynamic range of the detector-preamp system by fitting it into the telemetry's dynamic range of about 1000. Finally, common mode rejection for the amplifier circuit is 550.

Temperature compensation is achieved by the circuit in the lower left portion of Figure III-36. Two Eveready E146X 8.4 V batteries, which are kept warm in the copper battery box, drive a pair of FET's matched to those in the preamp circuit, so that no relative drift in DC level takes place.

The focal plane monitor uses a photodiode identical to that in the visible star telescope. The photodiode responds to a signal transmitted by fiberoptics bundle and is coupled to the input FET by a .047 μF capacitor. While the FET stages are identical to the corresponding IR channel stages, the opamp is noninverting, with the compensated reference running to the inverting input. The feedback is to the amplifier input, making it a transimpedance amplifier with effectively zero input impedance — a transconductance amplifier — rather than a voltage amplifier. A voltage gain of 24, determined by a voltage divider at the channel's output, encounters a 2×10^5 ohm resistor as it feeds back to the input, furnishing a transimpedance of 5×10^{10} ohm. As in the visible star telescope, a cur-

produced by the photodiode is converted to a voltage. The noise amounts to 5.3×10^{-15} A/Hz$^{\frac{1}{2}}$ at 13 Hz, measured with open inputs, equivalent to an 11.5 magnitude star for the 16 inch telescope.

Alongside the preamp lies a copper box containing the preamp and bias batteries (see Figure III-35), a pair of double pole relays, and the thermostatic heater circuitry for both the battery and preamp boxes. Mercuric-oxide cells are used because of their quietness, but they must be operated above 5 ^{o}C. The specific batteries used for bias are given in the appropriate section for each detector. Teledyne relays (712D-26), controlled by the preamp heater power command, switch bias power off during flight to provide a reference for the DC voltage measurement that is used to determine the detector resistances, which indicate background levels. The thermostatic heater circuit uses a "cool" thermistor (see III. E. 3.) to detect decreasing temperatures by increasing its resistance; the growing voltage drop eventually flips a transistor switch that allows current to flow through power dissipating components in proportion to the need for heat. A chassis mount 10 W resistor and a 2N3740 25 W power transistor are heat sunk to the battery box, and a TIP34C 80 W transistor is mounted to the preamp box. Nominally, the heater operates on 200 mA; the 24 V gondola supply then delivers 4.8 W to the circuit. At maximum, 1 A or 24 W is available. The nominal wattage keeps the battery box at about 13 ^{o}C and the preamp box at -12 ^{o}C under stratospheric conditions, which is acceptable.

Layers of "green foam", a rigid polyurethane foam manufactured by CPR/Upjohn Corporation with a thermal conductivity of 0.020 W/m-^{o}K, faced with aluminum foil, line the inside of the chassis box, affording two inches of insulation over most of the preamp and battery box surface. Fiber-

glass pillars with tapped holes rigidly connect the two boxes to the bottom of the chassis box, which is gusseted by 1 inch aluminum angle. We gain access to the units by removing the chassis box top, retained by short studs and nuts, and extracting the top layer of foam. The preamp and battery cases have covers that can be dismounted without further disturbance, permitting quick checkout and battery replacment. Three fasteners attach the chassis box to the dewar: two 10-32 bolts meet tapped holes in the octagonal collar, and one 5/16-18 bolt mates with a clear hole in the dewar's upper circumferential mounting ring.

Other components in the box are arrayed along the left side of Figure III-35. Two- and four-pole toggle switches control the preamp and bias power, respectively; a divider reduces by 80% the bias battery voltage for the CUPC's. Finally, an array of RFI filters interrupts all leads departing from the chassis box. The signal leads successively encounter 470 ohm resistors inside the box, Erie 9920-100-6002 capacitors feeding through the box (0.15 μF to ground), and 100 ohm resistors outside the box, where a small chassis box carries a 19-pin connector for a cable to the electronics box. The 3 db point for incoming radiation is around 10 kHz; the circuit was tested to confirm that no oscillation or excess amplification occurred. For the higher current heater power circuit, Erie 1225-002 filters, rated at 3 A, block RFI. Lastly, Erie 1200-020 filters handle the preamp power and temperature sensor indicator leads, whose low DC currents are not amplified.

Cables inside the chassis box are carefully restrained to avoid both strain and microphonics. Low noise Microdot coax runs from the collar feedthroughs to the preamp input, and RG-188A/U coax carries the bias and output voltages. Grounds are all referred to one set of lugs on the chas-

box near the RFI filters. When flight ready, the entire unit can be turned on by flipping two toggle switches and plugging in one cable at the bulkhead connector box.

This concludes the description of the detection system and of the entire gondola. The next chapter introduces corresponding pieces of specialized ground support equipment and the procedures for testing and staging the package for flight.

CHAPTER IV

Testing and Staging

A. Ground Support Equipment

In an experiment involving remote sensing and remote control, the ground station plays a role no less vital than the balloon-borne package. Also, since most of the instrument was built in-house, we needed an array of test equipment as the components were developed. Finally, the flight rigging brings nearly everything into play as all systems in our stratospheric observatory are integrated and checked. In this chapter, I'll start by taking each system in the order followed in Chapter Three and briefly describe the corresponding ground support equipment. The second part takes up the lengthy tests we undertook in 1975 and 1976 at the University of Arizona and at Hughes Aircraft/Tucson to prove the system. Flight staging at the NSBF is the topic of Part C.

Electronics System

The electronics contains the telemetry and telecommand capability plus the main batteries. For ground testing, we simulate the ground station at the NSBF with our own electronics (see Figures III-6 and IV-1), shock-mounted in Zero aluminum-enclosed racks. Up and down links are replaced by a special set of cables that run from the Zero boxes to the Elco connectors on the interface module; the batteries are relieved by a power cable from a dedicated power supply. A second small test plug plus connector permits direct control and monitoring of some gondola functions after the above cables have been removed to permit connecting the telemetry. The two Zero boxes also hold other support apparatus.

Beginning with the front panel of the left-hand box in Figure IV-1,

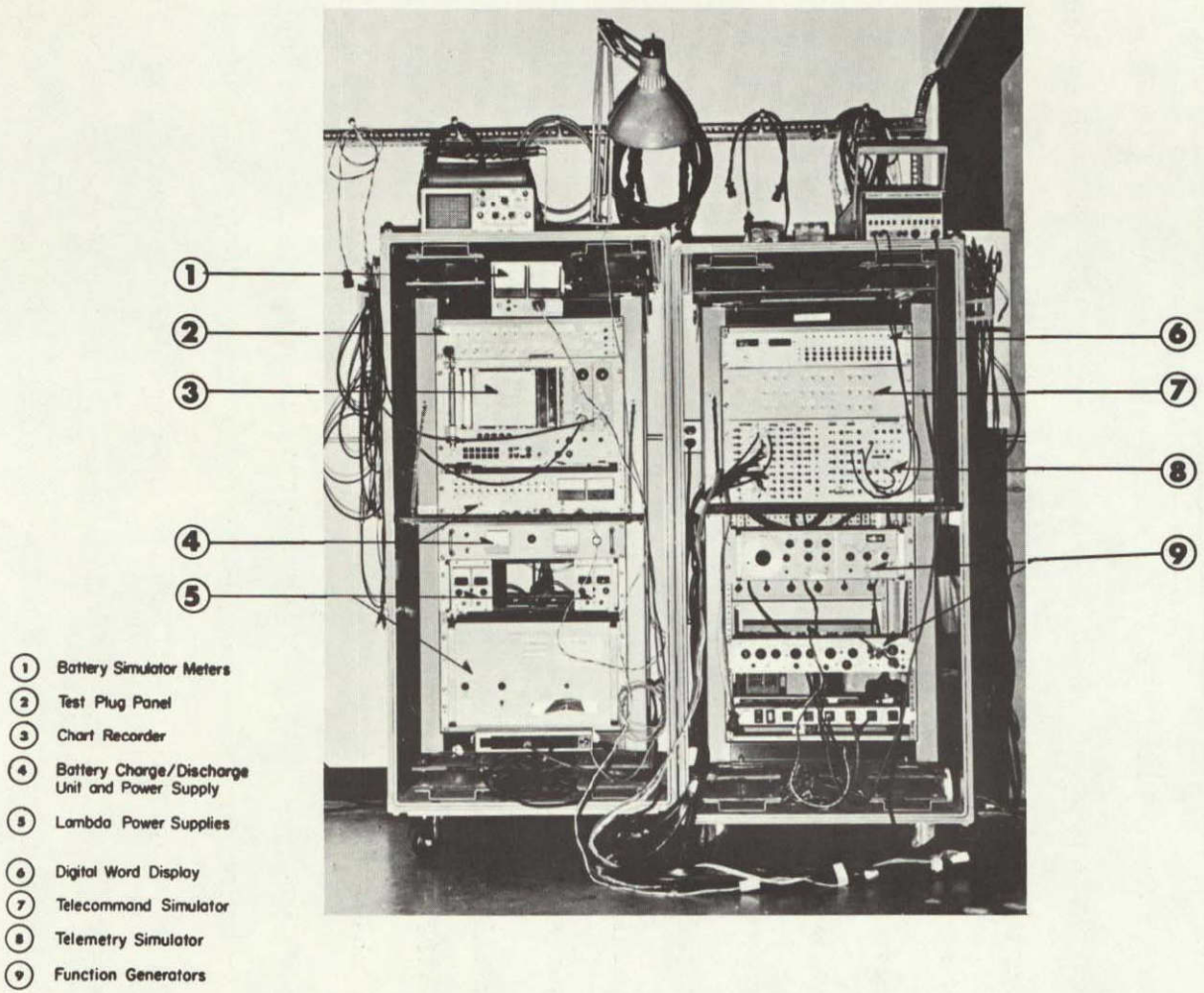

Figure IV-1: Ground Station Simulator.

the test plug panel sits near the top; it receives a cable from the interface and features most of the telecommands and some outputs. Below, a versatile two channel Sanborn chart recorder is available for data-taking. Next, the battery charge/discharge unit enables one to service either the separate cells or the entire battery pack (22 cells in series). For the former task, most of the 26 relays provided are used to cut off the charge or discharge sequence; for the latter job, only two are employed. Pots are furnished to set the cutoff points. An Elco terminated cable carries the power in the cell mode, while a standard eight-pin MS connector serves in the battery mode. In cell mode, a cycle drive with 4 and 8 second options steps the power supply through the cells. DC meters for voltage and current monitor the 36 V, 5 A Harrison power supply immediately below. At the bottom of the rack, a pair of small (40 V, 1.3 A) general purpose Lambda power supplies and a large (36 V, 25 A) Lambda supply are located; the latter substitutes for the batteries during tests and is monitored by another pair of DC meters at the very top of the rack. Lastly, the back panel holds a Lafayette audio amp and speaker for the bleep.

The first three components of the right-hand box in Figure IV-1 are the digital word display, telecommand, and telemetry simulators. The digital display is connected to the telemetry simulator and employs LED's to show various command statuses encoded in three digital words, while the remaining analog information appears between banana jacks for the PCM data and on BNC's for the FM data on the telemetry simulator itself. A complete array of toggle switches on the face of the telecommand simulator controls pulse generators which send commands to the interface. Under these panels, HP function generator and trigger/lock units provide useful test

signals, while a homemade low frequency function generator at the bottom of the rack fills a similar role. Meanwhile, the back panel holds two circuit card testers and a dual module tester for convenient checkout of the standard Vector cards and modules. They are powered by the ground station power supply at the bottom, which takes AC line current and delivers 28 VDC at 15 A, 30 V at 2 A, 5 V at 2 A, ±15 V at 200 and 700 mA, and 175 V at 700 mA, thereby acting as a surrogate power module. Another dual module and three circuit card testers are held in a table-top rack. Additional electronics associated with testing and the computer are discussed in Part C.

Gondola Pointing and Suspension Systems

To determine whether azimuth and elevation systems behave properly, a means of suspending the gondola is necessary. During our laboratory's residence at the University of Arizona's warehouse, a pyramid with four legs, built of 2 inch steel pipe, bore an electric hoist at its apex, which lifted the gondola. Our present lab in the Flandrau Planetarium basement features an empty elevator shaft with just enough area to accommodate the package, and a hook thoughfully left by the contractor supports the hoist. Another device employed in checking the pointing is the telescope simulator, a pair of 160 pound concrete weights and a massive aluminum tube that can be bolted to the elevation shaft to substitute for the telescope. To add realism, a balloon simulator is inserted above the active bearing; it tries to rotate the gondola as the balloon might do. Finally, styrofoam pads, a stool, and removable casters protect the electronics box, bearing box, and telescope, respectively, when on the floor for servicing or assembly.

Structural System

A trio of mechanics' levels is utilized for passively balancing the gondola, while a couple of dynamometers (spring scales) is used to adjust the clutch in the elevation system and the active balance drive. Testing of the tent for leaks is discussed in Part C. The crush structure's quality could only be predicted by tugging at various points, estimating landing conditions, and calculating crude strengths. The same was true for the main framework, but its generous overdesign was proven sufficient in the first impact.

Cryogenic System

Cryogenics requires a great deal of ground support equipment. Part B takes up the drama of cooldown, but let me introduce the cast of characters here:

1) Cryogen — Liquid nitrogen, LN_2, and liquid helium, LHe, are exploited to chill the telescope by direct contact. Heat from the telescope boils cryogen and more heat is absorbed as the gas heats up to near ambient temperatures and escapes from the dewar. We have handled storage dewars of various types and sizes: LN_2 in vacuum jacketed containers of 25, 50, and 160 liters capacity, and LHe in LN_2 jacketed vessels of 25, 50, and 110 liters capacity. The bitter cold of these liquids requires some care in handling, so that insulated gloves and eye protection are recommended.

2) Cryogen manifolds — While large storage dewars often have built-in supply and pressure relief valves, the smaller ones require plumbing for safe and efficient removal. For LN_2, a stainless tube soldered within a larger manifold of copper fittings is coupled to the dewar neck with a short piece of rubber tubing. Dry nitrogen gas under pressure flows into

a tee and forces the LN_2 out of the dewar via the stainless tube. While large LHe dewars have nested O-ring seals, one of which fits the transfer line, small vessels lack them, so we use our own Quikonnect vacuum coupling. The coupling is soldered to a short metal tee, which is coupled to the dewar neck by the ubiquitous lengths of rubber tubing.

3) Pressurization — At times, a sealed dewar builds up sufficient gas pressure to force liquid out without assistance. However, this entails a certain lack of control over the flow rate, so that pressurizing the supply manifold is preferable. A small air pump does work, unless excess humidity freezes, blocking the line. A better approach involves dry nitrogen or helium in large cylinders, suitably reduced through regulators, monitored by pressure gauges, and relieved by pop-off valves or hand-held clips on an in-line tee. By manipulating the diaphragm and output valves on the reducer, a range of flow rates for optimum cooldown can be maintained.

4) Transfer lines — For LN_2, a simple, bent stainless tube inserted into the lid port, down the aligned holes in the baffle, and into the helium vessel's fill channel works adequately. A cryogenic ball valve on the upper end of the line allows throttling or quick shutoff. For LHe, a custom made stainless line from Cryogenic Associates, the company that constructed the dewar, has performed flawlessly for four years. Shaped like an inverted U, an inner tube transports the LHe and an outer tube creates an evacuated space in between. The horizontal outer section is a flexible stainless bellows, which helps enormously when placing one end in a large supply dewar and threading the other into the telescope while standing far above the floor.

5) LN_2 Removal — After the instrument has been pre-cooled, we can

either permit the LN_2 to evaporate or actively pump it out. Since the former can take days, we usually try the latter. A massive Stokes Microvac pump, capable of moving 80 cubic feet/minute, terminates a sequence that begins with the LN_2 transfer line whose end sits in the liquid and passes through an LN_2 storage dewar, which collects the cryogen, and a heat exchanger, a soup pot of water immersing a copper coil and resting on a hot plate.

6) Vacuum lid — To test the detectors in the lab at the 1.7 ^{o}K assumed by the LHe in the stratosphere, we must create low pressure in the dewar. A special vacuum lid, similar to the flight lid in insulating properties and layout, has a ½ inch thick aluminum disk gusseted by a 3 inch channel instead of a light stainless superstructure. Using this lid and the Stokes pump, extreme cold tests are feasible.

7) Sensors and controls — The internal cryogen level sensor is explained in III. E. 3. Other level sensors for use in storage dewars contain 18 ohm carbon resistors at the end of long stainless tubes. The resistor is part of a Wheatstone bridge; immersion in cryogen increases that arm's resistance so that no current flows across the bridge. This is reistered by an ammeter in a box at the top of the tube. Also, a cryogenic solenoid valve can be put in series with the LN_2 transfer line and can be controlled by an adjustable circuit with hysteresis, which switches at levels sensed by diodes and trimmed by pots. The same device can be made to oscillate at low frequencies and drive a relay for other applications.

Optical System

Focusing and collimation of the main optics and boresighting the visible star telescope are the fundamental procedures requiring support equipment. A gantry to which the optical assembly, the telescope minus the

helium vessel and detector/filter block, can be bolted, permits us to reach the focal plane behind the primary mirror. Here we mount a wide-angle, 32 mm focal length Erfle eyepiece which inspects a plexiglass reticle, ruled on a milling machine and illuminated by a pair of LED's. The gantry, in turn, is hinged to one edge of a rolling laboratory cart. This crude altazimuth mount serves to acquire Polaris, whose image we project on the reticle at the focal plane. Focusing the instrument for the optimal image is accomplished by moving the secondary along the optical exis. We use a modified plastic slide rule to measure the distance from the inner diameter of the collar to the edge of the beam by sliding an LED on the moving scale into the beam. Tilting the secondary into the plane perpendicular to the optical axis, as indicated by the beam edge, achieves collimation. We can also check the chopper throw this way. Boresighting the two telescopes at the NSBF made use of the main telescope's focal plane monitor and a pair of Tensor lamps flashed at low frequency by the LN_2 flow control circuit from a nearby hilltop (see III. F. 5.).

Detection System

Dewars manufactured by Infrared Laboratories and at Cornell University were used to test detectors before integration in the detector block. We require, of course, typical soldering iron sources and rotating sector wheel choppers, and a Fourier spectrophotometer provides data on filter characteristics. The dewars, including the main telescope dewar, are evacuated by either of two pumping stations, with both roughing and diffusion stages, one of which is mounted in a Zero box for field operations. A special source for detector testing in the Hughes chamber was also constructed. Deferring to military jargon, this "target" consisted of a boxlike frame bolted above the dewar with enough room for the flight lid to swing

open. The sides were sheets of masonite, and the top was a 31 by 51 inch copper plate with copper tubing for LN_2 soldered to one surface. The LN_2 flow control acted as a thermostat for the target; diode thermometers triggered the circuit. Two apertures, on- and somewhat off-axis, admitted radiation chopped at different frequencies to the telescope. These signals were clearly detectable over the low background generated by the cryogenic copper. Test details follow in Part B.

B. Laboratory and Chamber Testing

Of the six systems discussed above, four either could not be tested non-destructively (most of the structural system) or are checked through standard procedures I need not describe here in detail. Before final telescope assembly, the optics are focused and collimated; the latter is repeated afterward. Prior to departure for the NSBF, the entire gondola is integrated in the laboratory's elevator shaft. All electronics and the gondola pointing and suspension system undergo thorough examination. The cryogenic and detection systems require the greatest attention, along with those structural units with moving parts that might fail under stratospheric conditions. Three types of testing, related in more detail below, are performed: "lab cryo tests", in which the flight dewar is chilled and/or pumped, "chamber cold tests", in which a given electronic or mechanical component is tested at stratospheric temperature and pressure, and "chamber cryo tests", in which the cryogenic dewar is placed in a stratospheric environment.

Lab cryo tests are conducted with the goal of proving the detection and cryogenic systems of the telescope itself. Although unrealistic in that the lid remains closed, they provide much useful information and oc-

cur in house. The cooldown procedure for these experiments has evolved over the past two years. Figure IV-2 shows the entire array of equipment described in Part A, with the flight lid in place; the initial cooldown is essentially identical for the vacuum lid. To reduce water vapor content in the sealed dewar's interior, a day or two of flushing with about ten 225 cubic foot bottles of 99.995% pure nitrogen gas precedes the fill. The nitrogen cylinders are topped with Victor regulators and three are combined by a manifold to provide a single, uninterrupted stream of dry gas which enters the dewar via one of two ports in the center of the flight lid or on the edge of the vacuum lid. Flushing continues as the LN_2 fill begins and throughout the entire testing or preflight procedure in order to maintain a positive internal pressure, which discourages the entry of ambient air. We initiate the LN_2 fill by inserting the nitrogen transfer line and pressurizing the supply dewar manifold with another cylinder of dry nitrogen. About 30 liters are required to chill the vessel sufficiently to hold a few liters of liquid; slow transfer (between 2 and 4 lbs/square inch, or psi, of pressurization) is superior since one would prefer that gas leave the system as warm as possible to reap the maximum amount of cooling. When accumulation begins, we accelerate slightly (4-5 psi) and fill the vessel about halfway, or with about 14 liters. Roughly 80 liters, including the partial fill, are consumed before the telescope's temperature stabilizes, after which the cryogen boils away very slowly, about 1/3 liter/hour, allowing ample time for detector tests at 77 ^{o}K.

Normally, we push on, so we run the transfer line and supply dewar in reverse, pumping with the large Stokes pump through an in-line heat exchanger, a clear section of Tygon tubing as a visual flow monitor, and a

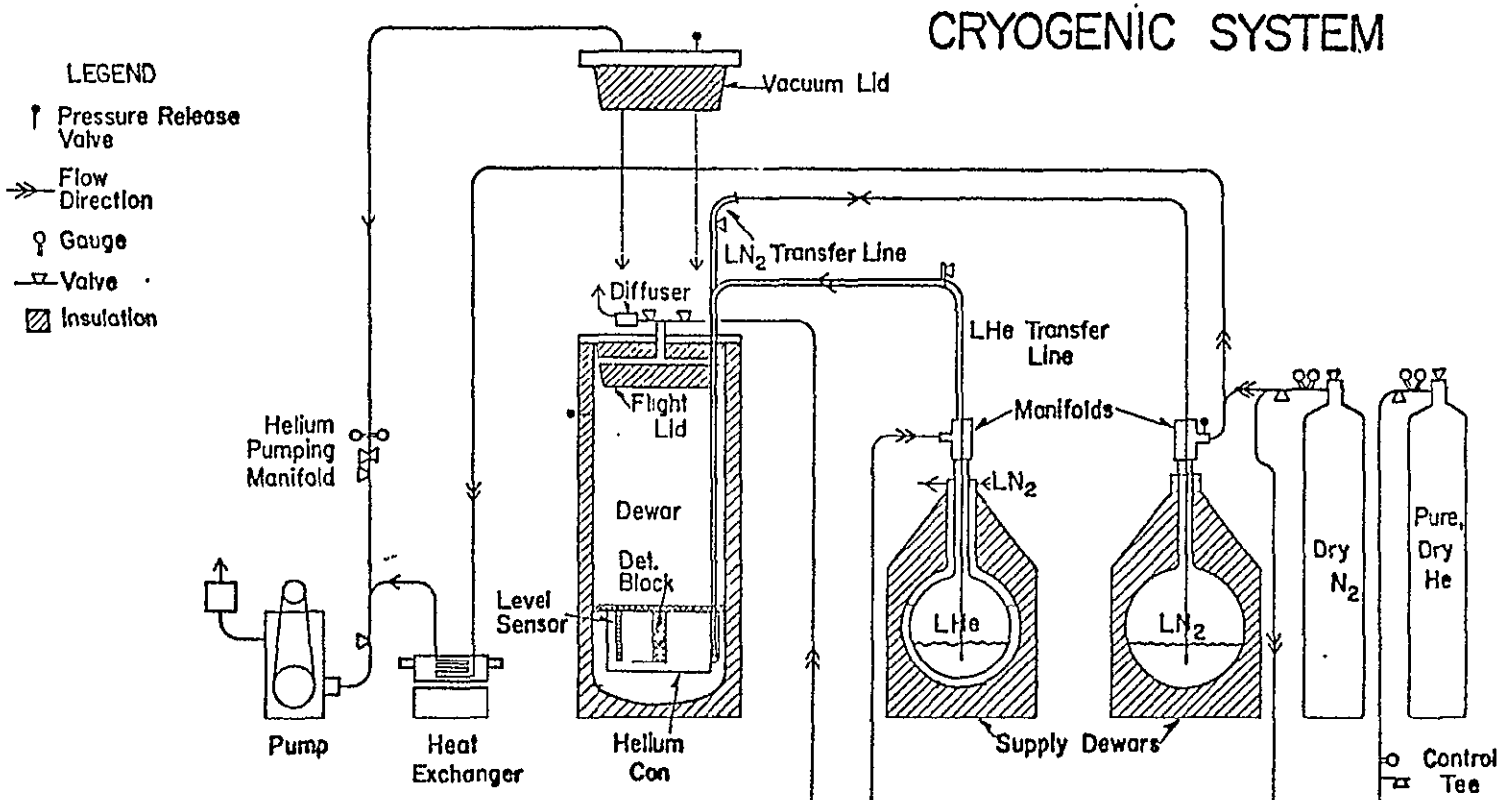

Figure IV-2: Cryogenic System. Arrows show the flow of liquid and gaseous nitrogen and helium among the different dewars, cylinders, pumps, etc. Where arrows merge or where arrowheads are opposed, more than one process is indicated. For instance, before and after precooling with LN_2, the LN_2 flows into and out of the telescope dewar, respectively.

cryogenic solenoid valve. About two hours are needed to empty the vessel; at the end of the process, the telescope is tilted to puddle the remaining cryogen near the fill line tip. Flushing with LN_2 occurs continually and speeds up as the pumpout terminates, which we do instantly with the solenoid valve to avoid sucking air into the telescope. Then, we start to flush with 242 cubic foot bottles of 99.998% pure helium gas to displace the nitrogen; after roughly four hours, we commence the LHe fill. The LHe transfer line replaces that of LN_2; at least two people are involved in guiding it into both research and supply dewars gently and simultaneously. Another cylinder of He gas pressurizes the supply dewar manifold, and a gauge reading in ounce/square inch, or osi, is inserted next to a tee, so that the "fill operator" can regulate the transfer rate. Again, care must be taken during the touchy transfer line insertion to prevent air from entering; both telescope and transfer line are flushed generously with helium gas prior to and during insertion.

At this point, we relax a bit and let the LHe boiloff cool the dewar toward 4.2 ^{o}K; should the boiloff be sufficient, we can slow or stop the flush for a time. Again, the LHe vaporizes instantly at first, so a slow transfer rate is preferable to maximize heat absorption by the gas. After 2-1/2 hours and 55 liters of LHe, transferred at about 8 osi, we begin to accumulate cryogen in the vessel. Increasing the rate to 12 osi, we fill the can completely with 28 liters and consume about 45 liters doing so. The transfer rate is controlled by the fill operator (see Figure III-5) who adjusts the regulator diaphragm and output valves, monitors the pressure gauge, relieves excess pressure at the control tee, and watches the level sensor's output on a one-channel Varian strip chart recorder. If no additional supply dewars are needed, filling the can takes two more hours;

if one runs out, the tricky process of removing the transfer line and setting up a fresh dewar can add at least half an hour and cause additional losses in accumulated cryogen. After the fill is complete, the vessel loses about one liter/hour, giving us a day or so of hold-time. The level sensor, whose heater resistors can be put on a timing circuit with an 11% duty cycle, keeps track of LHe loss during lab testing. Topping off is performed daily and takes approximately two hours and 35 liters of LHe.

If temperatures below 4.2 ^{o}K are desired, mainly for bolometer tests or stratospheric simulation, we must pump on the liquid helium, which brings the vacuum lid into play. After the dewar has stabilized at ambient pressure, we connect the Stokes pump to the lid through a helium pumping manifold, which contains coarse vacuum (400 inches of H_2O) and fine pressure (50 mm of Hg) gauges plus bellows, needle, and bleeder valves. We typically bring the dewar's internal pressure down to 12 mm Hg in about 2-1/2 hours, simulating the package's climb out to 90 thousand feet, although we have pumped down to 8.4 mm Hg, or 100 thousand feet. This consumes another ten liters of LHe, after which losses do not exceed 2-1/2 liters/hour, even with disruptive tilting to low elevation angles or extreme changes in pumping speed during the lab tests. Losses in flight are definitely less, and our experience with Flight C-1 indicates that boiloff did not surpass 1-1/2 liters/hour, since we still had cryogen when the flight ended.

During the entire cooldown, we periodically move the calibrator arm into and out of the beam with the LED switched on to check for ice or fog formation. Any sudden increase in scattered with respect to reflected radiation suggests trouble; the only way out is to warm the dewar by flushing with helium gas until the ratio drops and recool. For this and other

reasons, we must keep extra cryogen and flushing gas in reserve, because delay in procurement makes cooling more difficult and increases the chances of ice formation. In fact, once the cold test is underway, the investment of time and money (LHe costs several dollars/liter) demands completion.

On the other hand, chamber cold tests are much less traumatic. Fortunately, a small Conrad environmental chamber is located in the Lunar and Planetary Laboratory adjacent to the Planetarium. Capable of mimicking the stratosphere, it is perfect for testing the performance of electronic and mechanical gondola components, such as the inertia wheel, preamp/battery box, calibrator, and active balance. Easy to operate and quick to turn around, this chamber has pinpointed several problems prior to integration.

Finally, when the time came to check out the whole telescope with an open flight lid, the availability of a large (23 feet long, 7 feet wide and high) environmental chamber just outside of Tucson was an incalculable blessing. This Conrad "walk-in" could achieve 100 thousand feet and -65 ^{o}C, although the temperature rose slowly as pumping proceeded, since forced air cooling became less effective. Despite this difficulty, the performance was adequate for our purposes. By placing the telescope, fully charged with LHe and suitably rigged, into the chamber and pumping, we learned the few critical facets of cryogenic behavior that ultimately led to success. In addition, a target mounted over the dewar opening permitted detector system testing with an open lid.

Once the gondola is cold, lab and chamber cryo tests are concerned with the proper functioning of electromechanical components in such units as the lid mechanism, chopper, and calibrator. Problems we often

encounter involve bearings that seize, time constants that change, or shorts that appear due to materials that freeze, stiffen, or differentially contract at low temperatures. Although some problems are caught by the small chamber cryo tests mentioned above, many other remain for the more realistic simulation at Hughes. Next, the main purpose of the cryogenic system, after cooling the telescope, is to keep the detectors at a stable temperature, since even small fluctuations change detector properties enough to confuse or ruin the data. Chamber and lab cryo tests uncovered and confirmed a fluctuation problem, and a later chamber cryo test showed that a solution had worked.

Finally, the detection system needs review. Vulnerability to microphonics can be observed best in the lab situation, where the telescope is accessible. The same arrangment, with the lid closed and at a measurable temperature, provides a roughly computable background level. Direct measurement of their resistance casts the detectors in the role of thermometers and thereby indicates the rough background level as well. Comparison with the noise found in a narrow bandwidth by a lock-in estimates the quantum efficiency and the responsivity. With the chopper running, any offset — assymmetry in the telescope's radiation field — is perceived by the detectors as a signal, and can also be used to determine the responsivity; inversely, one can quantify the offset. Of course, the calibrator's emission, as figured from its diode thermometers, can be exploited to calculate the responsivity, too. This combination of approaches yields a good idea of the detectors' behavior. Witht the target in place in the Hughes chamber, further experiments at a higher background level are possible, as it carries two sources of known temperature on- and off-axis and chopped at different frequencies. Unfortunately, due to

the large size of the telescope relative to the chamber, we did not attempt to map the beam profile of the whole instrument, hoping that a celestial point source would be available. Another test we did perform was the construction of a load curve for the bolometer at the expected operating temperature of around 2 ^{o}K in order to select the proper bias voltage.

During lab and chamber cryo testing, the fundamental electronic tools are a PAR 124 lock-in amplifier, a Tektronix 434 two-channel storage oscilloscope, a Weston 1240 DVM, a Darcy 440 VTVM, and a homemade AC signal averager for broadband (3 db points: 0.1 and 100,000 Hz) conversion of rms to DC with 0.47 and 10 second output time constants. These units measure noise levels and overall detector voltages and resistances to carry out the above tests.

The major tests, excluding small chamber cryo tests, ran from April 1975 up to the first flight in August, 1976. The flight preparation is described in Part C.; the tests are summarized below:

21-25 April 1975 - Lab Cryo Test

As the first test for the integrated telescope, we sought basic information on the cryogenic and detection systems. While the LN_2 procedure went smoothly, the LHe fill was hard to control. The two original Ge:Ga photoconductors developed open circuits and microphonics were serious, but crosstalk was not a problem. A major effort was launched afterward to reduce microphonics, design a level sensor for LHe, and streamline assembly procedures.

2-7 December 1975 - Lab Cryo Test

Meant as a rehearsal for the first chamber test at Hughes, we again wanted basic performance information. Cryogenics was less of a problem, but microphonics remained, the ultraminiature cryogenic coax used inside

the dewar failed mechanically in several instances, the rebuilt chopper proved vulnerable to random excitation, and the calibrator arm, exposed to extreme cold from boiloff gas, froze. Indicated improvements included replacing the dewar leads with Microdot low-noise coax, changing bearings on the calibrator, and adding a second mode to the chopper electronics.

11-13 February 1976 - Chamber Cryo Test

Finally at Hughes, a number of problems arose. Cryogenic handling difficulties away from the lab undermined our schedule for a chamber test, which was postponed to the next series. Calibrator, lid seal, and pre-amp problems sent us back to the lab for two weeks of small changes.

22-27 February 1976 - Chamber Cryo Test

Except for air iceup of the primary, which we successfully reversed by warming, flushing, and recooling, the cryogenic handling went very well. However, just before entering the chamber, we attached the target and tilted the telescope to about 20 degrees elevation angle onto a Dexion skid built so that it would fit inside. By tipping the telescope with ambient pressure and a full charge of LHe inside the dewar, we set up a powerful convective cell as cold gas flowed over the warmer upper walls of the dewar interior. Surprisingly effective heat transfer led to the sudden loss of cryogen. We continued with the test anyhow and discovered an additional failure of the lid bearings in the cold. This debacle suggested that we try to tip the telescope after pumpdown.

3-8 March 1976 - Lab Cryo Test

We conducted a lab test with the vacuum lid in place and pumped the dewar down to around 10 mm of Hg. Tilting the telescope to low elevations did not cause sudden boiloff, so an arrangement for lowering the instrument by remote control after the chamber had been evacuated had to be de-

vised. A crude but effective mechanism using lead weights to unbalance the telescope on one side and an electric hoist to let it lean over and to pull it back up was built and installed in the chamber.

30 March-1 April 1976 - Chamber Cryo Test

Back at Hughes, we exposed two more serious problems. While the cooldown went well and microphonics had been conquered, ice formed on the primary while at float; pressure in the chamber and temperature fluctuations in the detector block, serious enough to affect the bolometer, became obvious. Solutions involved the addition of a tent with a thin membrane to the main structure and the rebuilding of the helium vessel. The latter lost its doughnut configuration and became a simple pot, and complementary modifications of the detector and filter block brought them into their present form.

31 May-4 June 1976 - Chamber Cryo Test

Done without a target in order to answer the basic remaining questions, the final Hughes test was rather successful. The new helium vessel--detector/filter block combination removed serious temperature noise, and a prototype tent, designed to fit into the chamber, kept the air at bay. Cryogenics proceeded smoothly, all four detector channels worked without microphonics, chopper and calibrator and lid operated properly, and the preamp achieved a reasonable configuration of gain and bandwidth. This cleared the way for our first flight without further tests in Tucson.

C. Flight Staging

Once in Texas, the final integration of the gondola took place. Again, I shall present the preparations systematically:

Electronics System

Before flight, all module circuit boards were cleaned and all cables were inspected for connector integrity, shorts, and opens. The, the ground station simulator participated in an exhaustive set of test instructions involving each module. Closer to launch, the focus shifted to the real ground station's control room, where testing continued through the actual telemetry, which was installed by that time in the right bay of the electronics box. The battery pack, already in place, was charged; until then, the simulator provided power.

In the control room, integration of our data-handling equipment with the NCAR system proceeded. Figure III-10 shows the general configuration. The NCAR discriminators separated the FM and PCM channels, although the entire video signal was taped as a precaution. The NCAR PDP-11 computer provided on-line printout on a Decwriter of some functions and routed others for recording on tape. The output from an array of digital-to-analog converters (DAC's) was displayed by a two-channel oscilloscope and by chart recorders. Our own GA SPC-16/65 computer and associated Wangco tape drive captured the FM channels through an eight-channel signal filter followed by an analog-to-digital converter bank. The former amplifies and filters signals from either the FM telemetry or the simulator to supply the proper voltage range to the computer and to remove components above a 3 db point of 4 Hz at the gondola. Such frequencies are higer than our scan rate would produce. Beyond the computer lies the "signal/sense and print" module. Actually a small computer, the unit accepts azimuth and elevation scan information plus one signal channel and the time from a Datametric SP-425 A/B time code generator and searches for profiles corresponding to either chopped or unchopped signals. Azi-

muth and elevation scan scales can be adjusted with external pots, as can the trigger level and the time delay between accidental triggering and reset. Resetting can also be done manually. Outputs for an HP 5055A digital printer and a DVM are provided; the former normally prints the signal level, azimuth and elevation scan locations, and the time.

Overall, the mission of our GA computer, aside from handling incoming data, is to introconvert among gondola, magnetic, terrestrial, celestial, and galactic coordinates to expedite observing decisions. Its memory also contains a catalog of bright stars and prominent infrared objects, including visible planets, to aid in position finding and source hunting. A standard Teletype machine lets us communicate with the computer. On the other hand, the job of the NCAR PDP machine is to manipulate all of the telemetered data; it is preprogrammed to print out selectively on a Decwriter printer whatever group of outputs we are interested in at whatever interval is convenient.

Gondola Pointing and Suspension Systems

Staging of the package took place in a tall, octagonal building known as the Stratoport. Several hoists were provided form which the gondola could be suspended and tested with plenty of elbow room. Aside from subjecting the pointing system to a rigorous, fully loaded checkout, flight rigging includes setting the magnetometer table, adding the "Tim fitting" to the flight train for the launch vehicle to grasp, adjusting the "ski-binding", and weighing the whole package.

Structural System

The major effort here was the construction of the crush structure below the package, to which NCAR-supplied cardboard crush pads were attached. Above the telescope, the tent was bolted to the framework; then

came the arduous task of completing the airtight space between the rectangular base of the tent and the circular top of the dewar. After about a week, we succeeded in sealing the system adequately. With everything bolted in place, we balanced the whole instrument, beginning with the telescope and continuing with the rest of the gondola. At the same time, active balance and slip clutch adjustments were made. Other mechanical devices, such as the lid and tent drives, were double-checked as well. Of course, we conducted a thorough inspection of all framework fasteners for tightness and locking devices.

Cryogenic System

We performed the cooldown as described in Part B. The major difficulty was ice formation, as sensed by our calibrator; the problem worsened over the three days spent at LHe temperatures, despite greater care than ever in flushing and keeping positive internal pressure. On the eve of the flight, we warmed the dewar to remove the ice, but it reformed as we cooled back down below the freezing points of air. Numerous constraints forced us to fly anyway. The afternoon of the flight, we draped another tent over the entire telescope and inflated it with helium gas to prevent condensation in the humid east Texas air on the half mile trip to the launch pad. As an extra safety measure, eight small bags of dessicant were hung inside the external tent. Just before launch, we jettisoned the external tent and dessicant bags, shut off the flush gas, and opened up the opposite port on the flight lid, allowing a diffuser to break up the strong stream of boiloff gas generated by cooling during climb out. Except for the ice buildup, the cryogenic system operated well, although it demanded considerable effort during fills. Improvements are discussed in Chapter VI.

Optical and Detection Systems

After telescope assembly in the first days in the field, we only adjusted the collimation and boresighted the visible star telescope. Once the detector/filter block was integrated into the optical system and inserted in the dewar, it was totally inaccessible, obviating any further action.

Chapter V follows with flight results. Chapter VI summarizes performances and suggests improvements, most of which are underway at present, the 1976-77 academic year.

CHAPTER V

Flight and Results

A. Flight C-1

We brought the package to the National Scientific Balloon Facility in Palestine, Texas at the end of June, 1976 and began flight preparations. A summer flight was propitious for several reasons. Due to our laborious cryogenic procedure, launch delays are extremely costly in both money and effort. Happily, the best month for launch weather is July, followed closely by August and June. Secondly, the short duration of our flights, one night, means that we can tolerate the steady float winds of summer. Finally, the Galaxy is best situated for Northern Hemisphere observers in the summer and fall. The galactic plane, as the main goal of the survey, determined the bulk of the flight plan, as described below.

Our requested float altitude was 30 km, so a 3.1 million cubic foot Winzen balloon, made of 1.2 mil or 30 micron Stratofilm polyethylene film, was chosen for the job. The predicted float winds — 45 miles/hour from the east — indicated 8 to 9 hours at float before descent and recovery near Midland, Texas, a hospitable region preferable to the more mountainous terrain further west. Launch time was set for 7:30 p. m. Central Daylight Time (CDT), bringing us to float at 9:30 p.m. Since sunrise on the balloon was at roughly 6:30 a.m. CDT, roughly eight hours of darkness, excluding twilight, were available.

Upon reaching float, our first target was to be the galactic plane in Cygnus, which was rising through our preferred elevation range (50-70^{o}) at the time. This region embraces several bright stars and strong IR sources by which we hoped to orient the gondola precisely and cali-

brate all channels. NML Cygnus (stellar object) and HFE 72 (a source detected by Gondola B: Hoffmann, et al, 1971b) were primary goals as we planned to move eastward from $l = 75^{\circ}$. The sequence moved into Cepheus, at $l = 100^{\circ}$, at around midnight, CDT, and into Cassiopeia, at $l = 110^{\circ}$, by 1:00 a.m. At 1:30 a.m., the plan called for slewing around to the southwest into Aquila and moving along the plane from $l = 30^{\circ}$ to 80° as the region set through our preferred elevation range. By 3:45 a.m., the major objective of surveying the plane from galactic longitude 30° to 115° was to be met, and more exotic sources were to be sought. They included M33 (a galaxy), the Crab Nebula (a supernova remnant), dust clouds in Taurus and Perseus, NGC 2264 (a young cluster), and R Monocerotis (a "cometary" nebula containing a near-IR source). Jupiter, the only well placed planet at any time of night in early August, 1976, was chosen for absolute flux calibration at 4:30 a.m. Our philosophy throughout was to accomplish the primary mission, a survey of the galactic plane, first, should unforeseen problems develop later in the flight.

Actually, the gondola was launched at 8:21 p.m., CDT, on August 4, 1976. The flight diverged from the plan for a number of reasons. (See Table V-1 for the flight chronology and Figure V-1 for the flight path.) Most important, the inertia wheel failed, leaving us with control over elevation angle only. Also, the float winds were slightly stronger and had backed a bit, adding a southerly component which aimed the package toward the extremely rugged Big Bend Country of Texas and Mexico beyond. Lastly, the telemetry deteriorated after the first few hours. Termination was executed about two hours early, at 4:40 a.m. Useful astronomical data was obtained between 11:23 and 11:51 p.m., CDT, bracketed by useful engineering data right up to termination. This portion of the

TABLE V-1: FLIGHT CHRONOLOGY

CDT*	FLIGHT TIME	EVENT (Flight C-1, August 4-5, 1976)
8:21 p. m.	0:00	Launch
8:40	0:19	Power On
9:13	0:52	Pass Tropopause
9:35	1:14	Open Lid
10:00	1:39	Release Telescope in Elevation
10:02	1:41	Lift Stow Bolt
10:07	1:46	Slew to 58° Elevation
10:17	1:56	Set Gain and Chopper Mode
10:31	2:10	Reach Float Altitude
10:35	2:14	Attempt Azimuth Stabilization
11:23	3:02	Slew to 66.5° Elevation
11:55	3:34	End Scans, Slew to 50° Elevation
12:16 a. m.	3:55	Active Balance and Noise Tests
1:30	5:09	Onset of Occasional Telemetry Noise
2:30	6:09	Onset of Frequent Telemetry Noise
3:42	7:21	Tilt Tests of Cryogenic System, Slew to 25° Elevation in Steps
4:08	7:47	Slew to 90° Elevation in Steps, Observe Balloon
4:36	8:15	Close Lid
4:40	8:19	Power Off
4:50	8:29	Separation
5:35	9:14	Impact

*The local time in Texas, Central Daylight Time, is five hours behind Universal Time (UT). The Local Sidereal Time (LST) at launch was 15:53.

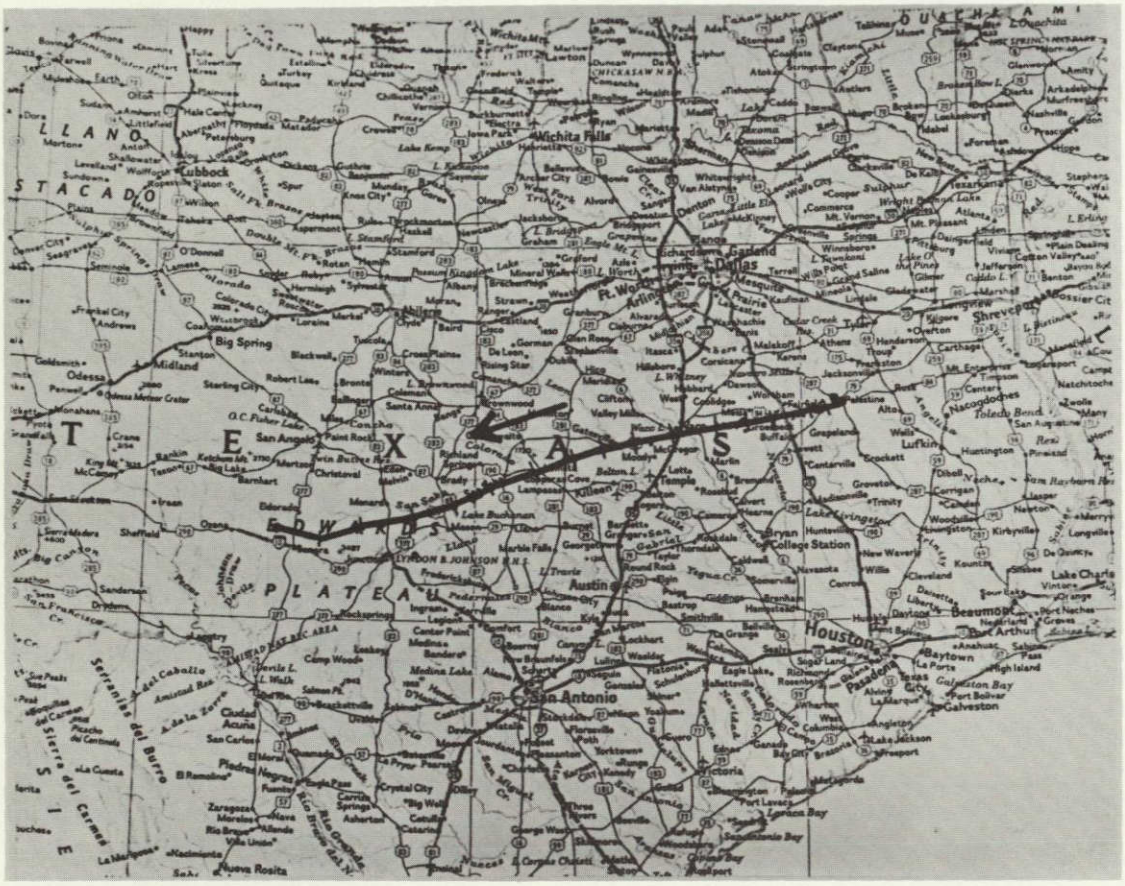

Figure V-1: Flight C-1 Trajectory. Map from National Geographic,(1970). Ticks along path are half-hour intervals. Times are Central Daylight.

flight is covered in more detail in the next part. The gondola landed at 5:35 a.m. after striking a tree and flipping over at a ranch about 12 miles northwest of Sonora, Texas. This unusual circumstance destroyed the crush structure, as desired, but also generated lateral forces that bent the lower, outboard side of the telescope frame and damaged the visible star telescope. The tent was demolished, as well, as the inverted telescope came to rest on the ground. However, all of this damage was rather superficial; no more than a man-month of work would have been required to return it to its pre-impact condition.

B. Data Reduction

Upon reaching altitude on the evening of August 4, 1976, we discovered that all systems were working, except for azimuth stabilization. When all efforts to resuscitate the system failed, we permitted the gondola to rotate freely at a possibly rewarding elevation. Guided by the existing flight plan, the telescope was stepped to 66.5° elevation at 11:23 p.m. We made no further offsets in azimuth, so that the high gain magnetometer could serve as a first-order guidepost to our azimuth. The resulting scan intersected the galactic plane twice, in Cygnus at $80^{\circ} < l < 90^{\circ}$, and in Aquila at $41.5^{\circ} < l < 42.5^{\circ}$. At 11:55 p.m., after five complete circuits, other tests resumed. Following lengthy engineering checks, our inability to stabilize in azimuth and deterioration of telemetry frustated our attempt to acquire a bright source, Jupiter, for calibration. Thus, we scanned with reasonable success for about 32 minutes, rotating, on the average, every 380 seconds.

Back in Tucson, the data analysis proceeded on several fronts. A crude stacking of scans exhibited a characteristic and recurrent base-

line drift, which we now believe to be due to the scattering of balloon radiation by air ice on the primary mirror. A set of earlier, half-degree steps in azimuth on the strip chart record indicated a positive — increasing in azimuth — sense of rotation. Moreover, the overall sense of the high-gain magnetometer trace removed the other ambiguity in azimuth, since the reading of 127° could easily have been 180° away at 307°. By associating the positive part of the trace with north, the decreasing zero crossing had to be 127°. Summing up, we knew that we were rotating, we knew which way we were rotating, and we had a rough but unambiguous null direction for the high gain magnetometer.

Concurrently, I pursued the second means of attack, the stars recorded by the visible star, or 1-micron, telescope. As described in III. 5. , the silicon photodiode responds to radiation between .35 and 1.05 microns and the system produces clear signals for stars as faint as eighth magnitude. In order to compare observed with expected signals on the basis of a known visual magnitude and spectral type, I defined a special magnitude incorporating very near-IR corrections. During flight, the Sanborn two-channel chart recorder monitored the bleep (time signal) and the visible star telescope. Using this record to find the brightest stars detected in the half hour of interest, I retrieved their digital output for greater precision. The two strongest signals were close together in the sky, as demonstrated by a crude analog computer: a transparent grid superimposed on a circumpolar star map. γ and α Aquilae (Tarazed and Altair), it turned out after a few weeks of analysis with the help of our General Automation SPC-16/65 computer, had been scanned three revolutions, or twenty minutes, apart. Once this was known, the celestial scan was methodically nailed down by about one hundred more iden-

tifications of detected stars. The GA computer, by transforming gondola into celestial coordinates for direct printout or for comparison with a small star catalog in its memory, expedited the process immensely.

In order to achieve the root-mean-square positional error of about 7 arcminutes, I took two steps. First, as the gondola's rate of rotation was not constant, zero crossings by the high gain magnetometer every three minutes could not provide sufficient azimuthal information. By retrieving the low gain magnetometer readings from the NSBF tape and synchronizing zero crossings, an azimuth accurate to a few tenths of a degree could be interpolated. Also, more faint stars close to our rough trajectory were added to the computer's star catalog; more weak signals on the strip chart were matched with stars in the Smithsonian Astrophysical Observatory Star Catalog (1966) and the Atlases Borealis and Eclipticalis (Becvar, 1972-74). These procedures led to a consistent set of corrections to the telemetered elevation and the assumed high gain magnetometer azimuth; the corrections permitted us to compute accurate IR positions.

A sample of the strip chart record appears in Figure V-2. The lowest channel traces the bleep, or time signal; small excursions represent seconds. The high gain magnetometer is next; since time runs from right to left, the non-constant segment of the trace depicts a decreasing zero crossing at an azimuth around 127°. Moving upward, the 100 micron channel appears, with both a true signal and a segment of baseline drift noted. The three remaining channels at 50, 20, and 100 microns complete the record.

The trajectory appears in Figure V-3 as a series of ellipses — circles in the sky distorted by the circumpolar projection — separated by about six minutes of time in right ascension, the gondola's period of ro-

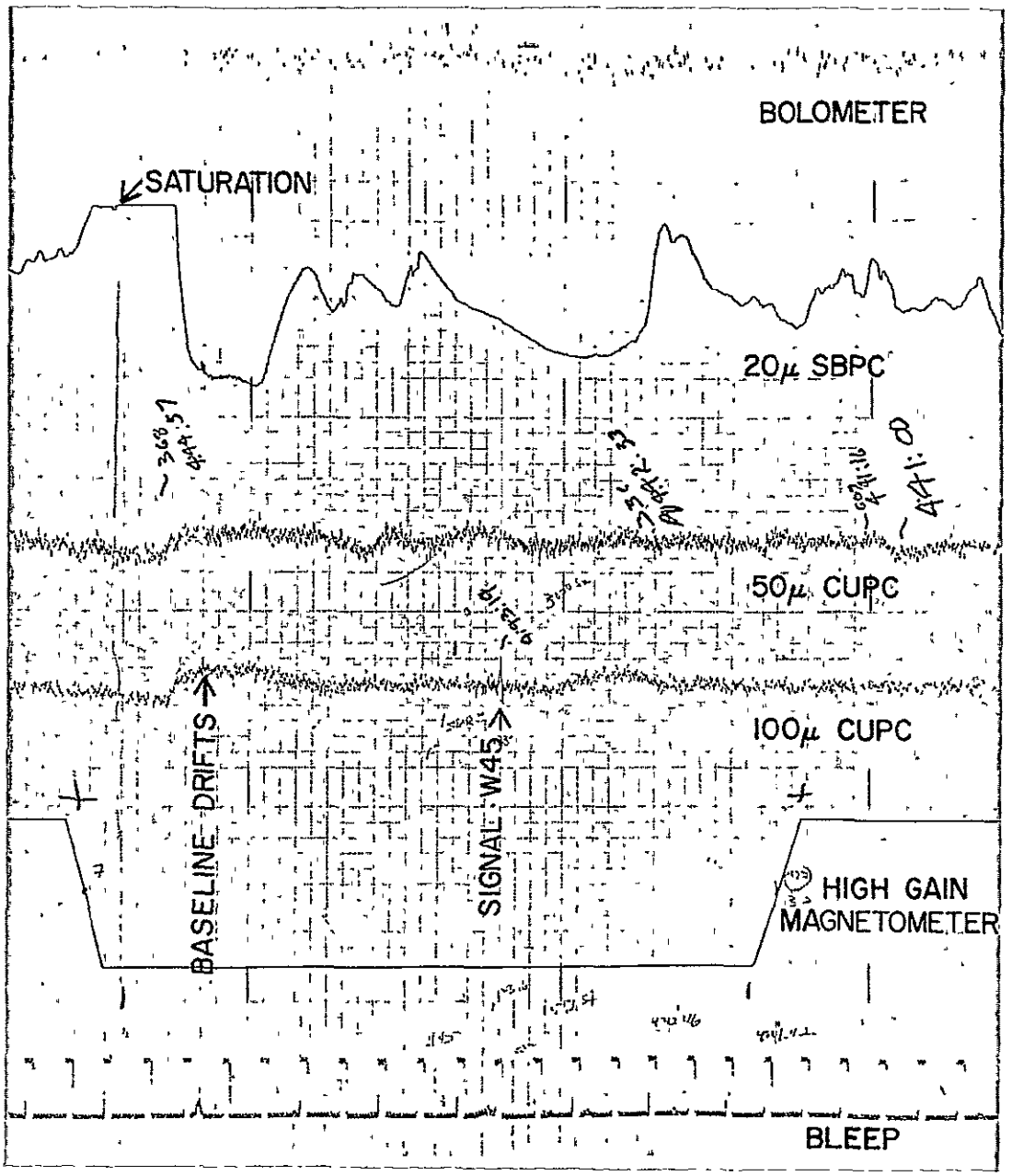

Figure V-2: Sample Strip Chart Record — Flight C-1. A few minutes during the half-hour of data-taking is shown. See Page 200.

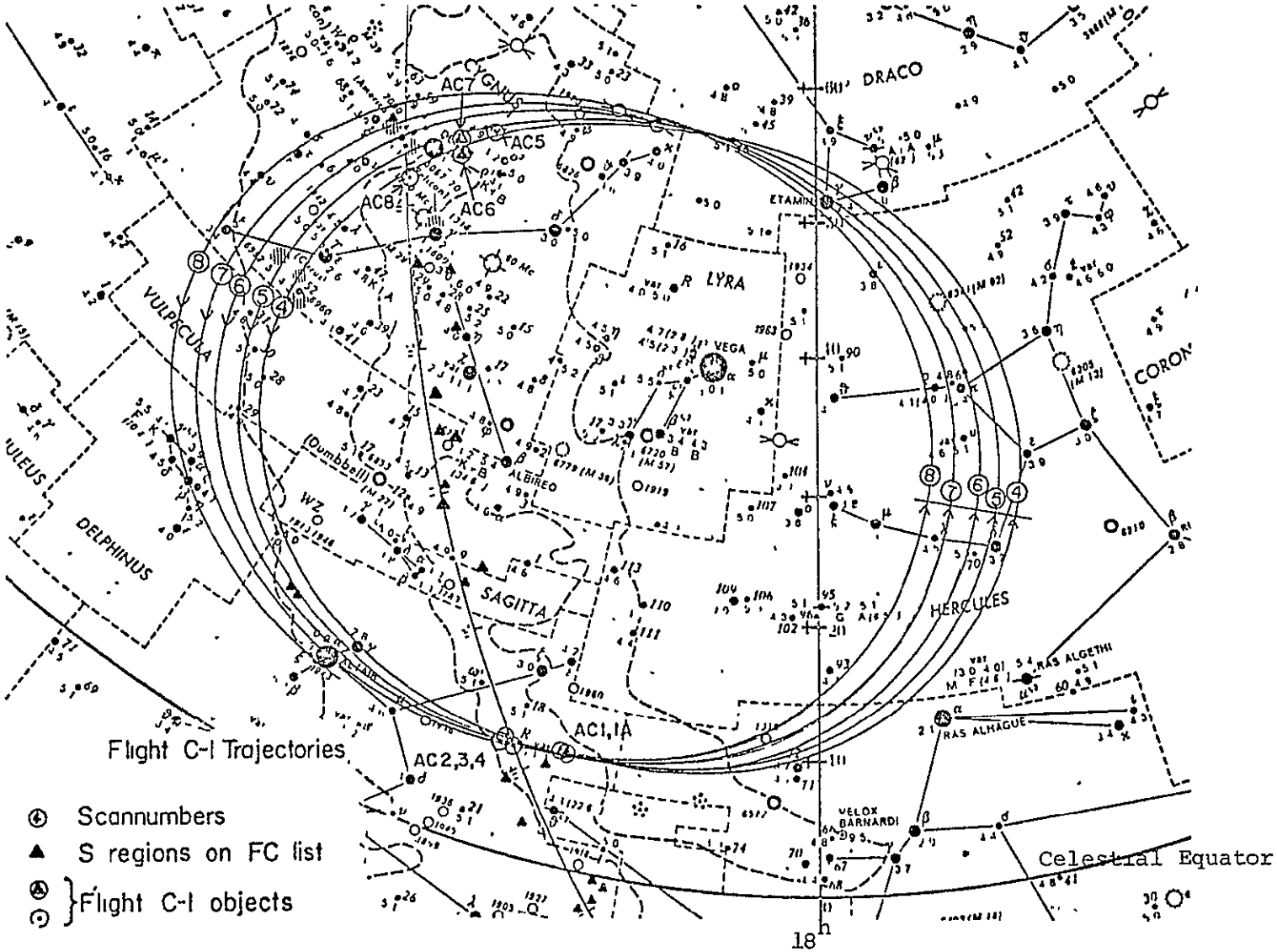

Figure V-3: Flight C-1 Scan Trajectories. Superposed on a circumpolar map of the northern celestial hemisphere (Rükl, 1965) are our scan trajectories, our IR sightings, and Sharpless HII regions observed at 1400 MHz by Felli and Churchwell (1972).

tation. The brighter stars shown on the trajectories were identified; fainter stars were included in some sparsely populated regions to produce fairly even coverage. To obtain local zero corrections, each rotation was divided in two by the magnetometer nulls; nine stars, on theaverage, were identified per semirotation. I compared true and indicated positions for each star in the set and averaged the results. The standard deviations were 7' in elevation and 5' in azimuth, close to what one would expect from the visible star telescope's 15' beam.[1] Azimuth corrections suffered little drift during the half hour of data taking, but the elevation did decrease from about 66.3° at the beginning to 66.0° after two rotations. Afterward, it was steady. When these zero corrections were satisfactory, the IR search began, keeping in mind the offset between the IR detector and the boresighted visible channel in the focal plane.

At this point, I concentrated my efforts on the strongest sightings in the 100 micron photoconductor channel. Two of these points were near the galactic plane in Aquila. More analysis revealed that the two spikes were the same object, corresponding to the radio position of W45, a continuum radio source (Westerhout, 1958). W45 lies 2½° north of the plane at l = 40.5°. Attempts to find W45 on other scans bore fruit; it appeared on four scans in all.

As the reader can see from Figure V-3, by a considerable stroke of good fortune, W45 was near the meridian at the proper declination to be encountered by four of the five scans. They remained quite close together as they intersected the galactic plane slightly to the east, providing us with additional opportunities for multiple sightings. The realities of

[1] Azimuth is determined by the low gain magnetometer as well as the visible star telescope detection; this makes the position slightly more precise.

galactic orientation, however, meant that the opposite transit took place in the less interesting southeastern corner of Draco. Where the scans cross the plane in Cygnus, they are separated by roughly one degree, obviating repeated sightings. The scans, or individual rotations of the gondola, are labelled by encircled numbers in Figure V-3. Scan #3, the small segment preceding scan #4, and scan #8, are incomplete rotations. The numbering begins with scan #3 due to the arrangement of the data tapes; the earlier scans, confused by attempts to correct the azimuth stabilization problem, may be analyzed at a future date. Figure V-3 also shows HII regions from the catalog of Sharpless (1959) that were subsequently detected by the radio continuum search of Felli and Churchwell (1972). Of course, it locates the nine sources we observed, too.

C. The Observations

Due to air ice on the mirror, the 50 and 20 micron channels contained no useful data, and a helium leak in the bolometer's vacuum cavity rendered the bolometer insensitive. Therefore, only the 100 micron photoconductor, our IR channel #1, yielded detections. In the half hour of undisturbed scanning, a total of nine sources in which we have reasonable confidence (3-σ) were observed and are presented in Table V-2. Column 1 carries a sequential number, based on right ascension and preceded by "AC", denoting Arizona-Cornell. Columns 2 and 3 furnish right ascension and declination for Epoch 1950.0; columns 4 and 5 provide galactic longitude and latitude. Where multiple sightings, enumerated in column 6, are involved, a flux-weighted average of individual scan positions is shown in columns 2 through 5. Column 7 gives our confi-

TABLE V-2 IR SOURCES DETECTED ON FLIGHT C-1

AC #	α^* h m	δ^* ° '	l °	b °	SCANS #	CL S/σ	FLUX Jy	IDENTIFICATIONS† OPTICAL	INFRARED	RADIO
1	18 54.1	+8 01	40.7	+2.6	4	11.9	3460	S76,L40.6+2.6	AFGL2284	W45,DA466,FC19,CC40.5+2.5,FF1853+07, ADG040.5+2.5,PG40 5+2.5
1A	18 55.1	+8 11	41 0	+2.4	1	7.2	3020			MOR44,LMH41,CTB61,HC15,4CP08.53A
2	19 04 3	+7 48	41.7	+0.2	1	3.4	1420			ADG041.4+0.4,HR39,DWC041.5+0.4
3	19 07.6	+8 19	42.5	-0.3	2	4.6	1540			ADG042.5-0.2,HR44,DWC042.5-0.2
4	19 08.4	+7 49	42.2	-0 7	2	5.6	1810			ADG042.1-0.6,HR42,DWC042.1-0.6
5	20 21.6	+49 39	86.1	+7.2	1	3.5	1460	L85 99+6.80		
6	20 31.3	+45 27	83.7	+3.4	1	4.0	1700	S112,J69,BCV, L83.77+3.32		FC44,HBMR21,NK2.07,FF2032+45
7	20 36.0	+46 27	85 0	+3.3	1	4.8	2000	S115,DWB180-190 L84.81+3.88		FC46,HBMR22,NK2.10&2.11,MUL19 3C416.1,BEN61,W71
8	20 39.8	+41 54	81.8	-0.0	1	3.9	1660		AFGL2631, HFE70	DR23,PD23,W75,CTB96,FF2039+41, WEN81.6+0.0

*1950.0 Coordinates.

†REFERENCES

ADG	Altenhoff, et al, 1970	FC	Felli and Churchwell, 1972	MOR	Moran, 1965
AFGL	Walker and Price, 1976	FF	Fanti, et al, 1974	MUL	Muller, 1959
BCV	Becvar, 1964	HBMR	Higgs, et al, 1964	NK	Kawajiri, 1970
BEN	Bennett, 1963	HC	Holden and Caswell, 1969	PD	Pike and Drake, 1964
CC	Clark and Crawford, 1974	HFE	Hoffmann, et al, 1971b	PG	Price and Graf, 1976
CTB	Wilson, 1963	HR	Hughes and Routledge, 1969	S	Sharpless, 1959
DA	Galt and Kennedy, 1968	IRC	Neugebauer and Leighton, 1969	W	Westerhout, 1958
DR	Downes and Rinehart, 1966	J	Johnson, 1955	WEN	Wendker, 1970
DWB	Dickel, et al, 1969	L	Lynds, 1965	3C	Edge, et al, 1959
DWC	Day, et al, 1970	LMH	Large, et al, 1961	4CP	Caswell, 1966

dence level in standard deviations, as discussed later in this chapter. Column 8 relates the peak flux in Janskys, while columns 9, 10, and 11 list possibly related objects at optical, infrared, and radio frequencies. The lower part of Table V-2 identifies 30 catalogs or surveys by a code that is used in the upper part of Table V-2 and in Tables V-3, V-4, V-5, V-6, and V-7. I have also used this code in the text for this part of Chapter V. The following are most frequently cited:

S, for Sharpless, (1959),

FC, for Felli and Churchwell, (1972),

W, for Westerhout, (1958),

HFE, for Hoffmann, et al, (1971b),

ADG, for Altenhoff, et al, (1970), and

L, for Lynds, (1965).

Tables V-3, V-5, V-6, and V-7 are keyed with symbols to Figures V-4, V-9, V-10, and V-12, respectively. Figures V-5 and V-11 show our scans superposed on radio continuum maps from Felli and Churchwell, (1972). All coordinates in Tables V-3 through V-7 refer to Epoch 1950.0. In Figures V-4, V-6, V-8, V-9, V-10, and V-12, the rectangles along our scans represent the RMS error for the center of the beam, as derived from the star identifications along that scan. Each detection is covered in more detail in the following set of descriptions.

Sources AC1 and AC1A

Of the sources we detected on Flight C-1, the one in which we have the most confidence is AC1. Not only did it display the strongest signals, but we observed it four times, and it has been detected previously

at optical, infrared, and radio frequencies. A rather exhaustive list of catalog entries for the source follows: from left to right, catalog number, beam size in arcminutes where applicable, symbol on Figure V-4, α and δ for Epoch 1950.0, frequency or wavelength, flux, and source extent are tabulated.

TABLE V-3: AC1 and AC1A

DESIGNATION*	BEAM '	SYMBOL	α h m	δ ° '	ν MHz	λ μ	FLUX Jy	EXTENT '
AC1	12	◉	18 54.1	+8 01		100	3460	
AC1A	12		18 55.1	+8 11		100	3020	
L40.46+2.46		□	18 54	+7 45		Optical		.8 × 5
S76		□	18 54	+7 45		Optical		7 × 7
AFGL2284	3 × 10	△	18 53.8	+7 50.0		11 20	103 435	
PG40.5+2.5	0.27§	△	18 53.8	+7 50.0	10700		2.4	1.75§
ADG040.5+2.5	11	△	18 53.8	+7 50.0	5000 1414		7 10	9 × 10
W45	34		18 53.7	+7 47	1390		22†	120 × 48
FC19	10	△	18 53.8	+7 50.2	1400		11.8	9 × 9
DA466	36	⬡	18 53.8	+7 59	1420		15	
CTB61	48	+	18 54.6	+8 14	960		19	18 × 18
MOR44	30		18 56.4	+8 7	610		110	114 × 114
LMH41	40 × 54		18 54.5	+8 18	408		50†	
CC40.5+2.5	3	△	18 53.8	+7 49.7	408		2.7	<3 × 3
FF1853+07	4 × 114		18 53.8	+7 56	408		4.1	2.8 × 2.8
HC15	23 × 25	+	18 54.6	+8 14	178		27	20 × 40
4CP08.53A	23 × 25	×	18 54.1	+8 11.5	178		27	

*See Table V-2. †Estimate. §Interferometer: Beamwidth and extent in α only.

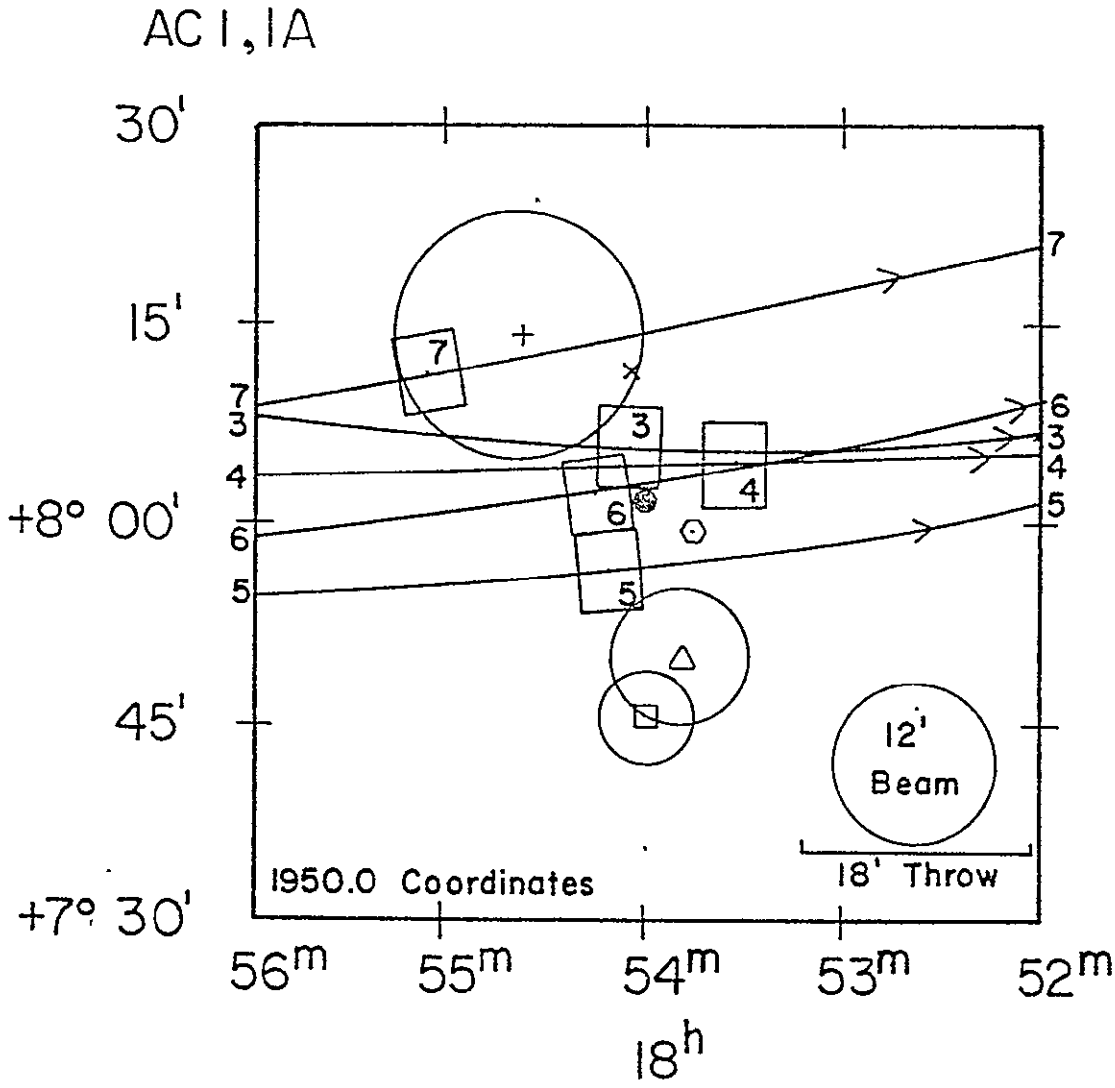

Figure V-4: AC 1, 1A. The numbered rectangles along the numbered scans show our nominal positions. The square gives the visible HII region position #1. The triangle is position #2, where many IR and radio positions coincide. The DA position, #3, is depicted by the hexagon, and the "+" locates position #4, common to low frequency radio surveys. The filled circle is the flux-weighted average of our scans #3, 4, 5, and 6. See Table V-3.

Beginning with spatial information, we see that four distinct positions emerge from the list. Optically, the nebula tabulated by Lynds and Sharpless is the brightest of the few emission regions in this heavily obscured area. Six arcminutes to the northwest is the second location, at which the near IR and many radio positions coincide. Moving nine minutes further north, we encounter a third point, recorded in the DA survey, although their ±12' uncertainty in declination embraces the second position. Finally, 20' more to the northeast lies a fourth position, popular among some low frequency observations.[2] Four of our five scans seem to center on the third position; the filled circle on Figure V-4 indicates the flux weighted average. The other scan, labelled 7, detected a source about 19 minutes to the northeast, which correlates with the fourth position. Because the two areas are probably related, I have named the 100 micron sightings AC1 and AC1A. However, due to our large beam, the nature of our scans, and the apparent complexity of the source, all five scans may have picked up just one extended source or more than two smaller components. For the same reasons, estimating the extent of the source or sources from out data would be unwise, except to say that it probably does not exceed 30' in right ascension.

The listed catalogs are in rough agreement on source extent. Optically, L and S agree on a diameter of about 7'. Continuum surveys with smaller beams above 1000 MHz by ADG and by FC (see Figure V-5) concur on a 9 circle at the second position, while continuum surveys below 1000 MHz by CTB and HC agree on an 18' dimension at the third position. Both are embedded in W45, a spur 0.8° wide extending 2° from the galactic plane at 1390 MHz. MOR define a similar perimeter for the spur at 610

[2]The 4CP position has been included for completeness, but the later HC list, also by Caswell, does not tally it; I assume HC is a revision.

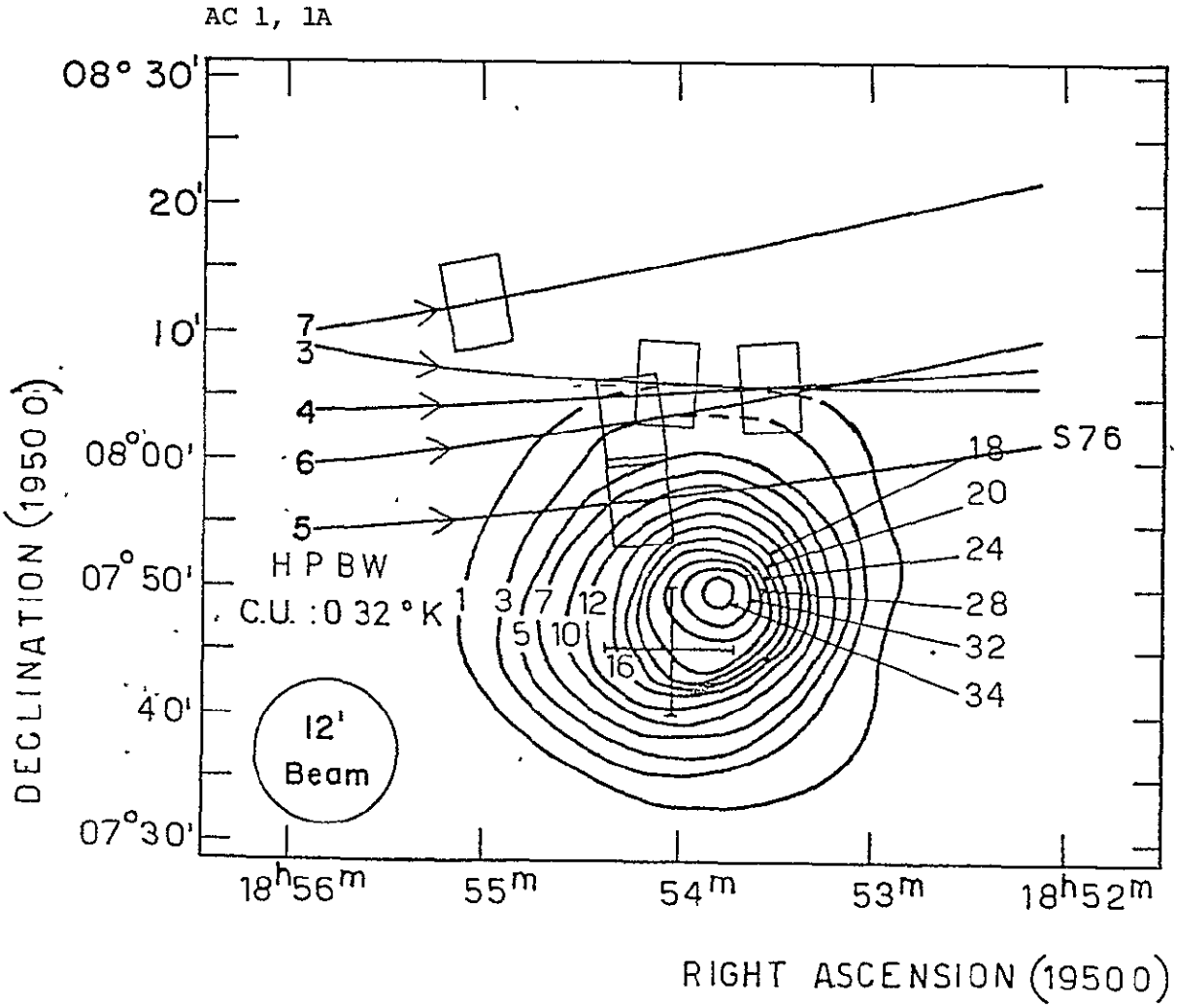

Figure V-5: AC1, 1A — Radio Continuum Map. Our numbered scans and rectangles showing our nominal positions are superposed on a 1400 MHz map from Felli and Churchwell (1972).

MHz. At the other extreme, CC at Molonglo, selecting small diameter radio sources at 408 MHz, measured 2.7 Jy within 3' at the second position; FF at Bologna, searching similarly at 408 MHz in the northern sky, obtained 4.1 Jy from a 2.8' source near the third position. Lastly, PG, using the Stanford interferometer at 10.7 GHz, observed the finest structure: at the second position, the source subtended 1.75' in α and contained possibly two smaller peaks, separated by 0.75'.

Although differing beam sizes make comparison difficult, none of the radio measurements conflict with the conclusion of Holden and Caswell (1969) that the extended radio source is thermal, i. e., emits free-free radiation. In the infrared, three sets of observations are available: the AFGL catalog, our own data, and the measurement by Harvey, Campbell, and Hoffmann from a Kuiper Airborne Observatory (KAO) flight[3] in October, 1976. At 11 and 20 microns, the AFGL catalog lists 103 and 435 Jy respectively; their 3' by 10' beam probably covers the source. Our 100 micron flux peaked at 3460 Jy on our scan #6; our scan #5 registered 2570 Jy. Scans #3 and #4, at 1660 and 1960 Jy, were weaker and north of the mean position. Again, our inability to point on Flight C-1 prevented proper raster scanning and acquisition of a point source for calibration and beam profile determination, so we cannot determine the peak position directly or whether we passed through it. Harvey's preliminary data (Harvey, 1976) confirm the balloon detection; he reports 3500 Jy ± 50% in an 82-130 micron bandpass and a rough half-power diameter of 2' at position 2. Therefore, our measurements are consistent if we assume that the balloon scans passed north of the main IR source at the second position or that the region contains several components of similar brightness, of

[3]Our observation of W45 from the balloon motivated the flight.

which Source AC1A is a possible example. More observations are required.

In summary, Source AC1 represents the detection of a galactic HII region with a considerable infrared excess in a heavily obscured region near the plane. The flux peaks at about 3500 Jy in the vicinity of 100 microns; two far IR components are possible from our data. A crude model, based on a plausible kinematic distance and an rough estimate of the object's size, is discussed in Part E.

Sources AC2, 3, and 4

Where the five scans passed through the galactic plane in Aquila, six detections above or equal to three σ took place. Of these, two pairs are close to known radio sources, while the remaining two occurred between known sources. The large beam and chopper throw, both on the order of source separations in this complicated region, leave us vulnerable to confusion. With that caveat in mind, I have identified three sources, one of which is marginal. Figure V-6, covering all five scans in a region 1.5 degree square along the galactic plane, presents the situation. Included are the four brightest of six ADG sources in the area; their vital statistics, along with other observations, follow in Table V-4, with a format similar to Table V-3:

TABLE V-4: AC2, 3, and 4

DESIGNATION*	BEAM '	α h m	δ o '	ν MHz	λ μ	FLUX Jy	EXTENT '
AC2	12	19 04.3	+7 48		100	1420	
HR39	9	19 03.4	+7 39.7	3240		4	
DWC041.5+0.4	8	19 03.4	+7 41	2700		4	"extended"
ADG041.4+0.4	11	19 03.3	+7 39.1	2695 1414		7 9	17 × 12

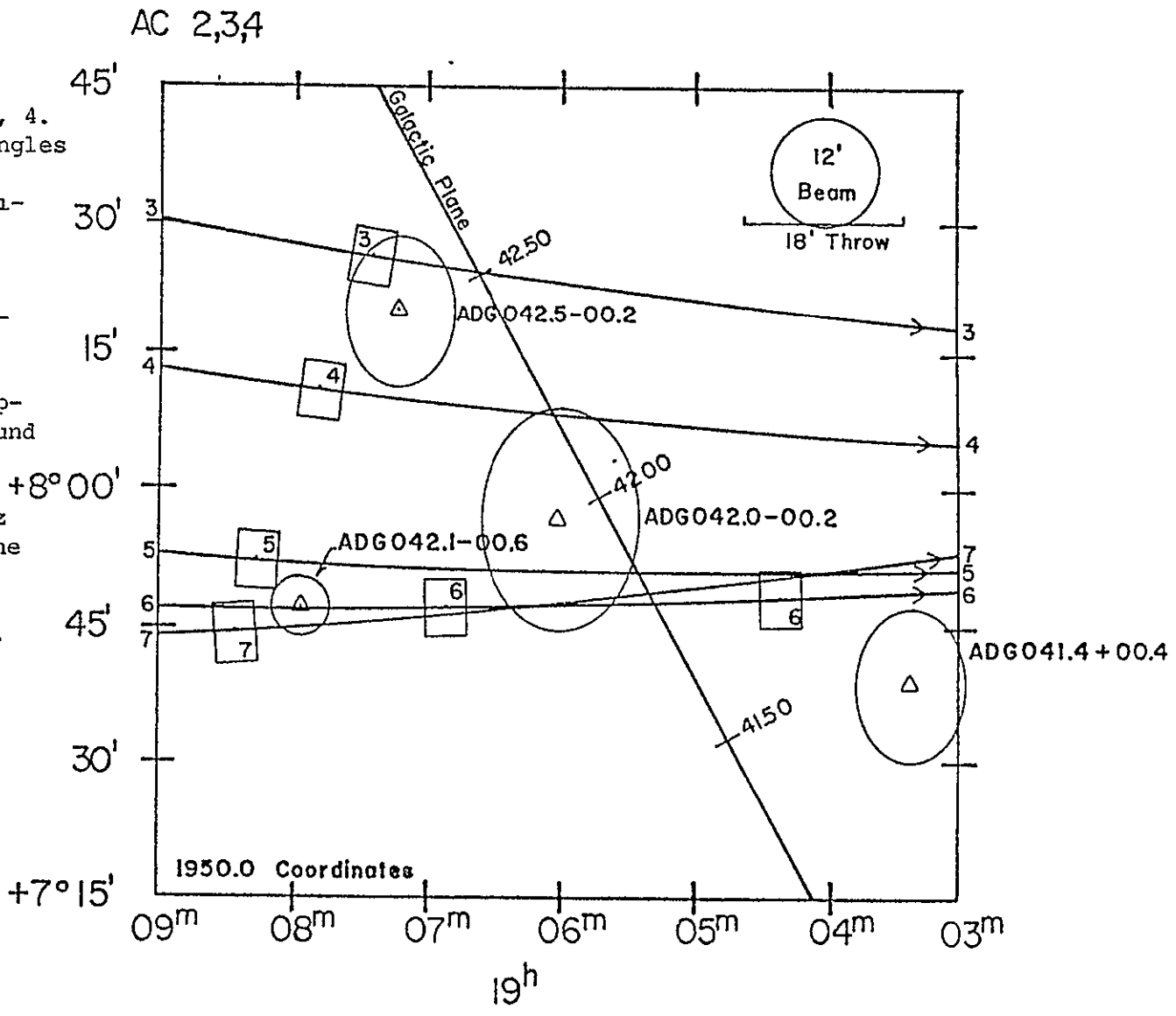

Figure V-6: AC 2, 3, 4. The numbered rectangles along the numbered scans give our nominal positions. The triangles depict the ADG positions of the four strongest sources from their list in the map area; the ellipses and circle around the triangles give the radio extents at 2695 or 5000 MHz (see Table V-4). The numbers along the galactic plane are galactic longitude.

TABLE V-4: Continued

DESIGNATION*	BEAM '	α h m	δ ° '	ν MHz	λ μ	FLUX Jy	EXTENT '
HR41	9	19 06.0	+7 51.8	3240		6	
DWC041.9-0.1	8	19 05.9	+7 52	2700		2	
ADG042.0-0.1	11	19 06.0	+7 57.7	2695		7	25 × 18
				1414		11	
AC3	12	19 07.6	+8 19		100	1540	
HR44	9	19 07.3	+8 18	3240		5	
DWC042.5-0.2	8	19 07.3	+8 20	2700		6	
ADG042.5-0.2	11	19 07.2	+8 19.9	5000		9	19 × 12
				2695		7	
				1414		7	
AC4	12	19 08.4	+7 49		100	1810	
HR42	9	19 08.1	+7 45.8	3240		2	
DWC042.1-0.6	8	19 07.9	+7 47.5	2700		3	
ADG042.1-0.6	11	19 07.9	+7 47.5	2695		4	6 × 5
				1414		6	

*See Table V-2.

The section of the plane between l = 41.8° and 42.5° is one of fairly uniform obscuration; neither bright nor dark nebulae are listed in catalogs by Lynds (1962 and 1965), nor are any arresting features discernable on Palomar prints. Parenthetically, our scans neatly fell between two much stronger sources: W49 on the north and 3C397 on the south (See Figure V-7 for the radio continuum.) Our scans #3 and #4, at 1540 and 1180 Jy, respectively, probably detected ADG042.5-0.2, a rather extended source with a flat radio spectrum near the 7 Jy level. The stronger signal sits closer to the radio peak; with some confidence, I designated it AC3.

The latter scans (#5,6, and 7) were very closely spaced near a path

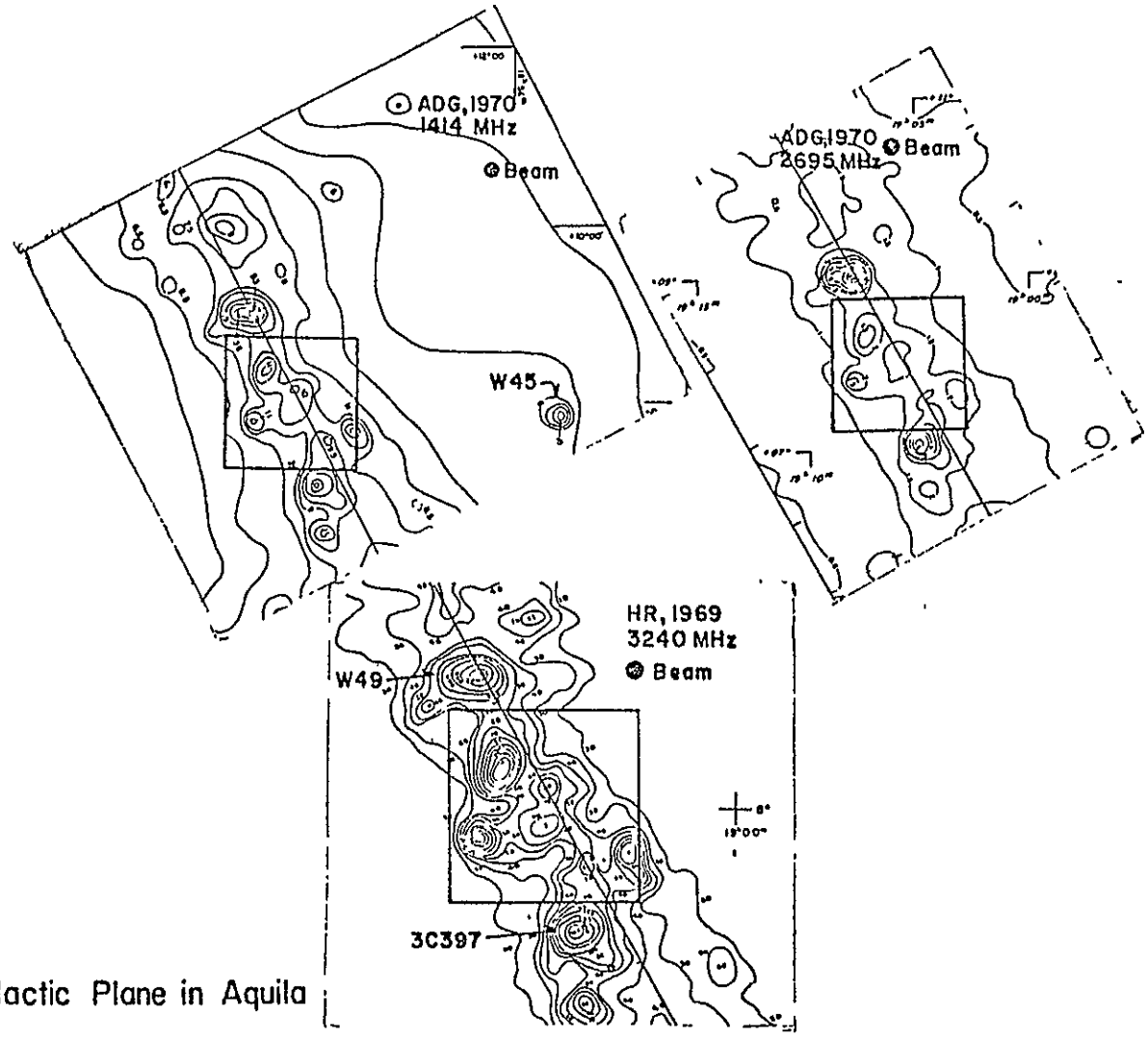

Figure V-7: AC 2, 3, 4 — Radio Continuum Maps. The region along the galactic plane in Aquila is shown at three frequencies. The superposed rectangles correspond to the edge of Figure V-6.

that encountered three radio sources in the ADG, HR, and DWC lists. Inspection of Figure V-6 suggests that scans #5 and #7 responded to ADG--042.1-0.6 at 1810 and 1500 Jy, respectively. This more compact radio object produces about 6 Jy at 1414 MHz and decreases somewhat with decreasing frequency. At a confidence level roughly equal to AC3, I denote this source as AC4. Scan #6 sensed signals of 1180 and 1420 Jy at points between the three sources in its path. The former, at the 3 σ noise level and equidistant from ADG042.1-0.6 and ADG042.0-0.2, will be ignored; the latter, closer to the stronger source ADG041.4-0.4, shall be called, with marginal confidence, AC2. ADG041.4-0.4 emits 9 Jy at 1414 MHz and less at lower frequencies; it covers roughly $19' \times 12'$. It remains clear, however, that the signal-to-noise for all these sources is not very high and the possibility of confusion must be considered in this crowded region. Thus, some of the sightings may be spurious; more on the topic of confidence follows in Part D.

Source AC5

Sources AC5 through AC8 were detected on trajectories that run parallel over a degree apart, so that no multiple sightings were possible. Moreover, AC5 lies farthest from the plane ($b = +7.2^{\circ}$) of the sources on our list in a spot devoid of known IR or radio sources. However, an elongated, moderately bright nebula, Lynds 35.99+6.80, does reside on the path, and our signal, 1460 Jy, was high enough to merit attention, with low confidence, as AC5. Figure V-8 shows the relevant spatial relations.

Source AC6

At 1700 Jy, AC6 represents the detection of another Sharpless HII

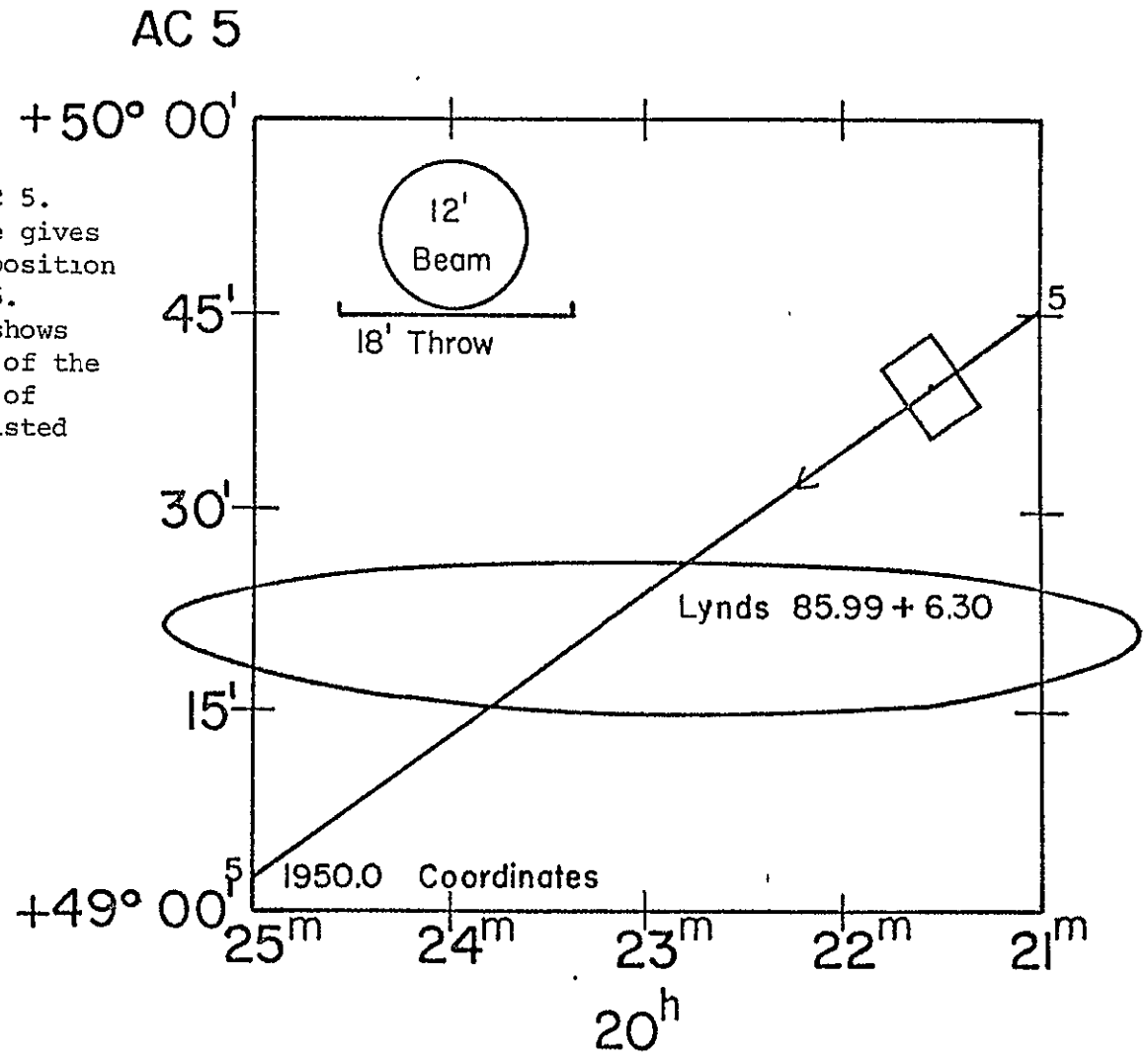

Figure V-8: AC 5. The rectangle gives our nominal position along scan #5. The ellipse shows the position of the bright patch of nebulosity listed by Lynds as 85.99+6.30.

region, #112. A list of previous observations, referenced to Figure V-9, follows as Table V-5, with the columns arranged as before.

TABLE V-5: AC6

DESIGNATION*	BEAM '	SYMBOL	α h m	δ ° '	ν MHz	λ μ	FLUX Jy	EXTENT
AC6	12		20 31.3	+45 27		100	1700	
L83.77+3.32		⬡	20 32	+45 30		Optical		13 × 13
S112		⬡	20 32.2	+45 29.2		Optical		15 × 15
BCV		⬡	20 32.2	+45 29		Optical		9 × 7
J69		⬡	20 32.2	+45 29		Optical		12 × 12
NK2.07	6	▽	20 32.0	+45 32	8000		2.7	10 × 14
HBMR21	38	□	20 31.2	+45 23	3200		20	30 × 30
FC44	10	○	20 32.2	+45 27.7	1400		13.6	12 × 12
FF2032+45	4 × 114		20 32.1	+45 37	408		7.9	6 × 6

*See Table V-2.

The HII region is quite circular and fairly bright, with size estimates ranging from 9 to 15 arcminutes. Dickel, et al (1969) divide this region into two smaller optical areas. Radio position and source extent, given by FC and NK, agree quite well, while the broader beam of the HBMR survey defines a larger source and a position about 20' to the west-southwest. With similar beams, FC and NK measure 13.6 and 2.7 Jy, respectively, indicating a non-thermal source; the 20 Jy found by HBMR presumably results from including a greater area. Lastly, a 408 MHz sighting tallies 7.9 Jy from a 6' source centered north of the optical center. Figure V-11 superposes our scan on FC's contour plot; the agreement is good, placing moderate confidence in this identification.

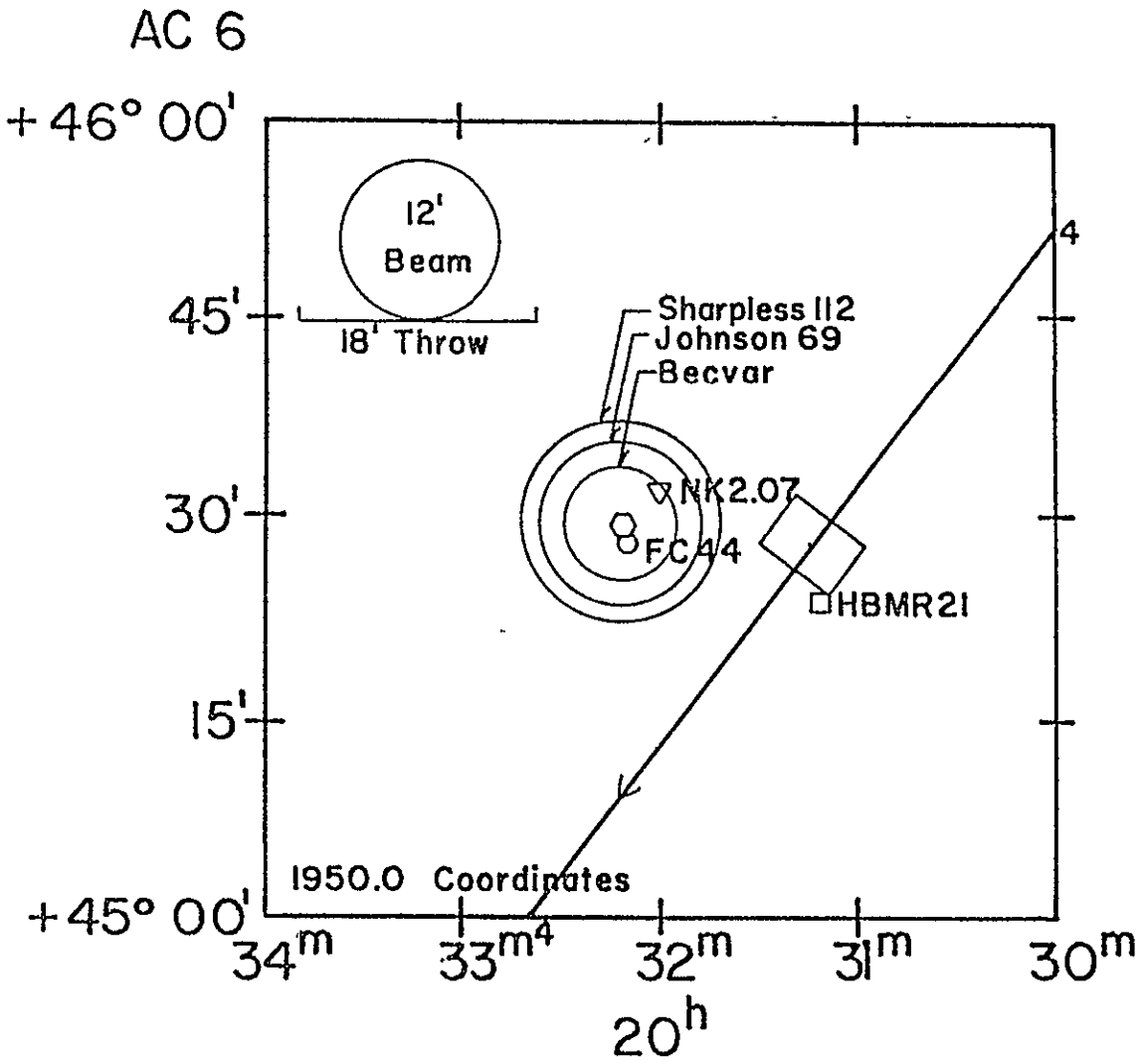

Figure V-9: AC 6. The circles about the hexagon show the mean visible extent of the HII region, according to three different catalogs. The rectangle gives the nominal position along our scan #4. See Table V-5.

Source AC7

Our third Sharpless HII region, #115, was observed along scan #5 at a level of 2000 Jy. Again, a roster of observations follows as Table V-6, keyed to Figure V-10 and formatted as usual:

TABLE V-6: AC7

DESIGNATION*	BEAM '	SYMBOL	α h m	δ ° '	ν MHz	λ μ	FLUX Jy	EXTENT '
AC7	12		20 36.0	+46 27		100	2000	
L84.81+3.88			20 33	+46 40		Optical		60 × 40
S115		□	20 33.0	+46 42.2		Optical		50 × 50
NK2.10	6		20 33.4	+46 51.0	8000		2.3	20 × 7†
NK2.11	6		20 33.5	+46 37.0	8000		2.7	8 × -†
HBMR22	38	▽	20 33.4	+46 39	3200		50	Point
MUL19	33 × 41		20 33.6	+46 42.6	1420		47.6	
FC46	10	⬡	20 33.5	+46 36.0	1400		71	27 × 33
W71	34	△	20 33.4	+46 52	1390		85	60 × 54
BEN61	14 × 276		20 33.4	+46 52	178		60	
3C416.1	72 × 460		20 33.4	+46 52	178		60	40 × 40

*See Table V-2. †Estimate.

Optically, the nebula contrasts strongly with circular, well-defined S112; S115 is large and amorphous, with considerable brightness variation. L and S define a diameter of nearly a degree, while the more detailed catalog of Dickel, et al (1969) subdivides the region into nine smaller sources (DWB 180-185, 187, and 189-190). Radio observations peak at two locations following the north-south ridge discernable in Figure V-11, another excerpt from the FC survey. NK detects both at 8000 MHz, while beams of increasing size move the peak northward from the southern point

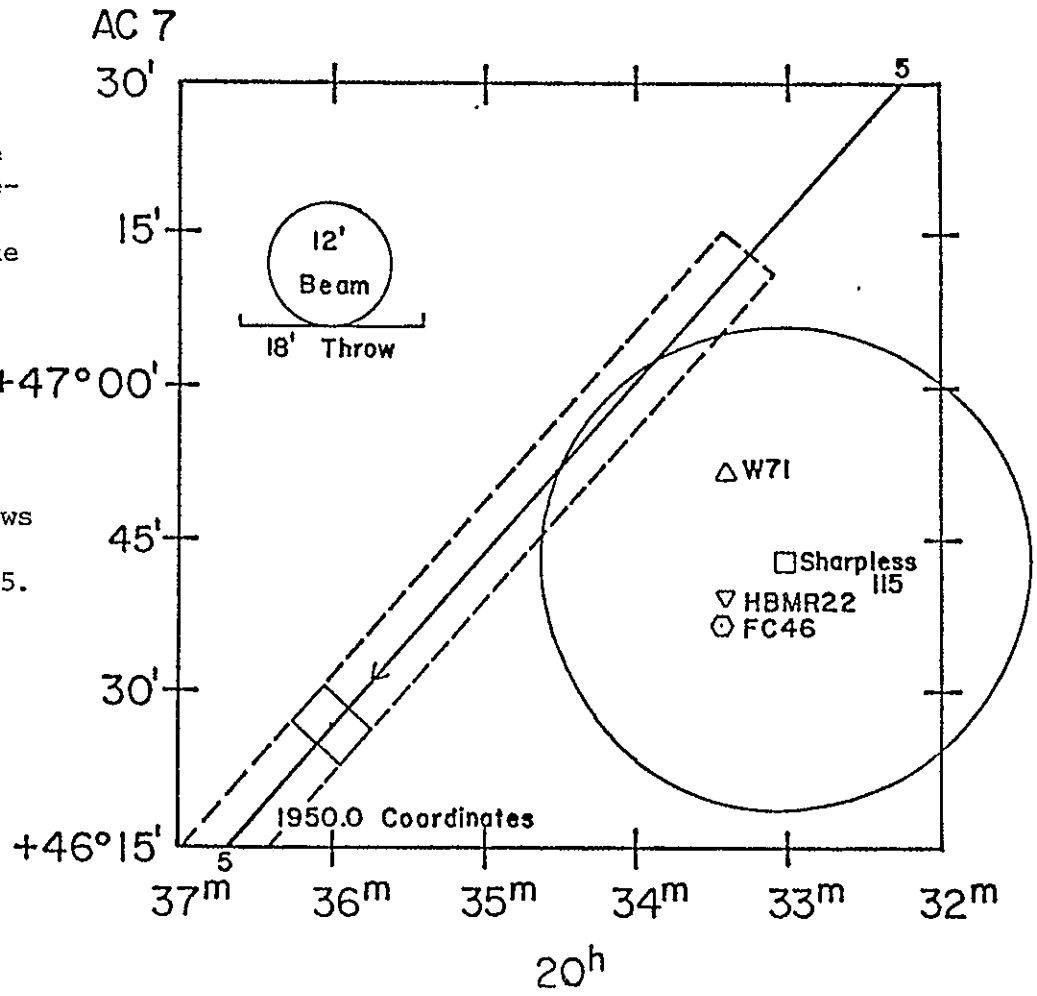

Figure V-10: AC 7. The dotted rectangle along our scan #5 represents our uncertainty in azimuth due to the vanished derivative in the low gain magnetometer output at this particular azimuth. The solid rectangle is the nominal position. The circle shows the mean visible extent of Sharpless 115. See Table V-6.

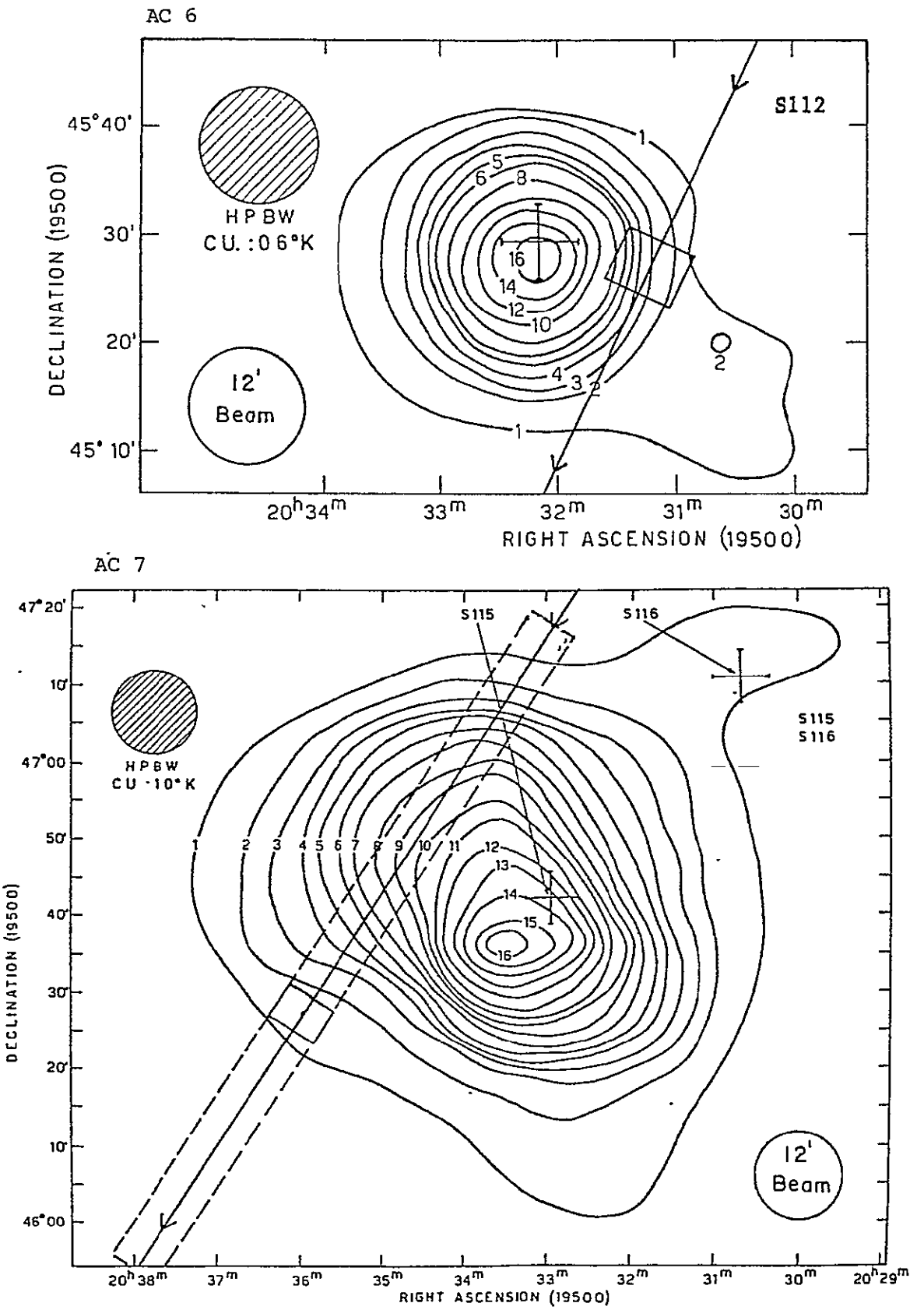

Figure V-11: AC 6, 7 — Radio Continuum Maps. Our scans are superposed on 1400 MHz maps from Felli and Churchwell (1972). See Figures V-9 and 10.

at +46° 36' to the center of the extended source at +46° 52'. General concurrence on overall size prevails; the flux from the extended source seems fairly constant at 50-100 Jy. Admittedly, the balloon position lies 45' to the east-southeast of the center, but two factors lead me to make the identification anyway: First, the detection happened just when the low gain magnetometer was peaking, causing the derivative to vanish. Therefore, our position along the scan may be in error by as much as a full degree of arc. Secondly, the nebula appears extremely irregular, so that components removed from the optical and radio peaks are plausible.

Source AC8

Our final source detection, at 1660 Jy, took place on our first scan through the galactic plane in Cygnus, grazing an extreme rich concentration of IR and radio sources: The Cygnus X Region. The usual compilation of other observations follows as Table V-7. It is keyed to Figure V-12 and is arranged as before.

TABLE V-7: AC8

DESIGNATION*	BEAM '	SYMBOL	α h m	δ ° '	ν MHz	λ μ	FLUX Jy	EXTENT '
AC8	12		20 39.8	+41 54		100	1660	
AFGL2631	3 x 10	□	20 39.4	+41 40.4		11 20	119 195	
HFE69	12	△	20 38.6	+41 29		100	65000	30 x 30
HFE70	12	△	20 39.4	+42 03		100	22000	Point
DR23	11	⬡	20 39.1	+41 46	5000		114	27 x 30
WEN81.6+0.0	11	⬡	20 39.1	+41 47	2695		134	25 x 20
PD23	10	⬡	20 39.0	+41 47	1414		186	27 x 40
W75	34	⬡	20 38.6	+41 57	1390		270	60 x 48

TABLE V-7: Continued

DESIGNATION*	BEAM	SYMBOL	α h m	δ ° '	ν MHz	λ μ	FLUX Jy	EXTENT '
CTB96	48		20 37.5	+41 55	960		1200	120 × 120†
FF2039+41	4 × 114	X	20 39.3	+41 54	408		12.2	6 × 6

*See Table V-2. †Estimate.

Before continuing, a note on nomenclature: W75 and CTB96 refer to a large area of emission, which PD and DR have subdivided into two objects. The former, PD21 = DR21, has been extensively observed in the IR and is a well known non-thermal source. The latter seems to be thermal and is included above.

Optically, the region is highly obscured, close to the axis of the Cygnus Rift. The AFGL and DR/PD positions are separated by about 7', while the position given for HFE70 resides roughly 16' to the north-northeast of DR/PD23. However, a recent paper by Emerson (1976) argues that all of the postions given by Hoffmann, et al (1971b) for sources in the Cygnus X region — HFE 64-70 — include a systematic error of about 20' in the same direction. Therefore, HFE70 can indeed be identified with DR/PD23. FF report a 6.1' subcomponent 5' to the northeast of DR23, close to our IR position, at 408 MHz. The radio extent seems to be around half a degree for the DR/PD23 part of W75, while HFE70 was described as a point source.

The IR flux climbs rapidly from 11 to 20 microns according to the AFGL measurements; HFE70 displayed a peak flux of 22,000 Jy. Radio observations by PD and DR indicate a spectral index of -0.2 for the object, an emission measure of 2.3×10^4 pc-cm^{-6}, an electron density of 46 cm^{-3}, and a mass of 1300 solar masses (Pike and Drake, 1966). Wend-

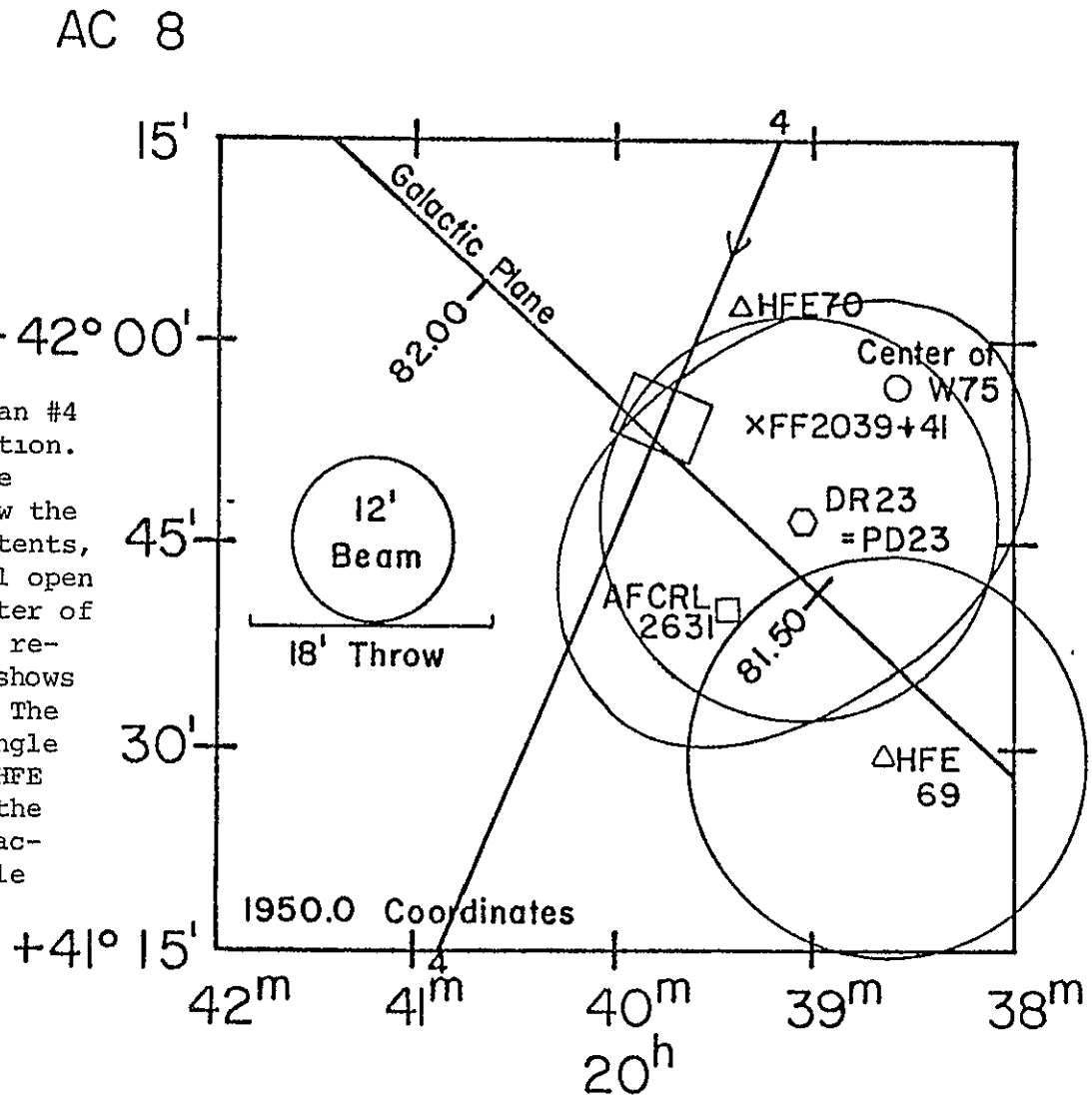

Figure V-12: AC 8.
The rectangle along scan #4 gives our nominal position. Around the hexagon, the circle and ellipse show the rough DR23 and PD23 extents, respectively. The small open circle locates the center of the extensive emission region, W75. The square shows AFCRL, now AFGL, 2631. The circle around the triangle depicts the extent of HFE 69. The numbers along the galactic plane are galactic longitude. See Table V-7.

ker (1970) has also observed the region at 2695 MHz and derived an emission measure of 2.6×10^4 pc-cm^{-6}. The W and CTB surveys, with larger beams, tally 270 Jy and 1200 Jy at 1390 and 960 MHz. Also in DR/PD23, the H158α line at +5.7 km/sec was found by Dieter (1967), and the H109α line at +0.2 km/sec by Reifenstein et al (1970). Mezger, et al (1967) adopted a distance of 1.5 kpc for PD/DR 21 and 23 on several grounds. Again, a thermal radio spectrum with a large IR excess is suggested. Our own detection apparently occurred on the eastern edge of the source, since our flux was roughly an order of magnitude lower than that of HFE.

D. Source Confidence and Statistics

Because of the unusual nature of our scans during Flight C-1, special problems arise in quantifying our confidence in the nine sources. At the same time, we enjoy the opportunity to exploit an unbiased sample of sky up to 44 degrees from the galactic plane. Finally, our "random" sample of sources, though quite small, suggests the type of object we are likely to observe at 100 microns on future flights.

Fortunately, the noise that emerged during the half hour of interest appeared well-behaved on the strip chart record, i. e., rather free from spikes and uniform. Spot checks of digital output obtained when far from the galactic plane confirmed this observation; the root-mean-square (σ) noise level was close to 420 Jy on several typical records. Consequently, I use this σ, rather than compute separate σ's for records adjacent to each suspected signal, since such adjacent records are slightly noisier, probably due to fainter emission sources near the plane.

Identifying potential sources involved a visual inspection of the strip chart record. Substantial and repetitive baseline drifts, presumably caused by air ice on the primary scattering off-axis balloon radia-

tion, were eliminated by virtue of their form and 10-30 second duration. Noise spikes were isolated by their appearance on several channels at once, without the proper intervals demanded by the offsets in the focal plane. Proper signals, on the other hand, display the characteristic "derivative" signature, due to chopping: sharp, positive and negative excursions of similar size in an order corresponding to the direction of the scan, between ½ and 2 seconds apart. All suspected data were examined in the digital output to determine heights and times of the peaks. The signatures that met the above criteria and whose amplitude equalled or exceeded $\sim 2.8\ \sigma$ I retained; the peak-to-peak amplitude, expressed in terms of σ, relates our confidence in the observation. Where multiple scans detected signals within 12' of a common center, the square root of the sum of the σ's squared was extracted. The least significant sources, AC2 and AC5, exhibited 3.4 and 3.5 σ deviations, while AC1, with strong signals and multiple detections, displayed 11.9 σ. Table V-2's column 7 contains this information.

Confidence in our source list is buttressed by the correlation of our positions with previously observed objects at optical, infrared, and radio frequencies that could plausibly emit far infrared radiation. I have not adjusted the source significances to reflect spatial correlation, but the coincidence of the signals with known sources, coupled with the absence of signals in areas devoid of known sources, can only improve the odds against spurious detections.

The only other 100 micron survey with substantial overlap is that of Hoffmann, et al (1971b), done by our present gondola's immediate predecessor, Gondola B. Their survey limit was set at about 10^4 Jy, brighter than any of our objects. Our source AC8, however, probably represents

a grazing detection of their source #70 (HFE70). HFE71 and 72 fell between scans #5 and #6 and between #6 and #7, respectively. Our null results far from the plane are apparently unique, since most surveys hug the galactic equator; insofar as Friedlander, et al (1974) report strong IR sources at high galactic latitudes, we cannot add any support.

As stated above, our 100 micron source positions suffer from standard deviations of 5' in azimuth or, more strictly, crosselevation, and 7' in elevation, due to the visible star telescope's beam size and the magnetometer error, except at the magnetometer's peaks, where the derivatives vanish and the errors in crosselevation are much larger, on the order of a full degree. The latter affected our position for AC7. In addition, our 12' beam superposes an additional uncertainty of about 6' on our positions. The flux calibration depends critically on the exact temperature distribution on the calibrator arm; the given fluxes are accurate to only ±50%. Finally, the identifications given in Table V-2 include continuum optical, infrared, and radio sources within 25' of the source positions.

As far as statistics are concerned, the following disclaimer applies: The sample is very small! Basing general conclusions on nine sources presents considerable peril, but in the interests of guiding future surveys, I shal forge ahead.

Over the 32.7 minutes of observing at 66.5° elevation, we covered 143 square degrees. Overlapping scans at the northern and southern transits made about 10 deg^2 redundant, so 133 distinct deg^2 , or .041 sr, were observed. We detected nine sources in this area, so that if the sky exhibited a uniform distribution, roughly 2800 objects brighter than

1400 Jy would exist. Alternately, I could retain the 143 deg^2 coverage and count each detection as a distinct source, but that approach would over-estimate the total population due to the fortuitous multiple detection of AC1.

At any rate, a uniform distribution is extremely unlikely, since other surveys and general models of IR emission associate 100 micron sources with the galactic plane, and our own list tallies no sources with $|b|>7.2^{o}$. When adding the number of sources in progressively wider bands centered on the galactic equator, I obtain the following table. Overlapping scans have been removed from the area tabulated in column 4.

TABLE V-8: SOURCE DISTRIBUTION WITH GALACTIC LATITUDE

ZONE	AREA OF ZONE deg^2	NUMBER OF SOURCES	AREA OF SCANS deg^2	SOURCES/ DEGREE^2	SOURCES IN ZONE
$\|b\|<1^{o}$	720	4	3.3	1.2	860
$\|b\|<3^{o}$	2159	6	11.4	0.5	1080
$\|b\|<5^{o}$	3595	8	20.0	0.4	1440
$\|b\|<10^{o}$	7164	9	42.9	0.2	1430

The sources are definitely concentrated on the galactic plane; about one half are within one degree of the plane. A thorough survey within a few degrees of the galactic equator would turn up on the order of a thousand sources. The absence of any sources beyond $b = 7.2^{o}$ in a sky area several times large, 90 deg^2 , suggests that 100 micron sources of similar flux density are at least one order and more probably two orders of magnitude less plentiful away from the plane. Note again that this conclusion derives from our overall confidence in the sources we did detect. Moreover, the character of the galactic longitudes observed on

Flight C-1 strikes me as rather typical. Hoffmann, et al, (1971b) showed a general concentration of IR objects toward the galactic center and in the Cygnus X area. Our scans grazed the Cygnus X area and intercepted the plane again in the comparatively IR-quiet Aquila region, producing a representative sample. These results are in close agreement with a similar analysis of the data from Gondola B and other observers by Hoffmann and Aannestad (1974).

Looking for explicit information in the ensemble of flux data is less rewarding. The small sample and large calibration uncertainty discourage any statement on source numbers as a function of flux density. The quantity of sources at 100 microns to be expected from a more sensitive survey, must, for the moment, be inferred from experience at other wavelengths.

Since a program for a far IR survey flight from a balloon is constrained by available time at float, orientation of the galactic plane, accessibility of calibration sources, and many other factors, the location of possibly strong 100 micron emitters would help to plan, conduct, and analyze a flight. Since extant far IR surveys are either patchy or unreliable or both, inference from other catalogs, optical, near-IR, and radio, is required. The most striking correlation I have found involves the set of HII regions listed by Sharpless (1959) and observed as continuum souces at 1400 MHz by Felli and Churchwell (1972). Our scans intercepted three of the 137 regions in the set: S76, S112, and S115; we responded to all three and denote them AC1, AC6, and AC7. Sharpless regions associated with strong, well known radio sources, extended beyond 100 arcminutes, or residing in areas mapped by Altenhoff, et al (1970)

were excluded from the Felli and Churchwell sample, but none of our other sources are associated with Sharpless regions. AC5, however, seems related to a Lynds (1965) bright nebula; I should add that Sharpless regions are included in the much more exhaustive Lynds catalog, which we may profitably add to our compilation of possible far-IR emitters.

Extended continuum around 1400 MHz provides another marker. All but one of our sources was clearly associated with radio emission. The Westerhout (1958) catalog has already provided handy nomenclature for areas of strong IR radiaton. AC1, AC7, and AC8 correspond to components of W45, W71, and W75. The smaller and more sensitive beam employed by Altenhoff, et al (1970) in a survey from $l = 335^{o}$ to 75^{o} defined sources near our positions for AC1 through AC4. The only source for which no one lists continuum, up to the completeness of the 1976 Master List of Radio Sources (Ohio State University, 1976), is AC5, but its higher galactic latitude may have permitted it to evade observation. A third aid, the AFGL Rocket Survey (Walker and Price, 1976), lists several sources with strongly rising fluxes between 11 and 20 microns. AC1 and AC8, identified with AFGL2284 and AFGL2631, manifest this behavior; a set of such AFGL objects would be another useful indicator.

Almost as important as the catalogs that suggest far IR emission are those that do not. The IRC catalog at 2 microns (Neugebauer and Leighton, 1969) contains no objects within $20'$ of any of the AC sources. Thus, no stellar, near-IR sources were detected. Similarly, no AFGL sources with spectra peaking shortward of 20 microns were matched. The emission of such objects would be well beyond our present sensitivity at 100 microns. Hopefully, our observations will bridge the gap that remains between near-

IR and radio surveys. Seeking such correlations with a larger sample and greater sensitivity should prove even more instructive.

E. Discussion

As mentioned in Chapter I, many 100 micron sources are associated with HII regions, and many of these are compact HII regions (as defined by Mezger, et al, 1967), which are high density cores amidst a more extensive volume with lower electron densities. These cores are often smaller than 1 pc in diameter and can have very large emission measures, often exceeding 10^7 $cm^{-6}pc$. By virtue of their large flux gradients, these compact regions are conspicuous to far-IR instruments employing differential chopping. Emerson (1976) shows that the 100 micron sources detected by Hoffmann, et al (1971b) in the Cygnus X region are those with the highest peak, rather than integrated, flux densities at radio frequencies. This indicates that compactness, or strong central concentration, rather than extended, uniform structure, is preferentially detected in the far-IR.

It is instructive to make a crude luminosity calculation for the two sources we detected for which distance estimates are available. For AC1, an OH emission line at 1665 MHz has a radial velocity of +29 km/sec (Turner, 1976) which corresponds to a kinematic distance of 2 kpc. Mezger, et al, (1967) give a distance of 1.5 kpc for DR 23, the radio source we identify with AC8.

Using the following formula from Olthof (1975),

$$\frac{L_{neb}}{L_{\odot}} = 3 \times 10^{13} (D)^2 (F_{IR}), \qquad (V.1)$$

where D is the distance in kpc and F_{IR} is the integrated infrared flux, we get the luminosity in terms of the solar luminosity. In the absence of additional far-IR spectral information and recognizing that the near-IR flux is rising steeply, I shall assume that the bulk of the IR flux is contained in a band about three times wider than that of our 100 micron detector. For AC1, with a flux density of about 3500 Jy at 100 microns,

$$F_{IR} = 3500 \cdot 10^{-26} \frac{W}{m^2\text{-Hz}} \cdot 3 \cdot 1.7 \times 10^{12} \text{ Hz} = \qquad \text{(V.2)}$$

$$1.8 \times 10^{-10} \frac{W}{m^2} .$$

This produces a luminosity of 2.2×10^4 $L_\odot$ for AC1, which corresponds to a BO ZAMS (zero-age main sequence) star (Panagia, 1973). Although we believe that AC8 represents the edge of HFE70, the flux of 1700 Jy we detected can serve as a lower limit; a similar computation yields 6×10^3 $L_\odot$, equivalent to a type B1 ZAMS star. For AC1, a BO star is capable of producing the free-free radio continuum observed; for AC8, the stronger free-free emission observed from DR23 suggests an earlier type star than B1, in keeping with the higher IR flux reported by Hoffmann, et al (1971b) and our lower limit. Anyway, BO and earlier stars can maintain HII regions, so the picture is consistent.

Multi-band observations of these objects would permit a much more precise estimate of the total luminosity, since the shape of the IR spectrum could be well determined. The greater sensitivity of our cooled telescope will extend the multi-band photometric work of Olthof (1975) and others to fainter, more typical galactic objects.

CHAPTER VI

Summary and Outlook

A. System Performances and Improvements

Like most scientific projects, our balloon-borne cryogenic telescope undergoes continuous development. Especially after the first flight, which pointed to several improvements while collecting a promising amount of data, a critical review of performances and possibilities is appropriate. This is done in Part A, system by system. A seventh category, data analysis, is added.

Electronics System

Both our and NCAR's electronics had no problems, except for slightly less telemetry range than we expected. Likewise, the batteries behaved properly, despite their age of about three years at the flight epoch; storage in a refrigerator apparently maintains their nominal shelf life of three years. No important module, telemetry, or battery electronic changes are contemplated. To expedite telemetry integration, a pair of telemetry shelves, adjustably bolted together with vertical columns of threaded rod and slipped into the electronics box on a pair of rails attached with split clamps to the inner structure, has been constructed. The shelf surfaces contain an array of 2 by 2 inch square holes so that components can be held down with nylon ties and cables can run directly between the two levels.

Gondola Pointing and Suspension Systems

The elevation system worked up to par; our star positions indicate an error of 7' rms in elevation, most of which stems from the visible star telescope's beam size. The average zero correction was 27' below the

nominal elevation. On landing, the clutch failed to slip, so at the drive end of the gear train, the solder joint joining the small spur gear to its shaft broke. The clutch has been improved with a better lining and truer adjustment. The main post weathered the flight successfully, but two of the three clamshells were lost before impact and the magnetometer cables were slightly strained when the clamshells separated.

Clearly, one of the two major failures of Flight C-1 was the loss of azimuth stabilization. Although the magnetometers functioned properly, the inertia wheel failed to rotate, which the tachometer reported. We suspected that telescope cables had slipped from a tie point and jammed the wheel, or that bearing lubricant froze, but a subsequent chamber cold test revealed that the motor simply shorted out. Disassembly found a tiny crack in the Teflon insulation of a power lead to the brush ring, which must have touched the case when cold. Occurring at a tight bend and hidden when the upper and lower torque motor housings are joined, the fault has been remedied by relieving the bend and twisting the wires more carefully. Less generous lubrication of the bearings is also in order.

Another potential difficulty is the large increase in rotational inertia over the previous gondola due to the weight of the new telescope and the consequent need for 175 pounds of extra lead weight on the electronics side to counterbalance the telescope. Although the torque motor seems capable of handling the load, moving the main post toward the telescope six inches would decrease the need for extra counterweight, cutting the gross load by 150 pounds and the rotational inertia by about 900 lb-ft^2.

Structural System

The main framework survived the flight with only minor bending below

the lower main square from a lateral blow. Telescope protection was excellent. The crush structure collapsed rather completely; few straight members remained, indicating that shock was absorbed evenly, just as planned. The next crush structure will be a copy of the first. The delicate tent superstructure was badly distorted by the impact, but it and the seal to the dewar below fulfilled their objective of preventing further leakage of air into the dewar, since the ice buildup either stopped or sublimed slightly at float. Again, the replacement will be virtually identical, except that .016 inch aluminum will comprise the sides instead of .004 inch polyethylene, and will house a lid opening downward rather than upward. Below the tent, the polyethylene barrier will also be replaced by aluminum, which will provide a floor for the tent from its foundation rectangle to just outside the O-ring groove on the octagonal collar. This will eliminate the difficult geometry of the dewar exterior below the collar and greatly simplify pre-flight sealing. One other change involves the helium vent; in place of the spring-loaded cord below an extension of the tent on the downside of the dewar, an aluminum tube will carry excess helium from the tent to the bottom of the main framework.

The other major failure of Flight C-1, which seriously affected the other telescope systems, concerned the leakage of air into the telescope, icing the optics. Very little ambient air — on the order of a few cubic centimeters — amounts to enough frost to degrade the experiment, so that trapped air pockets, imperfect gaskets, and cracks in the lid's rigid foam insulation represent serious weaknesses. The flight lid was designed with minimum weight and maximum insulation in mind; we assumed that the flow of boiloff and flush gas would keep the interior free of air. Nonetheless,

iceup took place during preparation for the flight. Post-flight analysis led us to build a somewhat heavier vacuum lid, capable of withstanding atmospheric pressure, with an insulating layer projecting into the dewar. This plug, made of polyester fiber (Frostline Company) instead of rigid foam, is sandwiched among stainless radiation shields. The new lid itself was machined into a waffled disk from a single 1-1/2 inch aluminum plate; its thickness and rigidity permit a reliable O-ring seal. The lid is hinged and clamped by a mechanical arrangement conceptually similar but more massive than its predecessor, except that clamping pressure is applied to the lid only at the center via a single aluminum beam instead of along parallel angles. We intend to pull a vacuum on the system before and after LN_2 precooling to remove ambient air and the nitrogen atmosphere, respectively. The new configuration replaces flushing with evacuation, uses a clamped O-ring instead of flexible polyethylene as a gasket, and features open fibers in place of rigid foam in the lid plug. Coupled with cryogenic improvements mentioned below, the condensation problem should disappear.

Cryogenic System

The main dificulty with cryogenics, other than the iceup problem dealt with above, was the inconvenience of filling the helium vessel. The need for around 100 liters of LHe for cooldown and 30 liters for refill meant that the standard 110 liter supply dewar, the largest we could accommodate with the existing transfer line and dewar access, was usually inadequate, since such dewars are rarely delivered full and lose a few liters each day. Switching from one supply dewar to another consumes time, wastes cryogen, and probably introduces more air. A longer, flexible line, part of which remains in the dewar permanently, is the obvious solution.

Now, 500 liter dewars, the next standard size, can be exploited, and the fill line can be connected by a bayonet mounting at the collar, rather than be inserted with each fill.

In flight, the cryogenic system behaved as the final Hughes test indicated. The block held a steady temperature, and the LHe lasted through the flight. No additional iceup occurred at float.

Optical System

The optics presented no difficulties during flight; the same held for the chopper and calibrator. A spectacular success was claimed by the visible star telescope, whose detection of faint stars along the scan trajectories enabled us to reconstruct the orientation. The landing damage to its preamp and long sky baffle was quickly repaired.

Detection System

Due to the ice on the primary, neither the 20 micron SBPC nor the 50 micron CUPC detected any sources. They did display, along with the sucessful 100 micron CUPC, long period (about 20 seconds) baseline drifts, which we believe were caused by scattered radiation from the balloon. These drifts were most pronounced at 20 microns, where the photoconductor was driven into saturation. Since the effect was strongest at 66.5° el, only a few degrees from the edge of the balloon, and diminished at lower elevations, balloon radiation, scattered by the frost, is implicated. Moreover, the drifts had characteristic profiles which repeated at the gondola's rotation period. Finally, the background flux was nine times that expected from the atmosphere and membrane. These three phenomena demonstrate that the SBPC behaved reasonably under the overwhelming background. It should be noted that the balloon itself, presumably at the ambient temperature of -55 °C, had a peak flux at 13 microns, close to

the SPPC's passband. The constant contribution to the excess loading was probably scattered from the warmer upper part of the dewar, which equilibrated at the temperatures shown in Figure III-24.

The 50 micron CUPC displayed the same drifts to a much smaller extent, remaining far from saturation. Again, the excess background apparently buried any IR detections. Finally, the 100 micron CUPC exhibited these drifts as well, but they did not mask sources as we scanned by in azimuth.

The bolometer, filtered for 100 microns, suffered from five times the noise and one quarter the sensitivity found in lab cryo tests. Because we could not pump on the dewar to achieve 2 ^{o}K during flight preparation, no immediate pre-flight measurements were made. We theorize that helium gas gradually leaked into the bolometer cavity through the epoxy seals under the lens or around the capillary. Such contamination would degrade the responsivity by increasing the thermal conductivity between the detector and the substrate in the cryopumped cavity.

A typical sample of the strip chart record for the IR channels appears in Figure V-2; a table summarizing the predicted performances of all four and the observed performance of the 100 micron CUPC falls on the next page as Table VI-1. Two changes have been made in the focal plane. The rehabilitated bolometer will be flown without its long-wave blocking metal mesh filter, so that IR Channel #4 will be wide, from 75 to several hundred microns. The 50 micron CUPC, IR Channel #2, developed a short in its mounting block during assembly and has been replaced by a somewhat better Ge:Ga PC from Santa Barbara Research Center. A redeployment of filters will have IR Channel #1 covering 45-130 microns and IR Channel #2 covering 75-130 microns on upcoming flights.

TABLE VI-1 DETECTOR SUMMARY

Detector Characteristics

Ch. No.	Wavelength	Type	Fabry Optics	Filters	Half-Power Points	Telescope-Filter Efficiency
1	100μ	Ge Ga Photoconductor	Off Axis Mirror	BaF_2, Black Polyethylene, Diamond Dust	75-130μ	.44
2	50μ	Ge:Ga Photoconductor	Off Axis Mirror	CaF_2, Black Polyethylene, KRS-5, Diamond Dust	45-70μ	.31
3	20μ	Si:As Photoconductor	KRS-5 Lens	Multilayer Interference	18.4-24μ	.41
4	100μ	Ge.Ga Bolometer	Crystal Quartz Lens	BaF_2, Metal Mesh Interference, Diamond Dust	75-120μ	.15

Calculated Performance (50° Elevation)

Ch. No.	Wavelength	Sky Flux at 100,000 Ft. $W\ cm^{-2}sr^{-1}$*	Membrane Flux $W\ cm^{-2}sr^{-1}$	Total Effective Sky and Membrane Emissivity (230 °K)	Power on Detector W	System NEP $W/\sqrt{Hz}$	System NEF $Jy/\sqrt{Hz}$
1	100μ	1.1×10^{-6}	$<7 \times 10^{-9}$	1.7×10^{-2}	3.8×10^{-9}	1.9×10^{-13}	120
2	50μ	2.6×10^{-6}	5×10^{-8}	1.0×10^{-2}	6.5×10^{-9}	3.0×10^{-13}	135
3	20μ	2.8×10^{-7}	1.5×10^{-6}	2.0×10^{-3}	5.8×10^{-9}	1.0×10^{-13}	30
4	100μ	1.0×10^{-6}	$<6 \times 10^{-9}$	1.7×10^{-2}	1.1×10^{-9}	2.1×10^{-13}	150

Observed Performance (50° Elevation)

Ch No.	Wavelength	Chopper Induced Offset, W	Power on Detector, W	System NEP $W/\sqrt{Hz}$	System NEF $Jy/\sqrt{Hz}$	System NEB $W\ cm^{-1}sr^{-1}\mu^{-1}Hz^{-\frac{1}{2}}$
1	100μ	2.5×10^{-12}	3.8×10^{-9}	3.2×10^{-13}	210	7.4×10^{-13}

*Traub and Stier, 1976.

Data Analysis

The unexpected nature of Flight C-1 forced us to use the computer extensively to determine the correct orientation. The small number of sources and amount of observing time involved permitted a direct, star-by-star identification procedure. However, should the instrument fly for, say, six hours, perform at the computed sensitivity, and remain near the galactic plane, hundreds if not thousands of detections will compel us to streamline the system.

Basically, the present identification system takes a position in gondola coordinates, transforms to celestial coordinates when gondola position and epoch are supplied, and looks for coincidences with a catalog of star and/or IR sources within an arbitrary angular distance stored in the computer's memory. After Flight C-1, stars were added in an ad hoc manner, using the Atlas Coeli Catalog (Becvar, 1964) and the SAO Catalog (Smithsonian, 1966). After future flights, we intend to use the SAO Catalog on tape as the star list and run through the sequence of sightings for identification. A large computer with disk storage will be necessary for this part. As for IR sources, the correspondences of certain optical, IR, and radio catalogs indicate that a number of such lists should be combined to form a specialized source list. Candidates include:

1) Optical:

   Lynds' Catalogs of Bright and Dark Nebulae, (Lynds, 1962 and 1965),

   Sharpless' Catalog of HII Regions, (Sharpless, 1959), and

   Marsalkova's Comparison Catalog of HII Regions, (Marsalkova, 1974).

2) Infrared:

   Cal Tech Two-Micron Sky Survey, (Neugebauer and Leighton, 1969),

   AFGL Four-Color IR Sky Survey, (Walker and Price, 1976), and shorter

lists from balloon survey groups mentioned in Table I-1.

3) Radio:

Master List of Radio Sources (Ohio State, 1976).

Again, we would put these catalogs on disk and look for coincidences with the sighting list. All positions would be reduced to Epoch 1950.0, as we do presently. With this identification information in hand, along with multiple, overlapping scans, an efficient, complete, useful survey will be possible.

B. Outlook

The success of Flight C-1, despite a number of problems, bodes well for the improved system. The instrument's simplicity and redundancy are well adapted to ballooning, which has the demanding character of space research. We expect to meet the basic observational program of a far-IR multi-band low resolution survey of the galactic plane and specific regions of interest off the plane in a series of flights beginning in the fall of 1977. As the results of Flight C-1 indicate, several thousand new sources can be expected at the sensitivity level of that flight, opening a rich spectral region to systematic study.

Looking ahead, improvements on the 210 $Jy/Hz^{\frac{1}{2}}$ noise equivalent flux level we met at 100 microns could come from two directions. First, new developments in far-IR photoconductor technology sponsored by NASA as part of the Infrared Astronomy Satellite program may provide a welcome improvement in detector sensitivity of a factor of 4. An additional factor of 2 is possible by flying at an altitude of 135,000 feet with the resulting lower sky background. Also, extending the flight into daylight hours, which may not greatly affect far-IR performance, is being consi-

dered. An extra filter in the visible star telescope will block much of the scattered visible background to preserve the reference star field.

Flight planning will again concentrate on the galactic plane as the primary objective; only when the plane is poorly situated for our telescope will we seek objects off the plane. The information gathered from reducing the data from Flight C-1 will help us choose specific objects or area for orientation or calibration purposes. For instance, the Cygnus X region, scanned by Gondola B (Hoffmann, et al, 1971b) and grazed during Flight C-1, has been carefully examined at optical and radio wavelengths. A good map of the region would refine the previous 100 micron picture and anchor the data from Gondola C in previous observations. As stated in Chapter I, in eight flights, a reliable map of the entire plane could be made; this illustrates the effectiveness of balloon-borne telescopes in survey work. We expect Gondola C to fulfill this promise in the coming flight series.

APPENDIX A

The Terrestrial Atmosphere and Infrared Astronomy

The development of infrared astronomy has been strongly influenced by the wavelength and altitude dependent properties of the earth's atmosphere. The wavelength dependence and the gases responsible for the absorption are shown in Figure I-1; water vapor, carbon dioxide, and ozone are the principal absorbers. "Windows" can be roughly defined as spectral regions where $\tau < 1$, or $\log b_\lambda < 0$ in Figure I-1. Several windows are evident between 1 and 14 microns, including those named J, H, K, L, M, and N at 1.25, 1.65, 2.2, 3.5, 4.8, and 10 microns, respectively. Between 17 and 40 microns, a broad but poor window exists, labeled Q (17-25 microns), and Z (28-40 microns). From 40 to 350 microns, the rotational band of water vapor intervenes, beyond which windows fall at 350, 450, 625, 715, and 860 microns. The emphasis of Figure II-1 is on the altitude dependence of transmission and emissivity. It shows these properties at 4.2 km, the altitude of a ground-based observatory on Mauna Kea, at 14 km, the altitude of a typical airborne observation, and at 28 and 41 km, heights relevant to balloon-borne telescopes. At rocket and satellite altitudes, the transmission would be essentially unity and the emissivity would be smaller than 10^{-6}. I shall sketch the development of each technique after discussing the second major factor in the emergence of IR astronomy, the availability of detectors.

Infrared detectors fall into two categories, thermal and quantum. Both have their roots in the early nineteenth century. Thermal detection began when William Herschel "discovered" the infrared around 1800 by placing thermometers beyond the red edge of a prismatic solar spectrum.

(This history follows Smith, (1956) and Kruse, et al (1962)). The thermoelectric effect was described by Seebeck in 1826, the radiation thermocouple was invented by Nobili in 1830, and the thermopile, thermocouples in series, was developed by Melloni in 1833. Langley devised the bolometer in 1880. The thermopile and bolometer were the primary IR detectors well into the twentieth century; they were improved by vacuum operation by Lebedev in 1895 and by Coblentz in 1920, respectively. Until World War II, these detectors were uncooled, observations were confined to the near-IR, shortward of about 30 microns, and studies were concentrated on strong, nearby solar system objects (see Figure I-2). After the war, the Golay cell, a sensitive gas thermometer or pneumatic detector, appeared and 1000 micron observations of the sun and moon were accomplished. Other thermal detectors were developed in the 1950's, but the germanium bolometer, invented by Low (1963), had the required sensitivity to open, in principle, the entire IR spectrum. In practice, high altitude platforms were needed as well.

Quantum detectors, in a strict sense, emerged with the photographic process in the early nineteenth century. Infrared quantum detection began when E. Becquerel noted the effects of IR radiation on emulsions in 1843.[1] Abney introduced IR sensitive dyes into emulsions in 1880, and by the 1920's, special plates for the "photographic infrared" — up to about 1 micron — were available. The first systematic stellar studies were made by Hetzler in the 1930's. However, photographic quantum detection is fundamentally limited by slow response time and the problems of background beyond 1 micron. Bulk photoconductivity, accidentally discovered by Wil-

[1] He also noticed that IR can stimulate or quench phosphorescence. His son, Henri, discovered radioactivity by means of emulsions in 1898, for which he and the Curies shared a Nobel Prize.

loughby Smith, who measured the different resistances of selenium bars in an opened and closed box in 1873, led to modern quantum detectors, photoconductive and photovoltaic devices. The potential of PbS was uncovered by Case in 1917, and military research during World War II speeded its application. PbS and similar intrinsic photoconductors (see III. G. 2.) had the sensitivity to open the near-IR spectrum to about 8 microns. Extrinsic photoconductors, based on silicon and germanium, followed in the 1950's and 1960's, pushing the detector thresholds to somewhat beyond 100 microns. Research up to 1960 is exhaustively covered in a monograph by Bube (1960); a rather current summary entitled The Infrared Brochure can be obtained from the Santa Barbara Research Center in Goleta, California.

The infrared spectral region also represents the technological watershed between incoherent optical and coherent radio astronomical detection. Application of the latter in the IR is impeded by antenna accuracy, local oscillatory availability and tunability, and atmospheric water vapor (Penzias and Burrus, 1973). However, none of these constraints are fundamental. Workers from the University of California at Berkeley (Peterson, et al, 1974) and from NASA-Goddard Space Flight Center (Mumma, et al, 1975) have used optical telescopes to make solar system observations with lasers as infrared local oscillators. The comparison between thermal and superheterodyne techniques around 1 millimeter was made by Low (1966).

Therefore, by the mid-1960's, thermal and quantum detectors sensitive over most of the IR spectrum had been developed.[2] However, at that time, almost all observations had been ground-based. Soon thereafter, new platforms carried these detectors aloft, as displayed in Figure I-3.

[2] Strong and Stauffer (1962) have written a general review of IR techniques for this period.

ORIGINAL PAGE IS
OF POOR QUALITY

Ground-based Observatories

Early work in IR astronomy was reviewed by Murray and Westphal (1965) and by Auguson and Spinrad (1965). The most influential work in the near-IR was that of Johnson and collaborators at the University of Arizona; they observed thousands of stars in many bands and set up a photometric system (Johnson, 1966). In the late 1960's, another major work, the Infrared Catalog, or IRC, was published (Neugebauer and Leighton, 1969). Using a 62 inch telescope with an epoxy resin mirror, they surveyed most of the sky at 2.2 microns. Most ground-based research was confined to the 20 micron window and shortward, but the murky windows at 35 microns (Low, et al, 1973) and at 350 microns (Low, et al, 1970, unpublished observations cited in Harper, et al, 1972) were explored from high altitude observatories in the early 1970's.[3]

Ideal sites for IR astronomy are at high elevations and have very dry air above. In the United States, the Western states offer the best conditions. Much of the research has been conducted on Mauna Kea in Hawaii, White Mountain in California, Mt. Lemmon and Mt. Hopkins in Arizona, and mountains in Colorado and Wyoming. Abroad, observatories in the Swiss Alps, the Pyrenees, the Canary Islands, the Chilean Andes, and in New Zealand have carried out IR observations. A recent book by Allen (1976) covers the near-IR, ground-based effort in some detail.

Airborne Observatories

The American effort commenced in earnest in 1965, when NASA's Airborne Science Office modified a Convair 990 (CV-990) four-engine airliner and a Lear two-engine executive jet for experimental purposes. The former, named the Galileo, could fly at 40,000 feet for about five hours[4],

[3] Two very poor windows lie at 200 and 225 microns (Mankin, et al, 1973).

[4] The Galileo suffered a mid-air collision and crashed near Moffett Field in 1973.

while the latter reaches 50,000 feet and stays up for around two hours. Aboard the CV-990, Kuiper, et al (1967) compiled a solar atlas from 0.85 to 5.1 microns and searched for water vapor in the atmosphere of Venus. However, the real breakthrough into the far-IR came in 1968, when Aumann, Gillespie, and Low (1969) observed Jupiter and Saturn with a bolometer open from 1.5 to 350 microns; the resulting IR excess over the value predicted by insolation represented a major finding. A year later, Low and Aumann (1970) detected the galactic center, M42 and M17, and external galaxies NGC 1068 and M82 from the Lear between 50 and 300 microns.

By then, the American program included a KC-135 (a military Boeing 707) flown by the AEC and AFGL and utilized mainly for eclipse observations and atmospheric research. In England, a Comet IV airliner, similar to the CV-990, was in operation. The French had installed a 32 cm telescope in a Caravelle airliner, slightly smaller than the CV-990, and in 1972, they placed an identical telescope in a Mystere 20, much like the Lear. Lena (1970) reviewed these earlier airborne observatories. A new era opened with the Kuiper Airborne Observatory (KAO), dedicated in 1975. A 36 inch telescope mated to a sophisticated acquisition and tracking system permits arcsecond pointing and versatile scanning programs; the instrument is mounted in a C-141 four-engine military cargo plane capable of maintaining 40,000 feet for about eight hours with 30 tons of equipment on board! The KAO has opened up the entire IR spectrum to detailed photometric, spectrometric, and mapping projects. In fact, we were reassured to learn from our colleague, Paul Harvey (1976), that ACl, the prime sighting of our balloon flight, was detected by his photometer at a comparable flux level from the KAO in October, 1976 (see Cameron, 1976).

The general advantages of airborne over ground-based observatories

are less and drier air above and mobility. The former factor is clearly shown in Figure II-1 and results from the reduction in precipitable water vapor from around 750 microns at Mt. Lemmon in Arizona to about 8 microns at the ceilings of the larger jets and to about 2 microns at those of the smaller jets. Mobility is often an enormous advantage, especially in rare events like occultations, since the aircraft can fly to an optimum location virtually free of weather problems. The benefits of airborne over higher altitude experiments involve the large payload, which includes the astronomers, the accurate pointing, and the high reliability and rapid turnaround of equipment. The hourly cost is relatively low and instrument recovery is not a problem. Nonetheless, enough residual atmosphere remains to restrict throughput, lest the background swamp the signal. Also, the nature of aircraft limits the beam to certain portions of the sky; best results are obtained when one object is examined in detail, making navigation tractable. Sky surveys with bigger beams and study of extended sources are the domain of balloon and rockets.

Balloon-Borne Observatories

The pioneering efforts in balloon-borne astronomy were made by Strong's group at Johns Hopkins and by Schwarzschild's group at Princeton. Strong organized the manned "Strato-Lab" planetary spectroscopy mission in 1959, finding water vapor on Venus, and rearranged the gondola for the unmanned "BAL-AST" series from 1962 through 1964 (Strong, 1965). Schwarzschild followed up the balloon-borne solar observatory Stratoscope I with Stratoscope II. The first of two flights in 1963 set an upper limit for water vapor in the Martian atmosphere (Danielson, et al, 1964, and the second obtained IR spectra for nine stars, in some of which water vapor was found (Woolf, et al, 1964). Since then, balloon infrared

astronomy has evolved in a number of directions (Hoffmann, 1977). Survey instruments are throroughly covered in I. D. High resolution mapping began with the University College, London group in 1971 (Furniss, et al, 1972), and progressed markedly with the 1-meter telescope first flown in 1974 (Fazio, et al, 1974 and 1976b) by a team from the Center for Astrophysics and the University of Arizona. Cosmic background studies were performed by Muehlner and Weiss (1973) from MIT, by Woody, et al (1975) from the University of California at Berkeley, by Robson, et al (1974) from Queen Mary College, and by Mercer, et al (1976) from Leeds College. A discussion of their measurements can be found in Rowan-Robinson (1976). Diffuse emission has been observed by Hayakawa, et al (1976) from Japan, at 2.2 microns, and by Serra, et al (1977) from France and by Low, et al (1977) of the University of Arizona in the far-infrared. Finally, a number of experiments have been designed for solar work; see Kiepenhauer and Mehltretter (1965), Zander (1974), Huguenin (1974), and Strong (1974).

The advantages of altitudes accessible to balloon-borne telescopes are much lower emissivity than at aircraft altitudes and nearly complete transmission. These advantages can be exploited with either much greater throughput for survey work or shorter integration times for mapping. Balloons can lift large packages (up to several tons) for long periods (up to several days) and within relatively low budgets and time periods. These qualities make gondolas attractive test beds for space instrumentation.

Rocket-Borne Observatories

The Naval Research Laboratory initiated rocket research when Tousey flew a UV spectrograph on a V-2 in 1946. Twenty years elapsed before rockets were used for IR research, due to the lag in cryogenic and detector technology. These problems were eventually solved, and groups at NRL

and Cornell University collaborated on a near-IR, LN_2 cooled diffuse background experiment in 1965. Sky brightness upper limits and the earth's nighttime limb darkening were measured (Harwit, 1969). A second attempt scanned the Orion and Crab Nebulae. Then, an LHe cooled telescope, built by Cornell, was flown in 1967 with detectors covering the entire IR spectrum, from 5 to 120 and from 400 to 1600 microns, in order to measure the cosmic background and other diffuse radiation. Houck, et al (1972) summarized the four flights that were eventually made. A similar instrument was built by NRL, sensitive between 10 and 1000 microns (Shivanandan, 1972). A third group at Los Alamos (Blair, et al, 1971) made three flights to measure the background radiation between 1970 and 1972.

The other noteworthy achievement of IR rocket astronomy, especially relevant to this thesis, was the near- to mid-IR survey undertaken by the Air Force Geophysics Laboratory (formerly the Air Force Cambridge Research Laboratory) between 1971 and 1974. A 16.5 cm telescope with four channels (4, 11, 20, and 27 microns) made nine trips above the atmosphere and mapped 37,000 square degrees (90%) of the sky. About 2,000 detections were made, forming the only catalog of the greater part of the sky between the IRC and centimeter-wavelength radio surveys (Walker and Price, 1976).

The main advantages of rocket observations is their extreme altitude, beyond virtually all of the atmosphere. At their ceiling, rocket-borne telescopes can achieve absolute flux measurements, since no window is needed and chopping is not necessary. However, rocket flights are quite short; a typical experiment yields 300 seconds of data. Yet, the very low background on the detectors improves their performance, making the short period more productive.

Space Observatories

Ultimately, IR satellites, the Space Telescope, and the Spacelab will carry the rocket-borne platform to its logical conclusion. The first of these, the Infrared Astronomy Satellite (IRAS), a joint U. S., U. K., and Dutch venture, will survey the sky from 8 to 120 microns with a 60 cm aperture and 2' beam (van Duinen, 1977). An IR photometer, proposed for the Space Telescope, will handle the whole 1-1000 micron range, with diffraction-limited resolution and a thousandfold better sensitivity than the KAO (Neugebauer, 1977). Spacelab, aboard the Shuttle, may be involved in two projects: a 1 meter liquid helium cooled telescope (Gillett, 1977) and a 2.8 meter uncooled telescope (Moorwood, 1977). I should mention here that a classified Air Force spacecraft executed a partial survey at 4, 10, and 20 microns, but the results are still unpublished (Harper, 1976).

APPENDIX B

Emission Mechanisms

Blackbodies, with temperatures lower than 150 ^{o}K, are the most important source of far-IR radiation. Solid particles, like opaque gases, contain huge numbers of atoms which inexorably distribute incoming photons until the body can be characterized by a temperature or small range of temperatures. An elegant derivation of the blackbody spectrum can be found in Harwit (1973) pps. 130-2; a Planck curve is shown, for comparison, in Figure I-4. Perfect blackbodies absorb photons of all frequencies and emit a blackbody spectrum of the appropriate temperature. Usually, the spectra are less tidy, with variations due to non-unity emissivities and temperature ranges within the object or the ensemble of objects.

When dust grains absorb stellar radiation and emit in the IR, the effect of particle size, which is usually assumed to be much smaller than the wavelength, must be considered. The magnitude of the effect is expressed as a dimensionless efficiency, with respect to the grain's cross-section; whether the wavelength dependence of this efficiency is closer to λ^{-1} or λ^{-2} is of great importance in deducing the amount and temperature of radiating dust from observations and in models of dusty HII regions, for example. Discussions of this question, among the many concerning grain size, shape, composition, and location, are frequent in the IR literature: van de Hulst (1957) is an early source, while Wickramasinghe and Nandy (1972) and a number of papers in Wickramasinghe and Morgan (1976), especially Bussoletti, et al (1976), bring the subject up to date.

Of increasing importance beyond 100 microns, free-free radiation refers to Bremstrahlung, the photons emitted by electrons accelerated in

the field of another charged particle. To occur, the medium must obviously be ionized, so that the presence of hot stars or violent activity is required. Radio astronomers call free-free radiation "thermal" to distinguish it from the more exotic synchrotron process, although both involve electrons in tenuous plasmas deflected by electromagnetic fields. Probably the clearly thermal source of most ionizing photons, hot stars, and the absence of blackbody reradiation at radio frequencies determined the usage.

Fortunately, free-free spectra have a distinct character; when optically thin, at high frequencies, the flux is nearly independent of frequency. This occurs because radiation from tenuous clouds is proportional to the free-free opacity, which, in turn, is proportional to $\lambda^2(\ln 1/\lambda)$. The flux is also related to the radiation field in the gas; since low IR frequencies and high HII region temperatures are involved, the Rayleigh-Jeans approximation holds, with its λ^{-2} dependence. Multiplied, the flux is constant, except for the logarithmic term. At low frequencies, the radiation is no longer proportional to the optical depth, since the medium becomes optically thick, and the spectrum falls as λ^{-2}.

Most observed far-IR sources peak around 100 microns, where the thermal emission from dust overwhelms any free-free component. Beyond these IR excesses, the thermal contribution drops precipitously, as the inverse dependences of both emissivity and blackbodies with wavelength combine. Around 1 mm, free-free contributes noticeable to some IR sources, such as DR 21 (Righini, 1975). Moreover, around some very hot Be stars and several cool stars (NML Tauri stars), circumstellar free-free dominates the photospheric continuum beyond a few microns. The turnover point in the free-free spectrum provides critical temperature and emission measure informa-

tion. For a more complete discussion, see Kraus (1966) pps. 311-3 or Harwit (1973) pps. 231-3. Figure I-4 shows a free-free curve similar to that of the Orion Nebula.

Synchrotron radiation is one of the non-thermal mechanisms, in the parlance of radio astronomy. Cause by relativistic particles, usually electrons, that spiral around magnetic fields, the synchrotron quanta are actually cyclotron quanta, strongly forward concentrated and blue-shifted. Again, Kraus (1966) pps. 313-8 and Harwit (1973) pps. 233-9 contain clear descriptions of this mechanism. Figure I-4 shows the spectrum of 3C 147, with wavelength dependences characterisitc of synchrotron self absorption at low frequencies and the convolved effects of a monoergic synchrotron electron spectrum and the declining power law dependence of the electron population with energy at higher frequencies.

Line radiation, while of little importance in broad-band far-IR observations, except with regard to the terrestrial atmosphere, will be of increasing importance as far-IR spectroscopy becomes established. Already, fine structure ionic lines have been observed by Ward, et al (1975) and Baluteau, et al (1977). Recombination lines should be observable, if sufficient resolution to overcome the dominance of thermal over free-free radiation is used (see Churchwell, 1972, and Chaisson, 1976). Molecular transitions, both in gases (planetary and stellar atmospheres and the interstellar medium) and in solids (planetary surfaces and interstellar grains) are more easily observed IR phenomena, on which an extensive literature exists.

REFERENCES

A number of symposia on infrared astronomy and balloon-borne research have been published since the early 1960's and are frequently cited in this thesis. A chronological list, not meant to be exhaustive, follows, with sponsoring agencies and locations. They are also cited in the full bibliography.

Brancazio and Cameron, eds., Infrared Astronomy; Goddard Institute for Space Studies; New York, 1966.

Manno and Ring, eds., Infrared Detection Techniques for Space Research; ESLAB, ESRIN; Noordwijk, Netherlands, 1971.

Swift, et al, eds., Telescope Systems for Balloon-Borne Research; NASA, NCAR; NASA-Ames Research Center, 1974.

Moorwood, ed., HII Regions and the Galactic Center; ESLAB, ESRO, CERS; Frascati, Italy, 1974.

Wilson and Downes, eds., HII Regions and Related Topics; Deutsche Forschungsgemeinschaft, Max Planck Gesellschaft, European Physical Society; Mittelberg, Austria, 1974.

Rowan-Robinson, ed., Far-Infrared Astronomy; RAS; Cumberland Lodge, Windsor, U. K., 1975.

Fazio, ed., Infrared and Submillimeter Astronomy; COSPAR; Philadelphia, 1976.

Dyal, ed., Symposium on Recent Results in Infrared Astrophysics; NASA, AAS; NASA-Ames Research Center, 1977.

A lucid and concise review of infrared astronomy, with an excellent bibiography of its own, has been written by Fazio (1976a). An exhaustive introduction to balloon technology is the compendium by Morris (1975), while the status of ballooning for infrared astronomy is reviewed by Hoffmann (1976). General background and technical information on infrared detection can be found in Kruse, et al (1962), Wolfe, (1965), Hadni (1967) and Kimmitt (1970). Rough comparisons among airborne, balloon-borne, and rocket-borne platforms for sky surveys are made in Ney (1969) and Gaustad (1973). Lastly, a book by Allen (1976), entitled Infrared:

The New Astronomy, is strong on ground-based, near-IR observations, but is inaccurate and incomplete in its discussion of the far-IR. In fact, the first book, excepting the symposium edited by Rowan-Robinson, on far-infrared astronomy, has not yet been written.

Allen, C. W., 1973, Astrophysical Quantities (Third Edition; Univ. of London, Athlone Press, London).

Allen, D. I., 1976, Infrared: The New Astronomy (Wiley, Halsted Press, New York).

Altenhoff, W. J., et al, 1970, "Surveys of the Galactic Plane at 1.414, 2.695, and 5.000 GHz", Astron. Astrophys. Suppl. 1, 319.

Armstrong, K. R., and Low, F. J., 1973, "New Techniques for Far-Infrared Filters", Applied Optics, 12, 2007.

Augason, G. C., and Spinrad, H., 1965, "Infrared Astronomy Review", NASA TM-X-1074.

Aumann, H. H., Gillespie, C. M., and Low, F. J., 1969, "Internal Powers and Effective Temperatures of Jupiter and Saturn", Astrophys. J. (Letters), 157, L69.

Avrett, E., ed., 1976, Frontiers of Astrophysics (Harvard Univ. Press, Cambridge, Mass.).

Baluteau, J. P., et al, 1976, "Infrared Line Emission from the Orion Nebula: Detection of [SIII] 18.71μ and [OIII] 88.35μ", Astrophys. J., (Letters), 210, L45.

Becvar, A., 1964, Atlas of the Heavens-II: Catalogue 1950.0 (Sky Publishing Company, Cambridge, Mass.).

Becvar, A., 1972, Atlas Borealis (Second Edition; Sky Publishing Company, Cambridge, Mass.).

Becvar, A., 1974, Atlas Eclipticalis (Second Edition; Sky Publishing Company, Cambridge, Mass.).

Bennett, A. S., 1963, "A Revised 3C Catalogue of Radio Sources", Mon. Not. Roy. Astron. Soc., 127, 163.

Blair, A. G., et al, 1971, "Superfluid-Helium Cooled Rocket-Borne Far-Infrared Radiometer", Applied Optics, 10, 1043.

Bok, B., 1977, private communication.

Brancazio, P. J., and Cameron, A. G. W., eds., 1968, Infrared Astronomy (Gordon and Breach, New York).

Bube, R. H., 1960, Photoconductivity of Solids (Wiley, New York).

Burton, W. B., 1976, "The Morphology of Hydrogen and other Tracers in the Galaxy", Ann. Rev. Astron. Astrophys., 14, 225.

Bussoletti, E., et al, 1976, "Considerations about the Absorption Efficiency of Dust Particles in the Infrared", in Wickramasinghe and Morgan (1976) p. 143.

Cameron, R. M., 1976, "NASA's 91-cm. Airborne Telescope", Sky and Tel., 52, 327.

Campbell, M. F., et al, 1977, "Discovery of Far-Infrared Sources with a New Balloon-Borne Helium-Cooled 0.4-m. Telescope", in Dyal (1977) p. 52.

Caswell, J. L., 1966, Thesis, Univ. of Cambridge; see also Caswell, et al, (1977).

Caswell, J. L., et al, 1967, "A Survey of Radio Emission at 178 MHz", Mem. Roy. Astron. Soc., 72, 1.

Chaisson, E. J., 1976, "Gaseous Nebulae and their Interstellar Environment", in Avrett (1976) p. 259.

Churchwell, E., 1972, "Radio Recombination Lines: An Observer's Point of View" in Carson, T. R. and Roberts, M. J., eds., 1972, Atoms and Molecules in Astrophysics (Acad. Press, London) p. 277.

Clark, D. H., and Crawford, D. F., 1974, "A Catalogue of Small-Diameter Radio Sources Close to the Galactic Plane", Aust. J. Phys., 27, 713.

Danielson, R. E., et al, 1964, "Mars Observations from Stratoscope II", Astron. J., 69, 344.

Day, G. A., et al, 1970, "A Low Latitude Survey from $l = 37^{\circ}$ to 47° at 2.7 GHz", Aust. J. Phys. Suppl., 13, 11.

Dickel, H. R., et al, 1969, "The Cygnus X Region: Catalogue and Distances of Optically Visible HII Regions", Astron. Astrophys., 1, 270.

Dickman, R. L., 1977, "Bok Globules", Sci. Am., 236, 66.

Dieter, N. H., 1967, "Observations of the Hydrogen Recombination Line 158α in Galactic HII Regions", Astrophys. J., 150, 435.

Downes, D., and Reinhart, R., 1968, "Microwave Observations of the Cygnus X Region", Astrophys. J., 144, 937.

Dyal, P., ed., 1977, Symposium on Recent Results in Infrared Astrophysics, (NASA TM-X-73, 190).

Edge, D. O., et al, 1959, "A Survey of Radio Sources at a Frequency of 159 MHz", Mem. Roy. Astron. Soc., 68, 37.

Emerson, J. P., 1976, "Identification of the 100-Micron Sources in Cygnus X", Mon. Not. Roy. Astron. Soc., 177, 113.

Fanti, C., et al, 1974, "A 408 MHz Fan Beam Survey at Low Galactic Latitudes: The Observations and a Catalogue of Small Diameter Sources", Astron. Astrophys. Suppl. 16, 43.

Farmer, C. B., and Key, P. J., 1965, "A Study of the Solar Spectrum from 7 Microns to 400 Microns", Applied Optics, 4, 1051.

Fazio, G. G., et al, 1974, "A High Resolution Map of the Orion Nebula Region at Far-Infrared Wavelengths", Astrophys. J. (Letters), 192, L23.

Fazio, G. G., 1976a, "Infrared Astronomy", in Avrett (1976) p. 203.

Fazio, G. G., et al, 1976b, "Far-IR Observations with a 1-m. Balloon-Borne Telescope", in Rowan-Robinson (1976) p. 21.

Fazio, G. G., ed., 1977, Infrared and Submillimeter Astronomy (D. Reidel, Dordrecht, Holland).

Felli, M., and Churchwell, E., 1972, "Radio Emission at 1400 MHz from Galactic HII Regions", Astron. Astrophys., 5, 369.

Friedlander, M. W., and Joseph, R. D., 1970, "Detection of Celestial Sources at Far-Infrared Wavelengths", Astrophys. J. (Letters), 162, L87.

Friedlander, M. W., et al, 1974, "Detection of New Celestial Objects at Far-Infrared Wavelengths", Astrophys. J. (Letters), 194, L5.

Furniss, I., et al, 1972, "Detection of Far-Infrared Astronomical Sources", Astrophys. J. (Letters), 176, L105.

Furniss, I., et al, 1974, "Far-Infrared Photometry of HII Regions", in Moorwood (1974) p. 61.

Furniss, I., et al, 1975, "40 - 350 Micron Observations of Galactic Sources", Astrophys. J., 202, 400.

Furniss, I., et al, 1976, "Some Balloon-Borne Infrared Telescope Developments at University College, London", in Rowan-Robinson (1976), p. 15.

Galt, J. A., and Kennedy, J. E. D., 1968, "Survey of Radio Sources Observed in the Continuum near 1420 MHz, Declinations -5° to $+70^{\circ}$", Astron. J., 73, 135.

Gatley, I., et al, 1977, "Airborne Far-Infrared Observations of the Galactic Center Region", in Dyal (1977) p. 70.

Gaustad, J. E., 1973, "Infrared Astronomy", in National Research Council - Astronomy Survey Committee, 1973, Astronomy and Astrophysics for the 1970's: Volume 2, Reports of the Panels (National Academy of Sciences, Washington) p. 50.

Gillett, F. C., 1977, "A 1-m. Cryogenic Telescope for the Space Shuttle", in Fazio (1977) p. 195.

Goss, W. M., and Shaver, P. A., 1970, "Galactic Radio Sources: I. High Resolution 5000 MHz Observations", Aust. J. Phys. Suppl. 14, 1.

Hadni, A., 1967, Essentials of Modern Physics Applied to the Study of the Infrared (Pergamon, London).

Harper, D. A., and Low, F. J., 1971, "Far-Infrared Emission from HII Regions", Astrophys. J. (Letters), 165, L9.

Harper, D. A., et al, 1972, "Observations of Planets, Nebulae, and Galaxies at 350 Microns", Astrophys. J., 177, L21.

Harper, D. A., 1976, "Infrared Space Astronomy", Transactions of the IAU, XVIA, (Reports on Astronomy), Part 3, 210.

Harvey, P., 1976, private communication.

Harwit, M. O., 1969, "Infrared Rocket Astronomy", in Maeda, K., ed., 1969, Small Rocket Instrumentation Techniques (N. Holland, Amsterdam) p. 155.

Harwit, M. O., 1973, Astrophysical Concepts, (Wiley, New York).

Hayakawa, S., et al, 1977, "Balloon Observations of the Milky Way at 2.4 Microns", in Fazio (1977) p. 12.

Higgs, L. A., et al, 1964, "The Cygnus X Complex", Mon. Not. Roy. Astron. Soc., 127, 367.

Hoffmann, W. F., et al, 1967, "Far-Infrared Surveys of the Sky", Science, 157, 187.

Hoffmann, W. F. and Frederick, C. L., 1969, "Far-Infrared Observation of the Galactic Center Region at 100 Microns", Astrophys. J. (Letters), 155, L9.

Hoffmann, W. F., et al, 1971a, "100-Micron Map of the Galactic Center Region", Astrophys. J. (Letters), 164, L23.

Hoffmann, W. F., et al, 1971b, "100-Micron Survey of the Galactic Plane", Astrophys. J. (Letters), 170, L89.

Hoffmann, W. F., and Aannestad, P. A., 1974, "100-Micron Surveys of the Northern and Southern Hemispheres", in Swift, et al (1974) p. 7.

Hoffmann, W. F., 1976, "Infrared Astronomy", in National Research Council - Balloon Survey Committee, 1976, The Use of Balloons for Physics and Astronomy (National Academy of Sciences, Washington) p. 107.

Hoffmann, W. F., 1977, "Balloon-Borne Telescopes for Far-Infrared Astronomy", in Fazio (1977) p. 155.

Holden, D. J., and Caswell, J. L., 1969, "178 MHz Observations of Galactic Radio Sources", Mon. Not. Roy. Astron. Soc., 143, 407.

Houck, J. R., et al, 1972, "The Far-Infrared and Submillimeter Background", Astrophys. J. (Letters), 178, L29.

Hughes, V. A., and Routledge, D., 1969, "A Detailed Survey of the Galactic Plane at a Wavelength of 9.26 cm between Longitudes 32° and 49°", Astron. J., 74, 604.

Huguenin, D., 1974, "The Stellar and Solar Tracking System of the Geneva Observatory Gondola", in Swift, et al (1974) p. 167.

Jeffers, W. Q., and Johnson, C. J., 1968, "Spectral Response of the Ge:Ga Photoconductive Detector", Applied Optics, 7, 1859.

Johnson, H. L., 1966, "Astronomical Measurements in the Infrared", Ann. Rev. Astron. Astrophys., 4, 191.

Johnson, H. M., 1955, "Symmetric Galactic Nebulae", Astrophys. J., 121, 604.

Jones, R. C., 1953, "General Theory of Bolometer Performance", J. Opt. Soc. America, 43, 1.

Kawajiri, N., 1970, "Two Continuum Surveys along the Galactic Plane at 8000 MHz", Pub. Astron. Soc. Japan, 22, 165.

Kiepenhauer, K. O., and Mehltretter, J. P., 1964, "Spectrostratoscope: A Balloon-Borne Solar Observatory", Applied Optics, 3. 1359.

Kimmitt, M. F., 1970, Far-Infrared Techniques (Pion, London).

Kraus, J. D., 1966, Radio Astronomy (McGraw-Hill, New York).

Kruse, P. W., et al, 1962, Elements of Infrared Technology (Wiley, New York).

Kuiper, G. P., et al, 1967, "A Program of Astronomical Infrared Spectroscopy from Aircraft", Comm. Lunar Plan. Lab., #93.

Large, M. I., et al, 1961, "A Radio Survey of the Galactic Plane at a Frequency of 408 MHz", Mon. Not. Roy. Astron. Soc., 123, 113.

Lemke, D., and Haussecker, K., 1976, "Chopping Primary for a Balloon-Borne Infrared Telescope", in Rowan-Robinson (1976) p. 47.

Lena, P., 1970, "L'Avion, Plateforme D'Observations Scientifiques", Space Sci. Rev., 11, 131.

Lion, K. S., 1959, Instrumentation in Scientific Research (McGraw-Hill, New York).

Low, F. J., 1963, "A Low Temperature Germanium Bolometer", J. Opt. Soc. America, 51, 1300.

Low, F. J., 1966, "Thermal Detection Radiometry at Short Millimeter Wavelengths", Proc. IEEE, 54, 477.

Low, F. J., and Aumann, H. H., 1970, "Observation of Galactic and Extragalactic Sources between 50 and 300 Microns", Astrophys. J. (Letters), 162, L79.

Low, F. J., et al, 1973, "Ground-Based Observations at 34 Microns", Astrophys. J., 183, 405.

Low, F. J., and Rieke, G. H., 1974, "Instrumentation and Techniques of Infrared Photometry", in Carleton, N., ed., 1974, Methods of Experimental Physics: Astrophysics, Part A: Optical and Infrared (Academic Press, New York).

Low, F. J., et al, 1977a, "Far-Infrared Scans of the Galactic Plane", Astrophys. J. (Letters), 214, L115.

Low, F. J., 1977b, "Infrared Space Astronomy — An Overview", in Fazio (1977) p. 3.

Lynds, B. T., 1962, "Catalogue of Dark Nebulae", Astrophys. J. Suppl. 7, 1.

Lynds, B. T., 1965, "Catalogue of Bright Nebulae", Astrophys. J. Suppl. 12, 163.

Mankin, W. G., et al, 1973, "Observations of Far-Infrared Atmospheric Windows at 44 cm^{-1} and 50 cm^{-1} from Pikes Peak", Nature Phys. Sci., 245, 8.

Manno, V., and Ring, T., eds., 1972, Infrared Detection Techniques for Space Research (D. Reidel, Dordrecht, Holland).

Marsalkova, P., 1974, "A Comparison Catalogue of HII Regions", Astrophys. and Space Sci., 27, 3.

Mercer, J. B., et al, 1976, "A Lamellar Grating Interferometer Experiment to Detect the Spectrum of the Cosmic Background Radiation", in Rowan-Robinson (1976) p. 103.

Mezger, P. G., et al, 1967, "A New Class of Compact HII Regions Associated with OH Emission Sources", Astrophys. J. (Letters), 150, L157.

Mezger, P. G., 1976, "The Distribution of Ionized Gas and Dust in W3(A) and W3(OH)", in Rowan-Robinson (1976), p. 231.

Moore, W. J., and Shenker, H., 1965, "A High-Detectivity Gallium-Doped Germanium Detector for the 40 - 120 Micron Region", IR Phys., 5, 99.

Moore, W. J., 1976, "100μ Detector Development Program — Final Report", NASA Contract NAS-2-8706.

Moorwood, A. F. M., 1974, HII Regions and the Galactic Center (ESRO/ESTEC, Noordwijk, Netherlands).

Moorwood, A. F. M., 1977, "LIRTS: Large Infrared Telescope for Space-Lab", in Fazio (1977) p. 207.

Moran, M., 1965, "Observations of the Radio Emission from the Galactic Plane at 408 MHz", Mon. Not. Roy. Astron. Soc., 129, 447.

Morris, A. L., ed., 1975, Scientific Ballooning Handbook (NCAR-TN/1A-99, NCAR, Boulder).

Muehlner. D., and Weiss, R., 1973, "Balloon Measurements of the Far-Infrared Background Radiation", Phys. Rev. D, 7, 326.

Muller, H. G., 1959, "Messung des Kosmischen Radiokontinuums bei 1420 MHz mit Hohen Temperaturauflösung", Pub. Univ. Bonn, #52.

Mumma, M., et al, 1975, "Infrared Heterodyne Spectroscopy of Astronomical and Laboratory Sources at 8.5 Microns", Nature, 253, 514.

Murray, B. C., and Westphal, J. A., 1965, "Infrared Astronomy", Sci. Am., 213, 21.

National Geographic Society, 1970, Atlas of the World (Nat. Geog. Soc., Washington).

Neugebauer, G., 1977, "Use of the Large Space Telescope for Infrared Observations", in Fazio (1977) p. 185.

Neugebauer, G., and Leighton, R. B., 1969, Two-Micron Sky Survey: A Preliminary Catalog (NASA-SP-3047, NASA, Washington).

Ney, E. P., 1969, "Infrared Space Astronomy", in Doyle, R. O., ed., 1969, A Long-Range Program in Space Astronomy (NASA SP-213, NASA, Washington).

Ohio State University Radio Observatory, 1976, Master List of Radio Sources (Ohio State University, Columbus).

Olthof, H., 1974, "Multicolor Far-Infrared Photometry of Galactic HII Regions", in Swift, et al (1974) p. 51.

Olthof, H., 1975, Far-Infrared Observations of Galactic HII Regions (Thesis, University of Groningen, Groningen, Netherlands).

Panagia, N., 1973, "Some Physical Parameters of Early-Type Stars", Astron. J., 78, 929.

Penzias, A. A., and Burrus, C. A., 1973, "Millimeter-Wavelength Radio Astronomy Techniques", Ann. Rev. Astron. Astrophys., 11, 51.

Peterson, D. W., et al, 1974, "Infrared Heterodyne Spectroscopy of CO_2 on Mars", Nature, 250, 128.

Pike, E. M., and Drake, F. D., 1964, "A High-Resolution Map of the Cygnus X Region", Astrophys. J., 139, 545.

Pipher, J. L., 1973, "Rocket Measurements of the Galactic Background at 100 Microns", in Greenberg, J., and van de Hulst, H., 1973, Interstellar Dust and Related Topics (D. Reidel, Dorcrecht, Holland).

Powell, R. L., et al, 1957, "Low Temperature Thermal Conductivity of Some Commercial Coppers", J. App. Phys., 28, 1282.

Price, K. M., and Graf, W., 1976, private communication.

Putley, E. H., 1964, "Far-Infrared Photoconductivity", Phys. Stat. Sol., 6, 571.

Reifenstein, E. C., et al, 1970, "A Survey of H109α Recombination Line Emission in Galactic HII Regions of the Northern Sky", Astron. Astrophys., 4, 357.

Ricker, G. R., et al, 1973, "Far-Infrared Radiometry from a Balloon-Borne Telescope", AAS Bull., 5, 437.

Righini, G., 1975, 350 Micron Photometry of Galactic Sources (Thesis, State Univ. New York at Stony Brook, Stony Brook, New York).

Robson, E. I., et al, 1974, "Spectrum of the Cosmic Background Radiation between 3 mm and 800 μ", Nature, 251, 591.

Rodriquez, L. F., and Chaisson, E. J., 1977, "A Comparative Study of High Radiofrequency and Far-Infrared Observations of Galactic HII Regions", Cent. for Astrophys. Preprint Series #727.

Rouan, D., et al, 1977, "Far-Infrared Observations of the Galactic Plane and Molecular Cloud S140", Astrophys. J. (Letters), 213, L35.

Rowan-Robinson, M., ed., 1976, Far-Infrared Astronomy (Pergamon, London).

Rowan-Robinson, M., 1977, "On the Unity of Activity in Galaxies", Astrophys. J., 213, 635.

Rükl, I. A., 1965, "Color Map of the Northern Sky", Sky Pub. Co., Cambridge, Mass.

Serra, G., et al, 1977, "Preliminary Results of a Balloon-Borne Observation of the Far-Infrared Galactic Diffuse Emission between $l = 38^{\circ}$ and 55°", in Dyal (1977) p. 71.

Sharpless, S., 1959, "A Catalog of HII Regions", Astrophys. J. Suppl., 4, 257.

Shivanandan, K., 1972, "Infrared Rocket Astronomy", in Manno and Ring (1972) p. 73.

Smith, E. E., 1974, "Flight Electronics, 1963 to Present", in Atmospheric Tech., 5, 14.

Smith, R. A., 1956, "Recent Developments in the Detection and Measurement of Infrared Radiation", Sci. Monthly, 82, 3.

Smithsonian Astrophysical Observatory, 1966, Star Catalog (Smithsonian Institution, Washington).

Soifer, B. T., et al, 1972, "Rocket Infrared Observations of HII Regions", Astrophys. J., 177, 315.

Strong, J., and Stauffer, F., 1962, "Instumentation of Infrared Astrophysics", in Hiltner, W. A., ed., 1962, Astronomical Techniques (Univ. Chicago Press, Chicago) p. 256.

Strong, J., 1965, "Infrared Astronomy by Balloon", Sci. Am., 212, 28.

Strong, J., 1974, "Balloon-Borne Infrared Coronagraph", in Swift, et al (1974) p. 1.

Swift, C., et al, eds., 1974, Telescope Systems for Balloon-Borne Research (NASA-TM-X-62, 397, NASA, Washington).

Traub, W. A., and Stier, M. T., 1976, "Theoretical Atmospheric Transmission in the Mid- and Far-Infrared at Four Altitudes", Applied Optics, 15, 364.

Turner, B. E., 1976, private communication.

Ulrich, R., 1967, "Far-Infrared Properties of Metallic Mesh and Its Complementary Structure", IR Phys., 7, 37.

van de Hulst, H. C., 1957, Light Scattering by Small Particles (Wiley, New York).

van Duinen, R. J., 1977, "Infrared Astronomical Satellite: IRAS", in Fazio (1977) p. 177.

Ward, D. B., et al, 1975, "Detection of the [OIII] 88.16μ Line in M17", Astrophys. J. (Letters), 202, L31.

Walker, R. G., and Price, S. D., 1976, The AFGL Four Color IR Sky Survey: Catalog of Observations at 4.2, 11.0, 19.8 and 27.4 Microns (continued)

(continued) (AFGL-TR-76-0208, Air Force Geophysics Laboratory, Hanscom AFB, Mass.).

Wendker, H. J., 1970, "The Cygnus X Region, VI. A New 2695 MHz Continuum Survey", Astron. Astrophys., 4, 378.

Werner, M. W., et al, 1976, "Infrared Studies of Star Formation", preprint.

Westerhout, G., 1958, "A Survey of the Continuous Radiation from the Galactic System at a Frequency of 1390 MHz", Bull. Astron. Neth., 14, 215.

Wickramasinghe, N. C., and Nandy, K., 1972, "Recent Work in Interstellar Grains", Rep. Prog. Phys., 35, 157.

Wickramasinghe, N. C., and Morgan, D. J., eds., 1976, Solid State Astrophysics (D. Reidel, Dordrecht, Holland).

Wijnbergen, J. J., et al, 1972, "Filters for Far-Infrared Astronomy", in Manno and Ring (1972) p. 243.

Wilson, R. W., 1963, "Catalog of Radio Sources in the Galactic Plane", Astron. J., 68, 181.

Wilson, T. L., and Downes, D., eds., 1975, HII Regions and Related Topics (Springer-Verlag, Berlin).

Wolfe, W. L, ed., 1965, Handbook of Military Infrared Technology (Office of Naval Research, Gov. Printing Off., Washington).

Woody, D. P., et al, 1975, "Measurement of the Spectrum of the Submillimeter Cosmic Background", Phys. Rev. Lett., 34, 1036.

Woolf, N. J., et al, 1964, "Infrared Spectra of Red Giant Stars", Astrophys. J., 140, 833.

Zander, R., 1974, "The Liege Balloon Program", in Swift, et al (1974) p. 26.

Zwerdling, S., et al, 1968, "A Fast, High-Responsivity Bolometer Detector for the Very Far-Infrared", IR Phys., 8, 271.

Zwerdling, S., et al, 1972, "Far-Infrared Spectral Properties of Compensated Germanium and Silicon", IR Phys., 12, 165.